



Université du Québec
à Rimouski

DIAGNOSIS OF WIND TURBINE BLADE DEFECTS AND ICING USING HYPERSPECTRAL IMAGING

A Thesis presented

in partial fulfillment of the requirements of the Doctoral Program in Engineering from UQAC,

offered by extension at UQAR,

for the degree of *philosophiæ doctor*

BY

© **PATRICK RIZK**

JANUARY 2022



Université du Québec
à Rimouski

**DIAGNOSTIC DES DÉFAUTS ET DU GIVRAGE DES PALES
D'ÉOLIENNES À L'AIDE DE L'IMAGERIE
HYPERSPECTRALE**

Thèse présentée

dans le cadre du programme de doctorat en ingénierie de l'UQAC,

offert par extension à l'UQAR,

en vue de l'obtention du grade de *philosophiæ doctor*

PAR
© PATRICK RIZK

JANUARY 2022

Composition du jury :

Mehdi Adda, président du jury, UQAR

Adrian Ilinca, directeur de recherche, UQAR

Jihan Khoder, codirectrice de recherche, Université Libanaise

Rafic Younes, codirecteur de recherche, Université Libanaise

Tiziano Bianchi, examinateur externe, Politecnico di Torino, Italie

Ihab Makki, Université Libanaise et CEA France

Initial deposit on January 27th, 2022

Final deposit on May 13th, 2022

UNIVERSITÉ DU QUÉBEC À RIMOUSKI
Service de la bibliothèque

Avertissement

La diffusion de ce mémoire ou de cette thèse se fait dans le respect des droits de son auteur, qui a signé le formulaire « *Autorisation de reproduire et de diffuser un rapport, un mémoire ou une thèse* ». En signant ce formulaire, l'auteur concède à l'Université du Québec à Rimouski une licence non exclusive d'utilisation et de publication de la totalité ou d'une partie importante de son travail de recherche pour des fins pédagogiques et non commerciales. Plus précisément, l'auteur autorise l'Université du Québec à Rimouski à reproduire, diffuser, prêter, distribuer ou vendre des copies de son travail de recherche à des fins non commerciales sur quelque support que ce soit, y compris Internet. Cette licence et cette autorisation n'entraînent pas une renonciation de la part de l'auteur à ses droits moraux ni à ses droits de propriété intellectuelle. Sauf entente contraire, l'auteur conserve la liberté de diffuser et de commercialiser ou non ce travail dont il possède un exemplaire.

To my dear parents, who have dedicated their lives to building mine, for their constant support, patience, tenderness, and affection in everything they have done to help me get to this point.

All words cannot explain my gratitude to my mother, who supported me throughout my studies and without whom I would not have succeeded. May she discover my love and affection at this moment.

All words cannot express my gratitude and appreciation for the dedication and sacrifices of my father. He is always available for us, and ready to help us, I confirm him my attachment and my deep respect.

In memory of my grandparents, I wish you could have been here at this moment to share my joy. You have always shown me love and affection, you are always present in my hopes and in my heart. Also, in this moment of joy, you have all my thoughts. May your souls rest in peace.

To all the people mentioned and to all the readers, I dedicate this modest work.

ACKNOWLEDGMENTS

First and foremost, I am deeply grateful to God for providing me with the good health and well-being that enabled me to complete this thesis.

There are numerous roots to the reflection that led to this thesis. Professor Rafic Younes` belief placed in me and the fact that he introduced me to Professor Adrian Ilinca are two of the most significant. Both of my supervisors were always open to discussion when I encountered a problem or had a query regarding my research or writing.

Professor Adrian Ilinca, my distinguished supervisor, deserves special thanks for his tremendous counsel, unending assistance, and patience throughout my Ph.D. studies. I am thankful for all of his time, ideas, and financial support in making my doctorate program fruitful and challenging. His excitement and enthusiasm for his study have been contagious, and it has inspired me throughout my Ph.D. journey. I am also grateful for the outstanding example of a successful professor that he has set for me.

I would like to convey my heartfelt gratitude to Professor Rafic Younes, my esteemed supervisor, for his essential guidance, insightful comments, and ideas, as well as his unwavering support and belief in me during my doctoral studies. I am grateful for all the suggestions and advice that have helped me along the way to completing my doctorate. Being one of his Ph.D. students has been a privilege. He was the one who first introduced me the hyperspectral imaging and taught me a lot about it. I am also grateful for the outstanding example of a successful dean, researcher, and professor.

Also, I would like to express my special thanks to Dr. Jihan Khoder for her unwavering support, kindness, and availability during my doctoral path.

For the financial support during my Ph.D. journey, I am grateful to the Lebanese University - Azm&Saade association and the Natural Sciences and Engineering Research Council – Canada (NSERC).

Finally, I want to express my heartfelt gratitude to my parents, particularly my darling sister, for their unconditional support and continuous encouragement throughout my years of study and through the process of research and writing of this thesis. Without them, this accomplishment would not have been possible. Thank you very much!

PREFACE

The wind turbine blade is one of the essential wind turbine components. However, these blades are subjected to different types of challenges such as continuously changing aerodynamic forces, gravitational loads, weather conditions, and lightning strikes. As a result, all blades experience cracking, crazing, delamination, holes at the leading and trailing edges, and ice build-up on the blades. All these challenges reduce the life of the blades, result in a loss of energy production of 30-70%, and some safety issues. Therefore, it is important to perform regular blade inspections. Today, to optimize the conditions for stopping and restarting wind turbines, it is essential to find an innovative solution that detects and quantifies the defect and limits or even prevents the formation of ice on the blades. Several detection systems are known (guided wave, ultrasound, tapping test, optical fiber, thermal imaging), but the detection and localization of these defects remain a significant problem. Indeed, the detection is based on global parameters (temperature, humidity, frequency, etc.), giving general information on the situation of the defect and does not allow a precise and localized quantification. Moreover, these sensors do not detect or forecast ice formation.

Our interest in diagnosing defects on wind turbine blades comes from our desire to expand the technical studies to obtain a better performance of the systems in question. Thus, the main objective of the thesis is to identify, compare and analyze the techniques allowing to have a reliable, effective, and complete detection of the defects on the blades of wind turbines without bringing modifications or significant disturbances to its architecture. Thus, this thesis aims to solve this problem via hyperspectral imaging. Frequencies outside the visible band will characterize the fault. This will optimize the power produced and the power dissipated during the blades' de-icing, whatever icing mitigation system is used.

RÉSUMÉ

À mesure que la demande d'électricité augmente, les réglementations environnementales limitent l'utilisation des centrales thermiques et des sources d'énergie renouvelable ; en particulier, l'énergie éolienne devient de plus en plus populaire dans le monde entier. L'électricité d'origine éolienne n'a cessé d'augmenter au cours des dernières décennies et continuera à le faire dans les années à venir. La production d'énergie éolienne est une technologie mature, avec plus de 740 GW de capacité installée dans le monde. L'exploitation des parcs éoliens pose des défis cruciaux pour maintenir le coût de l'énergie au plus bas. C'est pourquoi, dans ce secteur, la disponibilité des éoliennes et la capacité à détecter précisément les défauts à l'avance sont devenues très importantes. Les pannes inattendues d'un composant d'une éolienne peuvent entraîner des pertes financières importantes. Par conséquent, il est essentiel de détecter à l'avance ou de prévoir les pannes des éoliennes causées par divers facteurs tels que les défaillances électriques ou mécaniques, la dégradation des matériaux, les défauts ou les dommages, etc. Les pales des éoliennes sont les composants les plus chers et les plus exposés, et elles subissent une variété de défauts, notamment des fissures, l'érosion et le givrage, qui réduisent leurs performances. Par conséquent, l'une des tentatives les plus efficaces consiste à utiliser des diagnostics non destructifs des pales d'éoliennes pour prévenir les défaillances catastrophiques et les temps d'arrêt imprévus. Actuellement, l'optimisation des conditions d'arrêt et de redémarrage des éoliennes nécessiterait le développement d'un nouveau système qui identifie et quantifie les défauts tout en limitant, voire en éliminant, l'accrétion de glace sur les pales. La majorité des études dans le domaine du diagnostic des pales se concentre sur le développement d'un système de détection précoce des dommages. Si ces défauts sont découverts à un stade précoce, les temps d'arrêt et les coûts de maintenance seraient considérablement réduits. Cette thèse examine certaines des techniques non destructives récentes pour l'analyse des pales d'éoliennes, ainsi que leur applicabilité, leurs avantages et leurs inconvénients. En effet, la détection et la localisation de ces défauts restent un défi sérieux dans la plupart des systèmes de détection. Ces techniques sont basées sur des paramètres globaux qui fournissent quelques informations générales concernant la situation du défaut dans les pales sans créer une quantification localisée du défaut.

Néanmoins, ces inconvénients peuvent être surmontés par la télédétection. L'imagerie hyperspectrale est une technique d'imagerie spectrale qui intègre l'imagerie et la spectroscopie, permet l'analyse et l'identification de signatures spectrales distinctives, et les attribue aux éléments de l'échantillon examiné. Ainsi, l'objectif principal de cette thèse est d'améliorer la surveillance des pales d'éoliennes en appliquant la technologie d'imagerie hyperspectrale. Cette thèse décrit la mise en œuvre de l'imagerie hyperspectrale dans l'acquisition, le traitement et la reconnaissance des défauts et la détection des fissures, de

l'érosion et des événements de givrage. Les résultats de cette technique sur le terrain montrent que les défauts des pales peuvent être détectés à un stade précoce avec une grande exactitude et précision.

Mots clés : Défaillance des pales, Imagerie hyperspectrale, Détection des pannes, Fissure, Érosion, Givrage

ABSTRACT

As the demand for electricity increases, environmental regulations limit thermal power plants and encourage renewable energy sources. Specifically, wind power is becoming increasingly popular across the globe. Wind-generated electricity has been steadily increasing over the past few decades and will continue to do so in the coming years. Wind energy generation is a mature technology, with over 740 GW of installed capacity worldwide. The operation of wind farms poses crucial challenges to sustain the lowest possible cost of energy. Therefore, in this sector, the availability of wind turbines and the capability to accurately detect defects in advance have become very important. Unexpected breakdowns of a wind turbine component might result in significant financial losses. As a result, it is essential to detect in advance or predict wind turbine breakdowns caused by various factors such as electrical or mechanical failure, material degradation, defects or damage, and others. Wind turbine blades are the most expensive and the most exposed components, and they endure a variety of faults, including cracks, erosion, and ice built-up, which reduce their performance. Therefore, one of the most effective attempts is to use non-destructive diagnostics of wind turbine blades to prevent catastrophic failures and unscheduled downtime. Currently, optimizing wind turbines' shutdown and restart conditions would necessitate the development of a new system that identifies and quantifies faults while also limiting, if not eliminating, ice accretion on the blades. The majority of studies in the area of blade diagnostics focus on developing a system for early damage detection. If these flaws are discovered at an early stage, downtime and maintenance costs would be significantly reduced. This thesis examines some of the recent non-destructive techniques for the analysis of wind turbine blades, as well as their applicability, advantages, and disadvantages. Indeed, the detection and localization of these defects remain a serious challenge in most detection systems that require a large number of defect indications. These techniques are based on global parameters that provide some general information concerning the situation of the flaw in the blades without creating a localized quantification of the default.

Nevertheless, these drawbacks can be overcome by remote sensing. Hyperspectral imaging is a spectral imaging technique that combines imaging and spectroscopy, allowing for the study and identification of different spectral signatures and assigning them to the sample elements under examination. Thus, the main objective of this thesis is to improve wind turbine blade monitoring through the use of hyperspectral imaging technology. This thesis describes hyperspectral imaging's implementation in image acquisition, handling, flaw recognition, and detection of cracks, erosion, and icing events. This technique's field output results show that blade defects can be detected in their early stages with high accuracy and precision.

Keywords: Blade defect, Hyperspectral imaging, Damage detection, Crack, Erosion, Icing

TABLE OF CONTENTS

ACKNOWLEDGMENTS.....	x
PREFACE	xii
RÉSUMÉ.....	xiv
ABSTRACT.....	xvi
TABLE OF CONTENTS	xviii
LIST OF TABLES	xxii
LIST OF FIGURES.....	xxiv
LIST OF ABBREVIATIONS AND ACRONYMS.....	xxx
LIST OF SYMBOLS	xxxiv
GENERAL INTRODUCTION.....	1
CHAPTER 1 WIND TURBINE BLADE FLAWS AND DETECTION METHODS	7
1.1 WIND TURBINE COMPONENTS AND TYPES.....	7
1.1.1 Components of wind turbines	7
1.1.2 Types of wind turbines.....	32
1.2 WIND TURBINE BLADE FAILURE WITH STATISTICS AND DESCRIPTION	38
1.2.1 Reliability statistics of wind turbines and subsystems.....	38
1.2.2 Wind turbine blade failure modes.....	42
1.3 TECHNICAL, ECONOMIC, AND ENVIRONMENTAL CHALLENGES	49
1.3.1 Technical challenges	49
1.3.2 Economic challenges	51
1.3.3 Environmental challenges.....	52
1.4 DETECTION METHODS: ADVANTAGES AND INCONVENIENCES	54
1.4.1 Acoustic emission testing	55
1.4.2 Infrared testing.....	55

1.4.3	Fiber grating testing.....	56
1.4.4	Ultrasonic testing.....	57
1.4.5	Guided wave testing	58
1.4.6	Thermal imaging	59
1.4.7	Terahertz imaging.....	59
1.4.8	Visual inspection	60
1.4.9	Tap test	61
1.4.10	Electromagnetic testing.....	62
1.4.11	Vibration analysis.....	63
1.5	CONCLUSION.....	64
CHAPTER 2 CRITICAL DISCUSSION OF ICING DETECTION METHODS		65
2.1	ICING PHENOMENA AND IMPORTANCE FOR WIND ENERGY PRODUCTION AND WIND TURBINE SAFETY.....	65
2.2	ICING DETECTION METHODS: ADVANTAGES AND INCONVENIENCES	68
2.2.1	During the site assessment stage	68
2.2.2	During the operation stage.....	74
2.3	CONCLUSION.....	78
CHAPTER 3 SYNOPSIS ON HYPERSPECTRAL IMAGING TECHNIQUE.....		79
3.1	COMPARISON AMONG BROADBAND, MULTISPECTRAL, HYPERSPECTRAL, AND ULTRA-SPECTRAL IMAGING	79
3.2	CONCEPT OF THE HYPERSPECTRAL CUBE.....	81
3.3	THE NEED FOR DIMENSIONALITY REDUCTION.....	82
3.4	HYPERSPECTRAL IMAGE WORKING THEORY	83
3.5	APPLICATIONS OF HYPERSPECTRAL IMAGING.....	87
CHAPTER 4 PRELIMINARY STUDY		89
4.1	MATERIAL PREPARATION.....	89
4.2	EXPERIMENTAL PROCEDURE	91
4.3	PRELIMINARY RESULTS	92
4.3.1	Crack.....	93
4.3.2	Erosion.....	96
4.3.3	Icing event	98

CHAPTER 5 EXPERIMENTAL SETUP 103

 5.1 SENSOR SELECTION 103

 5.2 EXPERIMENTAL SETUP 104

 5.3 ACTIVITIES 106

CHAPTER 6 WIND TURBINE BLADE FLAWS DETECTION USING
HYPERSPETRAL IMAGING 109

 6.1 RGB 3-BAND BLADE IMAGE RESULTS 109

 6.2 FAULT SIGNATURE RETRIEVAL 110

 6.3 HYPERSPETRAL IMAGE ACQUISITION 114

 6.4 FULL-SPECTRUM FLAW DETECTION 115

 6.5 RGB VERSUS HYPERSPETRAL IMAGING 117

 6.6 SPECTRUM REDUCTION 118

CHAPTER 7 WIND TURBINE BLADE ICING DETECTION USING
HYPERSPETRAL IMAGING 121

 7.1 RGB 3-BAND BLADE IMAGE RESULTS 121

 7.2 ICE FAULT SIGNATURE RETRIEVAL 121

 7.3 HYPERSPETRAL IMAGE ACQUISITION 123

 7.4 FULL-SPECTRUM ICE DETECTION 124

 7.5 RGB VERSUS HYPERSPETRAL IMAGING 126

 7.6 SPECTRUM REDUCTION 126

GENERAL CONCLUSION 129

APPENDIX I ALGORITHM USED 133

APPENDIX II HYPERSPETRAL IMAGING APPLIED FOR THE DETECTION
OF WIND TURBINE BLADE DAMAGE AND ICING 143

APPENDIX III WIND TURBINE BLADE DEFECT DETECTION USING
HYPERSPETRAL IMAGING 157

APPENDIX IV WIND TURBINE ICE DETECTION USING HYPERSPETRAL
IMAGING 167

BIBLIOGRAPHIC REFERENCES181

LIST OF TABLES

Table 1 : Variety of wind turbine failures and faults (Find M. Jensen, Bladena) and its failure categories (Strange Skrifer from Danmarks Vindmølleforening) [129].....	46
Table 2 : Synopsis on cost and time of results of test methods.....	50
Table 3 : Scanning modes	86
Table 4 : Crack sample results	95
Table 5: Erosion sample results	97
Table 6 : Ice sample results	100
Table 7 : The detection probability (Pd) and false alarm rates (FAR) of fault types using an RGB image.....	110
Table 8 : The detection probability (Pd) and false alarm rates (FAR) for defect types using a hyperspectral image.....	116
Table 9 : Summary of band reduction results	118
Table 10 : Summary of Net Analyte Signal Results	127

LIST OF FIGURES

Figure 1. Cross-section of a typical fiberglass blade ©Peery and Weingart, 1980 [59]	11
Figure 2. Cross-section of wood-epoxy blade ©Hau,1996 [63]	12
Figure 3. Hütter root ©Hau,1996 [63]	13
Figure 4. Blade root stud in fiberglass reinforced plastic blade ©National Research Council, 1991 [62]	14
Figure 5. A tip flap aerodynamic brake.....	15
Figure 6. Wind turbine hub types ©Gasch, 1996 [75]	17
Figure 7. The drive train`s components [42].....	18
Figure 8. Main shaft options ©Harrison et al., 2000 [79]	19
Figure 9. Parallel shaft gearbox ©Hau, 1996 [63]	20
Figure 10. Exploded view of two-stage planetary gearbox [42]	21
Figure 11. A partially integrated, two-stage planetary gearbox [42]	22
Figure 12. A disc brake [42].....	25
Figure 13. Typical yaw drive with brake ©Van Bibber and Kelly, 1985 [104]	27
Figure 14. Typical nacelle cover [42]	29
Figure 15. Tubular tower, truss tower, guyed tower (from left to right) [42]	30
Figure 16. Wind turbine foundations ©Hau, 1996 [63]	31
Figure 17. An up-wind turbine.....	33
Figure 18. A down-wind horizontal axis turbine	34
Figure 19. Savonius turbine	35
Figure 20. Twisted Savonius turbines	36
Figure 21. Darrieus turbine	37

Figure 22. Giromill turbine	37
Figure 23. Failure rates for onshore and offshore wind turbine subassemblies [126].....	40
Figure 24. Downtime and repair times for onshore and offshore databases.....	42
Figure 25. Failure modes identified in a wind turbine blade that was purposely tested to fail [129].....	45
Figure 26. Scratch in coating [131]	47
Figure 27. A small area of coating damage [131].....	47
Figure 28. Crack in structure at the leading edge [131].....	48
Figure 29. Leading-edge erosion [131].....	48
Figure 30. Leading-edge erosion with large exposed surfaces of fiberglass [131]	48
Figure 31. Long leading-edge chordwise crack with spanwise cracking [131].....	49
Figure 32. Percentages of failure of wind turbine components [144]	52
Figure 33. Wind turbines accidents and incidents [151]	54
Figure 34. Acoustic Emission Testing Process [161]	55
Figure 35. Infrared Testing Process [167]	56
Figure 36. Fiber Grating Testing Process [170]	57
Figure 37. Ultrasonic Testing Process [171]	58
Figure 38. Guided Wave Testing Process [176]	58
Figure 39. Thermal Imaging Process [167]	59
Figure 40. Terahertz Imaging Process [182]	60
Figure 41. Visual Inspection Process [187]	61
Figure 42. Unmanned Vehicle [188]	61
Figure 43. Computer-Aided Tap Tester System [190]	62
Figure 44. Electromagnetic Testing Process [193].....	63
Figure 45. Vibration Analysis Process [195].....	64
Figure 46. Anemometer and Vane [225]	69

Figure 47. Ice Sensors [228]	70
Figure 48. Visibility and Cloud Base Detector [231].....	71
Figure 49. Dew Point Detector [232]	72
Figure 50. Example of Mesoscale Model [233].....	73
Figure 51. Video Monitor [239].....	75
Figure 52. Theoretical and Actual Power Curves [240].....	76
Figure 53. Vibration Sensors [241]	77
Figure 54. Comparison among the remote sensing technique	80
Figure 55. Comparison among broadband, multispectral and hyperspectral	81
Figure 56. Hyperspectral data cube.....	82
Figure 57. Elements of a hyperspectral imaging sensor.....	84
Figure 58. Hyperspectral operating theory.....	85
Figure 59. Whiskbroom, pushbroom, and staredown spectrometers outputs [257].....	86
Figure 60. Specimen of composite plates.....	90
Figure 61. Faults on the tested specimen	90
Figure 62. ASD FieldSpec4	90
Figure 63. Acquisition of ice signature	92
Figure 64. Acquisition of erosion signature	92
Figure 65. Spectral signature of cracked versus normal fiberglass composite	93
Figure 66. Detection process of crack a) reflectance distribution b) defect probability	94
Figure 67. Spectral signature of eroded versus normal fiberglass composite.....	96
Figure 68. Detection process of erosion a) reflectance distribution b) defect probability.....	97
Figure 69. Spectral signature of ice versus normal fiberglass composite	99
Figure 70. Detection of icing event a) reflectance distribution b) defect probability	99
Figure 71. 340-840 nm Sensor	104

Figure 72. 640-1050 nm Sensor.....	104
Figure 73. 950-1700 nm Sensor.....	104
Figure 74. Blade section	105
Figure 75. Ice accretion on blade sample	105
Figure 76. GRFP Setup for scanning	105
Figure 77. The flowchart of the methodology of the hyperspectral imaging experiment.....	107
Figure 78. Minor crack on the blade specimen.....	111
Figure 79. Light erosion on the blade specimen	111
Figure 80. Severe crack on the blade specimen.....	111
Figure 81. Severe crack on the blade specimen.....	111
Figure 82. Ice on the specimen	111
Figure 83. The spectrum of 0.1 mm width crack versus normal blade signature	113
Figure 84. The spectrum of 0.3 mm width crack versus normal blade signature	113
Figure 85. The spectrum of 1.0 mm width crack versus normal blade signature	113
Figure 86. The spectrum of 2.0 mm width crack versus normal blade signature	113
Figure 87. The spectrum of light erosion signature versus normal blade signature	114
Figure 88. The spectrum of severe erosion signature versus normal blade signature	114
Figure 89. 3D hyperspectral cube of the wind turbine blade specimen.....	115
Figure 90. 3D Blade image with iced section.....	115
Figure 91. 2D illustration of the crack detection	116
Figure 92. 3D illustration of the crack detection	116
Figure 93. 2D illustration of the erosion detection	117
Figure 94. 3D illustration of the erosion detection	117
Figure 95. Ice on specimen	122
Figure 96. The spectrum of 0.5 mm ice thickness versus clean blade signature	123

Figure 97. The spectrum of 0.7 mm ice thickness versus clean blade signature 123

Figure 98. The spectrum of 4.0 mm ice thickness versus clean blade signature 123

Figure 99. The spectrum of 7.0 mm ice thickness versus clean blade signature 123

Figure 100. 3D Blade Image with partial icing 124

Figure 101. 2D Illustration of ice detection 125

Figure 102. 3D Illustration of ice detection 125

LIST OF ABBREVIATIONS AND ACRONYMS

ACE	Adaptive cosine estimator
AVIRIS	Airborne Visible / Infrared Imaging Spectrometer
ASD FieldSpec4	Analytical Spectral Devices FieldSpec4 Spectroradiometer
BC	Before Christ
CCD	Charge-coupled device
CO₂	Carbon dioxide
COVID-19	Coronavirus disease
cm	centimeter
EPRI	Electric Power Research Institute
EUVIP	European Workshop on Visual Information Processing
etc	Et cetera (and others)
FAR	False alarm rate
FFE	Fill fraction estimator
GFRP	Glass Fiber Reinforced Polymer
GLRT	Generalize likelihood ratio test
GW	GigaWatt
HMDP	Hyperspectral Mine Detection Phenomenology

HSI	Hyperspectral imaging technology
IEEE	Institute of Electrical and Electronics Engineers
JPL	Jet Propulsion Laboratory
km	kilometer
kW	Kilowatt
m	meter
MF	Matched filter
MLE	Maximum likelihood estimate
MI	Mutual Information
mm	millimeter
m/s	meter per second
MW	Megawatt
NAS	Net Analyte Signal
NASA	National Aeronautics and Space Administration
NDT	Nondestructive technique
nm	nanometer
PROPID	Computer program for the design and analysis of horizontal axis wind turbines
P_d	Detection probability
RGB	Red, green, and blue

rpm	revolutions per minute
SHM	Structural health monitoring
SWIR	Shortwave infrared
TCP	Technology Collaboration Programs
UQAR	Université du Québec à Rimouski
US	United States
VSNR	Voltage signal to noise ratio
W/m²	Watt per square meter
WT	Wind turbine
WTB	Wind Turbine Blade
WWEA	World Wind Energy Association
° C	degree Celsius
° F	degree Fahrenheit
2D	Two-dimensional space
3D	Three-dimensional space

LIST OF SYMBOLS

%	per cent sign
x	scene's spatial dimension on the x-axis
y	scene's spatial dimensions on the y-axis
λ	spectral dimension
D	dark reference signal
H_n	calibrated/normalized image
HI	retrieved/scanned image
W	white reference signal
α	percentage of fault signature

GENERAL INTRODUCTION

The gradual heating of Earth's surface, oceans, and atmosphere triggered by human activity, mainly the burning of fossil fuels that emit carbon dioxide, methane, and other greenhouse gases into the atmosphere, has shifted nations' focus to renewable resources rather than non-renewables. Renewable energy, known as "clean energy," is a natural energy source that is constantly replenished, such as sunlight and wind. All these natural resources are freely accessible, without any security concerns on energy supply [1]. However, non-renewable energy, generally mentioned as "dirty energy," is a type of energy that exists in a limited amount and needs a long time to replenish, such as coal, gases, and oil [1]. But these resources are subjected to fluctuating prices, security issues with energy supplies, and some environmental issues. For instance, oil drilling may necessitate strip-mining Canada's boreal forest [2], fracking technology can cause earthquakes and water pollution, and coal power plants pollute the air [3, 4]. All these constraints pushed up the "clean energy," replacing the "dirty energy," especially in the power sector, resulting in lower carbon and other types of pollution emissions. Thus, in response to climate change, renewable energy is thriving as nations develop progressively modern and cost-effective methods of harnessing natural power resources, particularly wind [5].

For decades, wind energy has been used to power tasks such as thrusting cruising boats, milling grain, pumping water, and powering factory machinery [1]. As early as 5,000 BC, people used wind energy to thrust boats along the Nile River [6]. Simple wind-powered water pumps were used in China by 200 BC, and windmills with woven-reed blades were used in Persia and the Middle East to grind grain [7]. Wind energy was eventually used in new ways all over the world. Wind pumps and windmills were widely used for food production in the Middle East by the 11th century [8]. Merchants and Crusaders brought wind technology to

Europe. The Dutch constructed huge windpumps to drain the Rhine River Delta's lakes and marshes [6].

European immigrants brought wind energy technologies to the Western Hemisphere. American colonists utilized windmills to process grain, pump water, and cut wood at sawmills [9]. Homesteaders and ranchers erected thousands of windpumps when they inhabited the western United States. Small wind-electric generators were also popular in the late 1800s and early 1900s. As rural electrification programs in the 1930s extended power lines to most farms and ranches across the country, the number of wind pumps and turbines decreased. Some ranches, however, continue to use wind pumps to provide water to their livestock.

Small wind turbines are regaining popularity, primarily as a source of electricity in remote and rural areas [6]. In plus, several larger wind turbines were built or conceptualized in the first half of the twentieth century, which significantly impacted the development of today's technology [10]. The Smith–Putnam machine, built at Grandpa's Knob in Vermont in the late 1930s, was the most significant early large turbine in the United States [11]. This was the largest wind turbine ever built, with a diameter of 53.3 m and a power rating of 1.25 MW, at the time and for many years afterward [12]. This turbine was also significant because it was the first large turbine with two blades. It was a precursor to the two-bladed turbines built by the US Department of Energy in the late 1970s and early 1980s in this regard. The turbine was also notable because the company that built it, S. Morgan Smith, had extensive hydroelectric experience and planned to produce a commercial line of wind turbines. Sadly, given the state of wind energy engineering at the time, the Smith–Putnam turbine was too huge and too early. In 1945, the blade failed, and the project was abandoned [6].

During the 1990s, the focus of wind turbine manufacturing definitively shifted to Europe, particularly Denmark and Germany, following the demise, that happened in 1996, of the largest US manufacturer, Kennetech Windpower. Concerns about global warming and nuclear power have led to a tremendous demand for more wind generation in that country, as well as in other countries. Some of Europe's major suppliers are establishing

manufacturing facilities in countries such as Spain, India, and the United States. The largest commercial wind turbines have grown from about 50kW to 2MW over the last 40 years, with commercial machines planned for up to 5MW [6].

According to preliminary wind energy statistics published recently by the World Wind Energy Association (WWEA), the world set a record for new wind turbine deployments, contributing 93 GW in 2020 [13]. China, the United States, and Russia set new implementation records, while most European markets only saw a slight increase. Many countries have revealed delays in the past year due to distorted international supply chains and a shortage of labor availability, therefore the strong growth appears as a surprise to some observers. The global market for new turbines attained a total volume of 93 GW in 2020, roughly 50% more than the previous year and more than ever was installed in a single year. Currently, the total capacity of all wind farms globally reaches 744 GW, which is enough to cover 7% of the world's electricity demand. This impressive growth was achieved although the pandemic. While COVID-19 seems to be weakening advancement in some countries, it appears to have had no negative impact overall, rather accelerating the transition to wind and other renewable energy sources. China was still in a league of its own, constructing 52 GW in a year, equivalent to a 56% market share. With this regard, China will now have 289 GW of installed wind capacity, accounting for 39% of global capacity. The US market has also grown rapidly, with nearly 17 GW added in 2020. With this new record and wind farms totaling 122 GW, the United States has unquestionably cemented its position as the world's number two. Among the top ten wind power markets, there were few variations. With a reliable market volume of 2,5 GW in 2020, for a total of 18 GW, Brazil went up from eighth to seventh place, whereas France fell from seventh to eighth place. Without a doubt, the newcomer of the year was Russia, which increased its installed wind capacity from 312 MW to 1027 MW and rose from 53rd place in the wind power market at the end of 2019 to 37th place [13].

Despite its growth, the wind turbine market, like other developing sectors, still encounters some obstacles and constraints due to environmental and manufacturing factors

limiting its potential. Wind turbine blades, one of the most important and costly parts of the wind turbine, are expected to last up to 20 years. During this time, they withstand a fluctuating wind load distinguished by a combination of lift and drag in normal wind conditions. Blades become worn out after a long period. As a result, weariness promotes material degradation and results in the formation of cracks on the blade [14]. Some wind turbines are placed in areas where severe weather, such as high winds and icing, is common. Ice accumulations, cracks, delamination, and erosion, all pose problems for blades. These flaws will reduce the annual energy production by lengthening the turbine's downtime for wear and tear [15]. Most damage detection research focuses on developing an innovative method for detecting damage early on to reduce maintenance time and costs [16]. To decrease maintenance costs and extend the life of wind turbines, frequent inspections should be carried out [17], particularly on the blades, which account for 20% to 30% of the total cost of a wind turbine [18]. Visual testing in wind turbine blades is the mainstay of maintenance tasks.

Stutzmann et al. [19] analyzed the tests in a numerical simulation of fatigue cracks using a conditional probability model. They attempted to reduce uncertainty in estimating the useful life of wind turbine structures due to fatigue. However, it is dependent on the workers' experience and is subjective. Kim et al. [20] proposed a straightforward and necessary non-destructive technique for wind turbine blades. The pan-tilt-zoom camera system serves as the foundation for the damage detection system. This system is used to identify wind turbine failures. It can detect a 2 cm wide crack from a distance of 200 m. Numerous failures of wind turbine blades and the lack of images of these failures make failure diagnosis difficult.

Other methods such as ground-based inspection, internal inspection, ultrasound, thermal imaging, vibration analysis, and various ways are used to detect damage and ice, which is a type of surface contamination. However, defect detection and location remain important issues. Indeed, the detection is based on global factors (humidity, temperature, frequency, etc.), giving an overall knowledge of the defect on the blades and does not allow

a precise and localized quantification of the fault. Moreover, the sensors used in these techniques do not forecast ice formation.

Only a few researchers, such as Young et al. [21], have discussed the use of hyperspectral images for blade damage detection, and their analysis has been limited to erosion detection. To that end, this research will fill in the gaps and demonstrate the utility of hyperspectral imaging in detecting surface defects and icing events as a multi-target technology in the test phase of WTBs during manufacturing as well as in wind farm monitoring. Despite the opinion of Young et al. that detailed hyperspectral image information may not necessarily be needed during field conditions monitoring, but such information will present an unsubstantial qualitative and quantitative measurements of the defects under study. Additionally, this information can be useful for studying the physical properties of defects and later used as a dataset for various WTB monitoring on field windfarms or during manufacturing processes.

Hyperspectral imaging technology has been proven its accuracy and robustness in various application areas, including vegetation and water resource monitoring [22, 23], forensic medicine [24, 25], archaeology and art conservation [26, 27], security monitoring, and crime scene detection [28, 29], etc. This technology is a type of remote sensing that combines spatial and spectral data from a target object or scene.

Among the available wind turbine blade defect-recognition solutions, hyperspectral imaging is a promising technology [21]. By fusing spectroscopy with conventional imaging, hyperspectral imaging can create spatial maps that span a wide range of spectral information, leading to various applications in blade defect detection. [30].

The overall objective of this project is to research, study, compare, and analyze the different non-destructive inspection techniques of wind turbine blades and present and explain the potential of the hyperspectral imaging technique in the remote detection of these defects. Hyperspectral imaging is used to detect and quantify blade defects and ice accretion. It allows limiting or even preventing the formation of ice on the blade in conjunction with

anti-icing and de-icing equipment. It reduces the cost of wind energy without making any major modifications or disturbances to the blade architecture. Numerical simulations, practical tests, and technical analyses of these defects will be studied using the hyperspectral imaging technique, in which each defect will be characterized by frequencies outside the visible band, which constitutes the spectral signature of the defect.

This dissertation is divided into eight major chapters. The first chapter presents an overview of wind turbines, the challenges that hinder their availability, statistics showing components` failure, and a survey of flaws detection methods used on wind turbine blades. In addition, Chapter 2 describes the phenomenon of icing and its effects on wind power generation and wind turbine safety, as well as a survey of the icing detection methods. Chapter 3 introduces hyperspectral imaging technology. Chapter 4 presents a preliminary study showing the experimental setup, and the results found that assure the importance of the hyperspectral imaging technique in the inspection of a wind turbine blade. Chapter 5 details the experimental setup for hyperspectral imaging use in flaws and icing detection. The results of the defects and icing detection are then discussed in the two corresponding Chapters 6 and 7. Finally, a general conclusion and future work are presented.

CHAPTER 1

WIND TURBINE BLADE FLAWS AND DETECTION METHODS

1.1 WIND TURBINE COMPONENTS AND TYPES

Several factors interact to put the atmosphere in action, a phenomenon known as wind. This kinetic energy or natural motion exists, and it appears reasonable to find ways to harness it. Humans already used the wind's kinetic energy to turn windmills, sailboats, and pump water almost thousands of years ago [31]. The fundamental theory is that the wind's kinetic energy is the trigger element to turn apparatus. Nowadays, this wind energy constitutes the catalyst in energy production in wind turbines [32].

In general, wind turbines use the aerodynamic force of rotor blades to convert wind energy into electricity. When the wind blows, the air pressure on one side drops. Lift and drag are caused by the difference in air pressure on both sides of the blade. The rotor rotates because the lift force is greater than the drag force. The rotor is connected to the generator either directly, for a direct drive turbine, or via a shaft and a series of gears that speed up the rotation and allow for a physically smaller generator. The conversion of aerodynamic force to generator rotation results in the generation of energy [33]. As a result, knowing how different types of wind turbines look and where they can be used is extremely beneficial.

1.1.1 Components of wind turbines

A wind turbine's main component groups are the rotor, the drive train, the yaw system, the mainframe, and the tower [34]. The rotor is made up of the blades, the hub, and the aerodynamic control surfaces [35]. The drive train consists of the gearbox, generator, mechanical brake, and the shafts and couplings that link them [36]. The components of the yaw system are determined by whether the turbine uses free yaw or driven yaw, which is

determined by the orientation of the rotor. Yaw system components consist of, at a minimum, a yaw bearing and, in some cases, a yaw drive, yaw brake, and yaw damper [37]. The mainframe serves as a support for mounting the other parts. The tower group consists of the tower itself, its foundation, and possibly the machine's self-erection mechanism [38]. A more detailed overview of each of these subcomponents is presented in the following sections. Unless otherwise specified, the turbine is assumed to have a horizontal axis.

1.1.1.1 Rotor

Wind turbines have rotors designed to extract substantial power from the wind and switch it to rotary motion [39]. Wind turbine rotors must run under a variety of load circumstances, including constant, periodic, and stochastically variable loads. Because these fluctuating loads occur over a significant number of cycles, fatigue is a major factor to consider. The designer must make every effort to limit cyclic stresses to a minimum and to utilize materials that can endure such pressures for as long as possible [40]. The rotor also serves as a cyclic loading generator for the rest of the turbine, especially the drive train [41].

The following three sections concentrate on the rotor's main elements: blades, aerodynamic control surfaces, and hub [42].

a) *BLADES*

The blades are the essential elements of the rotor; they are the tools that transform the wind's force into the torque required to generate usable power. There are many factors to consider when designing blades, but most of them fall into aerodynamics or structural categories. Other factors can be the overall arrangement of the turbine, material characteristics, and its fabrication methods [43].

The blade aerodynamic design is based on the combination of several blades, design rated power and rated wind speed, solidity, design tip speed ratio, airfoil, rotor power control, and its orientation [44].

To begin with, increasing the number of blades will raise the fixed costs and the stresses at the roots of the wind turbine. Most commercial wind turbines have either two or three blades [45]. Secondly, design rated power and rated wind speed determine the length of the blade by affecting the overall size of the swept area [46]. Thirdly, a high tip speed ratio ensures the design of lighter and cheaper blades by outcoming low solidity due to a smaller overall blade area. In addition to that, a fast-rotating speed is beneficial to and supports the drive train [47]. However, extreme tip speed ratios develop more significant aerodynamic noise from the turbine and raise flap-wise loads at thin depths of blades. These vibration issues and large deflections may be the reason behind blade–tower collisions. Furthermore, these increased design tip speed ratios directly affect the blade's chord and twist distribution, necessitating the appropriate airfoil use [48]. Fourthly, while increasing the lift-to-drag ratio to boost the power coefficient, this lift coefficient will impact the rotor solidity and smaller the blade's chord [49].

Fifthly, the best-matched airfoil is chosen based on the rotor's aerodynamic control mechanism, which can be simplified by referring to data sets such as those created by Selig (1998). In plus, wind turbine blades feature a variety of airfoil shapes, often of the same family but with different relative thicknesses, running the length of the blade. Wind turbine blades can be made stronger by using thicker airfoils towards the root while retaining proper overall performance [50]. Sixthly, the power control technique (stall or variable pitch) has a considerable impact on the blade design, especially airfoil selection. In high winds, a stall-controlled turbine relies on the lift loss of a stall to restrict power output. Therefore, good stall qualities in the blades are desirable. They should progressively stall as the wind speed rises, and they should generally be devoid of transitory phenomena like a dynamic stall. Stall characteristics are typically less significant in pitch-controlled turbines [51]. Whereas it is crucial to note that the blades function admirably when thrown in strong winds. It is as well

worth mentioning that blades may be thrown to feather, with a lessening angle of attack, or stall, with the rising angle of attack [52]. Finally, the rotor's orientation about the tower influences the blade geometry, although it is largely secondary to the reckoning of the blades [53]. During preconing, the blades are skewed away from a plane of rotation indicated by the blade roots. To allow the rotors to track the wind and preserve some yaw stability, the blades must be coned away from the plane of rotation and must be kept away from colliding with the tower. For instance, whereas most down-wind turbines carry on with free yaw, preconed blades are present on certain upwind rotors [54].

To sum up, to adequately account for both aerodynamic and structural constraints, blade design generally takes several iterations. Each iteration begins with the development of a rough design, which is then assessed. Selig and Tangler (1995) devised an inverse design method as a way to speed up this procedure. It entails the use of a computer program (PROPID) to generate designs that fulfill specific criteria [55].

Aside from the stresses that a wind turbine blade must resist, the main structural design concerns are materials and production alternatives. The connection of the blades to the hub is also a major problem. Wind turbine blades were traditionally composed of wood and coated with linen. Steel blades for bigger wind turbines were used until the middle of the twentieth century [56]. The Smith–Putnam 1250 kW turbine from the 1940s and the Gedser 200 kW turbine from the 1950s are two examples of these types of wind turbines. Most blades for horizontal axis wind turbines have been built of composites since the 1970s [42]. Fiberglass in polyester resin is the most frequent composite, but wood–epoxy laminates have also been widely employed. The blades of most vertical axis wind turbines are made of aluminum. Because their blades have a continuous chord and no twist, they adapt themselves to aluminum pultrusion creation. Pultrusion is a method of creating the desired shape by pulling material (such as aluminum) through a forming die. The length of the shape is consistent. Although aluminum blades have been utilized in a few horizontal axis wind turbines, it is not currently widely employed in these types [56].

Following the discussion of the blade design's aerodynamics and structural characteristics, it is critical to present the blade production technique to produce a robust and light structure with an outer shape that matches the design [57]. Non-linear forms are ideal for horizontal-axis wind turbines, whose blades are typically tapered and twisted, with variable degrees of curvature. Two kinds of pieces are modeled for this purpose. The skin gives the airfoil its ideal shape, while the spar gives it stiffness [58]. A cross-section of a typical fiberglass blade is shown in Figure 1 [59].

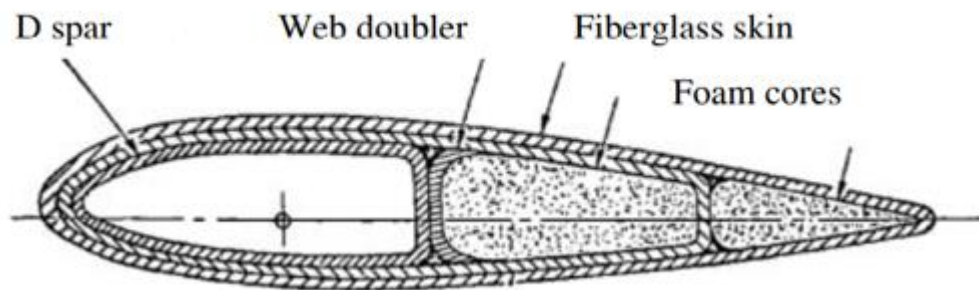


Figure 1. Cross-section of a typical fiberglass blade ©Peery and Weingart, 1980 [59]

Building a spar is usually the first stage in the fabrication of a blade. Spars come in a range of shapes and sizes, but the goal is to design a light component that can withstand applied moments. A web, a box beam, or a D are all possible shapes for the spar. A box beam or web will have an outside flapwise dimension that allows it to be attached to the interior of the skin on both the top and bottom of the blade. The blade skin is also attached to the front of the spar when using a D spar [60].

Spars in fiberglass blades are typically constructed by layering fiberglass and resin around a mandrel and then removing it. Inside a mold, layers of fiberglass fabric and resin are built up to create the skin of a glass-reinforced plastic blade. Pieces of the upper surface and the lower surface are melted, then taken from the molds and linked together, with the spar in the middle [61]. A similar process is used to make wood–epoxy blades anon-stall-regulated shown in Figure 2. Figure 1 The primary distinction is that wood plies are utilized in the laminate instead of fiberglass fabric. Furthermore, the skin thickness is generally larger

than the blade thickness in a glass-reinforced plastic blade, and instead of a box beam spar, a plywood strip is utilized to give rigidity. While it is worth noting that any conceivable surface may be created with the molds detailed here, the downside of making blades in this manner is that the lay-up requires a lot of manual effort leading to large expenses, as well as difficulty in ensuring uniformity from one blade to the next [62].

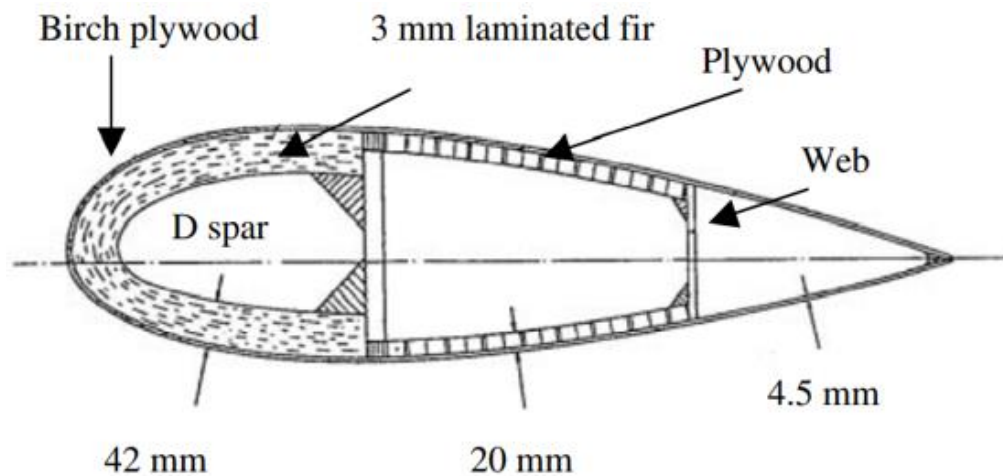


Figure 2. Cross-section of wood-epoxy blade ©Hau,1996 [63]

Filament winding is a distinct method of producing primarily fiberglass blades. It entails the simultaneous coiling of glass fibers around a mandrel and the application of resin. This technique, which was initially developed for the aerospace industry, may be automated. Nevertheless, it is challenging to be applied to concave forms [64].

The root, which is the end closest to the hub, is a valuable component of the blade subjected to peak loads. It is generally built as thick as possible in the flapwise direction to reduce stresses. The link between the root and the hub has been shown to be problematic in various circumstances. This is due to variations in material properties and rigidity between the blades, hub, and fasteners. The problem is made worse by the fact that the loads are constantly changing [65].

The Hütter design, named after its designer, the German wind energy pioneer Ulrich Hütter, is one form of the root. Long fiberglass strands are glued into the lower portion of the

blade using this approach. At the base of the blade, round metal flanges are supplied, and circular hollow spacers are connected to these flanges, as seen in Figure 3. The fiberglass strands are coiled around the spacers and reintroduced into the blade. Resin holds all of the strands and flanges in place. Bolts via the flanges and spacers finally connect the blades to the hub. This root design is best suited to fixed-pitch rotors and may be tweaked to accommodate variable pitch rotors [63].

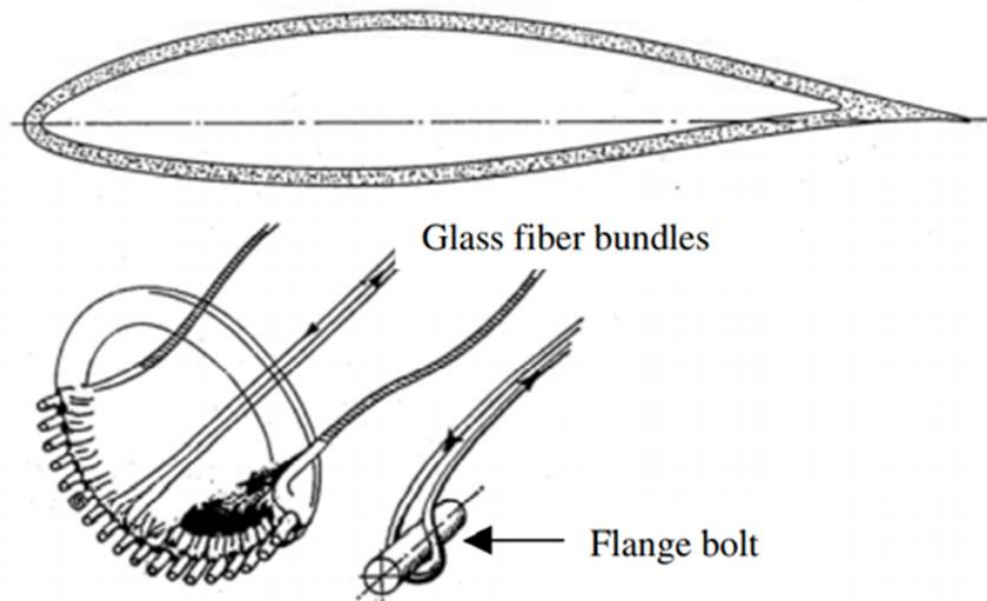


Figure 3. Hütter root ©Hau,1996 [63]

Another technique of connection is the use of studs or threaded inserts attached directly to the blades. Fixed-pitch wind turbine blades are often connected to the hub with bolts or studs oriented radially and perpendicular to the bottom of the blade root, as seen in Figure 4. These fasteners must withstand all the loads arising from the blades [62].

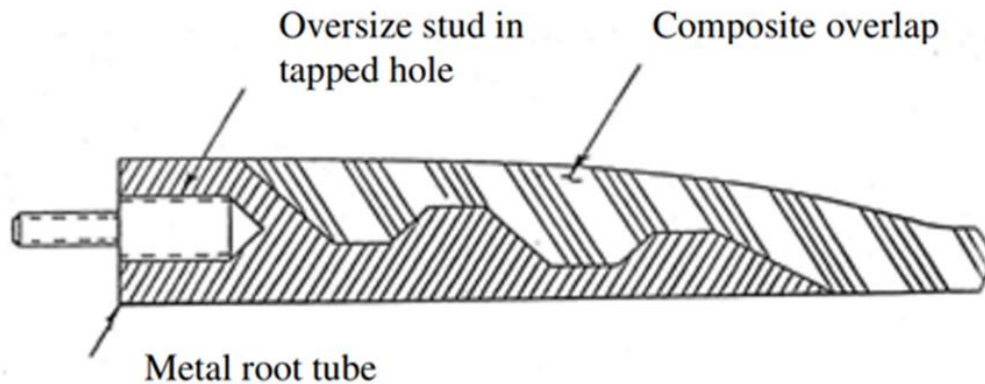


Figure 4. Blade root stud in fiberglass reinforced plastic blade ©National Research Council, 1991 [62]

A variable pitch blade's root is built differently than a fixed pitch blade's. For the blade to be turned, the root–hub connection must have bearings. These bearings must withstand the bending moments and shear pressures exerted by the remainder of the blade. Furthermore, these bearings must withstand the centrifugal force generated by the rotor's spin [66].

On medium and larger turbines, the blade attachment methods mentioned above are the most frequent. Small turbine blades usually use a variety of attachment methods. One approach involves thickening the root and installing bolts through it and a corresponding component on the hub. The bolts are steep to the blade's long axis and chord [67].

In terms of blade properties, the structural study of the rotor requires information on the entire blade, such as total weight, stiffness and mass distributions, and moments of inertia. The blade's strength, inclination to deflect under load, natural vibration frequencies, and fatigue resistance are all important considerations [68].

Due to the blade's complicated shape, which changes from root to tip, certain of the blade's characteristics can be difficult to acquire. The most common approach is to split the blade into pieces, similar to how aerodynamic analysis is done. The dimensions and material distribution are used to discover properties for each segment, which are then combined to find values for the whole blade [42].

b) AERODYNAMIC CONTROL SURFACES

Aerodynamic control surfaces, integrated onto wind turbine blades and coming in a variety of types, are devices that can be manipulated to adjust the aerodynamic characteristics of a rotor. Their design is affected by the blade's model, and their selection is based on the overall control philosophy. Aerodynamic brakes, such as tip brakes, flaps, and spoilers, are commonly used in stall-regulated wind turbines. Figure 5 shows an illustration of a tip flap [69].



Figure 5. A tip flap aerodynamic brake

More aerodynamic control is present in non-stall-regulated wind turbines. For instance, the entire blade can function as a control surface by spinning across its long axis in typical pitch-controlled turbines. Nevertheless, partial span pitch control is used in other turbine designs, where the inner section of the blade is fastened to the hub, and the outer section, supported by bearings, can rotate around the blade's radial axis. Moreover, the pitching mechanism for partial span pitch control does not need to be as enormous as it does for full-span pitch control [70].

The aileron, a movable flap situated at the blade's trailing edge, is another sort of aerodynamic control surface. The aileron may be about a third of the length of the blade and extend about a fourth of the way towards the leading edge [71].

Any control surface must be utilized in tandem with a procedure that either allows or pushes it to step in the desired direction. Bearings, hinges, springs, and linkages are all possible components of this system. Moreover, while electromagnets are commonly used in aerodynamic brakes to keep the surface in place during normal operation but release it when needed, motors are used to operate active pitch or aileron control mechanisms [42].

c) *HUB*

The hub is the wind turbine's element that joins the blades to the main shaft and the drive train's remainder [72]. The hub is responsible for transmitting and sustaining all of the loads generated by the blades [39]. Hubs are typically composed of welded or cast steel. Details of hubs vary greatly depending on the turbine's general design idea [73].

There are three fundamental categories of hub design in contemporary horizontal axis wind turbines: rigid hubs, teetering hubs, and hubs for hinged blades [73]. While rigid hubs have all their important elements fixed relative to the main shaft, teetering hubs provide relative motion between the blade-connected section and the main shaft-connected part. Hubs for hinged blades, on the other hand, allow for independent flapping motion about the rotation plane. One- and two-bladed wind turbines often use teetering hubs. Nevertheless, three or more bladed wind turbines are prevalent with rigid hubs. In comparison, only some commercial machines use hubs for hinged blades, although they have been used on several historically significant turbines (Smith–Putnam) and are currently gaining renewed interest. The following figure depicts some of the most popular types of hubs [42, 74].

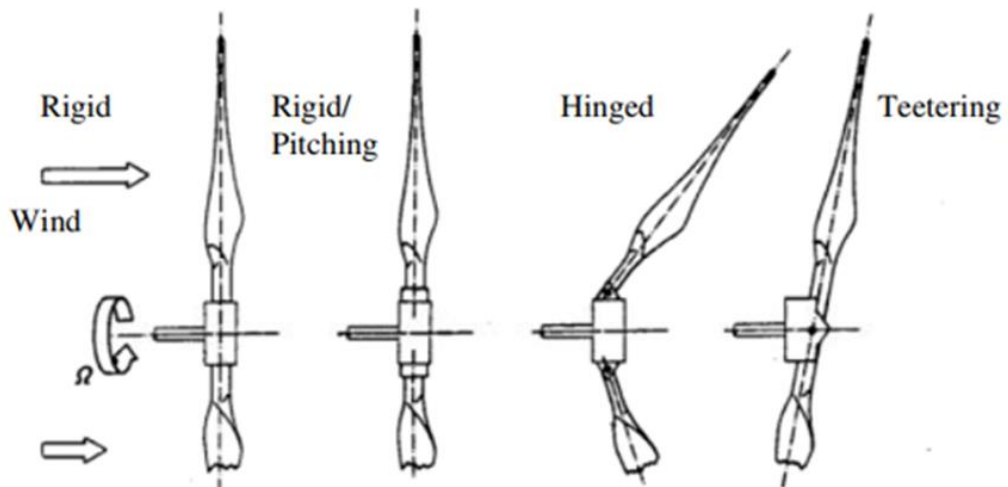


Figure 6. Wind turbine hub types ©Gasch, 1996 [75]

1.1.1.2 Drive train

All rotational components of a wind turbine drive train are included: the rotor, main shaft, couplings, gearbox, brakes, and generator [76]. All of these are detailed in the following sections, except the rotor components, which were discussed before. A typical drive train is depicted in Figure 7.

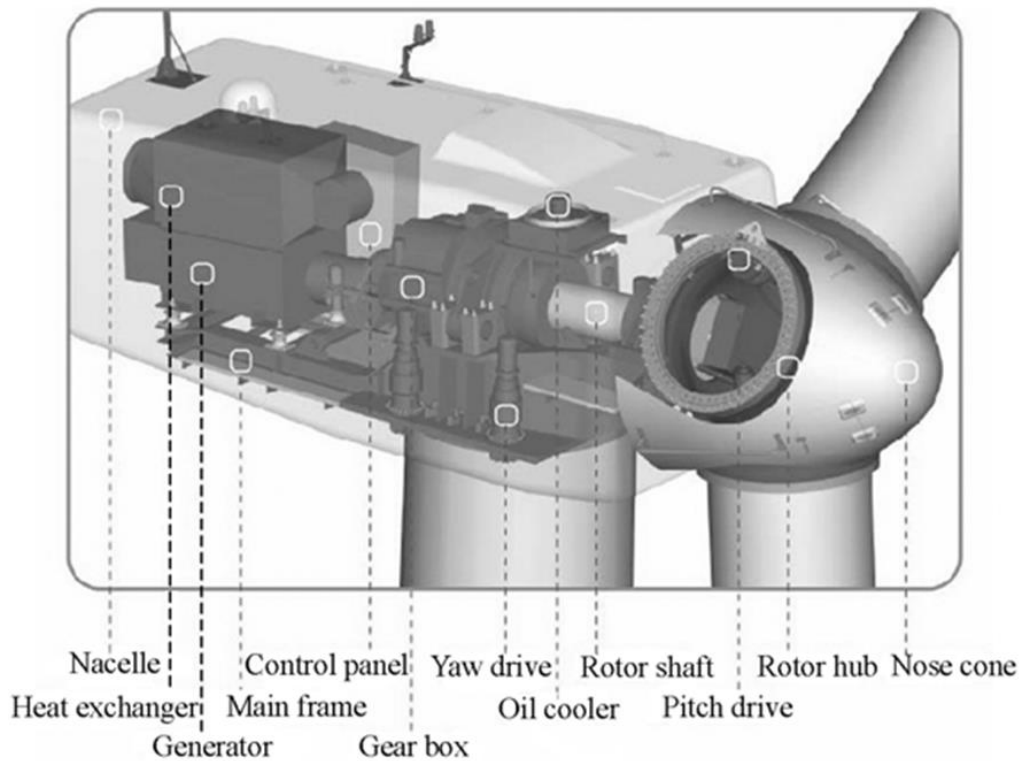


Figure 7. The drive train's components [42]

a) MAIN SHAFT

The main shaft, often known as the low-speed or rotor shaft, is present in every wind turbine. It is the major rotating member of the drive train, transferring the torque from the rotor to the rest of the system and supporting the rotor's weight [32].

Bearings, which transmit reaction loads to the turbine's main frame, support the main shaft. The shaft and/or bearings may be included within the gearbox or independent from it, connected merely by a coupling, depending on the design of the gearbox [77]. The primary shaft is sized, accounting for the torque and bending loads combined. Main shafts are frequently made of steel [78]. The primary shaft choices are shown in Figure 8.

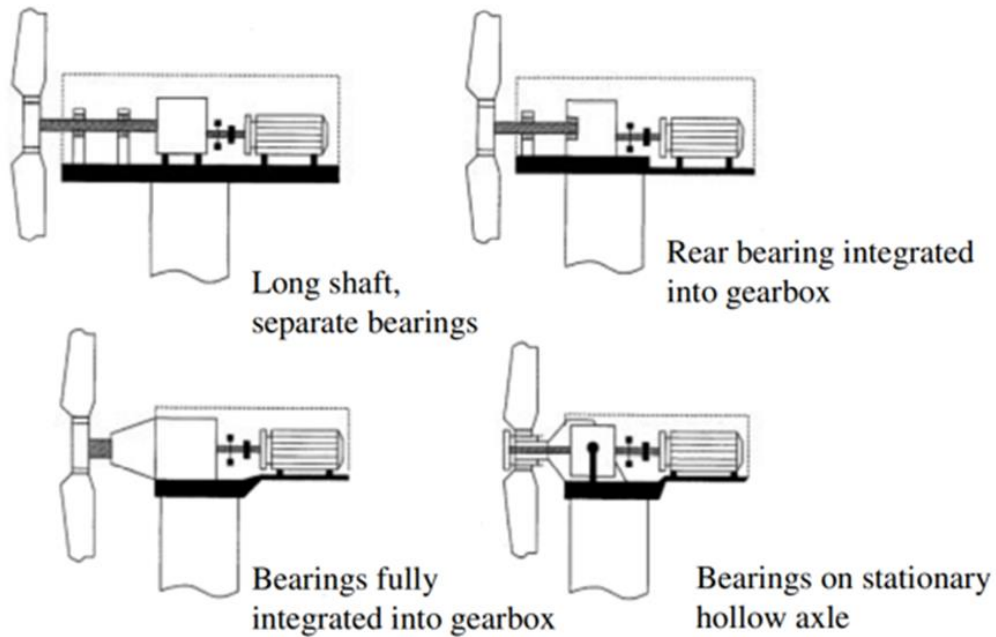


Figure 8. Main shaft options ©Harrison et al., 2000 [79]

b) COUPLINGS

Couplings have many roles, mainly joining the shafts and transferring the torque among them [80]. In other words, before the power is converted to electricity, it is sometimes beneficial to attenuate torque changes in the main shaft. This can be achieved by coupling of suitable design such as fluid coupling. Large couplings are most likely placed between the main shaft and the gearbox and between the gearbox output shaft and the generator [81].

c) GEARBOX

A gearbox is used in most wind turbine drive trains to raise the velocity of the input shaft to the generator. Increasing the speed is required as wind turbine rotors, and hence main shafts, rotate at a significantly slower rate than most electrical generators [82]. While the rotors of small wind turbines spin at speeds of a few hundred revolutions per minute, larger wind turbines rotate at a slower rate, and most common generators spin at 1500 or 1800 rpm

[42]. Other than boosting speed, some gearboxes have other purposes, such as supporting the main shaft bearings [82].

A case, shafts, gears, bearings, and seals are the most common components of all gearboxes. For instance, many wind turbine gearboxes include spur gears. However, helical gears can also be encountered. Depending on the stresses, bearings are either ball bearings, roller bearings, or tapered roller bearings [83]. Aside from that, there are two fundamental types of gearboxes used in wind turbines: parallel-shaft gearboxes and planetary gearboxes [42].

In parallel-shaft gearboxes, gears are mounted on two or more parallel shafts carried by bearings which are installed in the case. In a single-stage gearbox, there are two parallel shafts of different speeds, passed out through the case and attached correspondingly to the main shaft of the rotor and the generator. In addition, there is a gear on each shaft, with the largest one is mounted on the low-speed shaft. Furthermore, it is important to note that large speed-up ratio gearboxes employ several shafts and gears, forming a gear train. For instance, a two-stage gearbox would come up with three shafts: a high-speed output shaft, in which its gear is driven by the larger of the many gears that are installed on the medium-speed shaft, and a low-speed input shaft driving the smaller gear [42, 84]. The following figure depicts a common parallel-shaft gearbox.

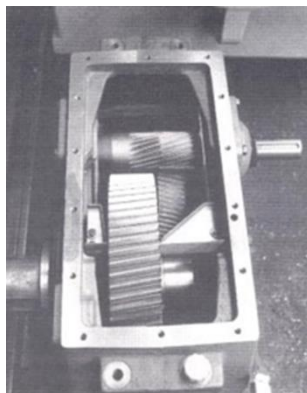


Figure 9. Parallel shaft gearbox ©Hau, 1996 [63]

However, planetary gearboxes have their input and output shafts coaxial and multiple pairs of gear teeth meshing at any time [85]. Hence, planetary gearboxes, shown in the following figure, are light and compact, and the loads applied on each gear are diminished. Moreover, there is a low-speed shaft firmly attached to a planet carrier, which bears three similar tiny gears known as planets, and is carried by bearings in the case. These free-turning gears are installed on short shafts and bearings. A large-diameter internal ring gear and a small-diameter solar gear interconnect with these planets. When the low-speed shaft and carrier spin, the planets in the ring gear mesh, causing the planets to rotate at a faster rate than the carrier. The interactions of the planets with the sun's gear cause it to rotate as well. The high-speed shaft, supported by the bearings in the case, is then driven by the sun gear, which is rigidly linked to it [42, 86].

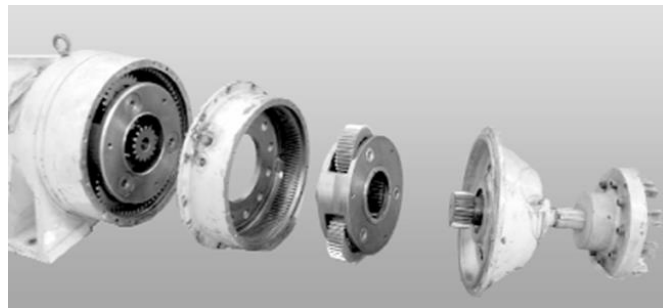


Figure 10. Exploded view of two-stage planetary gearbox [42]

A single-stage planetary gear set, like a parallel-shaft gearbox, has a threshold of speed-up ratio. For that, multiple stage planetary gears are connected in sequence to achieve a larger speed-up ratio [84].

When designing and selecting a gearbox, there are numerous factors to consider such as separate gearbox and main shaft bearings, or an integrated gearbox, basic type, number of stages, speed-up ratio, gearbox weight and costs, gearbox loads, lubrication, intermittent operating effects, and noise [87].

Wind turbine gearboxes can be purchased separately or in combination with other components known as integrated or partially integrated gearboxes. While the turbines with a

partially integrated gearbox have the main shaft and main shaft bearings integrated into the rest of the gearbox, the turbines with a completely integrated gearbox have the gearbox case functioning as the wind turbine's main frame. The rotor is attached to the low-speed shaft. The generator is attached to the case directly and is linked to the high-speed shaft. The generator is fastened directly to the case and is linked to the high-speed shaft. The yaw system is partially integrated into the case's bottom [42, 88]. A partially integrated, two-stage planetary gearbox is illustrated in Figure 11.

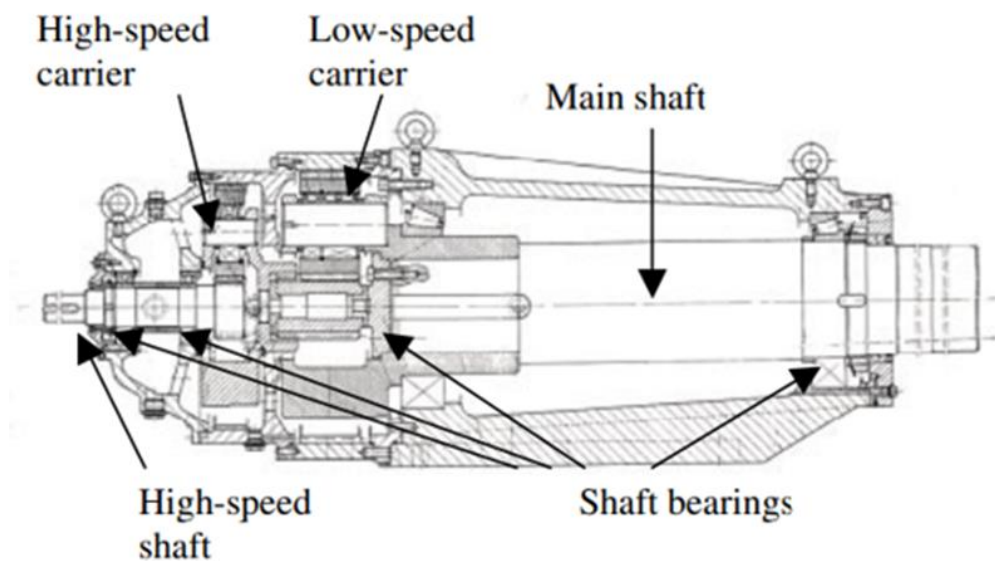


Figure 11. A partially integrated, two-stage planetary gearbox [42]

In most cases, the number of stages in a gearbox is of minor importance to the wind turbine designer. It is significant since it influences the gearbox's complexity, size, weight, and cost. Additional internal components, such as gears, bearings, and shafts, are required when stages are added [89].

A gearbox's speed-up ratio is proportional to the rotor's desired rotational speed, determined by aerodynamic considerations, and the generator's speed [90].

The weight of a gearbox rises considerably as the turbine's power rating rises and scales roughly with the cube of the radius. Because planetary gearboxes are lighter than

parallel-shaft gearboxes, they provide a weight benefit. However, because of their greater complexity, they cost more than their lighter weight would suggest [91].

The rotor is responsible for most of the loads that the gearbox must withstand. Loads may include at least the main shaft torque, as well as the weight of the rotor and several dynamic loads, depending on the degree of integration of the gearbox with the main shaft and bearings. Furthermore, the generator, both while starting and during normal operation, as well as any mechanical brake on the high-speed side gearbox side, imposed loads. Over time, the gearbox will be subjected to certain relatively constant loads, others that vary periodically or randomly, and yet others that are transitory. All of these factors contribute to gear teeth fatigue and wear, as well as bearings and seals [92].

Lubrication is a key factor to consider when operating a gearbox. For that, oils must be chosen to lessen wear on gear teeth and bearings while also having the turbines perform well under external environmental conditions. Filtering or active cooling of the oil may be required in some situations, and oil samples should be taken regularly to examine the status of the oil and look for symptoms of internal wear [93].

The intermittent operation, which is frequent in wind turbines, can significantly shorten a gearbox's life. Oil may drain away from the gears and bearings when the turbine is not working, leading to insufficient lubrication when the turbine starts. In cold weather, the oil's viscosity may be excessively high while waiting for the gearbox has heated up, and the use of gearbox oil heaters may be beneficial. In addition, moisture condensation can accelerate rust [42, 93].

Noise from gearboxes is a possibility. The type of gearbox, the materials used to make the gears, and how they are cut influence the noise produced [94].

d) *GENERATOR*

The generator transforms the rotor's mechanical energy into electrical energy. Most grid-connected generators run at a constant or virtually constant speed causing most wind turbine rotors to turn at an almost constant speed [95].

e) *BRAKE*

In addition to any aerodynamic brakes, a mechanical brake is used in almost every wind turbine's drive train. In the vast majority of circumstances, the mechanical brake is sufficient to stop the turbine's operation. It can be used too in some scenarios for parking and stopping the rotor from spinning at the stop of the turbine's operation [96].

Disc brakes and clutch brakes are the two types of brakes commonly used on wind turbines. The disc brake works the same way that a car's brake does. The shaft to be braked is securely attached to a steel disc. Brake pads are pushed against the disc by a hydraulically driven caliper during braking. The resulting force produces a torque that opposes the disc's rotation, slowing the rotor [42, 97]. Figure 12 depicts an example of a disc brake.

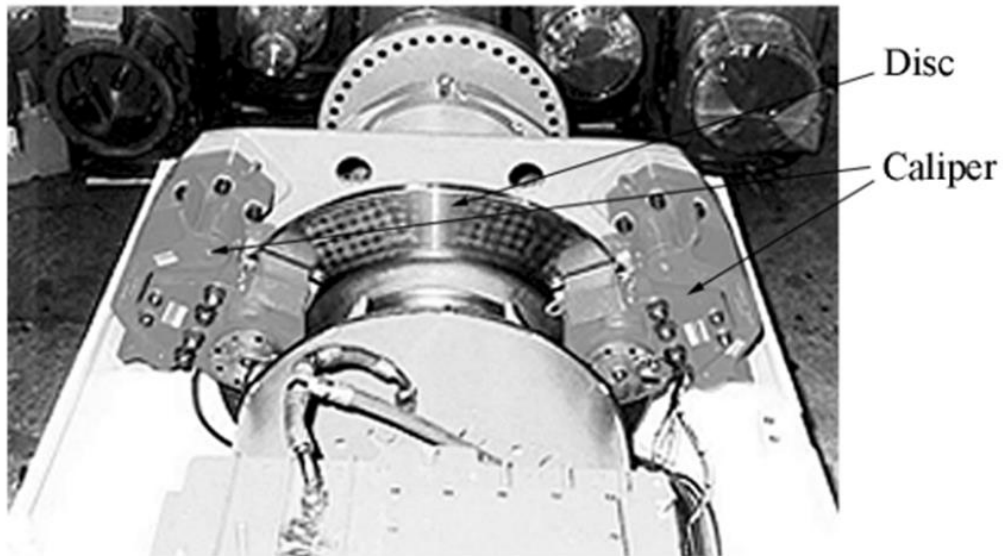


Figure 12. A disc brake [42]

Whereas clutch brakes are generally activated by springs, making them fail-safe by design. Compressed air or hydraulic fluid is used to release these brakes. Another, less popular type of brake is the 'dynamic brake,' which is powered by electricity [98]. After removing the wind turbine's generator from the electrical grid, the primary premise is to feed power to a resistor bank. This puts a strain on the generator and, as a result, torque on the rotor, slowing it down [42].

Mechanical brakes can be found in several places throughout the drive train. When mechanical brakes are installed on the high-speed side of the gearbox, they can be installed on either side of the generator. They can be too on the low-speed side of the gearbox, but they should apply significantly more torque than one on the high-speed side. As a result, it would be quite large. Nevertheless, when the brake is on the high-speed side, it must work through the gearbox, potentially adding gearbox wear. Moreover, if the gearbox experiences an internal breakdown, the high-speed brake may be incapable of slowing the rotor [42, 99].

The type of brake depicts its activation mode. Hydraulic pressure, provided by a hydraulic pump in union with an accumulator, is required for disc brakes. Springs can be used in some designs to exert brake pressure, and the brakes are released by a hydraulic

system. Whereas, spring-applied brakes are common on clutch-type brakes where they are released using either a pneumatic or hydraulic mechanism. An air compressor and storage tank, as well as necessary plumbing and controls, are required in the case of pneumatics [42].

Three significant factors are considered when choosing a brake: the maximum torque, length of time required to apply, and energy absorption.

A brake designed to stop a wind turbine must be capable of exerting a torque greater than that which might reasonably be expected to come from the rotor. According to recommended standards, the brake design torque should be equivalent to the wind turbine's maximum design torque [42, 99].

A turbine brake should apply almost instantly and ramp-up to full torque in a matter of seconds. The ramp-up period chosen strikes a balance between immediate, which would impart a significant transient load to the drive train, and gradual, which could cause rotor acceleration and brake heating during deceleration. In most cases, the full braking event takes less than five seconds from start to finish [42].

The brake's ability to absorb energy is a key issue. First and foremost, when the rotor is whirling at its maximum speed, the brake must absorb all of the kinetic energy in the rotor. It must also be capable of absorbing any additional energy acquired by the rotor during the stopping phase [32].

1.1.1.3 Yaw system

Almost all horizontal axis wind turbines should be able to yaw to be oriented in the direction of the wind [100]. Some turbines also use active yaw to regulate power. In any scenario, a mechanism must be supplied to allow yawing to occur, and it must do so at a moderate enough rate to avoid excessive gyroscopic forces [101].

Active yaw and free yaw are the two most common types of yaw systems. While upwind turbines are usually those with active yaw using a motor to actively orient the turbine,

down-wind turbines are usually the ones with free yaw using the rotor's aerodynamics to orient the turbine. Hence, all horizontal axis wind turbines have a yaw bearing, irrespective of the type of yaw system. This bearing must support the weight of the turbine's main component while also transmitting thrust loads to the tower. The yaw bearing of a turbine with active yaw has gear teeth around its perimeter. The yaw drive's pinion gear engages with those teeth, allowing it to be driven in any direction. This yaw drive consists of an electric motor, speed reduction gears, and a pinion gear. The speed must be decreased to allow for a slow yaw rate and sufficient torque to be delivered by a small motor [102].

One issue with active yaw has been the rapid wear or breaking of the yaw drive due to the turbine's continual tiny yaw movements and the shock load cycles that occur between the gears as a result of the motion. A yaw brake is now commonly utilized in active yaw systems to decrease these cycles. When the turbine is not yawing, this brake is activated. Just as yawing occurs, it is released. An example of a yaw drive with a brake is shown in Figure 13. Furthermore, in an active yaw system, the yaw motion is controlled by the yaw error as an input, detected by a wind vane installed on the turbine. The drive system is triggered, and the turbine is pushed in the appropriate direction when the yaw error is outside the allowable range for some time [103].

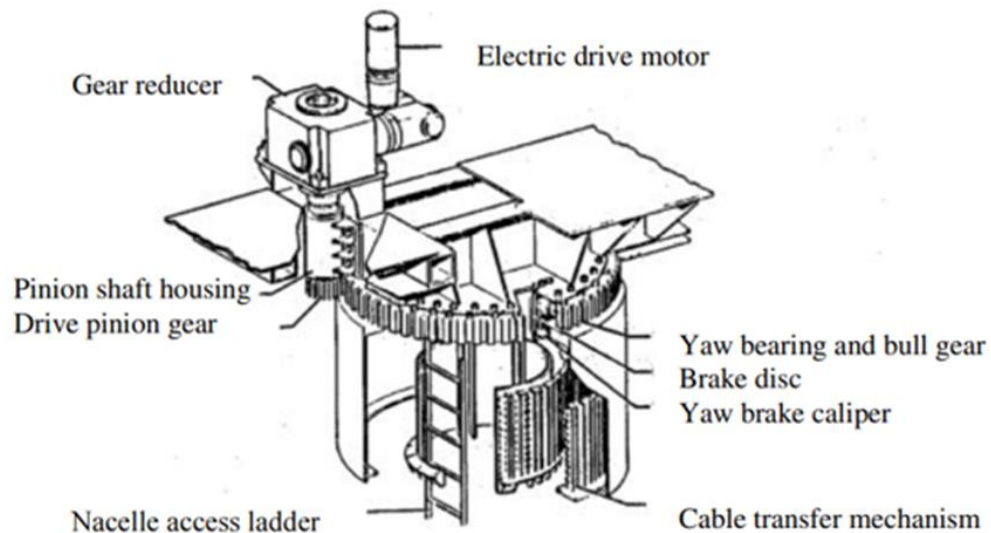


Figure 13. Typical yaw drive with brake ©Van Bibber and Kelly, 1985 [104]

However, the yaw system in turbines with free yaw is usually significantly simpler, it consists simply of the yaw bearing. However, some turbines have yaw dampers to lessen gyroscopic loads by slowing the yaw rate. They are best for machines with a low polar moment of inertia around the yaw axis [42].

1.1.1.4 Nacelle

The main components of a wind turbine except the rotor are housed in the nacelle, which consists of the main frame and the nacelle cover [105].

The main frame provides a sturdy structure to ensure that all components are aligned properly. It is joined to the gearbox, generator, and brake and serves as a connection point for the yaw bearing connected to the tower's top [32].

Main frames are divided into two categories: a separate component or a section of an integrated gearbox. While the main frame, as a separate component, consists of a stiff steel casting or weldment, the main frame, as a section of an integrated gearbox, has a thick case to carry the required weights. In both types, threaded holes or other attachment points on the main frames are provided for bolting on the other components [42].

All rotor loads, as well as reaction loads from the generator and brake, must be transmitted to the tower through the main frame. It also needs to be stiff enough to prevent relative movement between the rotor support bearings, gearbox, generator, and brake [106].

Nacelle covers are often composed of a light material like fiberglass. On larger machines, they are large enough to allow technicians to enter and examine or maintain the internal components. However, a separate nacelle cover is generally linked to the main frame on small and medium-size turbines, allowing easy access. The following figure depicts an example of a nacelle cover. The spinner or nose cone, a component closely related to the nacelle cover and found on various turbines, is where the hub is housed [105].



Figure 14. Typical nacelle cover [42]

1.1.1.5 Tower

The primary part of the turbine is supported in the air by towers. A tower's height is usually at least as tall as the rotor's diameter and may be higher for smaller turbines. Its height should be above 24 m as there is low and turbulent speed close to the ground [42].

For horizontal axis wind turbines, three types of towers are commonly used. Free-standing lattice towers were widely employed until the mid-1980s. Tubular towers have been employed more regularly since then. Guyed lattice or pole towers have never been very typical for machines of medium size or greater, with a few notable exceptions such as the Carter and Wind Eagle turbines [14]. The following figure depicts a few different tower types.



Figure 15. Tubular tower, truss tower, guyed tower (from left to right) [42]

Tubular towers offer a variety of benefits. Unlike lattice towers, they do not rely on a large number of bolted connections that must be torqued and checked regularly. They give a safe place to climb to gain access to the equipment. They give a form that some people find more appealing than an open truss in terms of aesthetics [107].

In terms of materials, wind turbine towers are typically composed of steel, though reinforced concrete is occasionally utilized. Steel is usually galvanized or coated to protect it from corrosion [108].

The tower can be subjected to static and dynamic loads. Steady loads can be primarily the aerodynamically produced thrust and torque and the machine's weight. Dynamic effects, particularly on soft or soft–soft towers, can be a substantial source of loads [109].

For evaluating the tower's loading, at least two conditions are considered: functioning at rated power and stationary at survival wind speed. The consequences of loading must be taken into account, especially when it comes to bending and buckling [42, 109].

The tower top allows the link of the primary structure of the wind turbine to the tower and is linked to the stationary section of the yaw bearing. The top tower is often made of cast steel, and its shape is based on the type of tower [42].

The tower foundation should be able to keep the turbine standing and stable under extreme design conditions. The most common type of foundation is a reinforced concrete pad, and the concrete's weight is designed to overturn resistance in all scenarios. Sometimes, turbines are erected on the solid rock where rods are grouted into holes bored deep into it. A concrete pad can be utilized to deliver a flat surface, but the rods will eventually bear any tensile loads [110].

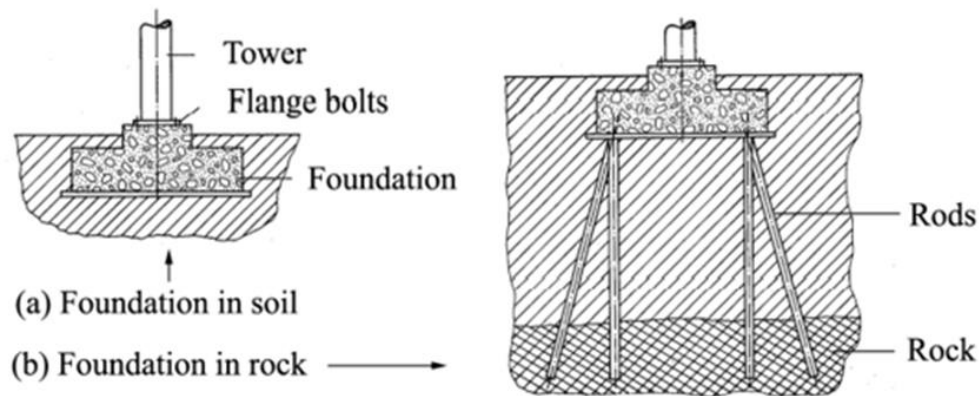


Figure 16. Wind turbine foundations ©Hau, 1996 [63]

The method of tower erection chosen will directly impact the tower's design. While cranes are commonly utilized in the installation of bigger turbines, self-erecting turbines are typical in small and medium-sized turbines. The loads that the tower will encounter during installation are a significant factor in the tower's design, regardless of the method of erection [42].

1.1.2 Types of wind turbines

Modern wind turbines are classified into horizontal-axis and vertical-axis turbines based on the rotating axis of the rotor blades. In addition, diffuser-augmented, multi-rotor, and co-axial wind turbines are examples of other types of wind turbines [111].

1.1.2.1 Horizontal axis wind turbines

Horizontal axis wind turbines have two or three blades or a disk with many blades, which is the multibladed type, attached to it [112]. They are one type of wind turbine that must be aligned with the direction of the wind. As a result, they necessitate a wind sensor to detect wind direction and some sort of yawing mechanism to spin the device to be successfully aligned against the wind. The need for facing the wind stems from both a more effective distribution of force on the rotors and the risk reduction of structural damage to the turbine due to inadequate loading on the turbine structure. In terms of structural consequences, the building of this sort of turbine demands significant tower support to support the weight of the blades, gearbox, and generator, as well as the use of a massive crane to bring the pieces to the top of the tower [113].

Furthermore, the mast's base must withstand strong winds that blow where the turbine is installed. Horizontal axis wind turbines are the most commonly used type of wind turbine due to their efficiency and higher power generation capability for the same footprint. As a result, most wind farms, which are power plants with several wind turbines generating electricity, employ these types of wind turbines [114]. This type of wind turbine also has low cut-in wind speeds and low cost per unit power output [31].

Horizontal axis wind turbines are classified into two types: up-wind turbines and down-wind turbines, based on the wind-flowing direction's configuration of the wind rotor.

The majority of horizontal-axis wind turbines in operation today are up-wind turbines, with wind rotors towards the wind [32]. Because up-wind horizontal axis wind turbines encounter the wind, the wind attains the rotors before the mast. As a result, the rotors are not affected by the wind shade behind the tower, resulting in a more efficient operation and less vulnerability to rotor wear and tear. Nevertheless, the yawing mechanism is required, which adds to the weight of the structure and avoids destroying the turbine [115]. Another consideration for up-wind wind turbines is that their rotors should not be flexible so that they do not bend and collide with the mast when the wind speed is high. To further avoid such incidents, the rotor is set back from the tower. This complicates the manufacturing of these wind turbines, and the relative inflexibility of the rotor blades necessitates the use of heavier material for blade construction [31]. Figure 17 depicts an up-wind turbine.



Figure 17. An up-wind turbine

However, down-wind horizontal axis wind turbines are one of the less prevalent types of wind turbines. Their design is similar to that of upwind horizontal axis wind turbines, with the exception that the rotor is placed downstream of the tower; wind strikes the mast before reaching the blades. Because the rotor blades are more flexible in this configuration, lighter materials can be used. As a result, this design achieves two goals: lighter structural weight and improved structural dynamics of the tower by shifting some of the load from the tower to the blades during bending. Downwind horizontal axis wind turbines do not require a

yawing mechanism if the rotors and casing are constructed so that the casing passively follows the wind direction. For large wind turbines with earthing wires connected to the casing, the passive yawing of these wind turbines would not be an opportunity [114]. Because the rotor of these wind turbines is located downstream of the mast, they endure wind shade. Wind shade not only causes fluctuations in the amount of power produced, but it also causes more fatigue in down-wind wind turbines than in up-wind wind turbines [31]. Figure 18 shows a downwind horizontal axis turbine.



Figure 18. A down-wind horizontal axis turbine

1.1.2.2 Vertical axis wind turbines

Vertical axis wind turbines are a type of wind turbine in which rotors rotate a vertically placed shaft. Such a design allows for less sensitivity to wind direction, making them ideal for places where the wind direction changes frequently. No matter which way the wind blows, the blades will still move and rotate the shaft to generate power [116].

The generator of these wind turbines is close to the ground. This is because, given the design of the rotors and their height, taking it to a higher altitude would be impractical. This configuration makes vertical axis wind turbines easier to maintain than horizontal axis wind

turbines, which have all their components installed at some height [117]. Vertical axis wind turbines, on the other hand, have poorer efficiency than horizontal axis wind turbines due to significant quantities of air drag on the rotors for some designs, as well as reduced power production because wind speed and flow are higher and softer at a distance from the ground [118].

The paragraphs that follow discuss some of the vertical axis wind turbine models.

One of the drag-type vertical axis wind turbine types is Savonius turbines, as illustrated in Figure 19. Their design concept is very similar to that of cup anemometers. Therefore, there is always one surface with the maximum drag, while others have less drag force applied to them [118].



Figure 19. Savonius turbine

The key feature of this design is that it will rotate regardless of which way the wind blows. These wind turbines can deal with low-speed winds, are simple to build and maintain, and perform well in turbulent winds. Despite these benefits, this design is extremely inefficient. It is because the favorable and adverse drag forces are not so dissimilar, and hence the rotational speed is not as fast. Because of the high torque created, these wind turbines can self-start, but there cannot be a lot of electrical energy produced at the generator due to their low revolutions per minute. As a result, they cannot be used for large-scale power generation

and may only be appropriate for small-scale applications where other types of wind turbines may perform better [119]. There are twisted Savonius turbine designs with long helical scoops that create torque smoothly and could be deployed on rooftops [118], as shown in the following figure.



Figure 20. Twisted Savonius turbines

Darrieus wind turbines, as opposed to Savonius wind turbines and shown in Figure 21, are lift-type vertical axis wind turbines that employ the concept of lift production of airfoils. These are the most commonly used vertical axis wind turbines for power generation, with curved, C-shaped blades that run from the top of the tower to the bottom, where they are connected to the generator shaft [120]. They are efficient because they rotate at higher rates, which allows them to create more power. Torque ripple, which is a periodic increase and drop in the generated torque, causes periodic stress on the tower structure. Torque ripple is not an issue with three-bladed Darrieus wind turbines [121].



Figure 21. Darrieus turbine

Darrieus turbines inspired the design of Giromill wind turbines. As a result, these wind turbines are lift-type vertical axis wind turbines with straight vertical blades rather than curved blades [122]. Giromill turbines, illustrated in Figure 22, do not self-start like Darrieus wind turbines and may not have a constant rotational speed. As a result, they are less efficient than Darrieus turbines. Nonetheless, they are less expensive, quicker to build, and can perform effectively in high winds [123].



Figure 22. Giromill turbine

Cycloturbines, a hybrid-type of vertical axis wind turbines, are extremely similar to Giromill wind turbines with airfoil blades having changeable pitch. During the turbine's startup, the wind is not fast enough. Because of that, the blades are pitched against the wind like the principle of Savonius wind turbines to produce the highest drag and torque to create a self-starting wind turbine. When the turbine reaches certain revolutions per minute, the blades change pitch to produce more lift rather than drag, allowing the revolutions per minute to rise even higher, as is the case with Darrieus wind turbines [124]. Being efficient and adaptable vertical axis wind turbines, it is evident that cycloturbines' design and production are more sophisticated than the other designs, making them more expensive. They will also have more components, making them heavier and requiring more maintenance [114].

1.1.2.3 Other designs

There are also other efficient and innovative wind turbine designs. For horizontal axis wind turbines, different designs are available, such as ducted rotors, shrouded wind turbines, co-axial multi-rotor turbines, and counter-rotating turbines. Furthermore, there are enclosed blades, H-rotors, O-wind turbines, and other types of vertical axis wind turbines [114].

Aside from these newer versions of the same horizontal axis wind turbines and vertical axis wind turbines concepts, there exist bladeless wind turbines such as vaneless ion wind generators and boundary layer turbines [125].

1.2 WIND TURBINE BLADE FAILURE WITH STATISTICS AND DESCRIPTION

1.2.1 Reliability statistics of wind turbines and subsystems

The probability that a subassembly will perform its needed function under specified conditions over a specific amount of time is defined as reliability. The rating scale for an

unrepairable system is reliability, while the rating scale for a repairable system is availability. Unrepairable and repairable systems, such as gears, bearings, bolts, and yaw components, are found in wind turbines. As a result, both reliability and availability should be taken into account while evaluating wind turbines [126].

Low reliability could lead to a series of breakdowns that necessitate significant repair. Although high levels of reliability can reduce the cost and frequency of failures, they can be prohibitively expensive to achieve. Breakdown and maintenance costs account for a large portion of a WT's (Wind Turbine) operating and maintenance expenditures. WT reliability also impacts overall system performance and power output, resulting in additional expenses due to income lost [127].

This section presents WT subassembly reliability data analyzed in terms of failure rates and downtimes to identify critical subassemblies and compare onshore and offshore WT reliability statistics. The failure and downtime per failure statistics are based on 15 data sources: 12 onshore and three offshore. Only 10 of the 15 data sources offer downtime information; the Windstats Denmark, India, CWEA, UK offshore round 1, and SPARTA data sources do not include downtime data [127].

The current trend in wind turbine design is for larger, heavier constructions, increasing the failure frequency. In actuality, failure rates for onshore and offshore wind turbine systems of the same type are vastly different. The failure rates of wind turbine systems and components are depicted in Figure 23. It shows that some essential components fail at a larger rate than others and that the same components, except yaw system and sensors, that work offshore fail at a considerably higher rate than those that work onshore [126].

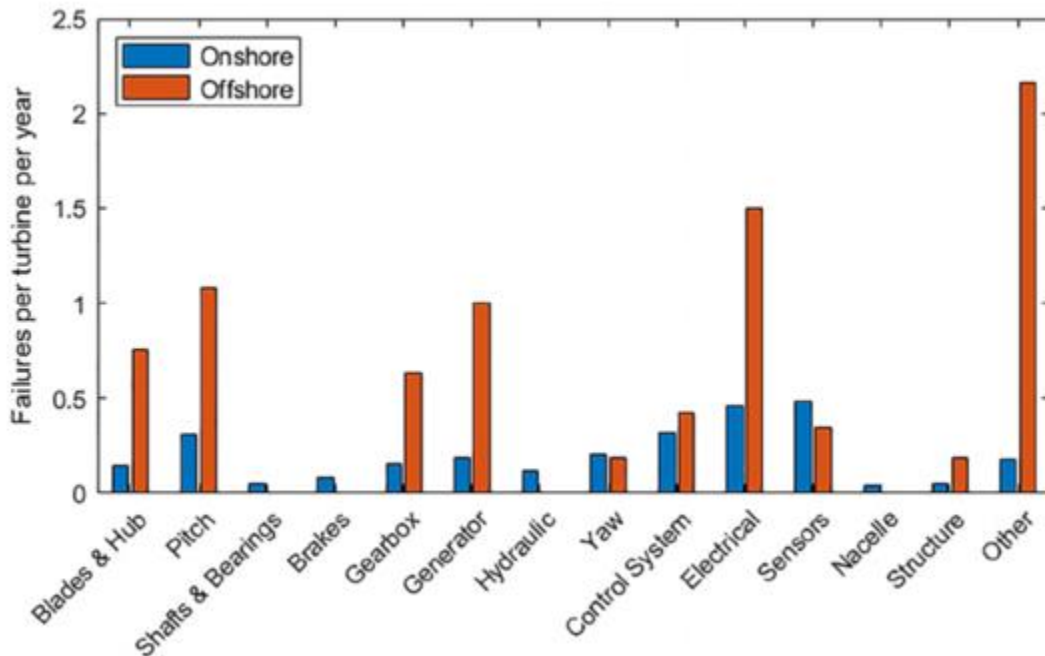


Figure 23. Failure rates for onshore and offshore wind turbine subassemblies [126]

The disparity in failure rates between onshore and offshore can be explained in part by the harsh working circumstances encountered offshore, such as greater mean wind speeds and corrosive salt water. Offshore WT structure is prone to a greater loading variation in high wind speeds due to the influences of the marine environment, including soil and wave conditions. As a result, several important subassemblies on offshore WTs, including blades and hubs, gearboxes, generators, structures, and electrical components, fail at higher rates than onshore WTs. For instance, the failure rates for blades and hubs of onshore and offshore wind turbines are correspondingly 15% and 75% per turbine per year [127].

It is also shown in the previous figure that the turbine blades, generator, and gearboxes are some of the prominent types of wind turbine failure. Because of the remote locations of wind farms and the size of the turbines, routine inspections and maintenance proved difficult. It can be tough to access the enormous rotor blades during periodic maintenance and assess the blade materials and the composite zones. Nowadays, emerging

innovations are paving the road in blade monitoring. For instance, drones are being used for blade inspections, which assists in the inspection process. Nevertheless, it is a must to do a proper, precise, and regular inspection of the rotor blades or components failures will occur [128]. When it comes to blade failure, the larger rotor blades, the more the blades can capture the wind to convert it into torque, driving the generators. Also, greater aerodynamic efficiency is achieved by using larger and longer turbine blades. Recently, the arcs of the turbine blades can stretch up to 80 meters. However, the rising size of the turbine blades might impose additional strain on the structure, leading to blade failures like delamination, gel coat cracks, and erosion. In addition to the size of the rotor blade, lightning strikes, material failure, damage from extraneous factors are all reasons leading to blade failure. Blade failure is the most common in wind turbine failures. However, when the rotor blades capture the wind, the generator is responsible for converting the mechanical energy into electrical energy to create electricity. Various reasons like extreme weather conditions, thermal cycling, some mechanical or electrical failure, improper installation, or some design faults cause the generator to fail. While the gearbox is meant to work in demanding conditions for 20 years, it may fail due to various contributing factors such as contaminated lubricant, bearing difficulties, temperature variations, or insufficient maintenance [128].

The weighted average downtimes per failure for different subassemblies of onshore WT populations are derived similarly to the failure rate comparison. Only one offshore data source reports the repair time per failure (Strathclyde). The onshore and offshore downtimes and repair times are illustrated in Figure 24. For example, the downtime of blades and hubs for onshore wind turbines is 100 hours per failure, whereas their repair time for offshore ones is 15 hours per failure. Furthermore, the repair time, lead time, and other logistic delays that may apply to bringing a maintenance team to the turbine to make a repair and bring the subassembly back to an operational state are expected to be included in the downtime per failure of each subassembly. As a result, downtime exceeds repair time. Onshore databases record downtime, whereas the offshore database (Strathclyde) reports simply repair time. Although there is little evidence to determine whether the population has more downtime or repair time, general tendencies can be noticed [127].

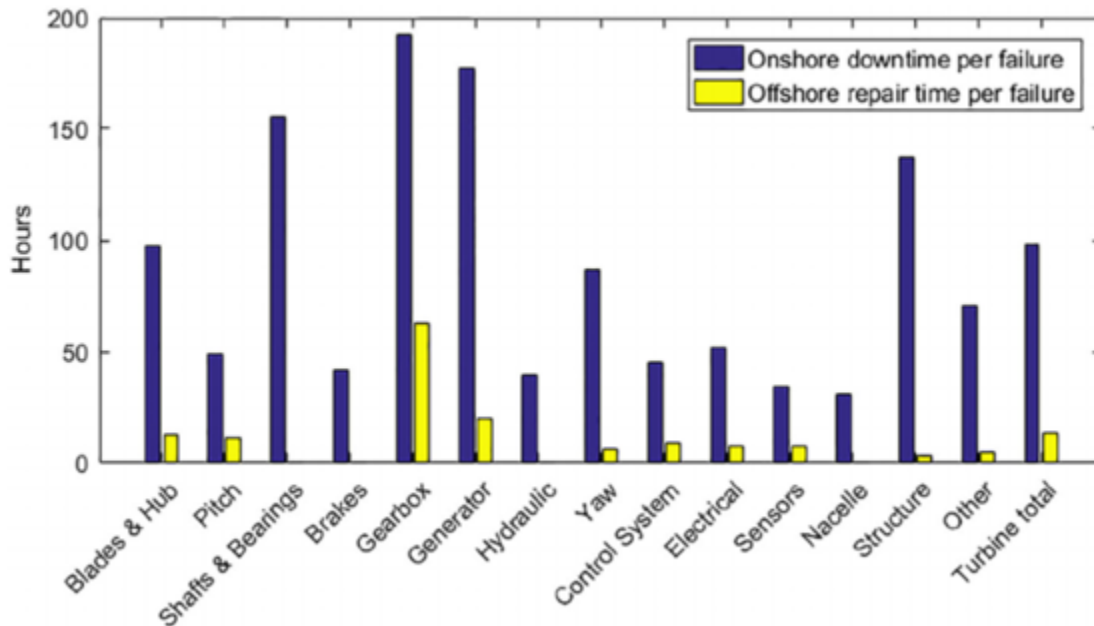


Figure 24. Downtime and repair times for onshore and offshore databases

Hence, offshore WTs have a higher failure rate than onshore WTs. However, the offshore WT's downtime at each stop is almost double that of an onshore WT. These disparities could be due to the harsh offshore working environment and the difficulties in repairing and maintaining offshore WTs [126].

1.2.2 Wind turbine blade failure modes

Wind turbine blades can fail due to various failure and damage modes. Depending on the blade design, the complexities of damage evolution will differ. Regardless of blade design, however, experience has proven that a blade can produce various material and structural damage patterns. These damage mechanisms can lead to blade failure or, in some situations, blade repair or replacement [129].

Failure of a composite construction can be triggered by several circumstances, as listed in the following lines.

1. Geometrical variables such as significant deflection, folding, buckling, and crushing
2. Material properties such as rupture, plasticity, cracking, and ductile/brittleness
3. Early fabrication flaws such as residual tensions, initial distortion, or manufacturing flaws
4. Temperature variables such as low temperatures related to operating in cold weather and high temperatures associated with fire and explosions
5. Dynamic factors (strain rate sensitivity, inertia effect, damage) associated with impact pressure caused by explosions, dropped objects, or similar events
6. Fatigue cracking and other age-related deterioration

A significant amount of knowledge is required to establish how damage builds in a wind turbine blade and design a blade against failure using analytical or numerical approaches [129].

Blades are occasionally tested to failure in full-scale testing to validate the design and provide insight into likely damage types and severity. A combination of axial tension, axial compression, torsion, and bending loads generate failure mechanisms in wind turbine blades at a global level. As a result, the global wind turbine blade analysis aims to find the worst combination of these loads for the local failure mechanism assessments, where all pertinent failure mechanisms must be examined for criticality across the blade as a whole. If a significant failure mechanism is discovered, design calculations or testing must be performed to show that the failure mechanism will not occur during the blade's design lifetime [130].

The five typical composite failure mechanisms are:

1. Global Buckling Fibre Failure where fibers fail with dominant strain parallel to the fiber direction surpassing the individual fibers' tensile or compressive strength capability. At both the micro and macro scales, fibers can buckle, and buckling will

dramatically lower compression strength, and flaws will amplify its effect. However, fibers rarely give and are prone to brittle fracture [130].

2. Matrix Failure can be caused by longitudinal/transverse tensile and compressive loads, as well as in-plane shear stresses. It reduces the laminate's strength and stiffness, leading to further delamination. Both the matrix and the interface to the fiber must be considered in matrix failure assessments, and the strength of the interface may be impacted significantly if the fiber seizes [130].
3. Inter-Laminar Failure exists in two types: Shear stresses cause inter-laminar shear failure, and tensile stresses cause inter-laminar tension failure in the matrix between neighboring plies/ laminae. De-lamination and sub-laminate buckling can occur due to these failure types [130].
4. Sandwich Failure is caused by tensile, compressive, and shear loads, which eventually lead to the breaking and local yielding of the sandwich core material. Wrinkling, shear crimpling, and face dimpling are three additional probable buckling failure modes for the sandwich structure [130].
5. Fatigue failure accumulated by cyclic loading and passing through many phases beginning with matrix cracking, delamination, progressive fiber breaking, and finally fracture if it can be demonstrated that the structure can tolerate the degradations inherent in the previous fatigue damage stages [130].

Erosion is an additional significant failure mode, contributed by various environmental factors such as rain, dust, and sand. In plus, wind turbine blades' leading edge and tip are particularly prone to erosion. Therefore, the basis for erosion protection must be expressly indicated in the technical specifications for the blade, and relevant surface finishes must be analyzed for projected erosion and tested at the highest projected surface temperatures if the blade has anti-icing functions [130].

Figure 25 depicts some failure mechanisms discovered in a wind turbine blade that was tested to failure.

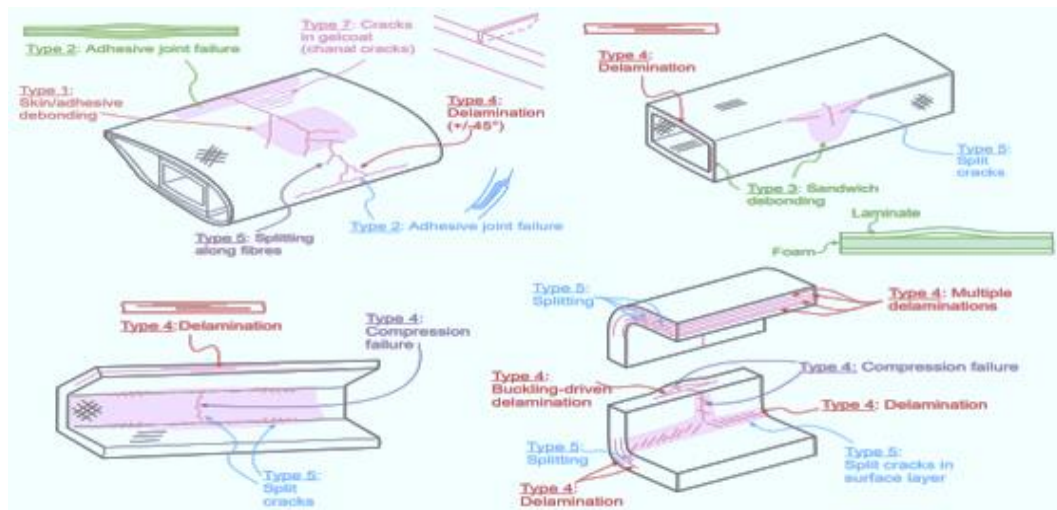


Figure 25. Failure modes identified in a wind turbine blade that was purposely tested to fail [129]

Inspecting these blade conditions is an important first step in blade maintenance which entails a thorough examination and evaluation of blades. Inspections result in findings that are analyzed to see if blades can satisfy their design goals, such as resisting fatigue and high structural loads during their entire design life and producing projected power levels [130].

Typically, identifying the severity and/or criticality of a finding is part of the assessment process; this procedure lends itself to grouping findings of common severity into categories. There is no standard system for categorizing wind turbine blade damage or defects. Turbine or blade producers, service providers and blade inspection/maintenance firms, drone operators, turbine owners, operators, consultants, and industry groups have all established and use various categorization systems [129, 130].

Individuals with varying levels of experience, knowledge, and motivations assign categories. The majority of defect and damage classifications, and hence judgments about repair execution and scheduling, are dependent on experience and judgment, as well as

practical and commercial concerns like the season, accessibility, downtime impact, and crew and material availability. Quality systems for blade and turbine manufacturers often set acceptance standards for faults, and structural repair guides typically define damage repair limits [129, 130].

Table 1 shows a variety of failures and faults in wind turbines as described in the presentation produced by Find M. Jensen, Bladena, with an additional column for failure categories based as published by Strange Skriver from Danmarks Vindmølleforening [129].

Table 1 : Variety of wind turbine failures and faults (Find M. Jensen, Bladena) and its failure categories (Strange Skriver from Danmarks Vindmølleforening) [129]

Failure mode	Category	Reason
Interlaminar failure	V2-V3	Brazier effect, Bending moment
Delamination – faulty injection	V1	
Peeling / wear	V1	Wear
Erosion of the sealing of the root	V2	
Flacking of the topcoat	V1	Air bubbles from the manufacturing/poor quality
Missing external parts	V2-V3	Flacking and external objects impact
Fine cracks in topcoat	V1	Low quality of material
Transverse cracks from trailing edge	V2-V3	Poor design
Transverse cracks on blade surface	V2-V3	Poor design
Front edge cracks (transverse and longitudinal)		
Web failure	V3	Brazier effect, Bending moment, poor design
Fatigue failure in root connection	V3	Poor design
Fatigue failure in the root transition area	V1-V2	

Fatigue failure in bond lines, longitudinal cracks in the trailing edge	V1-V2	Transversal shear distortion, Deformation of the trailing edge panels, Trailing edge buckling
UV effect on the fibers	V1	Wear, flaking,
Lightning damage	V3	Lighting
Tower hit by blade	V3	High Tip deflection
Balsa / composite cracking (transverse and longitudinal)		
Transport damage	V0-V3	
Complete separation	V3	

Finally, the following figures are photographic examples of damage and defects taken from an EPRI research of current blade maintenance procedures [131]. It is presented in this section to provide an overview of the state of the industry in terms of categorizing damage and faults, as determined by examining the findings of an industry survey.



Figure 26. Scratch in coating [131]



Figure 27. A small area of coating damage [131]



Figure 28. Crack in structure at the leading edge [131]



Figure 29. Leading-edge erosion [131]



Figure 30. Leading-edge erosion with large exposed surfaces of fiberglass [131]



Figure 31. Long leading-edge chordwise crack with spanwise cracking [131]

1.3 TECHNICAL, ECONOMIC, AND ENVIRONMENTAL CHALLENGES

Many challenges hinder the process of generating electricity from wind energy. They fall under different orders: technical, economic, and environmental. Below is an overview.

1.3.1 Technical challenges

To further increase the performance of WT energy capture, longer and wider power blades are being manufactured [132]. However, an increase in the size of WTB (Wind Turbine Blades) is followed by the rise in the load, which directly affects the safety of WTBs in the service and leads to fault formation [133]. Furthermore, during the blade development process, some flaws may occur. In addition, blades can fail due to fatigue mechanisms when exposed to multiple cycle loads over their lifespan [134].

Moreover, a high degree of reliability should be achieved to get the best possible power production performance of the mounted wind turbine or increase the availability of turbines [135]. The wind turbine blades are crucial in the efficient operation and wind power plant reliability. Hence, high reliability can be accomplished by recognizing the early stages

of blade faults formation to minimize its failure events and depends also on external, indirect factors, such as the maintenance technique used, the availability of spare parts, the time required to repair the wind turbine, etc. [135].

While the offshore repair time per failure of wind turbine blades is about 15 hours, the onshore downtime per failure is about 100 hours [136], as shown previously in Figure 24. Hence, regular inspection and maintenance planning could make maintenance more successful and reduce breakdown situations. Furthermore, wind turbines' operation and maintenance constitute about 25-30% of the overall energy generation cost [137, 138]. Therefore, the maintenance plan should consider both the increase in reliability and the decline in maintenance costs. The wind turbine operation, regular inspection, and maintenance approach is geared towards improved condition monitoring systems [135]. Table 2 compares the cost and time of some non-destructive flaw diagnosis techniques. It is seen that the detection method is either expensive or the acquisition of the results is delayed. However, hyperspectral imaging is cost-effective and rapid.

Table 2 : Synopsis on cost and time of results of test methods

Test Method	Cost	Time of Results
Ultrasonics [139]	Expensive	Immediate
Eddy Current [139]	Expensive	Immediate
Infrared Thermography [140]	Very Expensive	Delayed
Visual Testing [141]	Unexpensive	Immediate
Acoustic Emission [142]	Unexpensive	Delayed

1.3.2 Economic challenges

Wind turbines, including blades, poles, transport, and construction costs, represent the primary cost portion of a wind farm, usually accounting for around 75 percent of the cost of production [143]. For instance, rotor blades contribute to around 22.2% of the total 5 MW wind turbine costs [143].

Wind turbines are typically designed to have a service life of approximately 20 years withstanding the vagaries of a specific local wind climate class, but they can endure longer, particularly in climates of low turbulence. However, some wind turbines were substituted earlier due to their failures which increased the operation and maintenance costs of the wind farm [143]. Moreover, according to a 15-year-long study performed in Germany, rotor blades breakdown is found to be 7% reported of the total failures [144], as shown in Figure 32. Moreover, wind turbine blade failure is very expensive, as when wind turbine blades are damaged, the overall wind turbine in itself will be broken down. Thus, more wind loads faced the neighboring wind turbines, which led in turn to its breakdown [145]. High construction costs and high wind energy leveling costs relative to energy market rates are also characteristics that need to be considered when calculating the feasibility of constructing a new wind turbine [146]. Hence, regular inspection of blade failures can help decrease the operation and maintenance costs of a wind turbine in particular and a wind park in general.

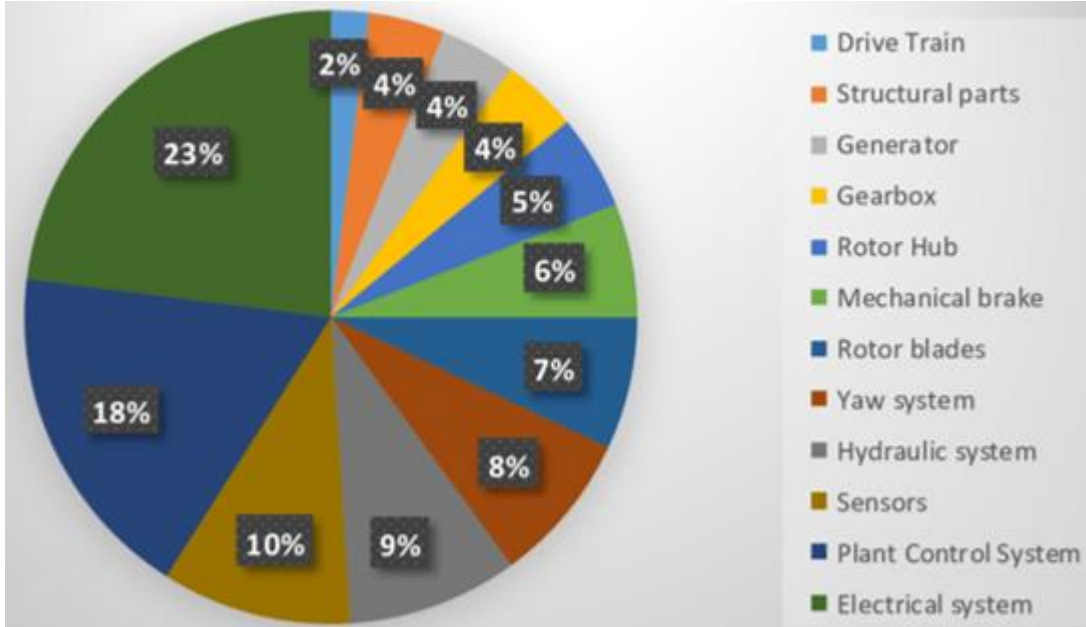


Figure 32. Percentages of failure of wind turbine components [144]

1.3.3 Environmental challenges

Wind turbine blades are vulnerable to damage when continually working in harsh and severe conditions, including moisture accumulation, sleet, ultraviolet irradiation, ambient degradation, fatigue, and wind gusts or lightning strikes. Thus, WTB suffers from many faults and damages [145]. For example, the abrasive airborne particles impact the blade's leading edge and particularly the area close to the tip, characterized by its high velocity, and ultimately lead to its erosion and cause delamination [147]. In addition, damage and cracks can occur around the lightning attraction point [18]. Furthermore, the condition of low temperatures and extreme icing contribute to imbalanced loads induced by ice mass on the blades that increase fatigue and shorten the lifespan of the framework [148].

The key disadvantages of wind farms are the visual effect, noise emissions, ecosystem-related problems such as environmental threats to flora and fauna, health risks due

to electromagnetic fields and potential causes of accidents, and the end of life defined by the wind turbine waste treatment [149].

For instance, the end-of-life wind turbine is a dilemma that is of high implication. A new wind turbine is planned to run for an estimated 20 years. It must be either renewed or recycled after this point. The critical issue with the decommissioning process for wind turbines is that, except steel, copper, and aluminum, the glass fiber reinforced plastics (based on polyester or epoxy) used in the rotor blades have proven difficult to recycle. The choices for blade material waste treatment are mechanical recycling (which is a labor rigorous process and uses the processed material as a filler in artificial wood, cement, or asphalt), incineration, pyrolysis, and landfill, which is the worst alternative [150].

Furthermore, the Caithness Wind Farm Information Forum has published a comprehensive table covering all reported cases of accidents and incidents related to wind turbines that have been identified and verified by press coverage or official releases of information up to 30 June 2020. The data include human incidents (deaths, injuries, etc.), fire accidents, failures of wind turbine components that cause significant harm (failure of structural parts, blade failures, etc.), damage to building and transport, ice throwing, damage to the atmosphere (damage to animals mainly to birds, oil leakage contamination, etc.). This data clearly reveals that the most common wind turbine accident is blade failure, closely followed by fire [151]. A chronological overview of the accidents discussed earlier is shown in Figure 33. The pattern is as predicted – more incidents occur as more turbines are installed.

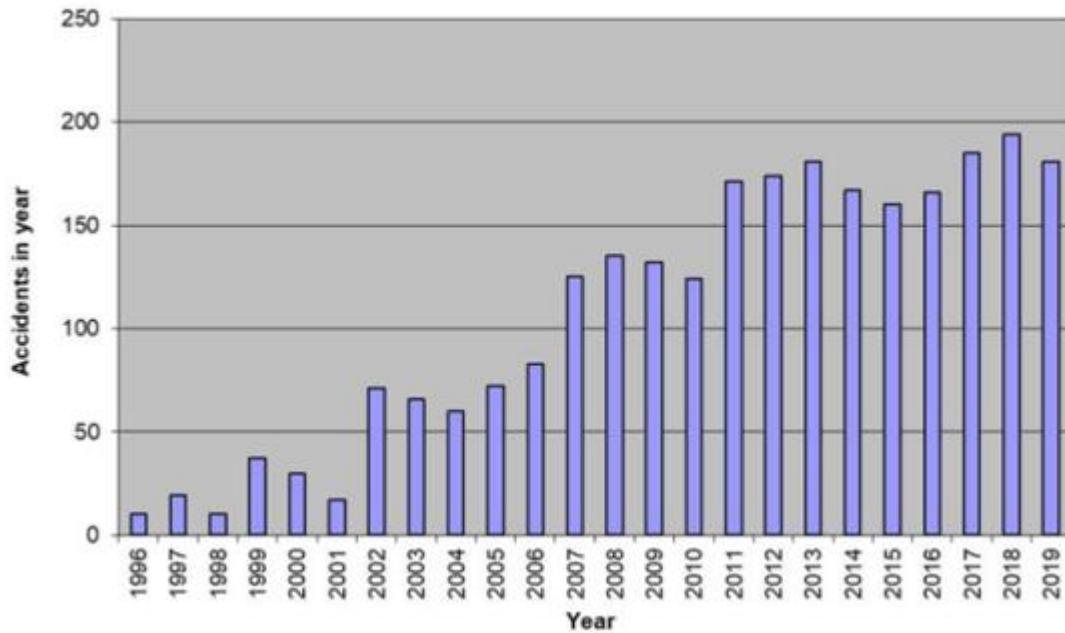


Figure 33. Wind turbines accidents and incidents [151]

To reduce the listed environmental risks, existing wind turbines should be inspected regularly to detect the blade flaws at their early stage of formation and maintained immediately to avoid replacing them with a more significant number of new parts for the wind turbines.

1.4 DETECTION METHODS: ADVANTAGES AND INCONVENIENCES

Several reviews on damage detection methods were presented. Shohag et al. presented a fault diagnosis of the rotor blade with structural health monitoring (SHM) [18]. Yang et al. did a review on all NDT used in the fault detection in wind turbine blades [152]. To avoid premature defects and high maintenance costs, a routine inspection of the wind turbine blades must be done[153]. Different methods are employed for this aim, but each has advantages and limitations. This section summarizes the techniques that can be used to detect crack and erosion on the wind turbine blade.

1.4.1 Acoustic emission testing

The acoustic emission method passes a signal from a source through a propagation medium and is captured by a transducer [154, 155]. This latter sends an electrical signal, which parameters indicate the tested sample's state [156, 157]. The wind turbine blades emit a non-stationary time-varying acoustic emission signal in the presence of mechanical breakdowns or material defects such as cracks and erosion [141, 157, 158]. This method can inspect, even during operation, large areas and many micro-damage types [152, 155]. However, the static condition is not covered, and errors in processing algorithms can lead to misleading results [159, 160].

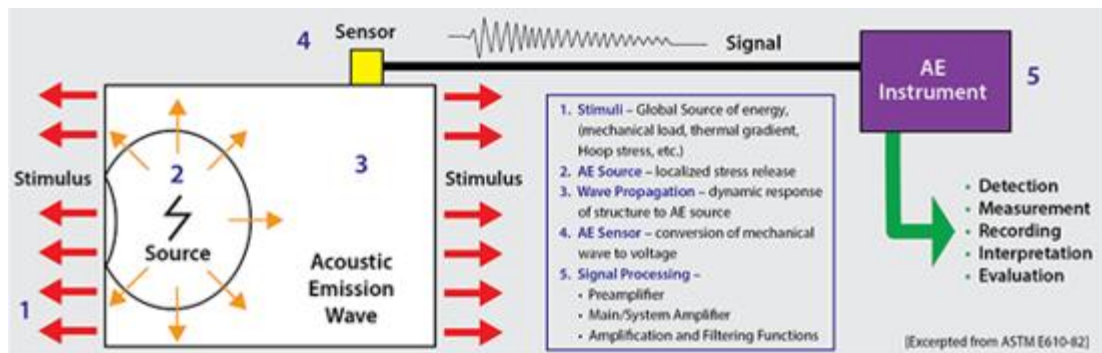


Figure 34. Acoustic Emission Testing Process [161]

1.4.2 Infrared testing

Every material whose temperature is over 0K emits infrared radiation due to the movement of its molecules. This radiation can be measured using an infrared thermal imager receiver [162]. This latter transfers the energy disseminated onto a photosensitive element [158]. Infrared thermography displays the heat variation of the examined sample on the monitor. In the presence of blade defects, the cooling during the heat conduction process is disturbed [163]. The size and shape of the flaws are visualized [164]. This method is highly

sensitive, efficient, and relatively easy to implement [165]. Nevertheless, it is costly and hard to detect a point temperature [166].

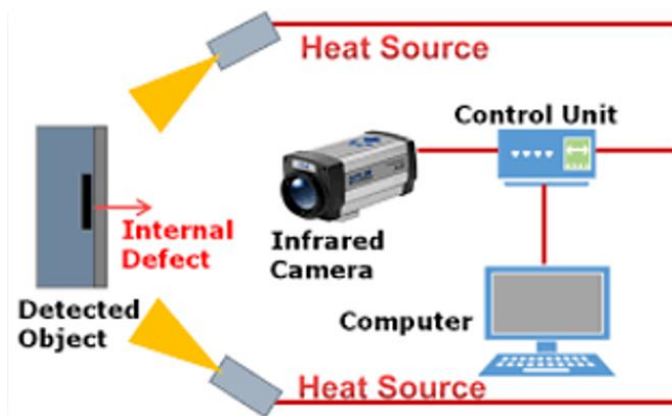


Figure 35. Infrared Testing Process [167]

1.4.3 Fiber grating testing

This method draws incident light into the fiber core using the light sensitivity of optical fiber materials. Therefore, its sensor measures the refractive index variations inside the fiber core [168]. A fiber grating sensor can be positioned anywhere on the wind turbine blade to test and detect any damage signal. Then, the blade damage can be identified by analyzing the data [169]. This method helps predict blade lifetime and its stress level. Furthermore, it works for either static or dynamic signal defect detection [158]. Yet, this method has many drawbacks for long-term monitoring, such as its sensitivity to power source alterations [17].

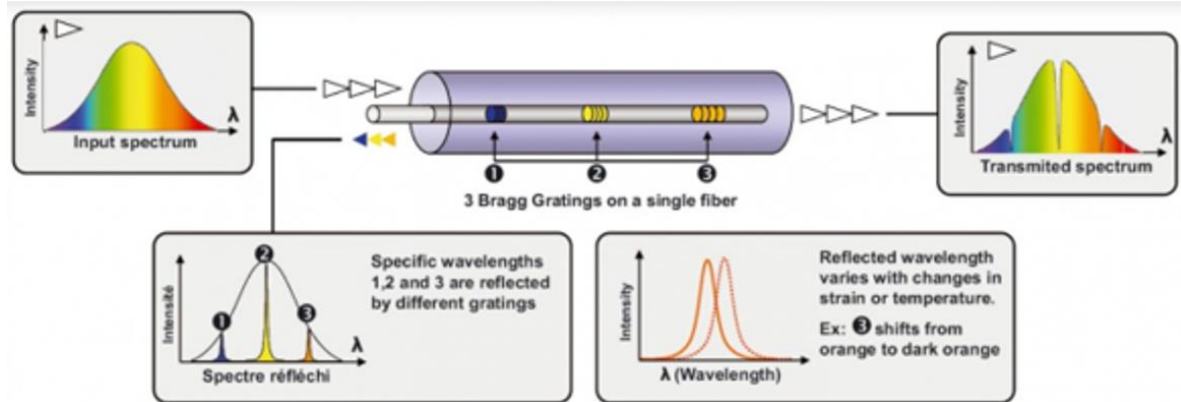


Figure 36. Fiber Grating Testing Process [170]

1.4.4 Ultrasonic testing

This method uses the change of materials' ultrasonic diffusion wave reflection and energy during the conveyance to detect internal faults [157]. The transit time is used to calculate the distance between the surface and the imperfection. Furthermore, the flaw size is determined by referring to the echo signal's size and the transmitting transducer location [155]. In the presence of defects, the received signal has reduced wave amplitude and velocity, variation in frequency, and others [157, 160]. This method is rapid and inexpensive. It is also effective, delicate, and secure. Nonetheless, it is a tough inspection technique, especially for non-smooth surface evaluation, and pretentious to subjective and objective factors [141, 155].

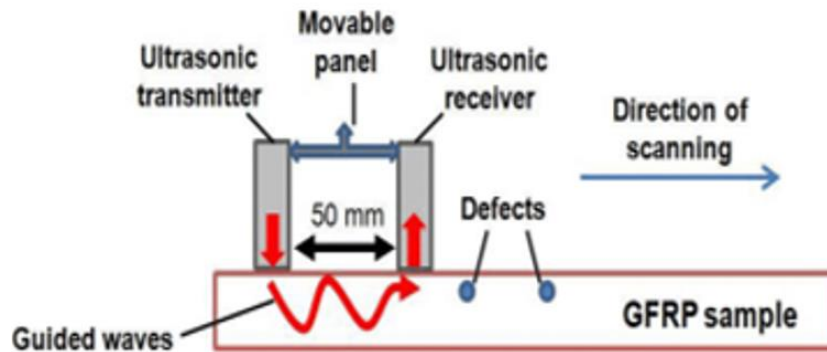


Figure 37. Ultrasonic Testing Process [171]

1.4.5 Guided wave testing

This method uses an actuator that generates a high frequency of guided waves [172]. They act as stress waves and propagate following the studied sample's boundaries [173]. If the guided waves diffuse in all directions and their regular pattern is changed, structural damage such as cracks and erosion is present [152]. This method can inspect large areas for external and internal flaws not far from the sensing equipment [174]. However, the guided wave detection method's equipment is expensive and occupies large spaces [175].

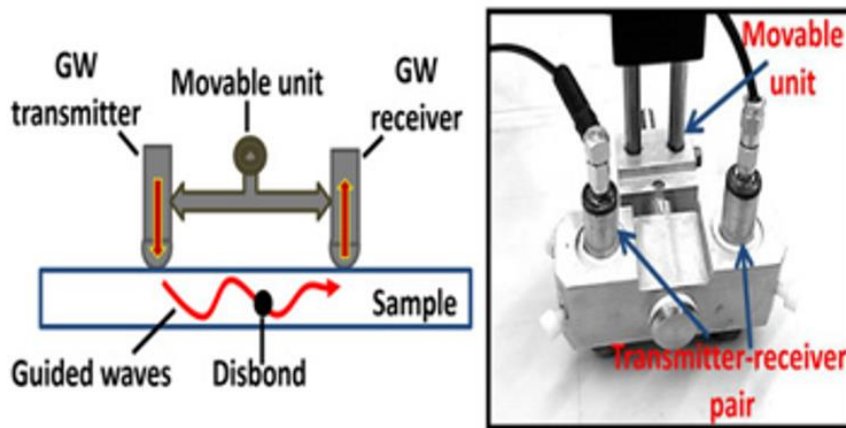


Figure 38. Guided Wave Testing Process [176]

1.4.6 Thermal imaging

This method uses the thermoelastic effect [177]. In other words, variations in stresses lead to variations in temperature detected by sensors or cameras [17]. Higher temperature indicates the presence of defects in the tested region [178]. This method helps in structural health monitoring by locating hot spots on the blade and reducing the damage [178]. However, it is a costly method. Moreover, conduction and convection processes affect the spotting of temperature variations that make the inspection more difficult on a localized scale [179].

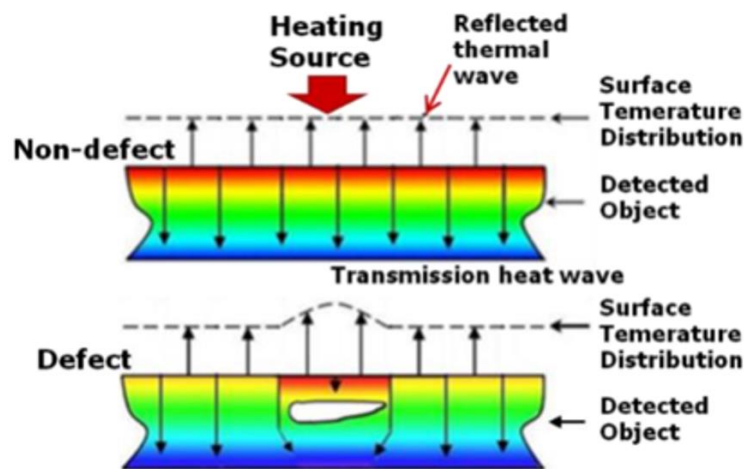


Figure 39. Thermal Imaging Process [167]

1.4.7 Terahertz imaging

This technology inspects dielectric structures in a non-ionizing, non-invasive, and non-contact manner by propagating electromagnetic radiations with frequencies ranging from 0.1 to 10 THz [152]. The refractive index shows variations in the presence of flaws [164]. Flaws are detected using pulse terahertz time-domain spectroscopy, and thickness is calculated by comparing the hindrances of the propagating pulses and their echo [180].

Although this method is recommended for detailed inspection of the defect area [181], its main drawback is the duration, as the analysis is done point by point [164].

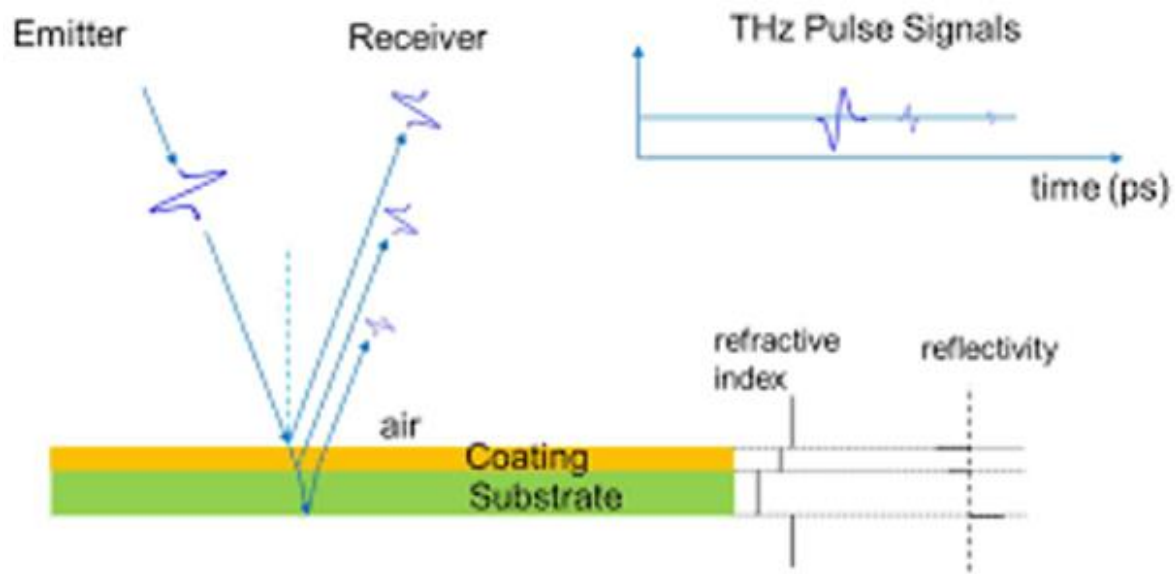


Figure 40. Terahertz Imaging Process [182]

1.4.8 Visual inspection

This procedure is dependent on the technician's experience and vision [183]. Its current applications are being broadened to be performed remotely [184] via drones that scan and send the image to a processing algorithm for further investigation [185]. This method is cheap as no equipment is required if done manually without the use of drone and camera. However, it is time-consuming and affected by human subjectivity and light conditions [186].

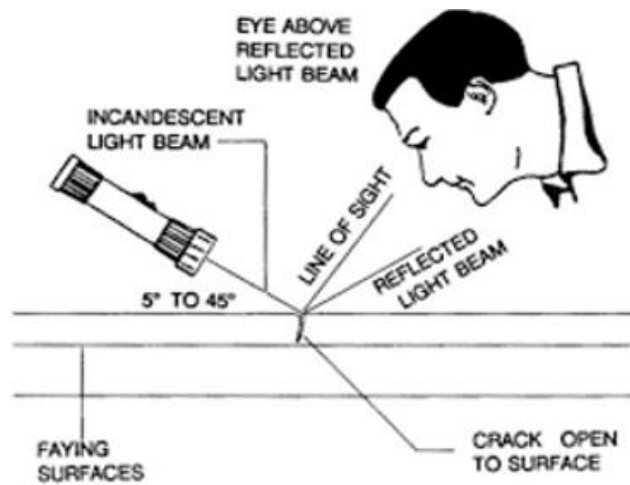


Figure 41. Visual Inspection Process [187]



Figure 42. Unmanned Vehicle [188]

1.4.9 Tap test

This method entails lightly striking the inspected structure and listening for variations in emitted sound caused by material changes, thickness variations, or the existence of material degradation or defects [152]. It can also be automated using a Computer-Aided Tap Tester System [163]. This method helps discover irregularities in the tested sample, and its results can be automated [189]. However, it leads to ineffective results for thick structures [181].

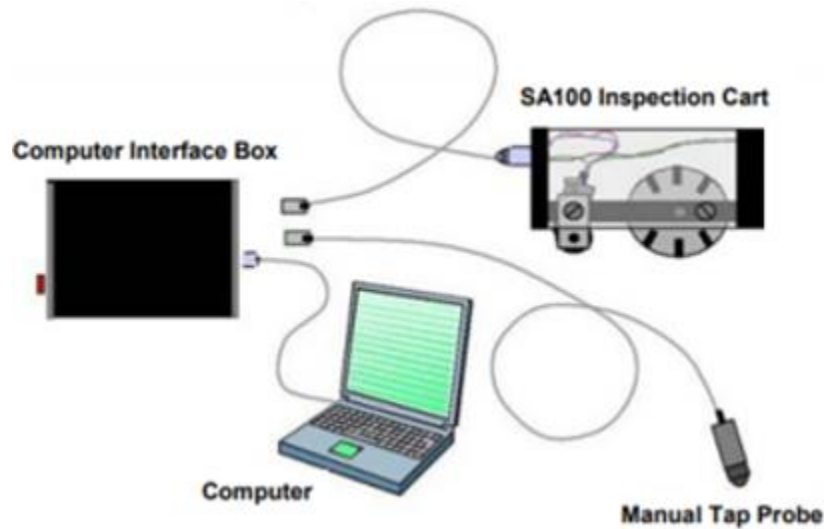


Figure 43. Computer-Aided Tap Tester System [190]

1.4.10 Electromagnetic testing

This method uses electric or magnetic fields and studies the electromagnetic response of the structure [141]. An example is the Eddy Current Testing that produces eddy currents at the magnetic field application on a sample [191]. The coil impedance and the intensity of these currents change in the presence of faults [192]. This technique is cheap, simple, and can detect surface and subsurface flaws [165]. However, it is a time-consuming job [152].

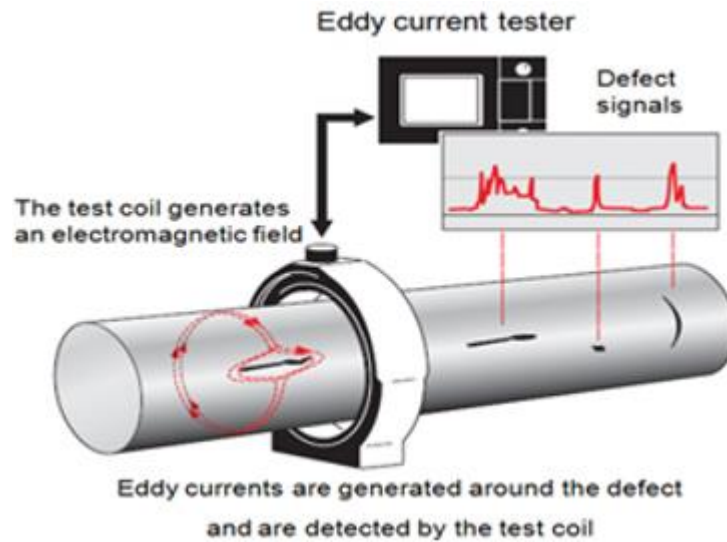


Figure 44. Electromagnetic Testing Process [193]

1.4.11 Vibration analysis

This method is based on applying external forces to the investigated structure and studying its dynamic response as represented by modal specifications and vibration characteristics [194]. The change in these responses can detect the flaws, and the location can be determined using vibration transducers [160, 189]. This method can be applied during both the static and fatigue laboratory tests of wind turbine blades [181]. Nonetheless, it is untrustworthy for structural health monitoring since the many transducers on the blade can produce false data [155].

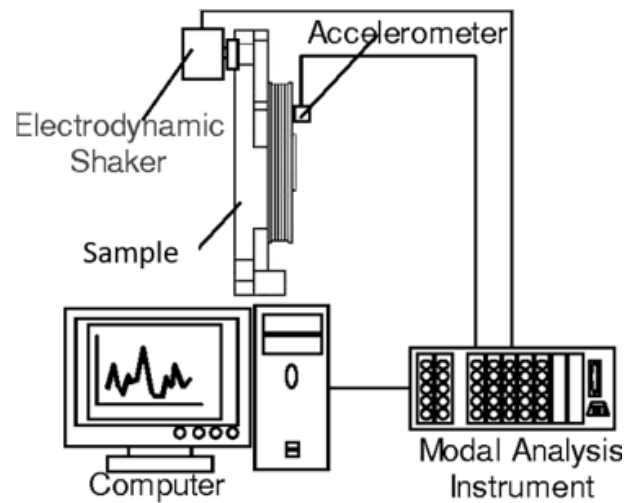


Figure 45. Vibration Analysis Process [195]

1.5 CONCLUSION

To summarize, Chapter 1 presented the different types of wind turbines and their main components, statistics on wind turbines failures, some challenges facing the development of the wind energy sector, and finally a review on some methods used in the wind turbine blade monitoring industry for surface defects. However, the following chapter will present an extensive literature review on icing morphology and accretion phenomena, and the detection methods used for this external problem. Additionally, the drawbacks of ice accumulation on wind energy production are cited.

CHAPTER 2

CRITICAL DISCUSSION OF ICING DETECTION METHODS

2.1 ICING PHENOMENA AND IMPORTANCE FOR WIND ENERGY PRODUCTION AND WIND TURBINE SAFETY

While the windy seasons and increased air density with the falling temperature make winters the optimum season for wind energy harvesting, wind turbine icing is the most severe hazard to the integrity of wind turbines in cold locations. While total wind power capacity reached 800 GW globally in 2020, including 120 GW in the United States alone, statistics from the International Energy Agency TCP Task 19 of "Wind Energy in Cold Climates" show that wind power installation in cold climates accounts for 30% of total installed wind power capacity worldwide. In the climate regions of North America, Europe, and Asia, respectively, 72 percent, 94 percent, and 19 percent of wind turbines are exposed to various icing incidents [196].

It has been discovered that even a mild icing event, such as frost, can cause enough surface roughness on turbine blades to significantly lower their aerodynamic efficiency, resulting in significant wind turbine power reduction. In the event of severe ice, the wind turbine may be unable to start, resulting in the loss of all available electricity for extended periods [197].

Wind turbines in Sweden, for example, were reported to have been shut down for over seven weeks during the best operating season due to icing in the winter of 2020. Since February 14, 2021, numerous wind turbines on Texas wind farms have been forced to shut down due to a winter storm that battered the state. Millions of Texans were affected by the over week-long blackouts in Texas, which were partly blamed on frozen wind turbines [196].

During wind turbine operation, ice accretion and irregular shedding can cause load imbalances and excessive rotor vibration, which can cause the wind turbine to shut down. Icing can potentially cause structural failures in tower structures by raising strains, especially when combined with high wind loads. The icing was also discovered to influence anemometer dependability, resulting in erroneous wind speed measurements and resource calculation inaccuracies. Because of falling and anticipated huge ice chunks, icing difficulties can directly impact worker safety in the surrounding area. It's worth noting that the icing risk is typically greatest in places where wind turbines are best suited, such as northern latitudes, offshore wind farms, and high elevations. In cold weather, wind turbines in these areas are more prone to water contamination and icing [196].

According to a field study done by Gao et al. (2021) to illustrate the effects of ice accretion on the power production of utility wind turbines, it was found that, despite the high wind, frozen wind turbines rotated substantially slower and even stopped down repeatedly throughout the icing event, with icing-induced power losses of up to 80% [198].

Various types of icing may appear at various locations. Precipitation icing, in-cloud icing, and frosting are the most common types of wind turbine icing. Precipitation icing is separated into two types: wet snow and freezing rain, and in-cloud icing is divided into two types: rime icing and glaze icing [196].

The occurrence of freezing drizzle, freezing rain, or wet snow is connected with precipitation icing. When drizzle or rain droplets fall onto a cold surface, they freeze over with a relatively high ice density and adhesion strength, resulting in freezing drizzle or rain. The drizzle or rain droplets are much larger than the freezing fog for in-cloud icing, ranging from 50 microns to 5000 microns [199-202]. Wet snow is most common when the air temperature is between -3°C and 0°C . Wet snow adheres to blade surfaces significantly more easily than dry snow [203]. Frost icing occurs when the surrounding temperature is below the freezing point of water and ice forms on cold surfaces. In comparison to other types of icing, frost icing frequently happens overnight with a lower chance of occurrence [204-207].

When super-cooled water droplets in the environment, such as freezing fog, impinge on a cold surface and freeze into ice, this is known as in-cloud icing. The droplets are usually

smaller than 50 microns in diameter. In-cloud icing is the most prevalent type of atmospheric icing, and it typically lasts for a long time, making it the focus of wind turbine icing research [208-212].

Rime icing is most common in areas with relatively dry air and a colder ambient temperature, mainly below 20°F, which is typical of wind turbines in Iowa and other Midwest states. Glaze icing is typically seen for wind turbines located along the coast in the Northeast States and is connected with highly wetted air and warmer ambient temperatures mainly above 20°F. The most hazardous sort of ice is glaze ice. Because of its wet nature, glaze ice would form far more intricate ice formations over turbine blades. Glaze ice, as opposed to rime icing, could have a bigger impact on the aerodynamic performance of turbine blades, resulting in a considerably higher icing-induced power loss for wind turbines. When the cold air from the north collided with the wet air from the Gulf Coast during the disastrous energy collapse in February 2021, this is believed to be what happened to the frozen wind turbines in Texas [196].

The development of effective and reliable anti-/de-icing devices for wind turbine icing mitigation and protection necessitates a thorough understanding of the underlying physics, including how ice forms and the performance reduction caused by ice on turbine blades [196].

Moreover, studies describe that ice accretion on solid surfaces can be measured in three ways. It can be directly measured by revealing the variations in physical properties such as mass, inductance, thermal conductivity, and others. However, indirect measurements are related to the change in meteorological situations indicating icings such as wind speed, humidity, and temperature. Moreover, a decrease in power production or other icing effects is also considered in indirect methods [213]. In comparison, numerical modeling is based on creating an empirical model that determines the duration and severity of icing situations [214].

2.2 ICING DETECTION METHODS: ADVANTAGES AND INCONVENIENCES

Several reviews on icing detection methods were presented, and relative conditions for ice accretion measurements and various methods employed in ice detection and de-icing systems. Parent et al. described the ice precipitation phenomena and its different types [213]. To avoid premature icing formation and high maintenance costs, a routine inspection of the wind turbine blades must be done [153]. Different technologies are employed for this aim, but each has advantages and limitations. Some of these technologies are presented in this section.

2.2.1 During the site assessment stage

To evaluate a blade heating system financially, the severity of icing and the potential wind energy during the icing event should be determined [215]. For that, the geometry and operation of the turbine and the weather conditions related to icing events (liquid water content, temperature, pressure, etc.) should be studied [213]. Unfortunately, the measurements of these meteorological parameters are costly or complicated. Furthermore, icing duration is empirically calculated [216], and its severity is barely accessible [217]. We should also note that the icing events should be measured reliably at the same elevation of the top blade tip [214] in the intended implementation site [218] with a radial distance from the turbine of 1 km [215].

The following lines describe the icing evaluation methods during the site assessment phase.

2.2.1.1 Double anemometry and vane

Icing occurrences can be identified using heated and unheated anemometers when the difference in observed wind velocities exceeds 5% [219] and sometimes can achieve 20% for values above 2 m/s [220]. This method is cheap, can depict the ice climate and its

persistency [219], and is reliable at temperatures around 0°C [221]. However, Craig proposes the use of a permanently heated anemometer, an unheated anemometer, and an intermitently heated anemometer. This latter is used when detection of 15% difference in wind speeds is measured using the other anemometers. With the relative humidity measurements, these methods can determine the duration of the ice that affects the blade's performance [222] by correlating it to the duration of ice disturbance of the unheated anemometer [219], which is longer than the real icing period. Nevertheless, the main drawback of the double anemometry method is the difference in elevation between the anemometer and the blade where ice is mostly accumulated [223]. Other disadvantages can be the false indication of icing provided by the unheated anemometer and caused by low temperatures [219], as this equipment displays both higher and lower wind velocities. Furthermore, at zero wind, no indication can be provided [224] and at higher values, snowfall can be occurring. Whereas, at lower values, inertial characteristics can affect the measurements and provide misleading results.

Although, Talhaug suggests calculating the standard deviation of an unheated wind vane, at temperatures below zero, from 6 succeeding 10-minute averages to state the occurrence of an icing event [213].



Figure 46. Anemometer and Vane [225]

2.2.1.2 Ice sensors

Ice sensors can be found based on many methods such as vibrating probes, longitudinal wire waves, ice mass measurement method [226], and others [223, 227]. However, they are either costly or inaccurate, unreliable, and asynchronous [223]. Sometimes, ice sensors undervalue the icing conditions due to the heating cycle. For that, a heated detector should be used to determine the severity of the icing event and an unheated one to define its duration [213, 223].

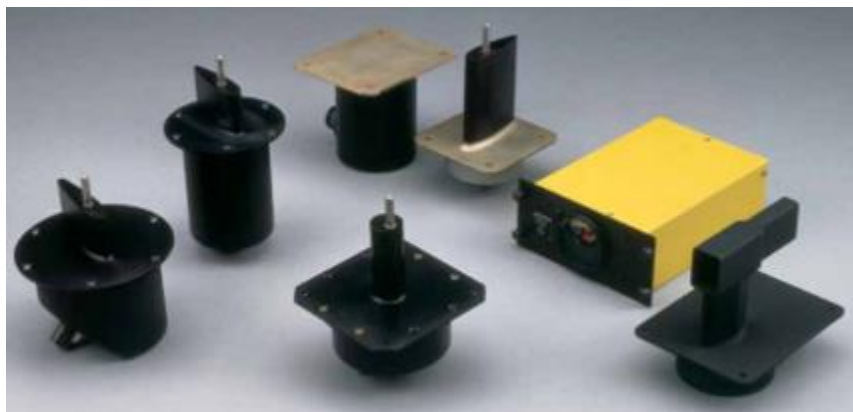


Figure 47. Ice Sensors [228]

2.2.1.3 Visibility and cloud base

In-cloud icing is formed when an object is bounded by a cloud at an approximately wind velocity of 2 m/s and a temperature less than 0°C. Clouds can be spotted using horizontal visibility or the cloud base height via airport observation, video monitoring, a pyranometer, or automatic sensors.

Ice accretion is detected when the cloudiness index measured by the airport observation is higher than 6/8, and the wind turbine is higher than the cloud base altitude. Its intensity can be measured using this index [220]. Furthermore, cloud density can be numerically determined by video monitoring using tinted poles far from the met mast of 50

m to 300 m [229]. At the same time, a pyranometer can detect icing when its measurement of solar radiation intensity is less than 300 W/m^2 [216]. Lastly, radar and microwave radiometers can estimate the liquid water content quickly and automatically detect icing events [230].

However, this method is very costly and underestimates the real ice accretion [223].



Figure 48. Visibility and Cloud Base Detector [231]

2.2.1.4 Relative humidity and dew point

Ice events can be identified by detecting humidity higher than 95% with temperatures below 0°C . Furthermore, it can also be done using a dew point detector [222]. The first method is more applied, but icing conditions are not detected simultaneously with the ice detectors, and thus the expectedness of icing events is low [213, 223].



Figure 49. Dew Point Detector [232]

2.2.1.5 Models

Icing events can be detected using physical mesoscale models and statistical models that consider further information such as temperature, wind speed and direction, cloud cover and height, and others. Using this method, the frequency and rate of icing can be determined [213, 215].

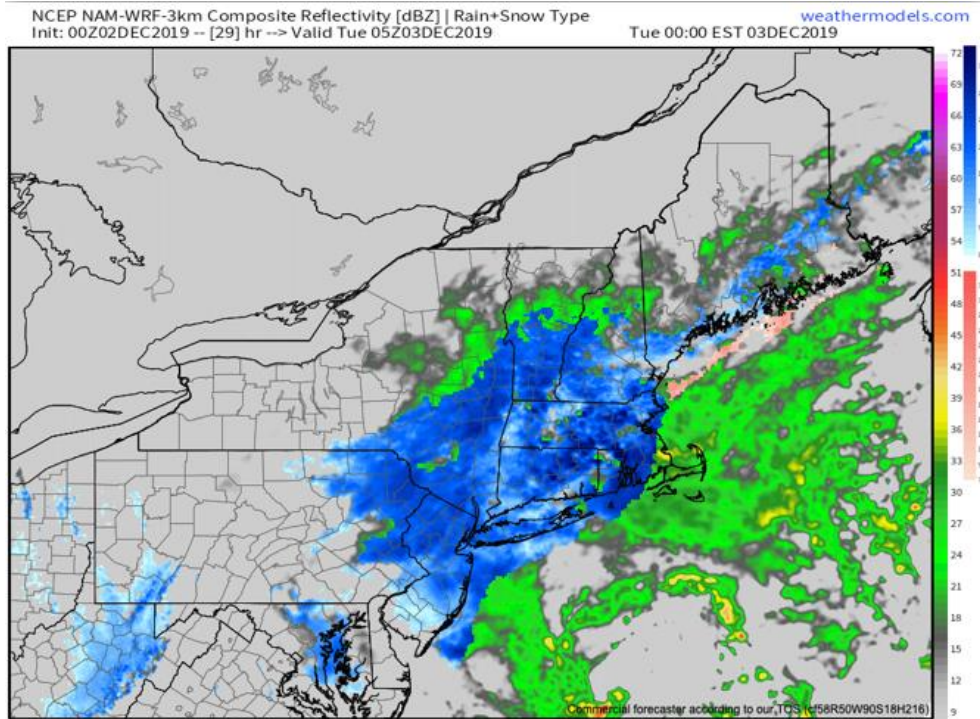


Figure 50. Example of Mesoscale Model [233]

2.2.1.6 Other methods

Icing incidents can be observed visually by videotaping guy cables, and their thickness can be calculated after taking into account the influence of wire vibration. The results of this method can be amended using the airport observations of cloud base [234]. Furthermore, icing conditions can be spotted using damage examination, such as the failure of power lines or climatic poles due to resonance or buckling [213, 224].

2.2.1.7 Recommendations on methods

Freezing precipitation and in-cloud icing are responsible for the different results of the ice detection methods, which none are always reliable and accurate [235]. It is

recommended to measure icing events along with the assessment phase for a minimum of 1 year using these methods. Furthermore, at least two methods should be used simultaneously to facilitate the estimated icing events. None of them shows preeminence on others, and each one is appropriate to specific weather and determination [223]. For instance, an ice detector could be used with the onsite weather indications. Moreover, the severity, which affects the whole ice resulted in production losses, and the duration of icing events, which affects the required heating energy, should be measured via different devices [213].

To have an illustration of the available icing conditions inexpensively, one heated and one unheated anemometer should be installed on the tested mast, and chronological cloud base height results should be compared to the nearest airport observations. In addition to that, a dew point detector intended for the subzero process could help detect the occurrence of in-cloud icing events [222].

2.2.2 During the operation stage

An optimized blade heating system is significantly related to an excellent controlling ice detector [236] that spots ice at its accretion start [237] and by that prevents power production losses that can sometimes attain 15% [238]. Although blade de-icing techniques operated successfully, the ice sensors could not consistently spot the beginning of icing events [214]. Moreover, ice detection on wind turbines should be measured by locating the sensor, having a high sensitivity to detect small accretion, on the blade tip. It should be able to spot icing at different points on the blade [213]. Some of the methods that respect these requirements are cited in the following lines.

2.2.2.1 Multiple anemometry

This method is already explained in the assessment section. The biggest disadvantage is the elevation difference between the anemometer's highest attainable location, the nacelle

roof, and the blade tip, which makes detecting all in-cloud icing incidents more difficult. Furthermore, the turbine wake effect should be taken care of to prevent misleading results [235].

2.2.2.2 Ice detectors

It is the same method described in the assessment section and most used in anti-icing-de-icing-system controlling. A heated detector is used to measure the severity of icing and the unheated one for its duration [223]. However, slight ice masses cannot be instantly detected [215].

2.2.2.3 Video monitoring

A webcam in the hub placed on the expected pressure side of the iced rotor blade can be used to test the blades' surface and compare its appropriate resulting information with others ice detection techniques. The main drawback of this method is that it is costly, a non-stop monitoring, and depends on the visibility of the controller [224]. Thus, it can be appropriate for a short duration of testing [214].



Figure 51. Video Monitor [239]

2.2.2.4 Power curve

Continuous monitoring and comparison between calculated and actual production power curves with temperature and air pressure measurements should be made to detect icing events for stall regulated wind turbines where a power decrease of 50% is suggested as a datum [223]. The difference between the calculated production power curve, indicated by the anemometer, and the actual production power curve, based on the ice detectors [219], can be present for reasons other than icing [214].

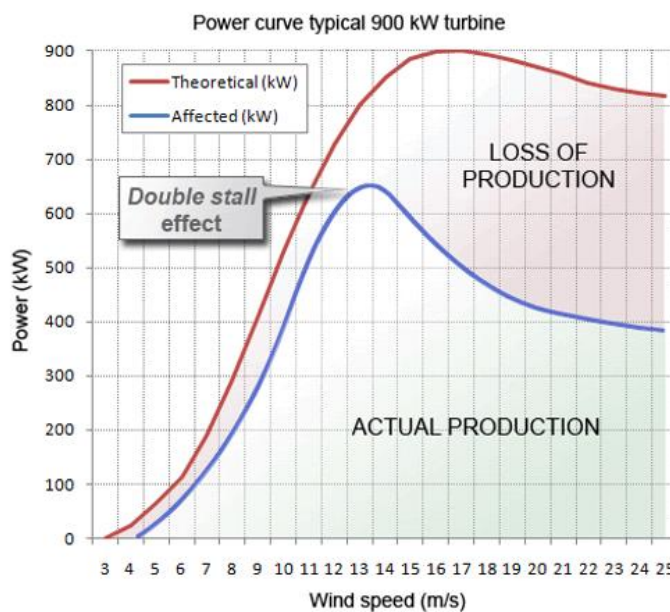


Figure 52. Theoretical and Actual Power Curves [240]

2.2.2.5 Vibration and noise

Vibration sensors can be linked to the de-icing control system to detect unusual high vibrations [222]. After that, the blade starts heating at the onset of turning off the turbine [223]. Small masses of ice accretion can also be detected by noticing the rise of aerodynamic noise from the rotor blades at higher frequency ranges [224]. Furthermore, more studies should be done to determine how the results are affected by the changes in wind velocities

and background noises [213]. Along with stall operation, icing cannot be spotted using these two methods [223].



Figure 53. Vibration Sensors [241]

2.2.2.6 Recommendations on methods

To summarize the study results done by Homola et al. (2006), none of the 29 tested icing detection methods always show reliable results [214]. The fundamental issue limiting the methods' implementation is that the equipment utilized in various ways, such as double anemometry and ice collecting cylinders, is situated on the nacelle of the turbine rather than on the blade tip. Furthermore, the most suitable methods for icing detection on wind turbines are the installation of ice sensors near the blade tip in an inner ultrasound of the blade and a capacitance, impedance, or inductance-based sensor, infrared spectroscopy via fiber-optic wires, and a flexible resonating diaphragm [213].

2.3 CONCLUSION

To summarize, the icing phenomena has been presented in this chapter. In addition to this, some of the methods for detecting icing events have been detailed in this chapter. In spite of the various methods presented, none of these methods presents a powerful method; each of these has its corresponding disadvantage from misleading induction due to the anemometer-blade tip elevation, visibility, sensitivity to temperature and humidity, and the power drop for various reasons. All these drawbacks can be overcome by the use of hyperspectral imaging technology which is presented in Chapter 3 and its experimental icing results are presented in Chapter 7.

CHAPTER 3

SYNOPSIS ON HYPERSPECTRAL IMAGING TECHNIQUE

With the advancement of remote sensing technologies, the usage of hyperspectral imaging is becoming incrementally pervasive. Hyperspectral imaging is based on the capture of images in adjacent-continuous visible and infrared wavelengths [242]. It combines standard imaging and spectroscopy to obtain spatial and spectral information about a sample. This technique allows researchers to analyze the composition of the specimen and synchronously visualize its spatial distribution [243]. Accordingly, they obtain a reflectance spectrum for each pixel of the scene, which allows them to use this signature in various fields of application to find objects, identify materials, or detect processes [244, 245].

3.1 COMPARISON AMONG BROADBAND, MULTISPECTRAL, HYPERSPECTRAL, AND ULTRA-SPECTRAL IMAGING

Figure 54 depicts the distinction between multispectral and hyperspectral imaging. Broadband sensors often generate panchromatic pictures with wide bandwidths. For example, WorldView-1 produced panchromatic images with a high spatial resolution of 50 cm. Most multispectral imagers use four fundamental spectral bands: blue, green, red, and near-infrared. Some multispectral imaging satellites, such as Landsats 7 and 8, have additional spectral bands in the shortwave infrared (SWIR) region [246]. Hyperspectral imaging systems are intended to capture images abounding hundreds of contiguous, continuous spectral bands with standard bandwidths of 10 nm or less. The NASA JPL AVIRIS airborne hyperspectral imaging sensor, for instance, collects spectral data across 224 continuous frequencies, each with a bandwidth of 10 nm and a spectral range of 400 to 2500

nm [247]. Ultra-spectral imaging sensors with very fine spectral resolution could be designated for interferometer imaging sensors. Because of the high data rate, these sensors frequently, but not always, have a limited spatial resolution of only a few pixels [246]. Therefore, the distinction between these remote sensing techniques is not only based on the number of bands used or the type of assessment but also on the continuity between the spectral bands and their spectral resolution.

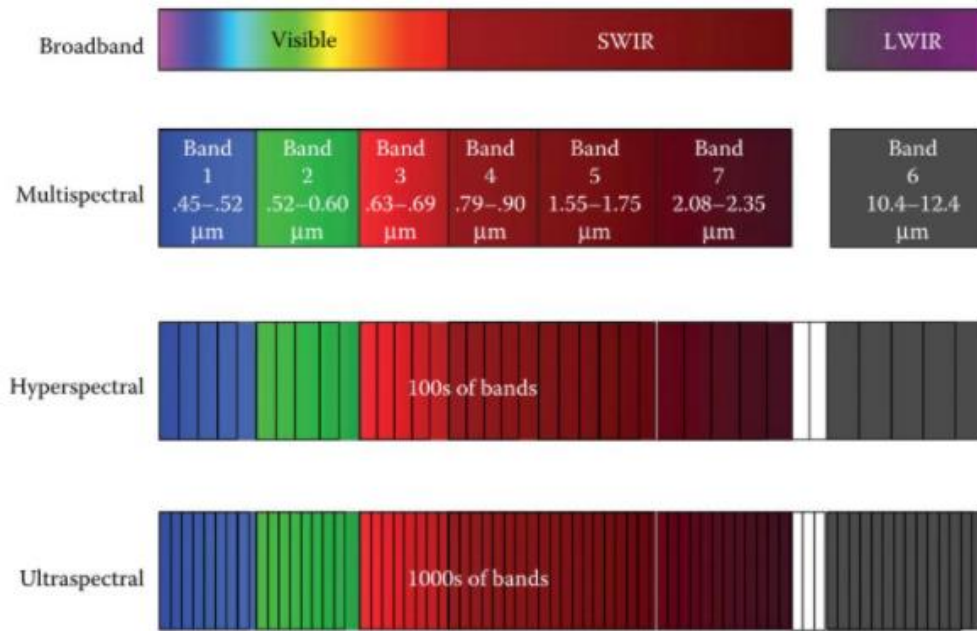


Figure 54. Comparison among the remote sensing technique

By way of illustration, Figure 55 below illustrates the previous explanation; an apple can be analyzed differently by using one of the three spectral imaging classes. First, the broadband, this remote sensing technique, has a single spectral band. Second, the multispectral image is presented where the intensity of the apple can be seen by the bar chart in Figure 55. The resulting image contains only several spectral bands, less than 10. In the third class, the result of a hyperspectral imager is presented, where a spectral signature of the apple is obtained with over 100 spectral bands [248].

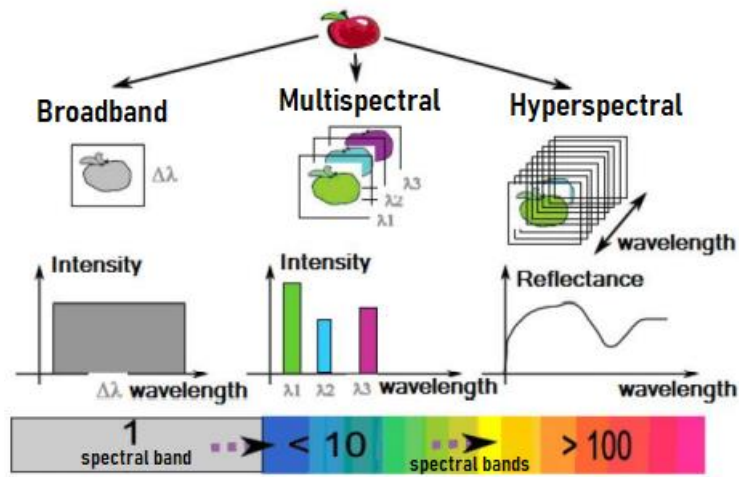


Figure 55. Comparison among broadband, multispectral and hyperspectral

3.2 CONCEPT OF THE HYPERSPECTRAL CUBE

In a metaphorical sense, hyperspectral sensors collect data as a series of pictures. Each image represents a spectral band, which is a wavelength range of the electromagnetic spectrum. These series are combined to generate a spectral cube. This spectral cube is a three-dimensional hyperspectral data cube for processing and analysis. The x and y axes represent the scene's two spatial dimensions, and the λ axis represents the spectral dimension [249], presented in Figure 56.

The (x, y, λ) spectral cube represents the different layered and graphical thicknesses that could be useful for the overall image analysis. The magnitude of the spectral signature is computed by mapping a color to the intensity of the spectral response at various wavelengths over a specified spatial area. Because these 3D cubes are formed over a wider area than the focal plane array can capture in a single frame, the second dimension of the spatial image develops over time [249, 250]. So, spatial resolution is a critical element recommended for discriminating attributes. However, this attitude of visualizing allows you to identify specific spectral properties in a scene [251].

The hyperspectral cube, often known as the hypercube, is a potent and vigorous element for visualizing data in terms of spatial and spectral properties that would otherwise be impossible to display in a single format[249, 251]. This hypercube is frequently used as an analytical tool at the initial data analysis and exploitation step. As the spectral and spatial dimensions decrease, the amount of data required to generate the hyperspectral data cube increases. This will lead to a massive volume of computational data [251]. Lossless compression ensures that no data is when restored. Thus, the need for lossless image compression is required; yet, this type of compression may be ineffective in some applications because it does not provide a significant data reduction. The criticality of the data defines whether image compression can be applied.

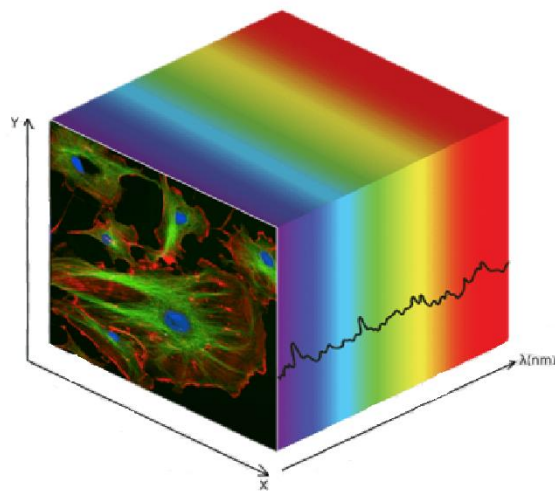


Figure 56. Hyperspectral data cube

3.3 THE NEED FOR DIMENSIONALITY REDUCTION

Hyperspectral images include far more information than conventional RGB imagery, which has both benefits and drawbacks. In fact, hyperspectral imaging of a scene can generate a hypercube of order gigabytes in size. This huge amount of data is one of the key drawbacks of this spectroscopy technic [249]. However, more than 90% of the information

may usually be explained by a small amount of the data due to considerable redundancy. This promotes the reduction of the size of hyperspectral images [248].

In practice, hyperspectral imagery leads to images of enormous size. Presently, the volume of data delivered is constrained by existing bandwidth and onboard storage space. As a result, the compression step becomes an essential aspect of the acquisition system to improve the ability to store, access, and transfer information [252]. Time continuous acquisitions can be made possible via onboard compression in space probes or satellites. The compression should ideally be lossless to ensure the highest possible information quality. On the other hand, lossless compression algorithms do not provide compression ratios greater than two or three [253, 254].

Because compression algorithms must be executed onboard prior to space-to-ground transfer, information losses due to compression will be irreversible [252]. Although the loss of information may be tough to believe, it will allow sensors to gather and send more images at a faster rate. Additionally, suppressing less significant information allows for the acquisition of more beneficial information. Together with the previously mentioned high redundancy in hyperspectral acquisitions, these considerations make users more prepared to accept lossy compression, also known as “data reduction.” This is mainly accomplished by dimensionality reduction methods applied to the hyperspectral image [255, 256]. Hence, by applying these methods, the spectral dimension λ of the 3-D data cubes (x, y, λ) is reduced by their index number.

3.4 HYPERSPECTRAL IMAGE WORKING THEORY

After describing the hyperspectral image, it is time to present the fundamental principle of operation of the hyperspectral sensor. Imaging spectrometers are used to generate hyperspectral images [251]. These advanced sensors are made by integrating remote sensing and spectroscopic technology [250]. Spectroscopy is the analysis of light beams that are

emitted or reflected by materials, as well as its energy variation with wavelength. By means, spectroscopy represents the amount of electromagnetic radiation in a wavelength. As applied to the field, the hyperspectral sensor receives the reflected light from an inspected target and converts this radiation into an electrical signal. Four basic components are required to accomplish this process. A focusing lens and a slit, as its name implies, focus the incoming light onto the sensor in an incredibly thin but wide light beam. An optical dispersing element such as a diffraction grating or prism in the sensor splits this inbound light into a spectrum of many narrow, adjacent wavelength bands. And the energy in each band is measured by a photoreceptor [249].

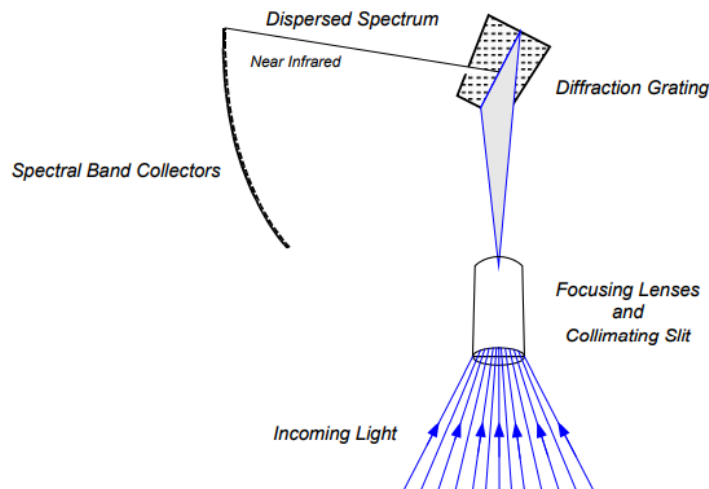


Figure 57. Elements of a hyperspectral imaging sensor

Figure 57 presents a graphical illustration of the elements of a hyperspectral imaging sensor. The lens of the hyperspectral imager acquires reflected light as the airborne, or spaceborne sensor hovers over a target zone. The gathered beam goes through a series of lenses. The light is focused by the lenses to generate an image of the ground. Once the incoming light is focused by the lenses, the beam enters a slit through which only a very thin, flat beam can pass. The permitted beam is projected onto a diffraction grating. A diffraction grating is a finely etched reflective surface that scatters light extremely accurately in its spectrum. A charge-coupled device (CCD) receives the scattered beam. These photoreceptors

measure the spectral intensities of the scattered beam. They then transform the measured intensities into electrical signals [249, 251]. As shown in Figure 58, the output from the photoreceptors includes electrical signals for each of the spectral bands for each of the pixels in the image.

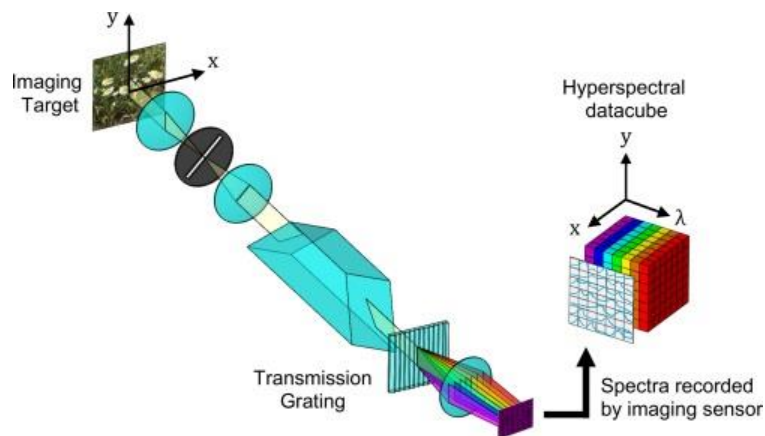


Figure 58. Hyperspectral operating theory

As the fundamental theory of the hyperspectral operating principle is developed in the preceding paragraphs, the hyperspectral data cube, shown in Figure 58 above, can be produced by using three main scanning modes. These modes are known as whiskbroom (or point scanning), pushbroom (or line scanning), and staredown (or area scanning) [246], and are seen in Figure 59.

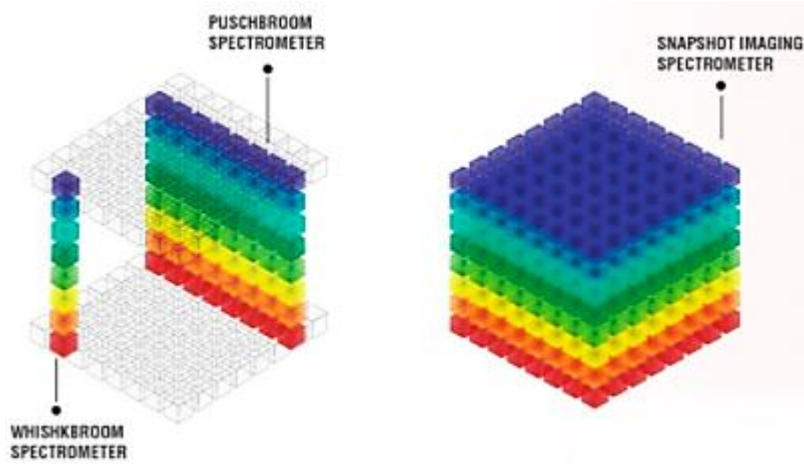


Figure 59. Whiskbroom, pushbroom, and staredown spectrometers outputs [257]

The table below summarizes the three scanning modes listed above.

Table 3 : Scanning modes

Scanning Mode	Whiskbroom / Point Scanning	Pushbroom / Line Scanning	Staredown / Area Scanning
<p>The whole spectrum is obtained at a single point of the scene. Light from this location passes through the objective lens, where it is divided into wavelengths by a spectrometer and detected by a linear array detector. After accomplishing spectral acquisition, another point's spectrum can be captured.</p> <p>To complete the hypercube, scanning must be done in both spatial dimensions [249, 251].</p>	<p>The spectra of all pixels in a single image line are recorded at the same time. This method yields a two-dimensional data matrix with one spatial and spectral dimension. While scanning across the target area in a direction perpendicular to the imaging line creates the datacube's second spatial dimension. This necessitates relative movement between the scanned sample and the hyperspectral sensor, by moving one of the two elements (sample or sensor) while maintaining the other in a fixed location [249, 251].</p>	<p>A two-dimensional data matrix is acquired by using this mode, but the collected data represents a more traditional image with two spatial dimensions. Thus, collecting a sequence of these photos for one wavelength band at a time yields a complete three-dimensional data cube. In this mode, a tunable filter is used to adjust the wavelength of the incoming light [249, 251].</p>	

3.5 APPLICATIONS OF HYPERSPECTRAL IMAGING

Although hyperspectral technology has been in the area for a few years, it has been integrated into various fields, but it has largely been dominated by government and military institutions. Particularly, the American Army deployed a program specified to the detection of landmines spectral characteristics entitled “Hyperspectral Mine Detection Phenomenology (HMDP)” [258]. However, agriculture and mining have traditionally dominated non-military applications. The use of commercial off-the-shelf computing equipment to perform real-time analysis of hyperspectral imaging data is a relatively new discovery [249]. For instance, airborne crop measurement is a popular hyperspectral imaging use. A hyperspectral sensor is used to fly over cropland in this manner. The results are evaluated to spectral characteristics of common crops. Rural economists can estimate crop yields for the coming harvest more promptly using this strategy [243, 256]. Aside from that, here is a list of some of the most common hyperspectral imaging applications. First, in the field of biotechnology, the use of hyperspectral technologies in biological and medical applications has grown in popularity.

Obtaining usable data in the laboratory is simple and rapid. They are mainly employed in cell biology research, fluorescence microscopy, and wound investigation. Second, this technology is booming in popularity for monitoring environmental changes. It is widely used to figure out how much CO₂ is released into the atmosphere, track pollution levels, map hydrological formations, and more [244].

Third, hyperspectral imaging is widely used in the food industry for a number of purposes, including apple bruise detection, seafood freshness inspection, citrus fruit inspection, sugar distribution in melons, and potato sorting [259]. Apple bruise, for example, is not evident at first and takes a few days to develop a dark color imprint. As a result, this technology can be used to trace the early stages of a bruise for quality control purposes. Moreover, as hyperspectral imaging is known in the quality control fields, it is commonly used to manage drug packaging and powder mixing, as well as to monitor illegal or counterfeit drugs. Similarly, in the realm of medical diagnostics, it is utilized for illness

diagnosis and prevention, including the early identification of cancer and retinal disease. As hyperspectral imaging technology can distinguish precise spectral resolution, thus it is an ideal technique for forensic laboratories [251, 260]. It can make the difference between analyzing questioned documents, visualizing bloodstains, fiber composition, fingerprint enhancement, and many other forensic studies.

CHAPTER 4

PRELIMINARY STUDY

Before beginning our research, we explored the possibility of using hyperspectral imagery in WTB monitoring to detect surface defects and ice accretion. We have created a preliminary experiment for this purpose, in which we will focus on detecting cracks, erosion, and ice on composite plates imitating the WTB composite. However, this preliminary study is published in “*Remote Sensing Applications: Society and Environment*” with an article title “hyperspectral imaging applied for the detection of wind turbine blade damage and icing”[261].

4.1 MATERIAL PREPARATION

As samples, three fiberglass composite plates measuring 30 cm in length, 21 cm in width, and 0.5 cm in thickness were employed, see Figure 60. Each sample contains one of the three types of induced defects defined above. Each defect was tested in detail aside. These two induced defects are of the same length of 1.5 cm and the same depth of 0.05 cm, as shown in Figure 61, but the only difference is that the erosion appears on the edge of the corner of the sample, but the crack emerges in the middle of the fiberglass sample. Similarly, a portion of the third sample is covered with 0.5 mm thick ice. Spectral signatures are obtained using an ASD FieldSpec4 spectroradiometer, presented in Figure 62. The spectral range of this spectroradiometer is 350 to 2500 nm, with a spectral sampling of 1 nm.

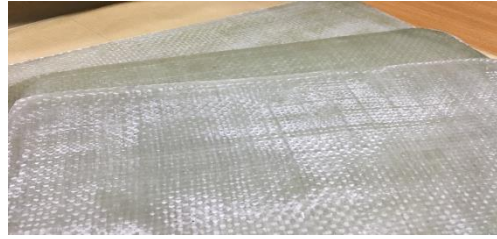


Figure 60. Specimen of composite plates



Figure 61. Faults on the tested specimen



Figure 62. ASD FieldSpec4

4.2 EXPERIMENTAL PROCEDURE

After preparing the fiberglass samples with the corresponding defect, the methodology that was used is as follow:

Each of the samples was induced with one type of surface defect. Also, to prepare the ice sample, cold water was sprayed on the sample and put in the freezer at a temperature of -27°C. Then, the signature of each defect was retrieved, and the signature of the fiberglass was used as a reference. The faults were dispersed on the fiberglass image at different locations. To clarify, the crack signatures can be found in different pixels in the normal fiberglass imaging data. Similarly, in the case of erosion, the image has the same number of defects. Ice signatures can be found in an area of the fiberglass image in the case of ice. The hyperACE algorithm is then employed in the detection procedure, which is based on the cosine/coherent adaptive estimator technique described in Appendix I.

To detect lighter defects using HSI (HyperSpectral Imaging), the spectral signature of each defect is combined with the spectral signature of the fiberglass sample as described in the following equation:

$$\textit{merged signature} = \alpha \cdot \textit{fault signature} + (1 - \alpha) \cdot \textit{normal signature} \quad (1)$$

Where α denotes the fault signature percentage. After that, the merged signature is introduced into the fiberglass sample image, which is then checked by the detection algorithm. By merging the signatures, we are experimenting with the effect of fault size.

The datacube is subjected to a band reduction algorithm to determine the optimum number of bands while retaining a high detection probability. Hyperspectral images usually present a high degree of end-to-end spectral band correlation. Consequently, reducing redundant data would reduce the volume of data that needed to be evaluated. So, to eliminate redundancy, Mutual Information (MI) and Net Analyte Signal (NAS) are used (see Appendix I). The MI is a tool that compares two images and determines how similar they are. Thus, images with low similarity are taken for further study in order to reduce duplicate information. Photos

with minimal similarity are taken for further study to remove redundant information. The low similarity image is next subjected to NAS, where NAS is a component of the analyte gamut that is unique to that analyte (Lorber, 1986). Furthermore, NAS is a useful method for determining a signal's figures of merit. Later, these figures of merit are utilized to compare different models in an optimum number of bands.



Figure 63. Acquisition of ice signature



Figure 64. Acquisition of erosion signature

4.3 PRELIMINARY RESULTS

After the acquisition, the data processing in the hypercube is a crucial step before the detection procedure. First, the spectral analysis is accomplished to differentiate the elements

that make up the hypercube. It is based on a comparison of spectra in the data cube with a target's reference signature. This analysis will enable the detection of a target's concentration and distribution in a scanned image.

4.3.1 Crack

The spectral signature of the crack surface versus the normalized reflectance is presented in the figure below.

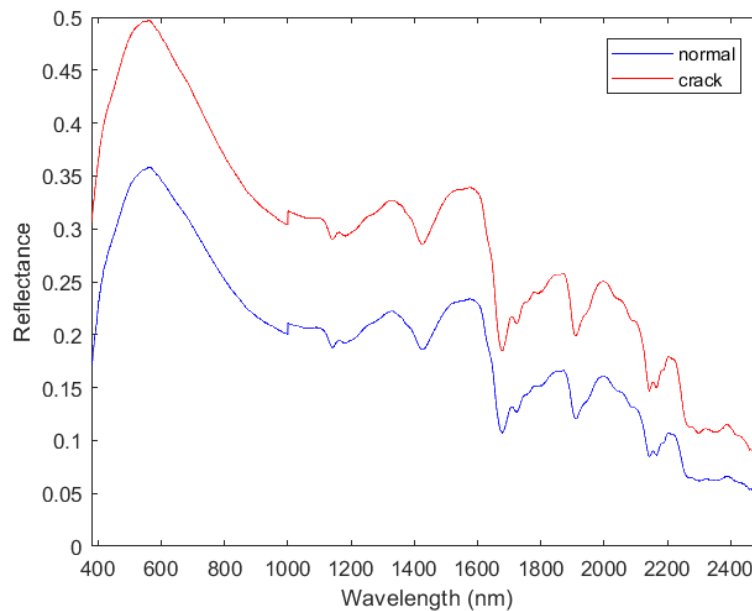


Figure 65. Spectral signature of cracked versus normal fiberglass composite

As shown in Figure 65, the spectral signature of the crack has a higher mean than that of the fiberglass sample. We can deduce that the crack has the same signature shape but a higher reflectance than the surface material. As stated in the previous section, several surface cracks are present in the composite fiberglass, and a detection algorithm was tested on it. The reflectance of the fiberglass sample is shown in Figure 66a. At the crack's position, the reflectance reaches its maximum levels. The spikes in this figure can then be used to identify

the location of these imperfections. Figure 66b depicts the detection probability of the cracks provided. The detection probability changes based on the crack reflectance abundance factor and its size. For example, the detection probability for an abundance factor of 80% of crack was shown to be about 85% in this figure, while the detection probability for a full-crack abundance factor was shown to be 100%, and the detection probability for an abundance factor of 20% of crack was nearly 25%.

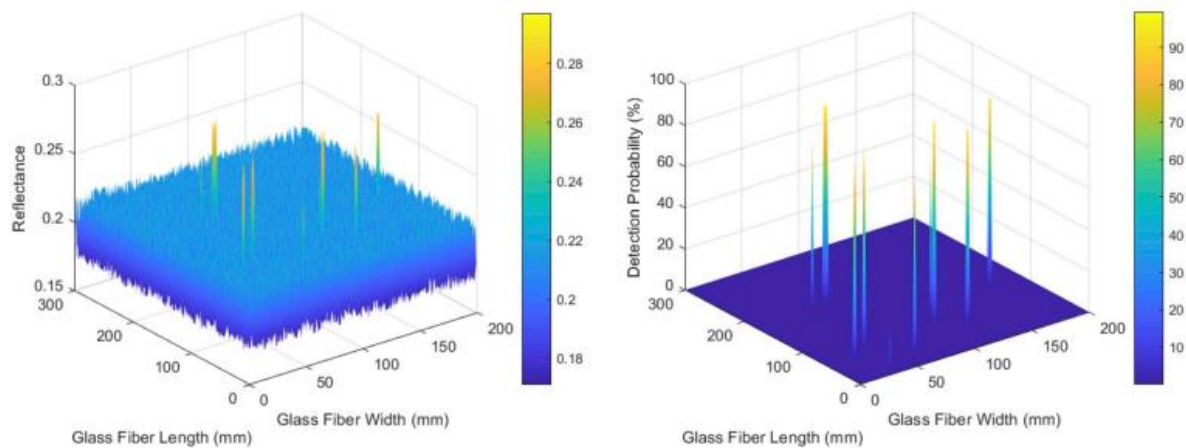


Figure 66. Detection process of crack a) reflectance distribution b) defect probability

The detection probability of non-crack signature is less than 0.1, as indicated by the blue plane. As mentioned in equation (1), the signature of the crack defect is combined with the signature of the composite material. The merged signature will support our research on the impact of surface defect size on HSI detection. The optimum number of bands is obtained by reducing the image with the merged signature while preserving a high detection probability. Mutual information (MI) reduces the 1827-band image to 193 bands, which is then fed to the NAS algorithm for further reduction. Table 4 summarizes the results of band reduction with different percentages of fault signature using NAS. The effect of size reduction and different percentages of fault insertion on the detection probability is presented

in Table 4. A good detection probability of 92.31% is maintained in the case of 10% of the crack signature, a 1.5 mm long crack, and after applying a 40% reduction to the image to achieve 116 bands. With only 20 bands, the chance of detection increases to 100% if the crack size is extended to 10.5 mm (90% reduction). This table demonstrates that as the fault size grows more prominent, the number of bands required decreases.

Table 4 : Crack sample results

Crack		
<i>Fault Insertion</i>	<i>Band Reduction</i>	<i>Detection Probability</i>
0.1 crack + 0.9 sample	90%	7.69 %
	80%	7.69 %
	70%	23.08 %
	60%	61.54 %
	50%	84.62 %
	40%	92.31 %
	30%	92.31 %
	20%	100.00 %
0.2 crack + 0.8 sample	90%	38.46 %
	80%	92.31 %
	70%	92.31 %
	60%	92.31 %
	50%	92.31 %
	40%	100.00 %
0.3 crack + 0.7 sample	90%	92.31 %
	80%	92.31 %
	70%	92.31 %
	60%	100.00 %
0.4 crack + 0.6 sample	90%	92.31 %
	80%	92.31 %
	70%	100.00 %
0.5 crack + 0.5 sample	90%	92.31 %
	80%	100.00 %
0.6 crack + 0.4 sample	90%	92.31 %
	80%	100.00 %
0.7 crack + 0.3 sample	90%	100.00 %
0.8 crack + 0.2 sample	90%	100.00 %
0.9 crack + 0.1 sample	90%	100.00 %

4.3.2 Erosion

Figure 67 below presents the spectral signature of the eroded sample versus the normal fiberglass reflectance.

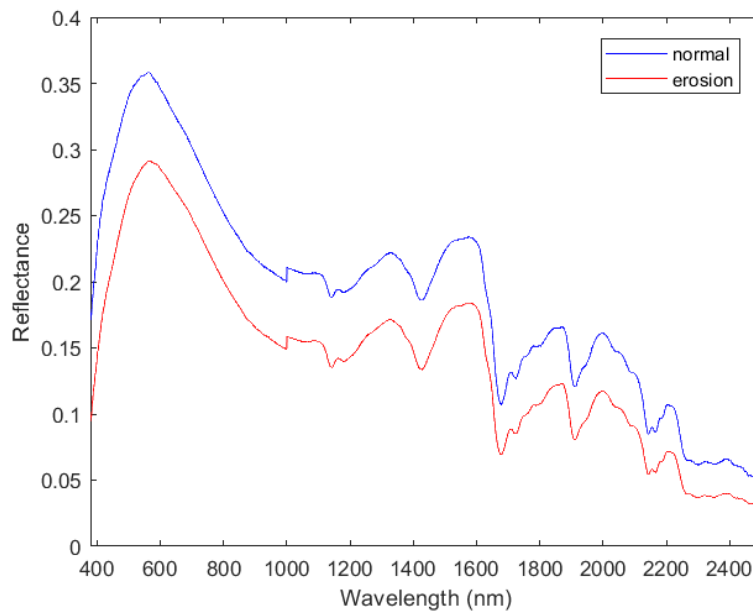


Figure 67. Spectral signature of eroded versus normal fiberglass composite

The spectral signature of the surface crack has a lower mean than that of the fiberglass composite, as illustrated in Figure 67. The erosion has the same signature form as the surface material with a lower reflectance. The composite fiberglass image had a corner erosion signatures, as described in the material preparation section, and a detection algorithm was evaluated on this image. The reflectance of the fiberglass specimen is shown in Figure 68a. At erosion's position, the reflectance reaches its lowest value. The position of these defects can be determined using the vertical nearly blue planes illustrated in Figure 68a.

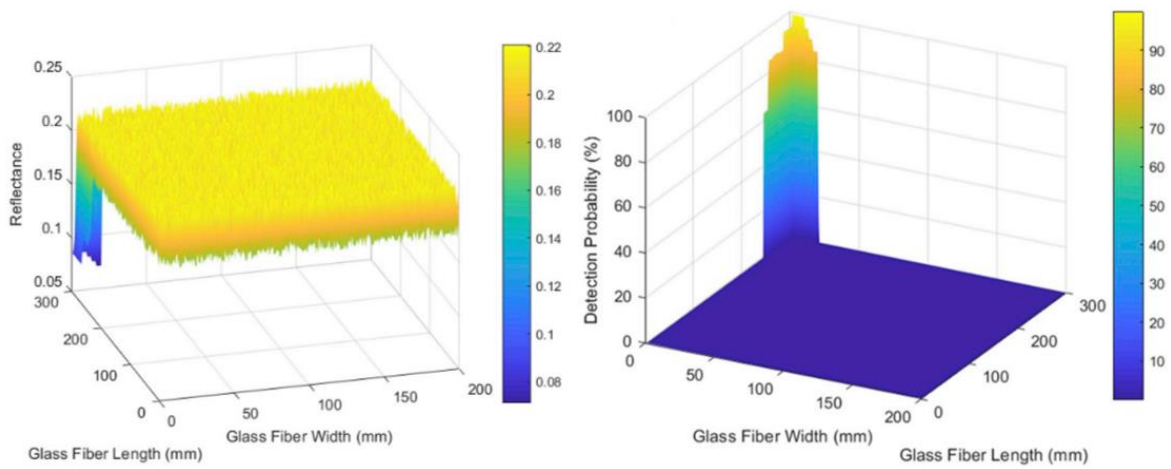


Figure 68. Detection process of erosion a) reflectance distribution b) defect probability

Figure 68b depicts the detection probability of the presented erosion. The probability of detection varies according to the severity of the erosion. For example, we can see that this figure presents high probability detection values on severe erosion locations. On the other hand, these values are at their lowest values in areas with light erosion. As stated in equation (1), the signature of erosion is combined with the signature of the composite sample. After that, the image with the merged signature is reduced to acquire the optimal number of bands while keeping a high detection probability. The MI on the damaged specimen results in a drop in the number of bands from 1827 to 157. At that moment, NAS reduces the resultant image, and these reduction results are summarized in Table 5: Erosion sample results.

Table 5: Erosion sample results

Erosion		
<i>Fault Insertion</i>	<i>Band Reduction</i>	<i>Detection Probability</i>
0.1 erosion + 0.9 sample	90%	0.00 %
	80%	15.39 %
	70%	46.15 %
	60%	53.85 %
	50%	69.23 %
	40%	84.62 %

	30%	92.31 %
	20%	92.31 %
	10%	92.31 %
0.2 erosion + 0.8 sample	90%	38.46 %
	80%	84.62 %
	70%	92.31 %
	60%	92.31 %
	50%	92.31 %
	40%	100.00 %
0.3 erosion + 0.7 sample	90%	76.92 %
	80%	92.31 %
	70%	92.31 %
	60%	100.00 %
0.4 erosion + 0.6 sample	90%	92.31 %
	80%	100.00 %
0.5 erosion + 0.5 sample	90%	100.00 %
0.6 erosion + 0.4 sample	90%	100.00 %
0.7 erosion + 0.3 sample	90%	100.00 %
0.8 erosion + 0.2 sample	90%	100.00 %
0.9 erosion + 0.1 sample	90%	100.00 %

4.3.3 Icing event

The icing event differs from the other two cases represented above. The spectral reflectance of ice presents a total absorption at 1400 nm, see Figure 69.

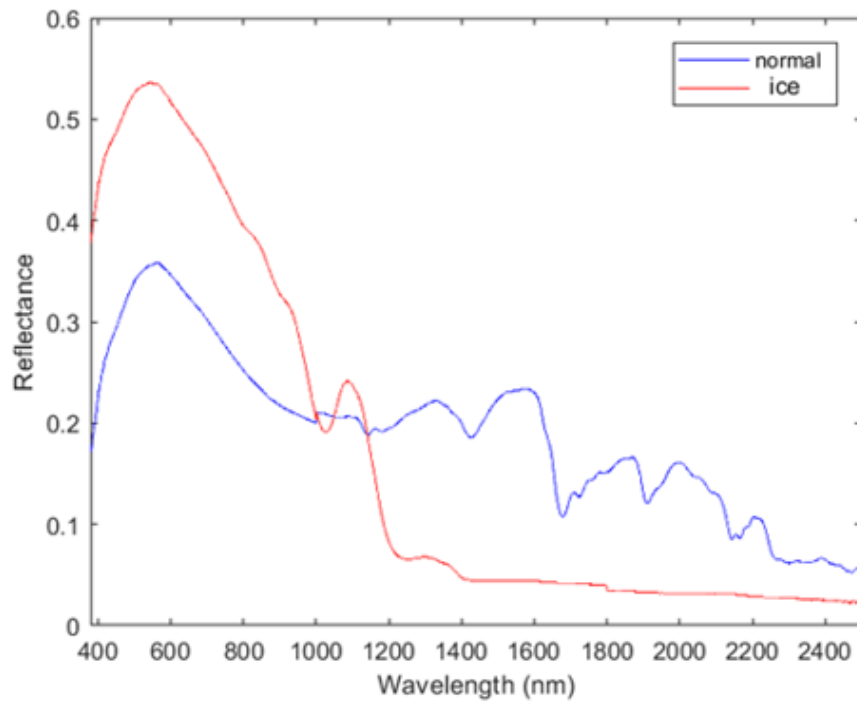


Figure 69. Spectral signature of ice versus normal fiberglass composite

Figure 70 illustrates the results of the hyperACE algorithm in the ice detection procedure.

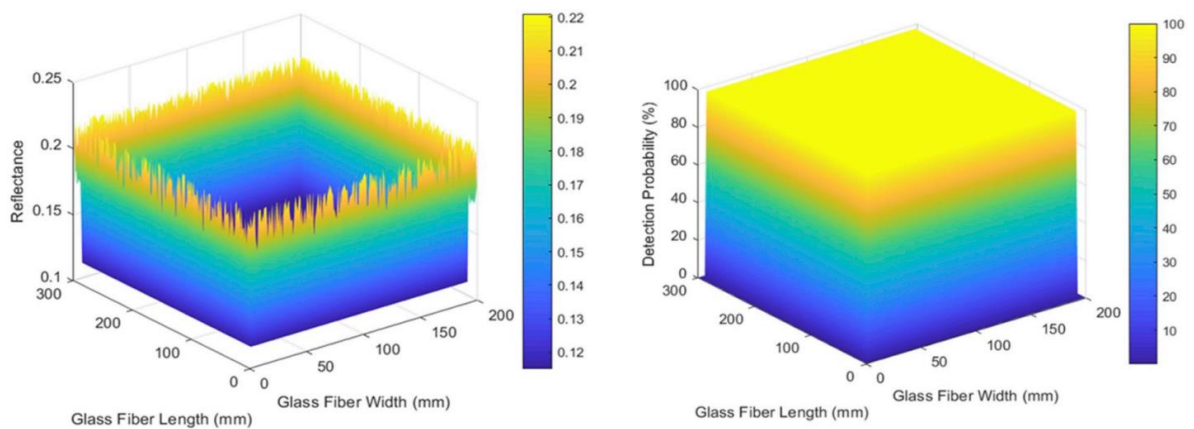


Figure 70. Detection of icing event a) reflectance distribution b) defect probability

In Figure 70a, we can see that the reflectance is at its lowest values where ice is present, about 0.12, and highest at no-ice regions, with a value of 0.21. The hyperspectral imaging technology (HSI) has a lot of potential in detecting icing problems, as shown in Figure 70. The ability of HSI to identify ice with a thickness of 0.5 mm was demonstrated in Figure 70b. A 100% detection probability is reached at ice accumulation spots, while no-ice areas have a 10% detection probability. As mentioned in equation (1), the ice signature is combined with the signature of the fiberglass composite sample. The image is reduced by MI from 1827 to 874 bands only, following the same approach as for the crack fault. Table 6 summarizes the results after applying NAS on the reduced image.

Table 6 : Ice sample results

Icing		
<i>Fault Insertion</i>	<i>Band Reduction</i>	<i>Detection Probability</i>
	90%	86.36 %
0.1 ice + 0.9 sample	80%	97.73 %
	70%	100.00 %
0.2 ice + 0.8 sample	90%	100.00 %
0.3 ice + 0.7 sample	90%	100.00 %
0.4 ice + 0.6 sample	90%	100.00 %
0.5 ice + 0.5 sample	90%	100.00 %
0.6 ice + 0.4 sample	90%	100.00 %
0.7 ice + 0.3 sample	90%	100.00 %
0.8 ice + 0.2 sample	90%	100.00 %
0.9 ice + 0.1 sample	90%	100.00 %

The effect of ice thickness and data-cube reduction is considered in Table 6. With only 88 bands, the HSI can detect ice development at a thickness of 0.1 mm in a strong and dependable manner.

According to the findings, HSI has a high potential for detecting all forms of crack, erosion, and ice accretion at an early stage of production robustly and dependably. HSI detected ice with a thickness of 0.5 mm in this simulation and demonstrated the ability to

detect ice with a thickness of 0.1 mm. There was also a demonstration of the detection of light surface faults.

After presenting these preliminary results of the potential of hyperspectral imaging in the diagnosis of wind turbine blades, this technology was applied on a real wind turbine blade, as detailed in the next chapters.

CHAPTER 5

EXPERIMENTAL SETUP

The methodology followed to achieve the main objective depends on the selection of the sensors, the experimental setup, and the performance of some other activities. After the preliminary experiment presented in Chapter 4, an experiment was done on a real WTB sample, with some predefined surface defects and icing. In this chapter, a detailed explanation of that experiment is presented.

5.1 SENSOR SELECTION

After a preliminary review of available sensors, it was determined that hyperspectral imaging technology (HSI) offers some advantages for detecting cracks, erosion, and ice that may reduce some of the limitations associated with the other monitoring systems summarized above. This work aims to introduce the hyperspectral imaging technique into the world of blade inspection methods. The fundamental concept of HSI is that radiance reaching every pixel is fractured into very many narrow adjacent wavelengths [181, 262]. These spectral bands constitute the spectral signature of the object being scanned. HSI provides both spatial and spectral information, which creates a three-dimensional data cube, identified as “hypercube data” or as an “image cube” [263]. As stated, each material or object has its signature which is used in detection and classification processes. For instance, ice detection using HSI depends on the difference in spectral signatures between the accreted ice and the blade surface. For this application, the ice and the blade shell will mutually reflect energy at distinct ratios giving a difference in the reflectance of each type of material.

We apply hyperspectral imaging of a wind turbine blade section for fault detection, like crack, erosion, and ice accretion. For this purpose, we use three hyperspectral sensors. These sensors cover a bandwidth from 300 to 1700 nm with a spectral resolution of 3 nm. These three sensors, shown in Figure 71, cover the range from 340 to 840 nm, 640 to 1050 nm, and 950 to 1700 nm, respectively.

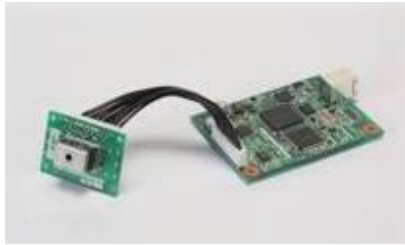


Figure 71. 340-840 nm Sensor



Figure 72. 640-1050 nm
Sensor



Figure 73. 950-1700 nm
Sensor

5.2 EXPERIMENTAL SETUP

The GFRP blade sample illustrated in Figure 74 has 53.0 cm in length, 34.5 cm in width, and a thickness of 4.0 cm. Also, we induced some predefined cracks and erosion on the blade. These faults were of different sizes ranging from unseen defects to severe ones dispersed between 13 cracks and 22 erosions. Furthermore, to accrete ice on this sample, as shown in Figure 75, cold water was sprayed on it, then placed in the freezer at a temperature of -25°C to be frozen. This work is done at different stages to achieve the required thickness (0.5 mm, 0.7 mm, 4 mm, and 7 mm). Finally, with the required conditions being available, the GFRP sample is scanned pixel per pixel using the hyperspectral sensors in turn, as illustrated in Figure 76. After this procedure, a data cube of information will be gathered.



Figure 74. Blade section

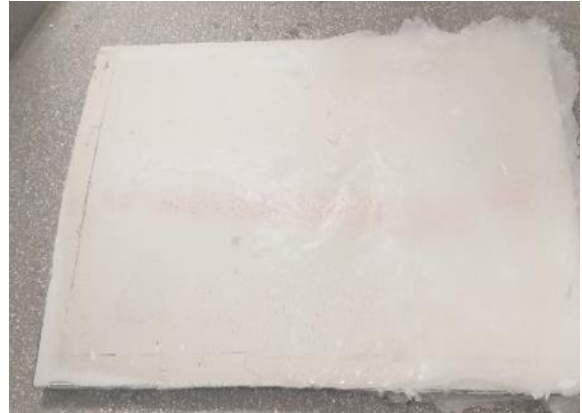


Figure 75. Ice accretion on blade sample



Figure 76. GRFP Setup for scanning

5.3 ACTIVITIES

Before starting the experiment, two reference signals must be retrieved: the white reference and the dark reference signal. These two signals will be used in the image calibration phase using the equation:

$$HI_n = \frac{HI-D}{W-D} \quad (2)$$

In equation (2), HI_n is the calibrated/normalized image, HI is the retrieved/scanned image, D is the dark reference signal, and W is the white reference signal.

The original hyperspectral image, built on black and white reference images, can be arranged into reflectance mode. While the dark reference picture suppresses the area detectors' obscure current effect, the white reference picture stands for the uppermost intensity values. Then, the sample blade is scanned with the sensors for the acquisition of the hyperspectral image. However, this image should be normalized to detect crack, erosion, and icing.

After the calibration phase, a normalized data cube is built. 542 bands compose this hyperspectral image.

Also, a preprocessing step removes the effect of dust and moisture on the blade. The spectra of the physical effects are removed to boost the resulting diversified regression, classification model, or exploratory research. This hypercube is fed into the detection algorithm "hyperACE" to check the detection capacity and ensure a 100% detection for crack, erosion, and icing signals [264, 265]. For each vector of this hypercube, we compute a metric that describes the degree of similarity between the pixel and the fault we are looking for. After that, we select a threshold to distinguish suspicious spots from normal ones. Changing this threshold affects the probability of detection as well as the FAR. In this thesis, we set the threshold for all targets to be detected, and then we registered the obtained FAR. By the way, the performance metrics Pd and FAR are defined as follow; Pd represents the probability of correctly detecting a fault, while the FAR states the percentage of false

positives samples from the total negatives samples. Spectral data of modern spectroscopy technologies have many wavelengths that make the computation complex, the detection ineffective, and the inspection slow. A band reduction reduces the computational time needed and the amount of data computed during the detection process [252, 266]. We select the optimal variables and the calibrated wavelengths using Multicriteria Classification and Net Analyte Signal algorithm. The Multicriteria Classification focuses on preserving the rare event inside the scene scanned while maintaining an optimum band reduction [252]. Also, the Net Analyte Signal algorithm has a vital role in computing the figures of interest in a calibrated model's characterization [267]. Hence, optimum bandwidth can be obtained [268]. Figure 77 illustrates the flowchart for the hyperspectral imaging experiment.

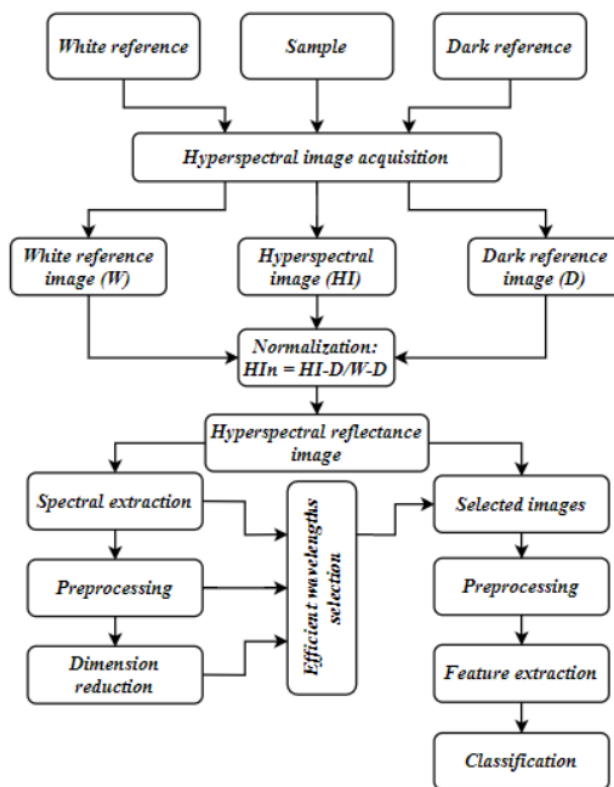


Figure 77. The flowchart of the methodology of the hyperspectral imaging experiment

After presenting in Chapter 5 the followed methodology during this study, the result of the crack and erosion faults are detailed in Chapter 6 while the results of the icing events are presented in Chapter 7.

CHAPTER 6

WIND TURBINE BLADE FLAWS DETECTION USING HYPERSPECTRAL IMAGING

To enlighten the enhancements of the results obtained using hyperspectral imaging, RGB image results are cited and compared. However, all the results discussed in this chapter are published in the journal “*Remote Sensing Applications: Society and Environment – ELSEVIER*” under the title of “wind turbine blade defect detection using hyperspectral imaging”[269].

Before exploring the following chapters, it is a necessary to specify how the RGB image is constructed. After scanning the blade sample with the hyperspectral sensors and building the 3D datacube, the RGB image is extracted from this 3D cube by choosing only the wavelengths corresponding of the red, green, and blue colors (625-740 nm, 520-565 nm, 430-500 nm respectively)[270]. Then, this figure is fed into a detection algorithm resulting the outcomes presented in section 6.1 and 7.1.

6.1 RGB 3-BAND BLADE IMAGE RESULTS

RGB imaging mimics human eye vision by scanning images through three filters (red, green, and blue) wavelengths.

Table 7 shows the detection probability (Pd) and false alarm rates (FAR) of crack, and erosion using the RGB image. The probability of crack detection using RGB is a full detection. Furthermore, the false alarm rate using RGB images for crack detection is 0%. In other words, RGB can detect crack faults without any false errors. In comparison, the probability of detecting erosion using RGB is 100.00%. The false alarm rate using RGB

images for erosion detection is 77.55%. In other words, RGB shows unsatisfactory results in erosion detection on the surface of the wind turbine blade specimen.

Table 7 : The detection probability (Pd) and false alarm rates (FAR) of fault types using an RGB image

	<i>Pd (%)</i>	<i>FAR (%)</i>
<i>Crack</i>	100.00	0.00
<i>Erosion</i>	100.00	77.55

6.2 FAULT SIGNATURE RETRIEVAL

The explored faults of the wind turbine blade specimen are of three types: crack, erosion, and icing, as shown in Figure 82. Crack and erosion real images were shown respectively in Figure 78 and 79.

Figure 78 illustrates a hairline crack (scratch) on the wind turbine blade specimen's surface, one type of external flaw that splits the surface without crashing apart. Figure 79 presents a light erosion, a different shell fault that gradually destroys the surface and diminishes the structure. The severe ones, severe crack, and severe erosion are shown respectively in Figure 80 and 81.



Figure 78. Minor crack on the blade specimen

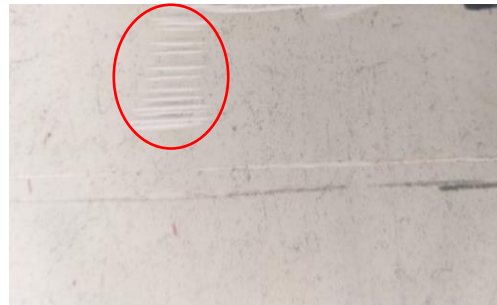


Figure 80. Severe crack on the blade specimen



Figure 79. Light erosion on the blade specimen



Figure 81. Severe crack on the blade specimen



Figure 82. Ice on the specimen

Reflectance mode allows us to inspect these surface flaws on the wind turbine blade and avoid specular reflection. The illuminated sample absorbs a small portion of the incident light, whereas the largest percentage of the reflected light conveys the more appreciated

information. The detector stands opposite to the light source to capture this data, the spectral signatures, as described in the following paragraphs.

The illustration of the crack surface signature with its different width value, in red, and that of the undefective blade signature, in blue, are shown in the following figures. The crack widths in Figure 86 are respectively 0.1, 0.3, 1.0, and 2.0 mm. These figures prove that the crack reflectance values for the different tested thicknesses are lower than those of the normal blade signature for the wavelengths ranging between 300 and 600 nm and between 1000 and 1700 nm. Whereas, between these two ranges, the normal blade signature achieves higher reflectance values than the crack signature. The obtained crack signature differs from that obtained in the preliminary study (Chapter 4) due to the use of different materials representing the WTB sample. Each material has its own reflectance properties. The difference in reflectance values for these two signatures is not very important in Figure 83, where the tested crack width is 0.1 mm. For instance, these two signatures overlap for wavelengths less than 1000 nm. This difference increases and is easily noticeable in Figure 84 with crack width growth. We note that the normal blade signature and the crack signature have the same shape and achieve their peaks at the same wavelengths, such as 600, 800, 1100, 1300, and 1500 nm.

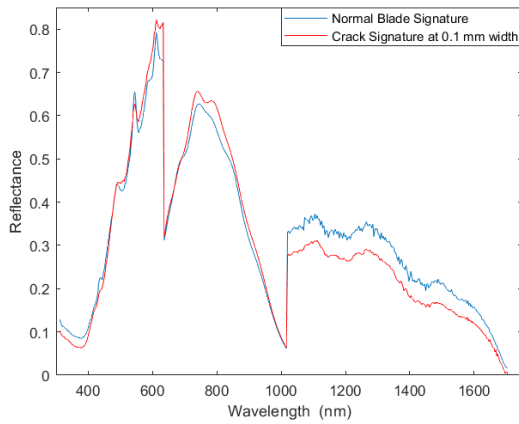


Figure 83. The spectrum of 0.1 mm width crack versus normal blade signature

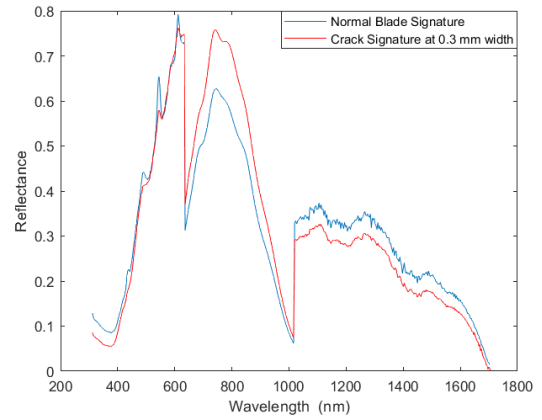


Figure 84. The spectrum of 0.3 mm width crack versus normal blade signature

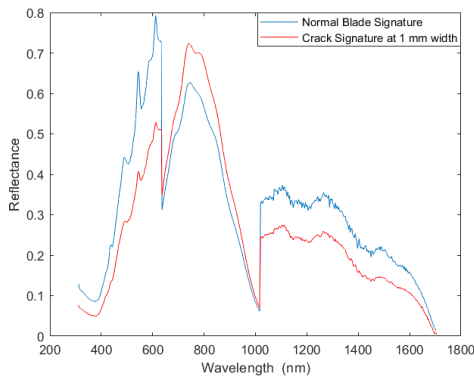


Figure 85. The spectrum of 1.0 mm width crack versus normal blade signature

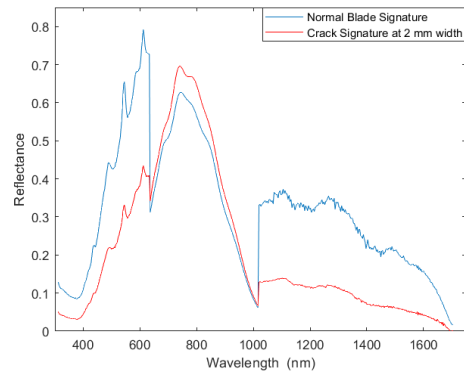


Figure 86. The spectrum of 2.0 mm width crack versus normal blade signature

Figure 87 and Figure 88 present the erosion flaw blade surface's spectral signature ranging from light to severe, in red, versus normal blade surface signature in blue. For the light erosion signature illustrated in Figure 87, its reflectance is lower than that of the normal blade for the wavelength range between 300 and 400 nm. Then, for wavelengths between 400 and 500 nm, these two signals overlap. After 500 nm, the spectral signature of light erosion is higher than the normal blade signature. This difference switches starting for wavelengths higher than 1000 nm. Slope variations are similar for both signatures, and peak

locations appear at the same wavelengths, 600, 800, 1100, 1300, and 1500 nm. Furthermore, a zero-reflectance value appears for a wavelength of 1700 nm. For the severe erosion illustrated in Figure 88, the reflectance signature is lower than the normal blade for the wavelengths ranging between 300 and 1700 nm. The difference is as large as 50%. Same signature shapes are noticeable for the normal and severe erosion signature with peaks at wavelengths equal to 600, 750, 1100, 1300, and 1500 nm.

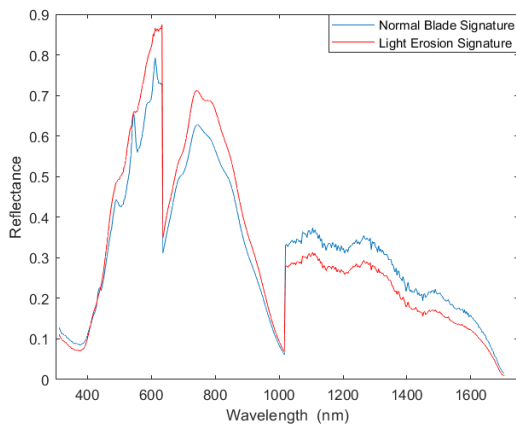


Figure 87. The spectrum of light erosion signature versus normal blade signature

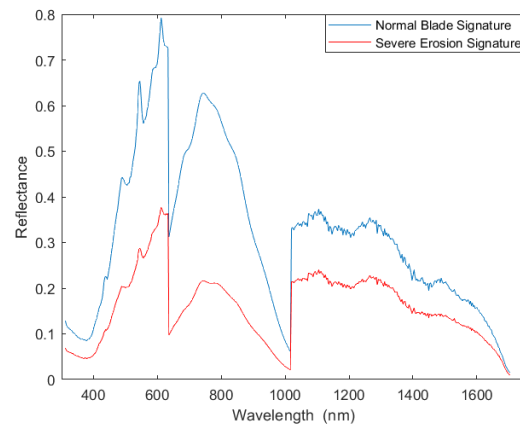


Figure 88. The spectrum of severe erosion signature versus normal blade signature

6.3 HYPERSPECTRAL IMAGE ACQUISITION

Figure 89 and Figure 90 illustrate a 3D hyperspectral cube image of the wind turbine blade specimen consisting of one wavelength and two spatial dimensions. It comprises 542 bands, 44 pixels in blade length and 29 pixels in blade width. It results from scanning the wind turbine blade specimen by moving the detector along two spatial dimensions. This data cube presents the blade specimen over 542 layers of different frequencies. The reflectance is increased from light red to dark red.

Figure 90 shows that the reflectance intensity varies differently in the region with accreted ice and in faulty regions. Furthermore, it varies with the wavelength in an

unarranged manner, slightly different along with the wind turbine blade specimen where ice accretion occurs. For instance, at the uppermost band index, the reflectance is around 0.8 at regions of faults and negligible elsewhere.

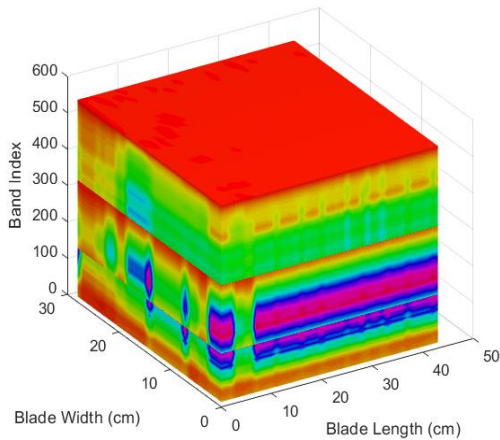


Figure 89. 3D hyperspectral cube of the wind turbine blade specimen

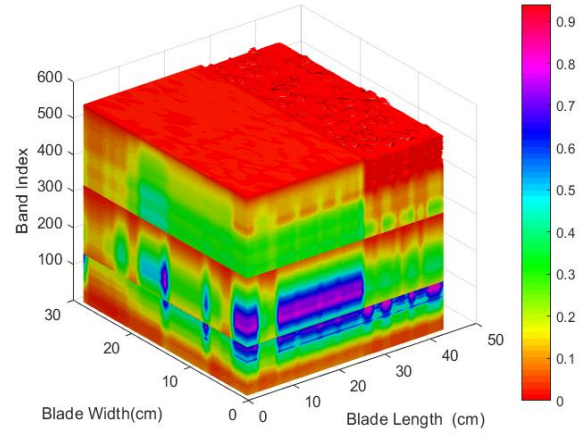


Figure 90. 3D Blade image with iced section

6.4 FULL-SPECTRUM FLAW DETECTION

At this step, the hyperACE algorithm is applied based on an adaptive cosine/coherent estimator algorithm to detect crack, erosion, and ice accretion regions. It sees the points of defects by scanning the sample and locating the faults on its signature. The detection probability of these types of flaws (crack and erosion) is 100%, and the likelihood of its false alarm rate is 0%, as shown in Table 8. We conclude that this detection algorithm using the hyperspectral imaging technique leads to a full and reliable detection of these flaws.

Table 8 : The detection probability (Pd) and false alarm rates (FAR) for defect types using a hyperspectral image

	<i>Pd (%)</i>	<i>FAR (%)</i>
<i>Crack</i>	100	0.00
<i>Erosion</i>	100	0.00

The crack abundance factor on a 2D illustration of the wind turbine blade surface appears in Figure 91. In this figure, the regions free of cracks are dark blue, light crack locations are light blue, and severe ones are yellow. Figure 92 presents a 3D illustration of the crack detection on the wind turbine blade sample's surface. In this figure, the cracks on the surface of the wind turbine blade specimen appear as spikes. Their severity is indicated by the scaled color, as for the 2D illustration, and the spike height. The cracks of width less than 1 mm appear as light cracks, and the others as severe ones.

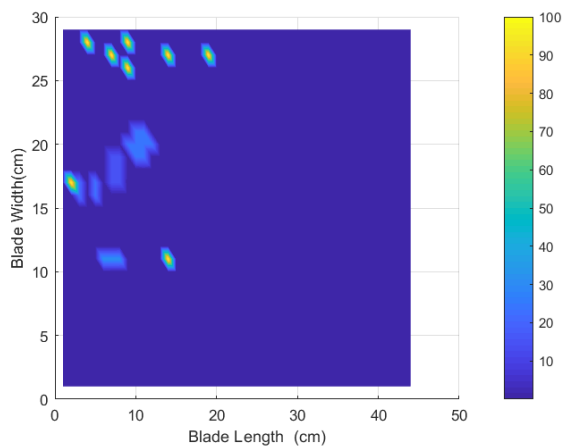


Figure 91. 2D illustration of the crack detection

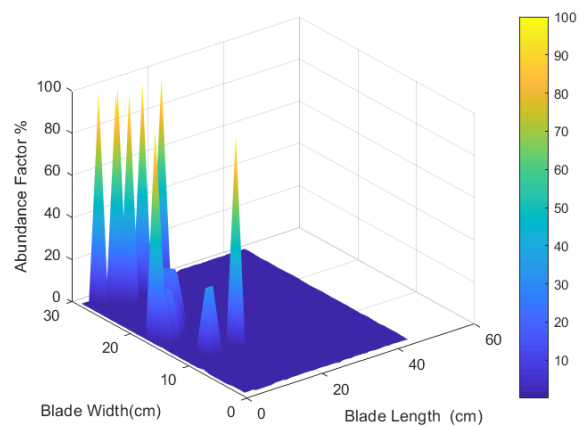


Figure 92. 3D illustration of the crack detection

Figure 93 displays the erosion abundance factor in a 2D illustration of the wind turbine blade sample. In this figure, dark blue indicates the areas uneroded, light blue designates the light erosion regions, and yellow, the severe ones. Also, a 3D representation of the erosion inspection of the blade sample appears in Figure 94. The spikes represent the eroded regions. The light erosion spikes have the top in light blue, the severe ones in yellow, and the uneroded areas appear dark blue. As shown in Figure 93 and Figure 94, light and severe erosion are at two corners of the wind turbine blade sample's surface.

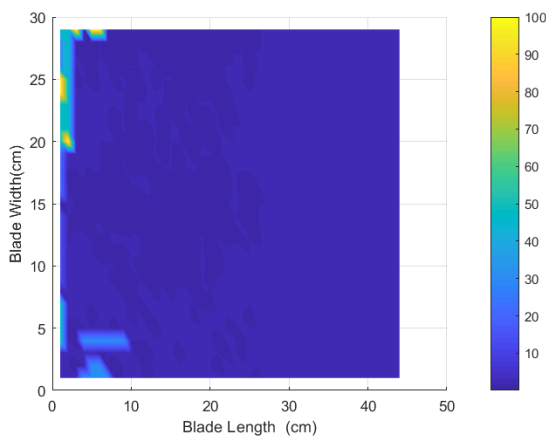


Figure 93. 2D illustration of the erosion detection

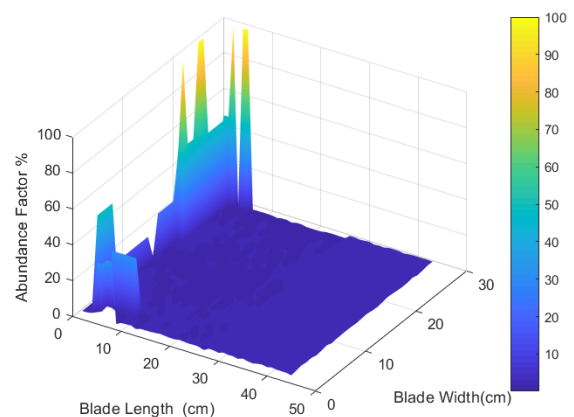


Figure 94. 3D illustration of the erosion detection

6.5 RGB VERSUS HYPERSPECTRAL IMAGING

The hyperspectral imaging technique shows a complete crack and erosion detection of 100% without any false alarm rate. Although a 100% detection probability using the RGB analysis for both faults (crack and erosion) was 100%, this technic presented a high false alarm rate in the erosion case; 0.00% and 77.55% is detected as false alarm rate respectively for crack and erosion detection using the RGB method.

In conclusion, hyperspectral imaging, consisting of multiple monochromatic images and a wide range of continuous wavebands, is superior to RGB images for blade flaw detection. These characteristics demonstrate hyperspectral imaging capacity to detect external surface defects (crack and erosion accretion at their early stages of formation) otherwise misleading results using the naked eye or conventional RGB image analysis.

After achieving the 100% detection probability and decreasing the computational time and the amount of data computed, a band reduction should be performed.

6.6 SPECTRUM REDUCTION

Finally, we explored the detection performance using a reduced spectrum to accelerate image processing. Table 9 presents the detection performance parameters (Pd and FAR) with a band reduction of the image's full spectrum. The original hyperspectral image consists of 542 bands. After performing a 90% reduction, only 55 bands are required to maintain a 100% detection of crack and erosion. The bandwidth ranges from 706 to 822 nm.

Table 9 : Summary of band reduction results

Percentage of Reduction	Number of Bands	Crack		Erosion	
		Pd	FAR	Pd	FAR
95%	28	62.07%	37.93%	79.59%	20.41%
90%	55	100.00%	0.00%	100.00%	0.00%
80%	109	100.00%	0.00%	100.00%	0.00%
70%	163	100.00%	0.00%	100.00%	0.00%
60%	217	100.00%	0.00%	100.00%	0.00%

50%	271	100.00%	0.00%	100.00%	0.00%
40%	326	100.00%	0.00%	100.00%	0.00%
30%	380	100.00%	0.00%	100.00%	0.00%
20%	434	100.00%	0.00%	100.00%	0.00%
10%	488	100.00%	0.00%	100.00%	0.00%

After all the results presented in this chapter, HSI presented an accurate and sensitive technology capable of quantifying, qualifying, and locating the surface defects studied from the crack or the erosion by offering the spectral signature of each defect. Also, these defects can be detected by using only 55 bands instead of 542 bands, mainly in the bandwidth ranging from 706 to 822 nm without any false alarm unlike the RGB image which presented an ability to detect these types of defects accompanied with a high false alarm rate. Thus, HSI is one step ahead of other monitoring conditions.

CHAPTER 7

WIND TURBINE BLADE ICING DETECTION USING HYPERSPECTRAL IMAGING

To enlighten hyperspectral imaging performance, we compare the results with RGB images. However, all the results discussed in this chapter are published in the journal “*Remote Sensing Applications: Society and Environment – ELSEVIER*” under the title of “wind turbine ice detection using hyperspectral imaging”[271].

7.1 RGB 3-BAND BLADE IMAGE RESULTS

RGB imaging mimics human eye vision by scanning images through three filters (red, green, and blue) wavelengths. The same procedure stated in Chapter 6 has been done. For instance, in our experiment, the probability of icing detection is 100.00%, and the false alarm rate of icing is 94.44%.

7.2 ICE FAULT SIGNATURE RETRIEVAL

Ice covers a large surface of the blade, as shown in Figure 95. The thickness of the ice, as cited before, is 0.5 mm, 0.7 mm, 4 mm, and 7 mm.



Figure 95. Ice on specimen

The following figures present the normal blade spectral signature in blue versus the ice spectrum in red color for different thicknesses. The ice thickness in Figure 96, Figure 97, Figure 98, and Figure 99 is 0.5 mm, 0.7 mm, 4.0 mm, and 7.0 mm. In Figure 96 and Figure 97, the two signals almost overlapped for the wavelengths ranging between 400 and 600 nm. Starting from around 600 nm, the ice reflectance is lower than the clean blade signature reflectance and becomes zero at approximately 1450 nm. At about 600 nm, the ice reflectance is 0.2, and the clean one is almost 0.3.

Furthermore, we can notice that the peaks in signatures have the same wavelength. In other words, the shape of the graphs is similar for the clean and the iced blade. We observe similar behavior for the results in Figure 98. Still, the ice reflectance becomes zero at approximately 1500 nm and then increases slightly to a reflectance of about 0.01 and decreases again to zero at 1700 nm. We should note that we have a total ice absorption of emitted light at zero reflectance.

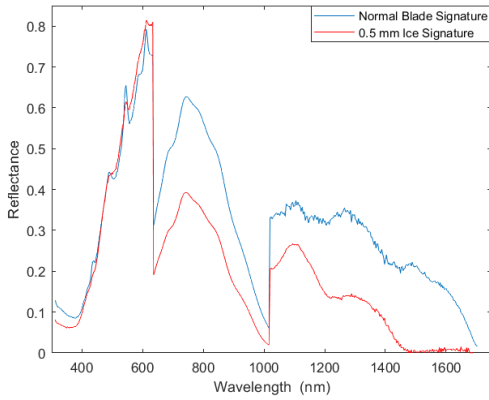


Figure 96. The spectrum of 0.5 mm ice thickness versus clean blade signature

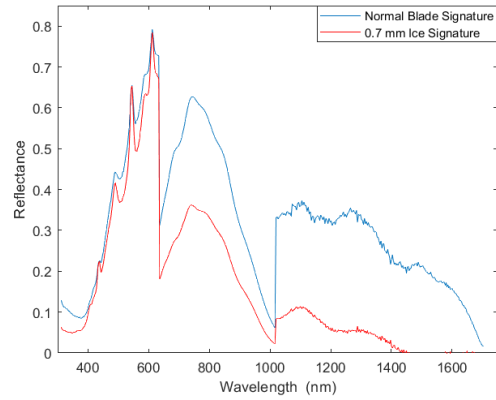


Figure 97. The spectrum of 0.7 mm ice thickness versus clean blade signature

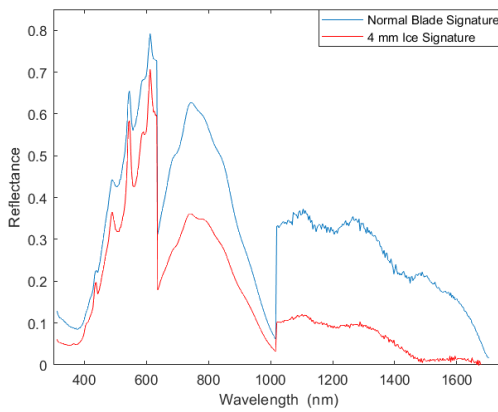


Figure 98. The spectrum of 4.0 mm ice thickness versus clean blade signature

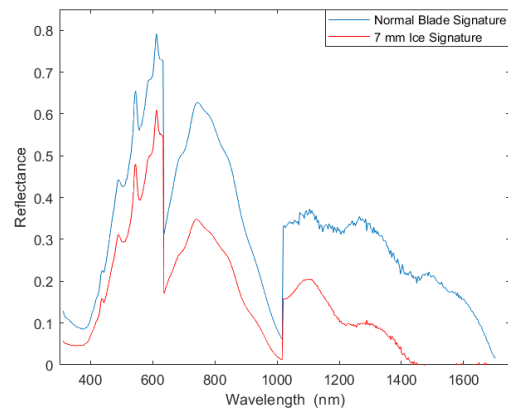


Figure 99. The spectrum of 7.0 mm ice thickness versus clean blade signature

7.3 HYPERSPECTRAL IMAGE ACQUISITION

After performing the scanning and calibration stages described before, the result shown in Figure 100 is a scanned blade image having 29 by 44 pixels over 542 bands. This data cube presents the blade specimen over 542 layers of different frequencies. The reflectance increases according to the color scale in the figure. We notice, confirming the previous section's conclusion, that ice reflectance at each band index is lower than the normal

reflectance of the clean blade, that icing is accreted over a length of 15 cm at one side of the blade along its width.

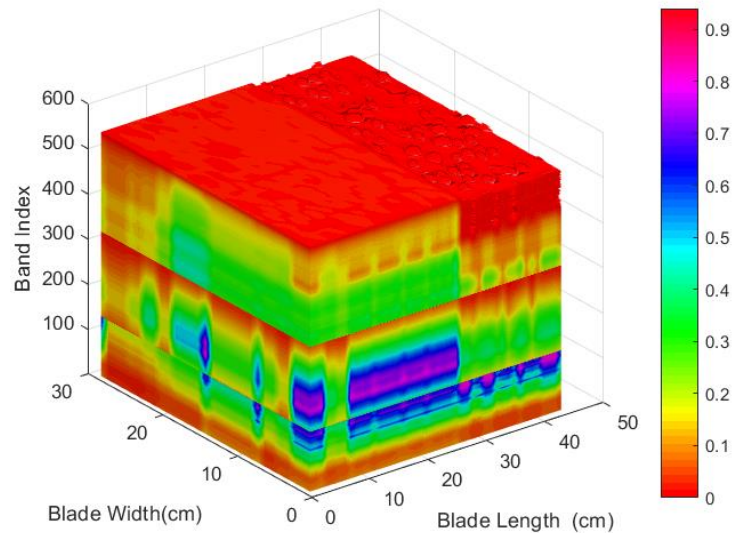


Figure 100. 3D Blade Image with partial icing

7.4 FULL-SPECTRUM ICE DETECTION

The hyperimage consisting of 542 bands, shown in Figure 100, is fed into the detection algorithm. The hyperACE algorithm shows an ice probability detection of 100% and a false alarm rate of 0%. These results are visualized in 2D in Figure 101 and 3D in Figure 102.

Figure 101 and Figure 102 show that the probability of detection for the region where ice is accreted, for the different mentioned thickness, is 100%, and this probability achieves 0% where no icing is present.

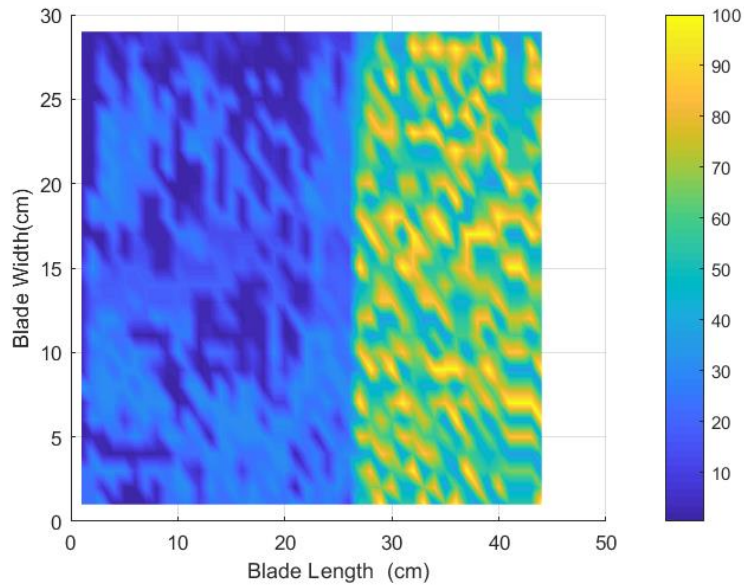


Figure 101. 2D Illustration of ice detection

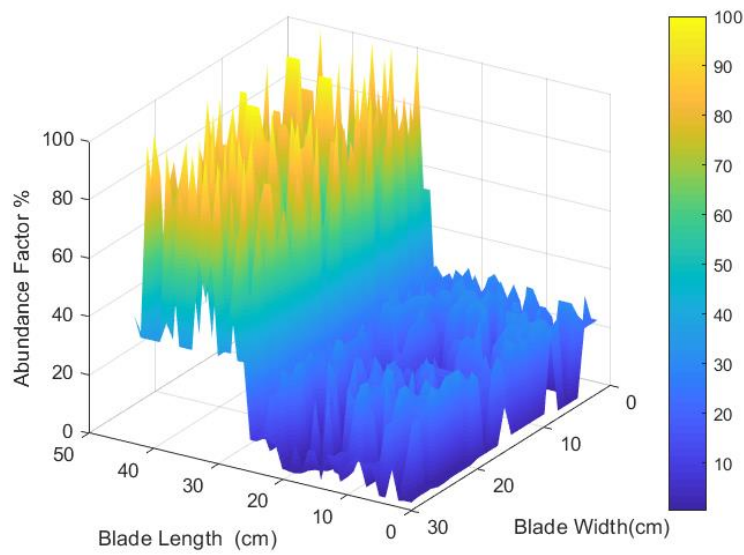


Figure 102. 3D Illustration of ice detection

7.5 RGB VERSUS HYPERSPECTRAL IMAGING

The hyperspectral imaging technique shows a complete ice detection of 100%, the same as in the case of an RGB image. However, no false alarm rate (FAR) is shown in hyperspectral imaging, whereas 94.44% false alarm rate occurs with the RGB case. Hence, hyperspectral imaging shows a robust ability to detect ice at its early stages of accretion. For instance, a human eye cannot notice a 0.1 mm ice thickness but can be detected using hyperspectral imaging. After achieving the 100% detection probability, we decrease the computational time and the amount of data by performing a band reduction.

7.6 SPECTRUM REDUCTION

Transforming the "hyper image" through multicriteria classification, we reduce the number of bands from 542 to 134. In other words, 134 bands are enough to detect the ice accumulation while maintaining the rare event in the resulted scene. These bands are from 354 to 636 nm, 740 nm, 776 nm, 824 nm, 992 nm, 1020 nm, from 1400 to 1450 nm, 1474, 1500 nm, from 1670 to 1675 nm. However, bypassing the "data cube" through Net Analyte Signal, with a 90% reduction, the number of bands is reduced to 55 while sustaining a 100% of ice detection. These bands are from 706 to 822 nm.

After combining the multicriteria classification and the Net Analyte Signal, 160 bands remained after a 70% reduction for 100% of ice detection. These bands are from 360 to 636 nm, from 726 to 784 nm, 824 nm, 991 nm, 1020 nm, 1400 to 1500 nm, 1670 nm, and 1676 nm.

We can notice that the Net Analyte Signal makes the most considerable reduction, but this reduction is made at different stages, as shown in Table 10.

Table 10 : Summary of Net Analyte Signal Results

Percentage of Reduction	Number of Bands	Ice	
		<i>Pd</i>	<i>FAR</i>
95%	28	88.47%	11.53%
90%	55	100.00%	0.00%
80%	109	100.00%	0.00%
70%	163	100.00%	0.00%
60%	217	100.00%	0.00%
50%	271	100.00%	0.00%
40%	326	100.00%	0.00%
30%	380	100.00%	0.00%
20%	434	100.00%	0.00%
10%	488	100.00%	0.00%

Nevertheless, the multicriteria classification reduces the number of bands at once. Furthermore, the combined result provides a higher number of reduced bands, which can help prevent the loss of the rare elements that are not representative of the ice detection points.

After all the results presented in this chapter, HSI presented an accurate and sensitive technology capable of quantifying, qualifying, and locating ice accretion on WTB by offering also its spectral signature (fingerprint). Also, this external problem can be detected by using only 55 bands instead of 542 bands, mainly in the bandwidth ranging from 706 to 822 nm without any false alarm unlike the RGB image which presented an ability to detect it accompanied with a high false alarm rate. Thus, HSI is one step ahead of other icing detection technics which does not lead to faulty results due to sensitivity to temperature, elevation or power generation drop.

GENERAL CONCLUSION

All in all, as a result of climate change, governments are developing increasingly sophisticated and cost-effective techniques of capturing natural electricity resources, particularly wind. Wind energy has been utilized for decades to power tasks such as propelling cruising boats, processing grain, pumping water, and powering factory machines. It is also used in wind parks to produce electricity from wind energy. At the moment, the total capacity of all wind farms in the globe is 744 gigawatts, which is enough to meet 7% of the world's energy demand.

Like other development sectors, wind turbines suffer some restrictions and constraints due to environmental and manufacturing factors that limit their potential despite their expansion. Wind turbine blades, one of the most significant and expensive components of wind turbines, are predicted to endure up to 20 years subjected to varying wind loads. After a long time of being exposed to lift and drag, the blade begins to wear, and fatigue promotes the material breakdown and causes blade cracks. Moreover, ice deposits, cracks, delamination, and erosion are all causes of blade difficulties. These flaws lower annual energy output by increasing turbine downtime. The majority of damage detection research is devoted to developing novel early damage detection systems to reduce maintenance time and costs. For that, frequent inspections are essential, particularly for rotor blades, which account for 20-30% of the entire cost of wind turbines. Therefore, non-destructive techniques are essential to improve wind turbines' efficiency and availability and reduce wind energy costs.

This report presents a thorough and systematic review of non-destructive blade inspection techniques. First, the material of the wind turbine blade and the common fault and defect in the blade's production and operation are investigated. Following that, the numerous non-destructive techniques for composite blade inspection (acoustic emission, infrared, fiber grating, ultrasonic, guided wave, thermal imaging, terahertz imaging, visual, tap,

electromagnetic, and vibration non-destructive techniques for composite blade inspection) were summarized and discussed. Indeed, the detection in these methods is based on global parameters (humidity, temperature, frequency, etc.), providing an overall picture of the state of the defect on the blades but not allowing for exact and localized quantification. Furthermore, the sensors used in these techniques do not qualify for the detection of frost formation.

Moreover, after describing some conventional methods used for ice accretion detection on wind turbine blades, this thesis proposes the hyperspectral imaging (HSI) technique, which has been rapidly evolving and broadly applied in many non-destructive diagnostics.

For that, this research concentrated on the use of hyperspectral imaging for the detection of wind turbine blade flaws and ice accretion. The technology has evolved over the years and is now widely utilized in non-destructive material analysis. Finally, this study describes the principles, developments, and uses of spectroscopic imagery technology in the non-destructive detection of wind turbine blade defects and ice formation. It also discusses the experimental setup, essential elements, and the related processing and analytical methods. This technique shows advantages compared with the other discussed methods in detecting the defects and their location and spotting icing at its early stages of accumulation regardless of its thickness and type.

It was demonstrated, in this study, that hyperspectral imaging can build spatial maps that span an extensive range of spectral information by merging spectroscopy with conventional imaging, leading to a variety of applications in blade flaw identification. This study also indicates that spectroscopy imaging and remote on-field assessment can detect icing events with high resolution, precision, and discrimination. It is a non-invasive and reliable tool for identifying variations between iced and clean surfaces, thus granting powerful monitoring capacity, especially in the early detection of icing events. HSI remote monitoring of wind turbine blades for icing detection can be an effective tool. It could robustly and accurately measure and identify the ice at a thickness of 0.1 mm at its early formation stage. Thus, HSI is the upcoming ice detection module of wind turbine blades,

which can offer a lower inspection shutdown time and lower maintenance costs by supplying a simple routine inspection of the wind turbine blade. As for future applications, HSI can also serve for the non-destructive monitoring of wind turbine blades.

In a future work, a monitoring of a real wind turbine farms using hyperspectral imager mounted on a drone must be conducted in order to validate the experimental results obtained in a laboratory study. Also, the study of the subsurface defects like delamination must be examined using hyperspectral imager with a higher bandwidth than those utilized in this study.

To sum up, this report demonstrates hyperspectral imaging's potential role in monitoring wind turbines' safety and saving wind energy costs. We anticipate that this research will aid various energy industries.

APPENDIX I

ALGORITHM USED

According to the thesis presented by Eric Truslow in partial fulfillment of the requirements for the degree of Master of Science in Electrical Engineering in the Northeastern University in August 2012, the performance evaluation of the adaptive cosine estimator detector for hyperspectral imaging applications is studied, and the following algorithm and equations are determined and analyzed.

The most common detectors used in HSI:

The matched filter (MF) and the adaptive cosine estimator (ACE). Both detectors arise under the hypotheses:

$$H_0: x \sim N(0, \sigma^2 \Sigma_b)$$

$$H_1: x \sim N(as, \sigma^2 \Sigma_b)$$

where a and σ are scalars, s is the target signature and Σ_b is the background covariance matrix.

To use hypotheses, we have to assume that the input x has been de-meaned, and the target signature has been demeaned making $s = s_t - \mu_b$. In this discussion here, the variable a is not to be confused with fill fraction α ; a is a scaling like α , but a is not constrained between 0 and 1, and it does not affect the covariance matrix under either hypothesis.

Derivation of the Matched Filter (MF)

The matched filter is probably the most well-known and best understood detector. It is also the easiest to derive. The likelihood ratio is a ratio of conditional densities where one is zero-mean, and the other is not.

$$L(x) = \frac{f(x|H_1)}{f(x|H_0)}$$

where the conditional densities $f(x|H_1)$ and $f(x|H_0)$ are

$$f(x|H_0) = \frac{1}{(2\pi)^{p/2} |\Sigma_b|^{1/2} (\sigma^2)^{p/2}} \exp\left(-\frac{1}{2\sigma^2} x^T \Sigma_b^{-1} x\right)$$

$$f(x|H_1) = \frac{1}{(2\pi)^{p/2} |\Sigma_b|^{1/2} (\sigma^2)^{p/2}} \exp\left(-\frac{1}{2\sigma^2} (x - as)^T \Sigma_b^{-1} (x - as)\right)$$

We can apply a monotonic function to $L(x)$ without not change the performance of the detector. Taking the logarithm (a monotonic function) of $L(x)$ results in the log likelihood ratio, which we denote $L'(x)$. Substituting the conditional densities into the likelihood ratio, the leading terms cancel, and the exponents combine, resulting in

$$L'(x) = -\frac{1}{2\sigma^2} (x - as)^T \Sigma_b^{-1} (x - as) + \frac{1}{2\sigma^2} x^T \Sigma_b^{-1} x$$

Dropping leading constants, expanding, and canceling like terms, yields

$$L'(x) = s^T \Sigma_b^{-1} x - s^T \Sigma_b^{-1} s$$

Applying the scaling $1/\sqrt{s^T \Sigma_b^{-1} s}$ and dropping the right-most term, we obtain the MF

$$y_{MF} = \frac{s^T \Sigma_b^{-1} x}{\sqrt{s^T \Sigma_b^{-1} s}}$$

This definition can be simplified by introducing the whitening transformation. Assuming that Σ_b is positive definite and has a square root matrix $\Sigma_b^{1/2}$ such that $\Sigma_b = \Sigma_b^{1/2} \Sigma_b^{1/2}$. The inverse of the square root matrix $\Sigma_b^{-1/2}$ is known as a whitening matrix or whitening transformation; multiplying x and s by this matrix yields the whitened vectors \tilde{x} and \tilde{s} :

$$\tilde{s} = \Sigma_b^{-1/2} s \text{ and}$$

$$\tilde{x} = \Sigma_b^{-1/2} x$$

The input under each hypothesis after whitening becomes

$$H_0: \tilde{x} \sim N(0, I)$$

$$H_1: \tilde{x} \sim N(a\tilde{s}, I)$$

where I is a p dimensional identity matrix. This allows us to write the MF as

$$y_{MF} = \frac{\tilde{x}^T \tilde{s}}{\sqrt{\tilde{s}^T \tilde{s}}}$$

where the numerator is simply the dot product of the whitened input with the whitened target, and the denominator is the length of the whitened target vector.

Statistics of the Matched Filter

There are many different versions and ways to define the MF; in order of decreasing verbosity, we can define the MF as

$$y_{MF} = \frac{s^T \Sigma_b^{-1} x}{\sqrt{s^T \Sigma_b^{-1} s}}$$

or in terms of the whitened vectors \tilde{x} and \tilde{s} :as

$$y_{MF} = \frac{\tilde{x}^T \tilde{s}}{\sqrt{\tilde{s}^T \tilde{s}}}$$

or for brevity as

$$y_{MF} = h^T \tilde{x}$$

where $h = \frac{\tilde{s}}{\sqrt{\tilde{s}^T \tilde{s}}}$. In the last case, the vector h is known as the matched filter vector.

We will generally use the brevity equation because it is extremely concise, and very general. Note that we can scale the MF arbitrarily but the definitions above are beneficial for this thesis because they facilitate the use of statistical relations, but others may choose a scale that is appropriate with no change in performance. As an example, we will use a different scaling to use the MF as a fill fraction estimator (FFE). We define the FFE as

$$y_{FFE} = \frac{1}{\sqrt{\tilde{s}^T \tilde{s}}} y_{MF}$$

where y_{FFE} is an estimate of the fill fraction α . To obtain basic statistical results for the MF, we assume that we have subtracted μ_b from the data and set $\sigma = 1$, resulting in the hypotheses

$$H_0: x \sim N(0, \Sigma_b)$$

$$H_1: x \sim N(as, \Sigma_b)$$

The mean of the output of the matched filter defined in brevity equation is called the Voltage Signal to Noise Ratio (VSNR), and its square is the Signal to Noise Ratio (SNR), defined as

$$VSNR = \mu_{MF}$$

$$SNR = \mu_{MF}^2$$

where $\mu_{MF} = ah^T \tilde{s} = a\sqrt{\tilde{s}^T \tilde{s}}$. Immediately we see that using the FFE, the mean of the output becomes the scaling of the target mean a . For the hypotheses H_0 and H_1 the distribution of the MF becomes

$$H_0: y_{MF} \sim N(0, 1)$$

$$H_1: y_{MF} \sim N(\text{VSNR}, 1)$$

The separation between the means of the target-absent and target-present distributions in the output is controlled by the VSNR; a high VSNR results in very good performance, while a low VSNR results in bad performance.

The Derivation of The Adaptive Cosine Estimator (ACE):

The Adaptive Cosine Estimator (ACE) or Adaptive Coherence Estimator is a simple extension of the Matched Filter where we compute the Matched Filter value, and then normalize by the length of \tilde{x} . This statistic is simply the cosine of the angle between \tilde{x} and \tilde{s} , which we designate θ . We see that ACE (y_{ACE}) is equal to $\cos(\theta)$, and is defined as

$$y_{ACE} = \frac{\tilde{s}^T \tilde{x}}{(\sqrt{\tilde{s}^T \tilde{s}})(\sqrt{\tilde{x}^T \tilde{x}})}$$

In the literature, ACE usually refers to cosine-squared ($\cos(\theta)^2$), but for simplicity we will use ACE to refer to cosine. The term ‘‘adaptive’’ in ACE generally refers to estimating the covariance matrix of the background Σ_b .

In deriving the MF, we assumed that the parameters a and σ were known, but if σ is unknown we may seek a generalized likelihood ratio test (GLRT) [30]. In this GLRT, we replace σ^2 with its maximum likelihood estimate $\hat{\sigma}^2$ under each hypothesis.

Returning to the likelihood ratio and canceling like terms we have

$$L(\mathbf{x}) = \left(\frac{\hat{\sigma}_1^2}{\hat{\sigma}_0^2} \right)^{-p/2} \exp \left\{ -\frac{1}{2\hat{\sigma}_1^2} (\mathbf{x} - a\mathbf{s})^T \Sigma^{-1} (\mathbf{x} - a\mathbf{s}) + \frac{1}{2\hat{\sigma}_0^2} \mathbf{x}^T \Sigma^{-1} \mathbf{x} \right\}$$

The maximum likelihood estimate (MLE) of the variance for each hypothesis can be shown to be

$$\hat{\sigma}_1^2 = \frac{1}{p} (\mathbf{x} - a\mathbf{s})^T \Sigma^{-1} (\mathbf{x} - a\mathbf{s})$$

$$\hat{\sigma}_0^2 = \frac{1}{p} \mathbf{x}^T \Sigma^{-1} \mathbf{x}$$

These estimates are obtained by differentiating $f(\mathbf{x}|\mathbf{H}_1)$ and $f(\mathbf{x}|\mathbf{H}_0)$ with respect to σ^2 , setting the derivative to 0, and solving for σ^2 . Substituting these estimates into $L(\mathbf{x})$ equation and dropping the constant right-hand term, yields

$$L(\mathbf{x}) = \left(\frac{\hat{\sigma}_1^2}{\hat{\sigma}_0^2} \right)^{-p/2}$$

and an equivalent statistic is

$$L''(\mathbf{x}) = \left(\frac{\hat{\sigma}_0^2}{\hat{\sigma}_1^2} \right)$$

Substituting $\hat{\sigma}_1^2$ and $\hat{\sigma}_0^2$ we have

$$L''(\mathbf{x}) = \frac{(\mathbf{x} - a\mathbf{s})^T \Sigma^{-1} (\mathbf{x} - a\mathbf{s})}{\mathbf{x}^T \Sigma^{-1} \mathbf{x}}$$

Distributing Σ^{-1} using its square root matrix $\Sigma^{-1/2}$ we have

$$L''(\mathbf{x}) = \frac{(\tilde{\mathbf{x}} - a\tilde{\mathbf{s}})^T (\tilde{\mathbf{x}} - a\tilde{\mathbf{s}})}{\tilde{\mathbf{x}}^T \tilde{\mathbf{x}}}$$

At this point we assume that the scaling a is unknown and substitute the MLE \hat{a} .

When a is unconstrained the MLE is

$$\hat{a} = \frac{x^T \Sigma^{-1} s}{s^T \Sigma^{-1} s} = \frac{\tilde{x}^T \tilde{s}}{\tilde{s}^T \tilde{s}}$$

when we constrain $a \geq 0$, the MLE becomes: $\hat{a} = \max\left[0, \frac{\tilde{x}^T \tilde{s}}{\tilde{s}^T \tilde{s}}\right]$. Substituting the unconstrained estimate,

$$L''(x) = \frac{\left(\tilde{x} - \tilde{s} \frac{\tilde{s}^T \tilde{x}}{\tilde{s}^T \tilde{s}}\right)^T \left(\tilde{x} - \tilde{s} \frac{\tilde{s}^T \tilde{x}}{\tilde{s}^T \tilde{s}}\right)}{\tilde{x}^T \tilde{x}}$$

The term resulting from $\hat{a}\tilde{s}$ can be written using projection matrix notation as $\tilde{s} \frac{\tilde{s}^T \tilde{x}}{\tilde{s}^T \tilde{s}} = P_{\tilde{s}} \tilde{x}$

Factoring \tilde{x} the numerator of $L''(x)$, yields

$$\tilde{x}^T (I - P_{\tilde{s}}) (I - P_{\tilde{s}}) \tilde{x} = \tilde{x}^T P_{\tilde{s}}^\perp \tilde{x}$$

Where $P_{\tilde{s}}^\perp$ is known as an orthogonal projection matrix. Finally, we have

$$L''(x) = \frac{\tilde{x}^T P_{\tilde{s}}^\perp \tilde{x}}{\tilde{x}^T \tilde{x}} = \sin^2(\theta)$$

where we are measuring the angle between \tilde{s} and \tilde{x} . This is monotonically related to cosine squared

$$\cos^2(\theta) = \frac{\tilde{x}^T P_{\tilde{s}} \tilde{x}}{\tilde{x}^T \tilde{x}}$$

which is the classic definition of ACE found in the literature. Since we assume α is nonnegative, we constrain the scaling a to be non-negative, so the log-likelihood function becomes

$$L''(x) = \begin{cases} \frac{\tilde{x}^T P_{\tilde{s}} \tilde{x}}{\tilde{x}^T \tilde{x}}, & \text{for } \hat{a} \geq 0 \\ 0, & \text{for } \hat{a} < 0 \end{cases}$$

In this case, $L''(x)$ is a monotonic function of

$$L''(x) = \begin{cases} \sqrt{\frac{\tilde{\mathbf{x}}^T P_{\tilde{\mathbf{s}}} \tilde{\mathbf{x}}}{\tilde{\mathbf{x}}^T \tilde{\mathbf{x}}}}, & \text{for } \hat{a} \geq 0 \\ 0, & \text{for } \hat{a} < 0 \end{cases}$$

and when \mathbf{s} is a single vector the first term becomes

$$y_{ACE} = \sqrt{\frac{\tilde{\mathbf{x}}^T P_{\tilde{\mathbf{s}}} \tilde{\mathbf{x}}}{\tilde{\mathbf{x}}^T \tilde{\mathbf{x}}}} = \frac{\tilde{\mathbf{s}}^T \tilde{\mathbf{x}}}{(\sqrt{\tilde{\mathbf{x}}^T \tilde{\mathbf{x}}})(\sqrt{\tilde{\mathbf{s}}^T \tilde{\mathbf{s}}})}$$

which is equivalent to the cosine between $\tilde{\mathbf{x}}$ and $\tilde{\mathbf{s}}$, as expected.

The Statistics of ACE

As with the MF, there are many equivalent representations for ACE. The most important versions are the cosine, cotangent and the t-detector, which we define only in terms of the whitened and de-meaned vectors $\tilde{\mathbf{x}}$ and $\tilde{\mathbf{s}}$ as

$$y_{ACE} = \frac{\tilde{\mathbf{s}}^T \tilde{\mathbf{x}}}{(\sqrt{\tilde{\mathbf{x}}^T \tilde{\mathbf{x}}})(\sqrt{\tilde{\mathbf{s}}^T \tilde{\mathbf{s}}})}$$

$$y_{cot} = \frac{\tilde{\mathbf{s}}^T P_{\tilde{\mathbf{s}}} \tilde{\mathbf{x}}}{\left(\sqrt{\tilde{\mathbf{x}}^T P_{\tilde{\mathbf{s}}}^\perp \tilde{\mathbf{x}}}\right) (\sqrt{\tilde{\mathbf{s}}^T \tilde{\mathbf{s}}})}$$

$$y_t = \sqrt{p-1} \frac{\tilde{\mathbf{s}}^T P_{\tilde{\mathbf{s}}} \tilde{\mathbf{x}}}{\left(\sqrt{\tilde{\mathbf{x}}^T P_{\tilde{\mathbf{s}}}^\perp \tilde{\mathbf{x}}}\right) (\sqrt{\tilde{\mathbf{s}}^T \tilde{\mathbf{s}}})}$$

We note that these three detectors are monotonically related; in particular, the cosine and cotangent are both ratios of sides from the same triangle. It can be shown that the cosine is related monotonically to the cotangent by

$$y_{ACE} = \frac{y_{cot}}{\sqrt{1 + y_{cot}^2}}$$

meaning they are equivalent detection statistics.

Interestingly, the t-detector has this name because it follows a t-distribution under certain circumstances. Although, these three detectors are equivalent, only the t-detector follows a well-known distribution; so, we will use this version when discussing statistical distributions. The distributions of the t-detector for the two hypotheses are:

$$H_0: y_t \sim t_{p-1}(0, 1)$$

$$H_1: y_t \sim t_{p-1}(\text{VSNR}, 1)$$

Under both hypotheses, the detector follows a univariate t-distribution. We note that this distribution only occurs when the detector is designed with the exact covariance matrix of the input x . When the design covariance matrix is different from the input covariance matrix, we say there is covariance mismatch.

Net Analyte Signal

According to Lorber (1986), the concept of Net analyte signal is introduced and used to find the part of the signal that belongs to the orthogonal plane of all materials other than the target. By this, we choose the most representative bands of the target. These bands will be used as input to the detection algorithm (HyperACE) in order to detect the targets instead of detecting the complete signal spectrum.

The chosen bands are calculated as follows:

$$n_j = (I - S_{-j}(S_{-j}^T S_{-j})^{-1} S_{-j}^T) s_j$$

where s_j is the target spectrum, S_{-j} is a matrix of background analyte spectra and n_j is the portion of s_j that is orthogonal to S_{-j} .

Mutual Information

The mutual information (MI) is also a measure widely used in evaluating the similarity of two images. This measure relies on the probabilistic relation and the distribution of intensities in the images used. MI is highly robust to changes in illumination, even to non-linear ones. The mathematical expression of the MI between A and B , of size $m \times n$, is defined in:

$$MI(A, B) = \sum_{i=1}^n \sum_{j=1}^m p_{AB}(a_i, b_j) \log_2 \frac{p_{AB}(a_i, b_j)}{p_A(a_i)p_B(b_j)}$$

Where $p_A(a_i)$ is the probability that a pixel in A has a gray-level a_i , $p_B(b_j)$ is the probability that a pixel in B has a gray-level b_j , and $p_{AB}(a_i, b_j)$ is the probability that a pixel in A has a gray-level a_i and the same pixel in B has a gray-level b_j . The probability distributions are determined using the normalized histograms of the images. In the histogram of an image, each possible gray-scale value has its corresponding number of occurrences in the image. Normalizing the histogram by the total number of pixels determines the probability distribution of the gray-scale pixel values of an image. The higher the value of the MI, the higher the similarity between two images. The MI describes the stochastic association between the two images and evaluates image similarity from the probabilistic aspect.

APPENDIX II
HYPERSPECTRAL IMAGING APPLIED FOR THE DETECTION OF WIND
TURBINE BLADE DAMAGE AND ICING

Publié dans Remote Sensing Applications: Society and Environment - ELSEVIER

Volume 18, April 2020

Citation:

P. Rizk, N. Al Saleh, R. Younes, A. Ilinca, and J. Khoder, "Hyperspectral imaging applied for the detection of wind turbine blade damage and icing," Remote Sensing Applications: Society and Environment, vol. 18, p. 100291, 2020/04/01/ 2020, doi: <https://doi.org/10.1016/j.rsase.2020.100291>

Résumé:

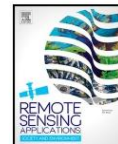
L'objectif principal de cet article est d'étudier le potentiel de l'imagerie hyperspectrale dans la détection des défauts auxquels la pale est soumise. Tout d'abord, il présente les différents types de défauts des pales. Puis, après avoir exposé certaines des méthodes traditionnelles utilisées pour la surveillance des pales d'éoliennes, cet article propose une technique d'imagerie hyperspectrale (HSI) à travers une expérience sur une fibre de verre composite polymère imitant la pale d'éolienne. Cette technologie s'est révélée très prometteuse pour la détection de défauts, quels qu'ils soient, en surface, sous la surface ou même en cas de givrage. Cette technologie d'inspection à distance sur le terrain offre une grande précision dans un temps d'inspection court. Elle peut être un outil puissant pour surveiller à distance les pales d'éoliennes de tous types de dommages. Elle permet de détecter la glace à différentes épaisseurs d'une manière robuste et fiable. Elle a le potentiel de quantifier et de localiser les défauts de surface et de subsurface à un stade précoce de leur formation. Ainsi, la HSI est la méthode d'inspection imminente des pales d'éoliennes qui permettra de réduire la période d'arrêt pour l'inspection, les coûts de maintenance et la

fréquence des pannes soudaines en fournissant une inspection régulière facile des pales d'éoliennes [181].



Contents lists available at ScienceDirect

Remote Sensing Applications: Society and Environment

journal homepage: <http://www.elsevier.com/locate/rsase>

Hyperspectral imaging applied for the detection of wind turbine blade damage and icing

Patrick Rizk^{a,b,*}, Nawal Al Saleh^c, Rafic Younes^d, Adrian Ilinca^a, Jihan Khoder^e^a Wind Energy Research Laboratory (WERL), Université du Québec à Rimouski, 300 allée des Ursulines, Rimouski, QC, G5L3A1, Canada^b Doctoral School of Science and Technology (EDST), Lebanese University, Beirut, Lebanon^c Faculty of Engineering, First Branch, Lebanese University, Tripoli, Lebanon^d Faculty of Engineering, Third Branch, Lebanese University, Rafic Hariri Campus, Hadath, Beirut, Lebanon^e LISV Laboratory, University of Versailles Saint-Quentin-en-Yvelines, 10-12 Avenue de l'Europe, 78140, Vélizy, France

ARTICLE INFO

Index Terms:

Blade
Hyperspectral
Crack
Defect
Delamination
Erosion
Icing

ABSTRACT

Despite the enhancement in the wind energy sector, the wind turbine industry still faces certain limitations due to some manufacturing and environmental factors. Blades are one of the major components of the wind turbine. During their lifetime, these blades are susceptible to deterioration and normal wear and tear that limit their efficiency and result in higher maintenance costs and longer turbine downtime. Periodic inspections must be performed to detect faults at an early stage and help in mitigating these shortcomings. Many methods were used for this purpose such as: ultrasound, sonic IR, vibration analysis and others. Recent developments have seen a trend of using remote inspection techniques that eliminate the need for human access to the blades. Hyperspectral imaging or imaging spectroscopy is a non-destructive and fast monitoring technique in remote sensing. It is widely used in various classification, and detection fields. In this study, the potential of the use of hyperspectral imaging system in the detection of wind turbine blade damage and icing incident is introduced. Specifically, this study lists the types of damage, its causes, and the techniques used to detect it. Finally, current problems and promising attempts for analyzing real-time turbine blade damage detection are discussed. The results demonstrated that hyperspectral imaging could detect surface and subsurface defects as well as icing events in their early stages of occurrence.

1. Introduction

With the conventional energy and fossil fuel resources moving toward an end, the necessity of using renewable energy is increasing, promising to provide sustainability for next generations (Aust, 2014). One of these promising resources that has a big potential in achieving long-term sustainability is wind energy. Wind turbines capture the kinetic energy on wind to generate electricity (Ellabban et al., 2014). According to World Wind Energy Association (WWEA), the worldwide installed wind capacity reached 597 Gigawatt by the end of 2018 with an increase of approximately 10% per year. The largest installed capacity of wind turbine in 2018 was shown in most of European and Asian countries, whereas Asia shares the largest market and USA occupies the second rank (World Wind Energy Association (WWEA), 2018).

As other developing sectors and despite its growth, the wind turbine

still faces some obstacles and constraints due to some environmental and manufacturing factors that limit its potential. Under normal wind conditions, wind turbine blades bear fluctuating wind load characterized by a combination of lift and drag. After a prolonged period, fatigue occurs in blades. Therefore, weariness stimulates material degradation that produces cracks on the blade (Technical Application Papers No.13, 1913).

In fact, some of the wind turbines exist in regions where severe weather like extensive wind and icing are present. Blades suffer from challenges like ice accumulations, cracks, delamination, as well as erosion. These defects will negatively affect the annual energy production by increasing the downtime period of the turbine for wear and tear (Ragheb, 2047). Most researches in the domain of damage detection focus on finding a method for early damage detection to lower the maintenance period and the cost (Qiu et al., 2012). In order to decrease

* Corresponding author. Wind Energy Research Laboratory (WERL), Université du Québec à Rimouski, 300 allée des Ursulines, Rimouski, QC, G5L3A1, Canada.
E-mail addresses: Patrick.Rizk@uqar.ca (P. Rizk), AlSaleh_nawal@hotmail.com (N. Al Saleh), ryounes@ul.edu.lb (R. Younes), Adrian.Ilinca@uqar.ca (A. Ilinca), jihan.khoder@hotmail.com (J. Khoder).

<https://doi.org/10.1016/j.rsase.2020.100291>

Received 6 December 2019; Received in revised form 28 January 2020; Accepted 30 January 2020

Available online 5 February 2020

2352-9385/© 2020 Elsevier B.V. All rights reserved.

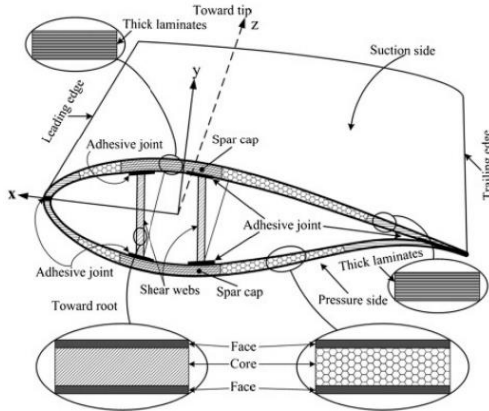


Fig. 1. Structure of the blade (Yanget al., 2013).

maintenance costs and have longer lifetime, frequent inspection of wind turbines should be performed (Ciang et al., 2008) especially on the blades which constitute 20% to 30% of the total cost of a wind turbine (Shohag et al., 2017).

Ultrasound, sonic IR, thermal imaging, vibration analysis, distributed fiber optic sensor and many other methods are used for damage detection (crack, erosion and delamination) and ice detection which is another form of surface contamination.

Few researchers such as Young & al. have discussed the use of hyperspectral images for blade damage detection and it was only limited to erosion detection. For that, this study will fulfill the gap and present the potential of hyperspectral imaging technique in the detection of surface, subsurface flaws, and ice detection. Section II.A introduces the blade structure and the blade's region most susceptible to damage is determined in section II.B. Section II.C discusses the main causes of turbine blade failure, and the resulted flaws are divided into different types and categorized in classes in section II.D where the icing problem is discussed and the ice accretion is modeled. A survey of turbine blades' flaws detection is detailed in section III. Section IV presents an experiment performed on four glass fiber composite material plates with different defect types (crack, erosion, delamination, and icing). Finally, section V, concludes by summarizing the discussed work and briefly describes our insight on the great potential of hyperspectral imaging technique and its advantages in detecting the flaws regardless of their types from surface, subsurface, or even icing events.

2. Blades structure and its failure

2.1. Blade structure

Wind turbine blades are formed by composite materials, specifically glass fiber or carbon fiber, balsa wood or foam (Eker et al., 2006). These materials are lightweight which increase both the strength-weight ratio and the efficiency (McGugan et al., 2015). The structure is described by vertical shear webs joined to the upper and lower spar caps by a highly-toughness adhesive, allowing all the loads on the blade to be supported while ensuring torsional rigidity and bending stiffness (Hernandez Crespo, 2016). Gel coat covers the outside of the blade to protect it from ultraviolet degradation and water penetration (Hernandez Crespo, 2016). The blade is composed of two sides: a suction side characterized by low pressure and high velocity and a pressure side characterized by high pressure and low velocity (McGugan et al., 2015).

The structure of the blade is shown in Fig. 1.

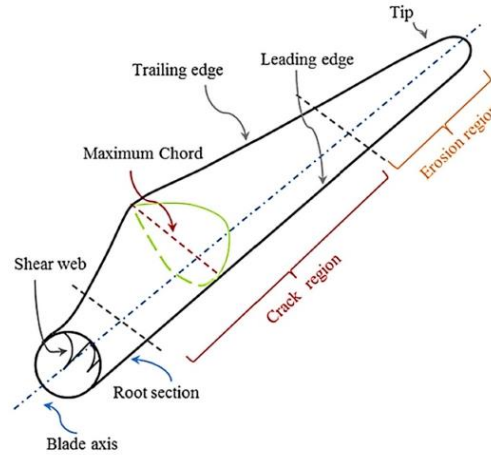


Fig. 2. Crack and erosion regions (Zhang, 2016).

2.2. Area prone to damage

Ciang et al. (2008) stated the four typical areas of the blade that are prone to damage as 30%–70% in the chord length from the blade root, the root of the blade, the maximum chord and the upper spar cap. They characterized two regions where cracks and erosion most probably can occur. The region between the root section and two-third of the blade length is mainly subjected to cracks (Jensen, 2009). However, erosion can occur at any location on the leading edge, typically found in the tip region because of the higher speeds than those in other regions (Ciang et al., 2008). These regions are shown in Fig. 2.

2.3. Causes of failure

This study discusses the faults caused by strong winds, lightning strike, ice and manufacturing defects. As known, wind is the driving force of wind turbine; however, winds of large scale can severely damage the turbine blades. Lightning strike is another main reason of wind turbine blade failure as it creates a destructive internal shock wave within its blades, subsequently the exceeding levels of pressure over-stresses the blade and causes its damage (Li et al., 2015). Furthermore, at greater speeds and with large centrifugal force caused by blade rotation, there is a high probability of facing uneven ice accumulation where ice is built unequally among the blades. That will lead to unbalanced rotation and consequently can stress the hub and lead to damage the turbine blades (Shohag et al., 2017). Finally, manufacturing defects cannot provide the best rigidity of the structure needed to have the effective operation and thus lead to damage the blades (Sørensen, 2009).

2.4. List of flaws

Continuously operating in harsh environments, wind turbine blades are susceptible to damage. The abrasive airborne particles impact the leading edge of the blade and especially the region close to the tip characterized by its high velocity, and subsequently lead to its erosion and creates delamination (Sareen et al., 2014). Damages and cracks can occur around the areas of lightning attraction or the receptors (Shohag et al., 2017). Cold climate and severe icing lead to imbalanced loads caused by the ice mass on the blades which increase the fatigue and shorten the structure lifetime (Hudecz et al., 2014). Fatigue occurs after many load cycles in wind turbine blades and leads to its collapse

Table 1
List of flaws (Giang et al., 2008; Shohag et al., 2017).

Type	Description
Type 1	Skin/adhesive debonding and/or main spar/adhesive layer where the damage is formed in the adhesive layer joining skin and main spar flanges
Type 2	Adhesive joint failure between skins where the damage is formed in the adhesive layer joining the up and downwind skins along leading and/or trailing edges
Type 3	Sandwich panel face/core debonding where the damage is formed at the interface between face and core in sandwich panels in skins and main spar web
Type 4	Delamination driven by a tensional or a buckling load where the damage is formed in laminates in skin and/or main spar flanges, under a tensile or a compression load
Type 5	Fiber failure in tension and laminate failure in compression where splitting and fracture of separate fibers in laminate occur on the skin and main spar of the table
Type 6	Skin/adhesive debonding induced by buckling where buckling of the skin due to damage occurs in the bond between skin and main spar under compression load. This is a specific case of type 1
Type 7	Gel-coat cracking and gel-coat/skin debonding where cracks are formed in the gel-coat leading to its debonding from the skin

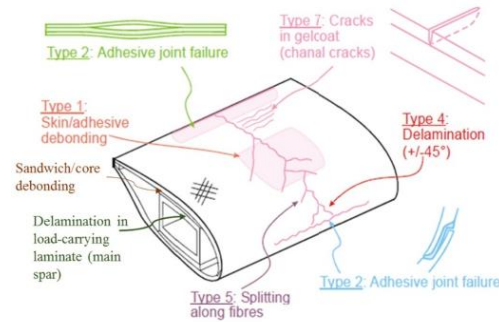


Fig. 3. Types of flaws of wind turbine blades (Li et al., 2015).

(Gallardo, 2011). Table 1 states the different types of damages as reviewed in (Sorensenet et al., 2004).

These seven types of flaws are summarized in Fig. 3.

In addition to these seven types, there is an external problem related to the environmental condition of the area where the wind turbines are installed which is ice accumulation (Froese). In fact, flaws can be divided into three categories or classes: icing event (type 8), surface flaws (type 1, type 5, type 7), and subsurface flaws (type 2, type 4).

2.4.1. Icing problem

Wind turbine suffers from severe weather conditions especially in high altitudes and in cold regions. In regions with northern climate, the wind power increases by 10% than other regions due to the existence of increased air density with low temperature (Fortin et al., 2005). Possible icing events may affect wind farms installed in some of the best wind sites around the globe and lead to some mechanical, electrical failure, and power losses (Lamraoui et al., 2014).

2.4.1.1. Types of ice. Ice formation can occur under three formats in-cloud, precipitation, and frost type (Homola et al., 2006). In-cloud icing occurs when super-cooled water droplets hit the surface of the turbine blade below 0 °C and freeze upon impact (Ilinca, 2011). This type is divided further into rime and glaze ice; the difference between these two types is that rime ice occurs at coldest temperature whereas glaze at warmest temperature (Politovich, 2003). Precipitation icing is the ice that is formed when wet snow or freezing rain occur and hit a

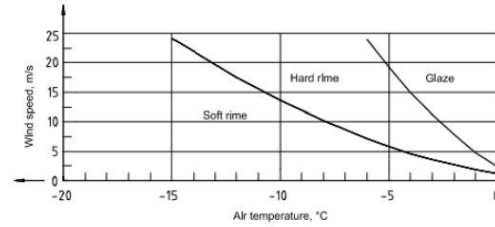


Fig. 4. Type of ice as function of wind speed and air temperature (Fakorede et al., 2016).

surface below 0 °C (Daniel, 2017). Fig. 4 describes the icing profile and characterizes the region where glaze, soft rime, and hard rime ice exist, and which parameter control their formation (Fakorede et al., 2016) (see Fig. 4).

2.4.1.2. Ice accretion model. There are two methods of ice modeling: one depends on some physical swell parameters, and the other depends on meteorological parameters that will influence the input of the system (Homola et al., 2006). Makkonen (1994) described the ice accretion phenomena by equation (1).

$$\frac{dM}{dt} = \alpha_1 \cdot \alpha_2 \cdot \alpha_3 \cdot w \cdot v \cdot A \quad (1)$$

where $\frac{dM}{dt}$ presents the icing rate, and α_1 , α_2 , and α_3 correspond respectively to the collision efficiency, the sticking efficiency, and accretion efficiency. While w presents the mass concentration of the particles by means of the liquid water content (LWC), v is the relative velocity of the particle, and A represents the cross-sectional area of object with respect to the direction of particle velocity vector (Makkonen, 1994).

2.4.2. Internal and external surface flaws

Since wind turbine may exist in harsh weather conditions, it faces rain, hail, as well as some insects that will lead to some defects on the external surface of the blade like erosion and crack (Zhang et al., 2014a). As erosion begins in the blade, the performance of the turbine will decrease, resulting a decrease in the output and an increase in the maintenance cost (Maniaci et al., 2016). Thus, a regular inspection is mandatory to avoid high maintenance cost. Due to fatigue, cyclic loads or uneven ice accumulation, the internal structure may be subject to delamination between the laminate of the blade as well as the external structure may also face induced crack (Mishnaevsky et al., 2017). Delamination is one of the most dangerous faults in the blade structure because it is not easily detected by some traditional detection methods especially if it was at its early stage (Doliński et al., 2018).

3. Detection methods survey

Several reviews on icing and damage detection methods were presented and relative conditions for ice accretion measurements and some methods used in the ice detection and the de-icing systems were evaluated. Parent et al. described the ice precipitation phenomena and its different types (Parent and Ilinca, 2011). Shohag et al. presented fault diagnosis of rotor blade with structural health monitoring (SHM) (Shohag et al., 2017). Yang et al. made a review on all NDT used in the fault detection in wind turbine blade (Yang et al., 2016).

In order to avoid premature defects and high maintenance cost, a routine inspection of the wind turbine blades must be done (Pinho, 2016). Different methods are used for this purpose but each one has its advantages as well as its disadvantages. Some of these methods are presented in this section.

3.1. Visual inspection (VI)

VI is a basic method that depends on the technician and skills to inspect blade structure (Boopathy et al., 2017; Tchakoua et al., 2014). As drawbacks, this time-consuming job (Yang et al., 2016) cannot provide good visibility in some weather conditions and some light crack or erosion may go unseen (Parent and Flinca, 2011; Gholizadeh, 2016). Moreover, some inspectors use video monitoring for ice detection; when the monitor visualizes an ice accretion occurs, the technician sends a signal to the operating room in order to shut down the turbine and activate the de-icing system (Yang et al., 2016). Nowadays, VI is remotely done via a robot or an unmanned vehicle. The latter is used to scan the blade structure and take snapshot of it to be fed to an image processing algorithm such as line and edge detection methods (Zhang and Jackman, 2013), Haar-Like features (Wang and Zhang, 2017), or using a deep convolutional neural network for damage recognition (Yu et al., 2017).

3.2. Ultrasound technique (UT)

UT is a nondestructive testing (NDT) technique widely used by the wind energy industry mainly for structural evaluation of wind turbines towers and blades (Tchakoua et al., 2014) such as estimating the location and nature of flaws in composite and other kinds of materials (Yang et al., 2017).

UT evaluation system comprises a transmitter and receiver circuit, transducer tool, and display device (Gholizadeh, 2016). The principle of measurement is quite simple. Elastic waves are propagated into the region to explore, and reflection within material are detected and revealed (Tchakoua et al., 2014).

The execution of this technique is related to the time of flight or delay, path length, frequency, phase angle, amplitude, acoustic impedance, and angle of wave deflection. Consequently, signal-processing algorithms such time-frequency techniques as the Wigner-Ville distribution, Hilbert-Huang transform, and wavelet transform, can be used to discover additional information on internal defects (Tchakoua et al., 2014; Raisutis et al., 2008).

This method stands as a fast, reliable, and effective tool for SHM of the principal turbine components (Gholizadeh, 2016). Ultrasound scanning can check the laminate for dry glass fibers and delamination under blade surface as attenuation caused by multiple fiber ruptures is less than natural attenuation variation in the laminate (Ciang et al., 2006). However, UT is difficult in setting up (Yang et al., 2017), it needs skill to scan a part accurately and test sample to insure accurate testing (Gholizadeh, 2016).

3.3. Guided-wave (GW)

GW method is based on the study of a propagated wave along the inspected structure. When the wave interacts with the imperfections like surface crack, delamination, its normal pattern is modified and that enables the detection of flaw. Two approaches can be presented: the Pulse-Echo, where the same transducer is used as a transmitter of the wave and receiver of the reflected echoes. The second approach is the Pitch-Catch; the reflected signal is assimilated by another transducer and the defect is detected due to amplitude change or time of the flight (Yang et al., 2016). GW technique has some advantages such as early damage detection of the internal and external structure. Small transducers implemented in few locations can inspect a large area. While the main disadvantage is its huge equipment (Hernandez Crespo, 2016).

3.4. Acoustic emission (AE)

AE is a powerful method of in-situ and laboratory imperfection investigation (Gholizadeh, 2016), with a large frequency range ranging from 50 kHz to 1 MHz (Tchakoua et al., 2014), for fast global flaw

detection in gearboxes, blades, shafts and bearings (Tchakoua et al., 2014), by allowing a global evaluation of the structural integrity of large wind turbine blades (Yang et al., 2017). It is an effective NDT and single harmonic motion (SHM) technique used to notice any further growth of earlier cracks or to distinguish failure mechanisms (Yang et al., 2016).

AE phenomena is based on detecting the fast release of energy of transitory elastic waves (Yang et al., 2017) that are produced by dynamic deformation process once crack pledges and proliferates within the blade (Tchakoua et al., 2014). These material defects can be localized as delamination, matrix micro cracking, fiber pullout and breakage or fiber-matrix debonding (Tchakoua et al., 2014). The stress waves caused by these types of defects diffuse concentrically from their origin and are discovered by a group of extremely sensitive piezoelectric transducers and optic fiber displacement sensors (Gholizadeh, 2016). The most usually measured AE factors for analysis are amplitude, kurtosis, root mean square value, crest factor, energy, events, and counts (Tchakoua et al., 2014).

There are two categories of acoustic condition monitoring: active type characterized by external application of excitation and passive type characterized by an excitation performed by the component itself (Raisutis et al., 2008). For instance, the source of AE for the testing of a fiberglass (FGL) structure is cracking of matrix and fibers (Raisutis et al., 2008). FGL structure produces some AE by itself during the early loading or at loads low compared with the normal load (Raisutis et al., 2008). Despite the presence of internal cracks and non-homogeneities in emission informative signals, such outcome can be used for localization of regions with high residual stresses (Raisutis et al., 2008).

Several studies and research present good results by combining vibration and AE monitoring effort that was performed over a continuous period on operating wind turbines (Tchakoua et al., 2014). AE technique has high sensitivity to detect different types of flaws, as stated before, using multiple and permanent sensors mounting for process control without the need to disassemble the desired specimen to be checked (Gholizadeh, 2016). It is also characterized by its high signal-to-noise ratio (Tchakoua et al., 2014). However, one of its limitations is the signal attenuation during propagation in composite blade material (Yang et al., 2017), thus the need for multiple AE transducers to carry out damage location (Raisutis et al., 2008).

3.5. Tap test

It is a non-visual defects detector which works effectively on thin laminates. The procedure consists of tapping on the blade shell and listen to the change in the emitted sound when the thickness or material type change, or when the presence of porosities or dis-bond occurs (Yang et al., 2016). When using an automated system (Drewry and Georgiou, 2007) such as the local resonance spectroscopy with an automated impulse hammer and a microphone, the excited sound is recorded (Juengert, 2008). The resonance sound emitted is dependent on the material inspected (Juengert and Grosse, 2009).

3.6. Sonic infrared

In this method, the sample is excited via an acoustical energy source like the ultrasonic horn and then the reflection of the thermal wave from the sample is investigated via an infrared (IR) camera (Zhang et al., 2014b). If a defect is present in the sample, the acoustical energy will trigger the defect surface to scrub which will induce a localized increase in temperature (Cheng et al., 2013). IR camera images the thermal reflected wave (Cheng et al., 2013). This method provides an effective, fast, and wide-area range detection method, as well as it can be used for surface and subsurface fault detection (Zhang et al., 2014b) (Fig. 5).

3.7. Thermography

Infrared thermography (IRT) is based on detecting flaws by assessing

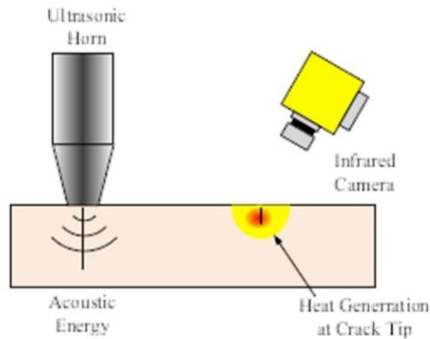


Fig. 5. Working principle of Sonic IR (Cheng et al., 2013).

the temperature distribution using nowadays IR cameras (Gholizadeh, 2016). The presence of a defect in the structure will vary the normal pattern of heat flow (Drewry and Georgiou, 2007) anticipated in sound pattern by varying the continuity of the structure (Yang et al., 2017; Chady, 2016). By that, the flaw is detected and located using the thermography image. This method is also used in blade SHM (Kaushal and Kiran, 2014) in laboratory tests as in its full-field measurements (Yang et al., 2016). The procedure for delamination detection using this technique is described in (Hwang et al., 2015) and that of ice detection in (Abdel-Moati et al., 2018).

IRT technique has two types: the active type and the passive type (Yang et al., 2016). Active thermography can be existed in non-equilibrium state in many situations (Kaushal and Kiran, 2014), such as the surface heating thermography when a lamp, flash, hot water or laser is used to heat the surface of the specimen to be tested and then, the heat is conducted from surface to inner and the volume heating thermography when the specimen is excited by high frequency induction current and microwave and then, the carbon fiber reinforced polymer (CFRP) and glass fiber reinforced polymer (GFRP) are volumetric heated (Yang et al., 2016). Passive thermography is performed in equilibrium state during the rotation of rotor blades from the ground level (Kaushal and Kiran, 2014; Gómez Muñoz et al., 2016).

Despite its efficiency in identifying subsurface flaws (Cheng and Tian, 2012), IRT is subjected to many limitations (Boopathy et al., 2017). The main one is the influence of high environmental temperature and its effect of hiding the small incipient defect detection in wind turbine blade in SHM practice (Yang et al., 2017).

3.8. Vibration analysis (VA)

VA inspects the structural health condition of blades by examining their dynamic responses that are revealed by external forces excitation. Any change in material or structural properties such as stiffness, mass and damping can be determined by these dynamic responses which are described by some modal parameters and vibration features. (Yang et al., 2017; Doliński and Krawczuk, 2009). VA technique is used for a wide range of frequency (0.01–100 kHz) by using different type of sensors (Raišutis et al., 2008; Juengert, 2008). In addition to its role in condition monitoring, VA can locate the damaged region by using many vibrations transducers to reduce the effect of high damping of composite materials on the dynamic response and to be able to have some of them near the position of defect to be well detected (Yang et al., 2017). This technique has been performed during the static and fatigue laboratory tests of wind turbine blades. But the fact of installing many transducers on an operating wind turbine blade leads to unrealistic in-situ application (Yang et al., 2017). Hence, VA cannot be a reliable method to

execute the structural health monitoring of wind turbine blades.

3.9. Eddy current testing (ECT)

ECT has been broadly used in identifying flaws in composite fiber reinforced polymer, metal-matrix composites and other conductive composite material (Yang et al., 2016).

When an alternating magnetic field is applied to a component, eddy currents (EC) are generated. The intensity of these currents varied with the conductivity, the set-up geometry and the permeability of the product. Any change of these parameters can be noticed by the excitation coil as the coil impedance will vary also. The cathode-ray tube will display the amplitude and phase information of the detected EC signals (Kaushal and Kiran, 2014). In addition to its role in detecting surface and subsurface defects (Cheng and Tian, 2012), ECT is able to define the composition, conductivity, hardness, permeability and other conditions of conducting materials such as engineering metals (Yang et al., 2016). Because of that, sometimes EC responses can lead to masked results.

Pulsed ECT has shown its good deep defect detectability, high reliability and good visibility over other ECT by the development in feature extraction technique (Cheng et al., 2013). C-scan imaging in this method visualize the flaw in large-scale structures (Yang et al., 2016).

3.10. Terahertz

Terahertz electromagnetic radiation is a NDT that allows non-ionizing, non-invasive and non-contact inspection of non-conducting polymer composites reinforced with quartz, glass, or Kevlar fibers, CFRP and GFRP (Yang et al., 2016) and dielectric structures such as wind turbine blades (Chady, 2016).

Terahertz waves are electromagnetic radiations with a wide range of frequency varying between 0.1 and 10 THz (Yang et al., 2016) and they are sensitive for changes of refractive index disturbed by any flaws such as void, inclusion, delamination, material inhomogeneities, surface roughness, fiber waviness and internal interfaces in layered structures (Chady, 2016). Generally, flaws are located by reflection of incident terahertz pulse or transmission imaging based on pulsed terahertz time domain spectroscopy (Chady, 2016). This reflection is caused by the interface between the separated layers and weakens the transmitted pulse. The thickness and the inner structure state are determined depending on the changes in delays of the propagated pulses and their echo (Chady, 2016).

3.11. Power curve

Power curve analysis method is used as an ice detection method in which the actual power curve is compared to the theoretical one while checking the weather conditions. A 50% decrease in the power generated is an indication of ice accretion (Parent and Ilinca, 2011). This method presents a robust and efficient detection approach of ice accretion during turbine operation in severe weather conditions, but it has a main disadvantage that the decrease in power can be triggered by other factors than icing event (Tesauro et al., 2014). A fast ice detection algorithm based on Langevin equation is tested offline on the power curve (Fang and Wang, 2016).

4. Hyperspectral remote sensing

Hyperspectral remote sensing is one of the spectral imaging techniques, it collects and processes information from across the electromagnetic spectrum (Adaöet al., 2017). It presents an image at different wavelengths thus forming a data cube of spectral and spatial information (Adaöet al., 2017). This data cube holds some information that the human eyes cannot see without the hyperspectral image (Adaöet al., 2017). The goal of this technology is to obtain the spectrum for each pixel in the image of a scene, in order to detect some specified targets

and identifying them (Adão et al., 2017). Hyperspectral imaging (HSI) is applied in different domains like agriculture, food quality monitoring, surveillance, target detection and many others (Makkiet al., 2018). On the other hand, a less powerful technology than the hyperspectral imaging is the multispectral imaging which acquires spectral information in a fewer number of bands than the HSI. The multispectral imaging technique is based on taking a snapshot of the scene at different wavelengths; in which a spectral signature of a specific object is obtained and can be used for the detection as well as for the classification of this target (Gregoris et al., 2004). This multispectral camera employs the spectral spectroscopy to detect icing, in a robust and reliable manner for a thickness less than 0.5 mm (Gregoris et al., 2004). This method offers a flexibility in the location of the inspected area and reduces the time needed to inspect a specific surface (Gregoris et al., 2004). HSI proved a good detection ability with ice (Nakauchi et al., 2012) and erosion (Young, 2017). Thus, we will use this technology in order to detect surface and subsurface flaws as well as ice accumulation on wind turbine blade.

4.1. Methodology

The experiment is done based on the procedure described below:

- Glass fiber samples preparation with their corresponding faults.
- Spectral signature extraction of each fault aside and that of the glass fiber is taken as reference. Several surface cracks are present in different positions on the glass fiber sample, as well as, for the subsurface delamination case. In the third glass fiber sample an erosion is present within its corner. In the fourth sample, a large area of the glass fiber is covered by an ice layer. After retrieving the signature of normal and faulty glass fiber composite several times, an image was reconstructed from these signatures which will be used in the simulation. The hyperACE algorithm, based on the adaptive cosine/coherent estimator algorithm (Broadwater and Chellappa, 2007; Zhang et al., 2010), is used in the detection process.
- With the intention of detecting lighter faults with the HSI, the spectral signature of each defect is merged with spectral signature of the glass fiber sample as described in the following equation:

$$\text{merged signature} = \alpha \cdot \text{fault signature} + (1 - \alpha) \cdot \text{normal signature} \quad (2)$$

where α represents the abundance factor of fault signature (Manolakis et al., 2003). The merged signature is then inserted in the glass fiber sample image and the image is tested by the detection algorithm. By merging the signature, we are playing on the effect of the size of the fault.

- Band selection algorithm is applied to the data cube in order to find the optimum number of bands while maintaining a high detection probability. Hyperspectral images commonly present a high correlation between end-to-end spectral bands. Consequently, eliminating the redundant information would minimize the volume of data to be interpreted by the processor (Khoder et al., 2017; Rizk et al., 2019). Mutual information (MI) and Net Analyte Signal (NAS) are used to remove the redundancy. The MI measures the similarity between two images (Khoder et al., 2017). To remove the redundant information, the images with low similarity are taken for further study. Then NAS is applied to the low similarity image; where according to (Lorber, 1986) NAS is a part of the analyte gamut that is exclusive to that analyte (Grahn and Geladi, 2007). NAS is a useful method to find figures of merit of a signal. These figures of merit are used latterly to compare different models in an optimum number of bands (Bro and Andersen, 2003).



Fig. 6. Glass fiber composite samples.

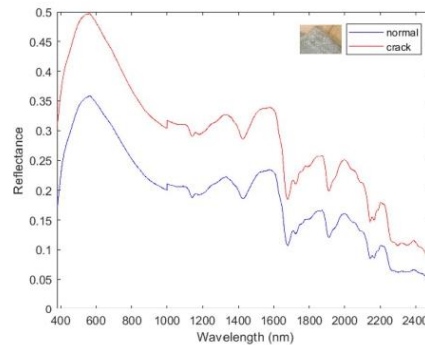


Fig. 7. Spectral signature of cracked versus normal glass fiber composite material.

4.2. Material preparation

For this purpose, four glass fiber composite material plates of 300 mm in length, 210 mm in width, and a thickness of 5 mm are used as samples. Each of these samples holds a type of defects. The first sample carries numerous crack surface defects of different sizes up to 15 mm length and 0.5 mm depth. The second sample presents delamination in the subsurface of the plate with the same size of the crack. The delamination was induced during manufacturing process. The third sample holds an erosion on the corner. The fourth sample is covered in a large part of it with ice of thickness 0.5 mm. The icing is based on spraying cold water on the composite sample and then put it in a freezing system with temperature between -15°C and -30°C until a thin layer of ice appears. An ASD FieldSpec4 spectroradiometer is used to retrieve the spectral signature. This spectroradiometer provides a spectral range from 350 to 2500 nm and a spectral sampling of 1.4 nm at 350–1000 nm and 1.1 nm at 1001–2500 nm (see Fig. 6).

4.3. Results

4.3.1. Surface flaw

4.3.1.1. Crack flaw. The spectral signature of the crack surface versus the normalized reflectance is presented in Fig. 7.

As shown in Fig. 7, the spectral signature of the surface crack has a higher mean than that of the glass fiber material. The crack has the same signature shape with a higher reflectance than that of the surface material.

As stated in the methodology section, several surface cracks exist in the composite glass fiber image and a detection algorithm was tested on it. Fig. 8(a) presents the reflectance of the glass fiber sample. The reflectance achieves its highest values at cracks' location. The spikes shown in this figure can determine the location of these flaws.

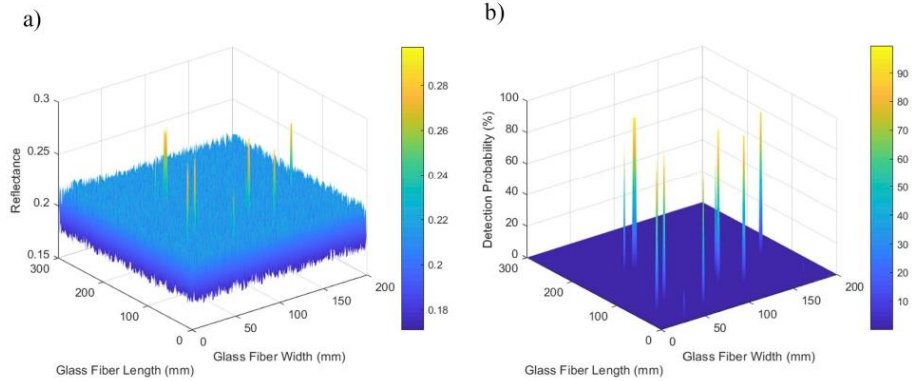


Fig. 8. Crack detection process a) before b) after.

Table 2
Crack sample results.

Crack Sample	Band Reduction	Detection Probability
0.1 crack + 0.9 sample	90%	7.692%
	80%	7.692%
	70%	23.077%
	60%	61.538%
	50%	84.615%
	40%	92.308%
0.2 crack + 0.8 sample	40%	92.308%
	30%	92.308%
	20%	100.000%
	90%	38.462%
	80%	92.308%
	70%	92.308%
0.3 crack + 0.7 sample	60%	92.308%
	50%	92.308%
	40%	100.000%
	90%	92.308%
0.4 crack + 0.6 sample	80%	92.308%
	70%	92.308%
	60%	100.000%
	90%	92.308%
0.5 crack + 0.5 sample	80%	100.000%
	90%	92.308%
	80%	100.000%
0.6 crack + 0.4 sample	90%	92.308%
	80%	100.000%
0.7 crack + 0.3 sample	90%	100.000%
0.8 crack + 0.2 sample	90%	100.000%
0.9 crack + 0.1 sample	90%	100.000%

The detection probability of these presented cracks is illustrated in Fig. 8(b). The detection probability varies depending on the abundance factor of crack reflectance and on its size. For instance, we can notice in this figure from the spikes color that for an abundance factor of 80% of crack, the detection probability was shown to be about 85%, while for a full-crack abundance factor, we can notice 100% detection probability and for an abundance factor of 20% of crack, the detection probability nearly achieves 25%. The blue plane indicates that the detection probability of non-crack signature is below 0.1. The signature of the surface defect is merged with the signature of the composite material as stated in equation (2). The merged signature will help us to study the effect of the size of surface fault on the detection by HSI.

The image with the merged signature is reduced in order to obtain the optimum number bands while maintaining a good detection

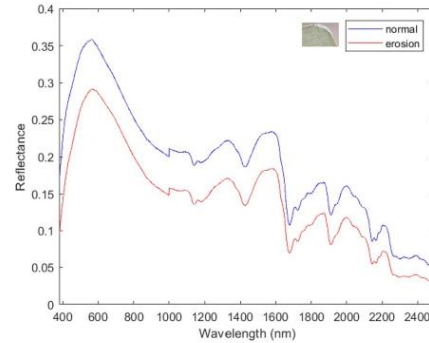


Fig. 9. Spectral signature of eroded versus normal glass fiber composite material.

probability. The image, of 1827 bands, is reduced by MI to 193 bands only, and then fed to the NAS algorithm for further reduction. The results of the band reduction with different percentage of fault signature, with NAS, are summarized in Table 2.

Table 2 presents the effect of size reduction and different percentages of fault insertion on the detection probability. In the case of 10% of the crack signature, a crack of 1.5 mm of length and after applying a reduction of 40% to the image to reach 116 bands, a good detection probability of 92.308% is maintained. If the crack size increased to 10.5 mm then the probability of detection will be 100% with only 20 bands (90% reduction). We can conclude from this table that as the fault size increases, the number of bands needed decreases.

4.3.1.2. *Erosion flaw.* The spectral signature of the eroded surface versus the normalized reflectance is presented in Fig. 9.

As shown in Fig. 9, the spectral signature of the surface crack has a lower mean than that of the glass fiber material. The erosion has the same signature shape but a higher reflectance than that of the surface material. As stated in the methodology section, a corner erosion signatures existed in the composite glass fiber image and a detection algorithm was tested on this image. Fig. 10(a) presents the reflectance of the glass fiber sample. The reflectance achieves its lowest values at erosion's location. The vertical nearly blue planes shown in this figure can

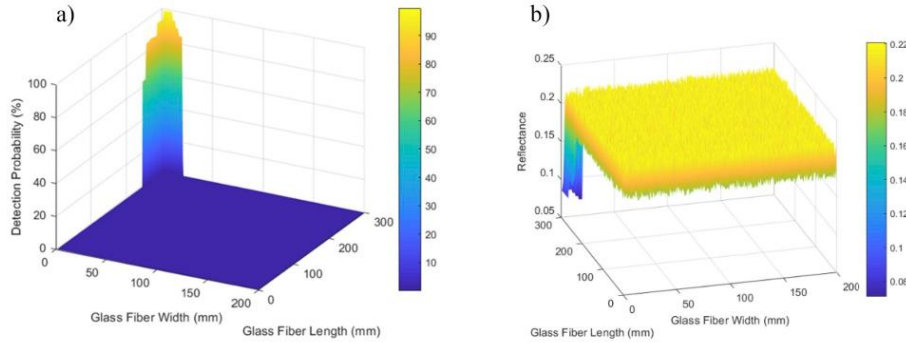


Fig. 10. Erosion detection process a) before b) after.

Table 3
Erosion sample results.

Erosion Sample		
Fault Insertion	Band Reduction	Detection Probability
0.1 erosion + 0.9 sample	90%	0.000%
	80%	15.385%
	70%	46.154%
	60%	53.846%
	50%	69.231%
	40%	84.615%
	30%	92.308%
0.2 erosion + 0.8 sample	20%	92.308%
	10%	92.308%
	90%	38.462%
	80%	84.615%
	70%	92.308%
	60%	92.308%
	50%	92.308%
0.3 erosion + 0.7 sample	40%	100.000%
	90%	76.923%
	80%	92.308%
	70%	92.308%
	60%	100.000%
	90%	92.308%
	80%	100.000%
0.4 erosion + 0.6 sample	90%	100.000%
	90%	100.000%
0.5 erosion + 0.5 sample	90%	100.000%
0.6 erosion + 0.4 sample	90%	100.000%
0.7 erosion + 0.3 sample	90%	100.000%
0.8 erosion + 0.2 sample	90%	100.000%
0.9 erosion + 0.1 sample	90%	100.000%

determine the location of these flaws.

The detection probability of the presented erosion is illustrated in Fig. 10(b). The detection probability varies depending on the severity of the erosion. For instance, we can notice in this figure that high probability detection values are shown on severe erosion locations. However, these values achieve their lowest values in lightest erosion locations. The signature of this surface defect is merged with the signature of the composite material as stated in equation (2). The image with the merged signature is then reduced in order to obtain the optimum number bands while maintaining a good detection probability. The result of the MI on the eroded sample is a reduction from 1827 to 157 number of bands. At that point, the resulted image is also reduced by NAS and the results of this reduction are summarized as percentage in Table 3.

Table 3 presents the effect of size reduction and different percentages of fault insertion on the detection probability. In the case of 10% of the erosion signature, a very light erosion can be detected with only 110 bands while maintaining a good detection probability of 92.308%. However, in the case of severe erosion like 90% of erosion, only 16

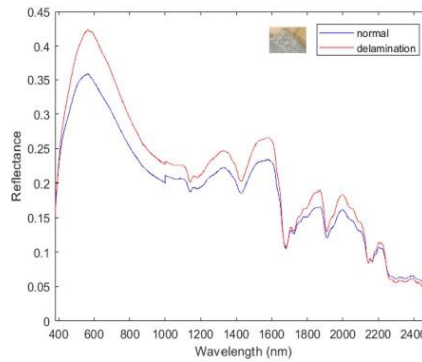


Fig. 11. Spectral signature of delaminated versus normal glass fiber composite material.

bands are needed for a 100% detection probability.

4.3.2. Subsurface flaw

Fig. 11 presents the subsurface delamination spectral signature versus the normal glass fiber composite signature. The delamination signature maintains a higher signature than that of the glass fiber sample until 1600 nm. The inflection point of the delamination signature is at 2250 nm and the reflectance becomes lower than that of the sample reflectance.

Fig. 12(a) presents the reflectance of the glass fiber sample. The reflectance achieves its lowest values at delamination's location. The spikes shown in this figure can determine the location of these flaws (see Fig. 12).

The detection probability of the presented delamination is illustrated in Fig. 12(b). The detection probability varies depending on the abundance factor of delamination reflectance and on its size. For instance, we can notice from the spikes color that for an abundance factor of 80% of delamination, the detection probability was shown to be about 82%, while a large delamination can achieve a 90% detection probability and for an abundance factor of 20% of delamination, the detection probability nearly achieves 10%. The blue plane indicates that the detection probability of non-delamination signature which is below 0.1. The signature of the subsurface delamination defect is merged with the signature of the composite material as stated in equation (2). The same

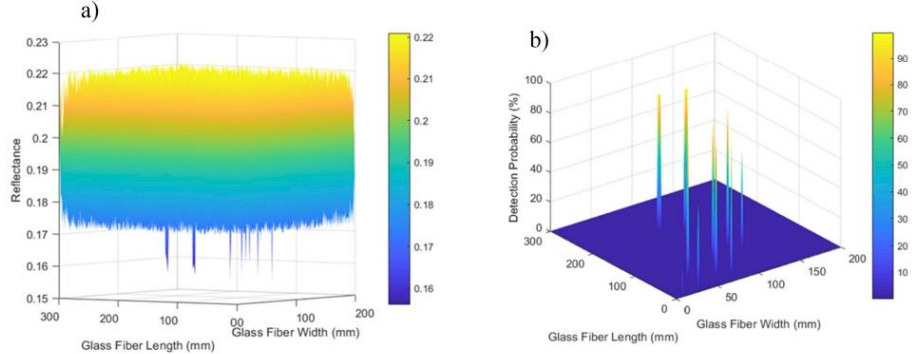


Fig. 12. Delamination detection process a) before b) after.

Table 4
Delamination sample results.

Delamination Sample	Fault Insertion	Band Reduction	Detection Probability
0.1 delamination + 0.9 sample	90%	90%–10%	0.000%
		80%–50%	7.692%
		40%	30.769%
		20%	38.462%
0.2 delamination + 0.8 sample	90%	90%–10%	0.000%
		80%–50%	7.692%
		40%	30.769%
		20%	38.462%
0.3 delamination + 0.7 sample	90%	90%–10%	0.000%
		80%–50%	7.692%
		40%	30.769%
		20%	38.462%
		10%	53.846%
		90%	7.692%
		80%	23.077%
		70%	38.462%
0.4 delamination + 0.6 sample	90%	90%–10%	0.000%
		80%–50%	7.692%
		40%	30.769%
		20%	38.462%
		10%	53.846%
		90%	7.692%
		80%	23.077%
		70%	38.462%
0.5 delamination + 0.5 sample	90%	90%–10%	0.000%
		80%–50%	7.692%
		40%	30.769%
		20%	38.462%
0.6 delamination + 0.4 sample	90%	90%–10%	0.000%
		80%–50%	7.692%
0.7 delamination + 0.3 sample	90%	90%–10%	0.000%
		80%–50%	7.692%
0.8 delamination + 0.2 sample	90%	90%–10%	0.000%
		80%–50%	7.692%
0.9 delamination + 0.1 sample	90%	90%–10%	0.000%
		80%–50%	7.692%

procedure done for the surface flaw is done here, the image is reduced by MI from 1827 to 196 bands only. The results, after applying NAS to the reduced image, are summarized in Table 4.

Table 4 shows the effect of the size of the delamination and the reduction on the detection probability. A delamination of 4.5 nm in length can be detected by the HSI with a minimum of 175 bands. As the size of the delamination increases, we can reduce the size of the image to fewer number of bands while maintaining a high detection probability. For instance, as seen in this experiment, HSI has an ability to detect a delamination of 9 mm with only 20 bands.

4.3.3. Icing case

The case of the icing event is different from the two cases above; there is a total absorption of the spectral reflectance of ice from the wavelength of 1400 nm (see Fig. 13).

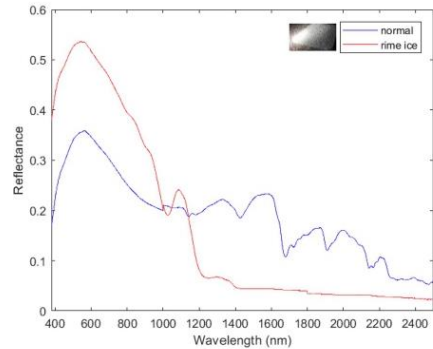


Fig. 13. Spectral signature of rime ice versus normal glass fiber composite material.

The results of the hyperACE algorithm in the ice detection process are presented in Fig. 14. We can notice in Fig. 14(a) that the reflectance achieves its lowest values at locations of accumulation of ice of around 0.12, and are higher with a value of 0.21 at no-ice locations.

We can deduct from Fig. 14 that hyperspectral imaging technique (HSI) has a great potential in the detection process of icing problem. Fig. 14(b) proved the potential of HSI to detect the ice of thickness 0.5 mm. A 100% detection probability is achieved at locations of ice accumulation and about 10% detection probability at no-ice locations. The signature of the ice is merged with the signature of the composite material as stated in equation (2). The same procedure done for the surface flaw is done here, the image is reduced by MI from 1827 to 874 bands only. The results, after applying NAS to the reduced image, are summarized in Table 5.

In Table 5, the effect of the ice thickness and the reduction of the data-cube is studied. The HSI is able to detect ice formation at a thickness of 0.1 mm in a robust and reliable manner with only 88 bands.

From the results presented, HSI presents a great potential to detect in a robust and reliable manner all types of surface and subsurface flaws as well as the ice accretion at their early stage of formation. In this simulation, HSI detected ice of thickness 0.5 mm and proved a potential to detect it at a thickness of 0.1 mm. Also, the demonstration of the detection of a light surface and subsurface flaws were presented.

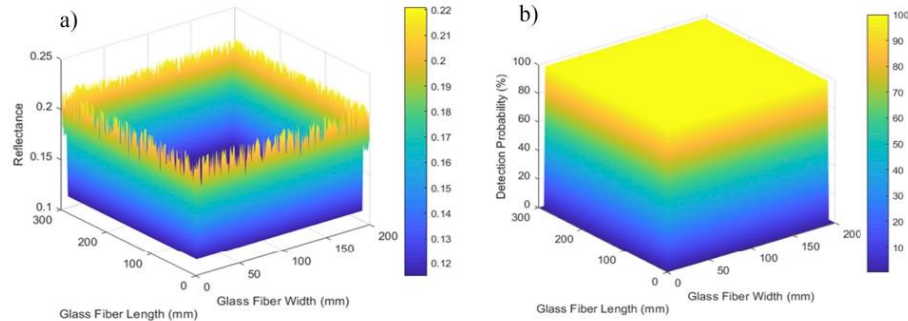


Fig. 14. Icing event detection a) before b) after.

Table 5

Ice sample results.

Ice Sample	Band Reduction	Detection Probability
0.1 ice + 0.9 sample	90%	86.364%
	80%	97.727%
	70%	100.000%
0.2 ice + 0.8 sample	90%	100.000%
0.3 ice + 0.7 sample	90%	100.000%
0.4 ice + 0.6 sample	90%	100.000%
0.5 ice + 0.5 sample	90%	100.000%
0.6 ice + 0.4 sample	90%	100.000%
0.7 ice + 0.3 sample	90%	100.000%
0.8 ice + 0.2 sample	90%	100.000%
0.9 ice + 0.1 sample	90%	100.000%

5. Conclusion

After stating some traditional methods used for wind turbine blades monitoring, hyperspectral imaging (HSI) technique is proposed in this paper. This technology proved a great potential to detect the flaws regardless of their types from surface, subsurface, or even icing event. This remote in-field inspection technology provides a high accuracy in a short inspection time. It can be a powerful tool to remotely monitor the wind turbine blades from all types of damage. It provides an ability to detect ice at a thickness of 0.1 mm in a robust and reliable manner. It has a potential to quantify and localize the surface and subsurface flaws at their early stage formation. Thus, HSI is the impending inspection method of wind turbine blades which will provide a less shutdown period for inspection, less maintenance cost, and low frequency of sudden breakdown by providing an easy regular inspection of the wind turbine blade. As for future work, HSI will be tested on different material types of blade in order to study the effect of material used in blade manufacturing on the detection process, and it will be implemented to scan a real blade sample and monitor a wind farm.

CREdIT authorship contribution statement

Patrick Rizk: Conceptualization, Methodology, Software, Validation, Formal analysis, Investigation, Data curation, Writing - original draft, Writing - review & editing, Visualization. **Nawal Al Saleh:** Investigation. **Rafic Younes:** Conceptualization, Methodology, Validation, Resources, Writing - review & editing, Supervision, Project administration, Funding acquisition. **Adrian Ilinca:** Validation, Writing - review & editing, Supervision, Project administration, Funding acquisition. **Jihan Khoder:** Resources, Writing - review & editing, Supervision, Project administration.

Acknowledgement

This work is sponsored by Azm and Saade Association.

REFERENCES

- Abdel-Moati, H., Morris, J., Zeng, Y., Corie, M.W., Yanni, V.G., 2018. Near field ice detection using infrared based optical imaging technology. *Optic Laser. Technol.* 99, 402–410. <https://doi.org/10.1016/j.optlastec.2017.09.029>.
- Adão, T., et al., 2017. Hyperspectral imaging: a review on UAV-based sensors, data processing and applications for agriculture and forestry. *Rem. Sens.* 9 (11) <https://doi.org/10.3390/rs9111110>.
- A. Aust. "Quest." *KQED Science*. <https://ww2.kqed.org/quest/2014/02/13/nonrenewable-and-renewable-energy-resources-2/>.
- Boopathy, G., Surendar, G., Nema, A., Anand, T.P.P., 2017. Review on non-destructive testing of composite materials in aircraft applications. *Int. J. Mech. Eng. Technol.* 8 (8), 1334–1342 [Online]. Available: <http://www.ineme.com/IJMET/issues.asp?JType=IJMET&VType=8&Type=8>.
- Bro, R., Andersen, C.M., 2003. Theory of net analyte signal vectors in inverse regression. *17* (12), 646–652.
- Broadwater, J., Chellappa, R., 2007. Hybrid detectors for subpixel targets. *29* (11), 1891–1903.
- Chady, T., 2016. Wind turbine blades inspection techniques. *Przegląd Elektrotechniczny* 1 (5), 3–6. <https://doi.org/10.15199/48.2016.05.01>.
- Cheng, L., Tian, G.Y., 2012. Comparison of nondestructive testing methods on detection of delaminations in composites. *J. Sensors* 2012, 1–7. <https://doi.org/10.1155/2012/408437>.
- Cheng, Y., Deng, Y., Cao, J., Xiong, X., Bai, L., Li, Z., 2013. "Multi-wave and hybrid imaging techniques: a new direction for nondestructive testing and structural health monitoring" (in eng). *Sensors (Basel)*. Research Support, Non-U.S. Gov't Review. Nov 27, 13 (12), 16146–16190. <https://doi.org/10.3390/s131216146>.
- Ciang, C.C., Lee, J.-R., Bang, H.-J., 2008. Structural health monitoring for a wind turbine system: a review of damage detection methods. *Meas. Sci. Technol.* 19 (12) <https://doi.org/10.1088/0957-0233/19/12/122001>.
- Daniel, M., 2017. All about freezing rain. *Earth* [Online], 20 January 2017. Available: <https://earthsky.org/earth/all-about-freezing-rain>.
- Doliński, L., Krawczuk, M., 2009. Damage detection in turbine wind blades by vibration based methods. *J. Phys. Conf.* 181 <https://doi.org/10.1088/1742-6596/181/1/012086>.
- Doliński, L., Krawczuk, M., Żak, A., 2018. Detection of delamination in laminate wind turbine blades using one-dimensional wavelet analysis of modal responses. *Shock Vib.* 2018 <https://doi.org/10.1155/2018/4507879>. Art no. 4507879. [Online]. Available:
- Drewry, M.A., Georgiou, G.A., 2007. A review of NDT techniques for wind turbines. *Insight* 49 (3) [Online]. Available: www.ndt.net/search/docs.php3?id=4550.
- Eker, B., Akdoğan, A., Vardar, A., 2006. Using of composite materials in wind turbine blades. *J. Appl. Sci.* 6 (4) [Online]. Available: <http://docsdrive.com/pdfs/ansinet/jas/2006/2917-2921.pdf>.
- Ellabban, O., Abu-Rub, H., Blaabjerg, F.J.R., Reviews, S.E., 2014. Renewable energy resources: current status, future prospects and their enabling technology. *39*, 748–764.
- Fakorede, O., Feger, Z., Ibrahim, H., Ilinca, A., Perron, J., Masson, C., 2016. Ice protection systems for wind turbines in cold climate: characteristics, comparisons and analysis. *Renew. Sustain. Energy Rev.* 65, 662–675. <https://doi.org/10.1016/j.rser.2016.06.080>.
- Fang, H., Wang, L., 2016. Fast ice detection for wind turbine blades via the Langevin equation. *J. Phys. Conf.* 753 <https://doi.org/10.1088/1742-6596/753/7/072016>.
- Fortin, G., Perron, J., Ilinca, A., 2005. Behaviour and Modeling of Cup Anemometers under Icing Conditions.

- Froese, M., "Cracking the icing problem on turbine blades." *Windpower Engineering & Development*. <https://www.windpowerengineering.com/business-news-projects/cracking-icing-problem-turbine-blades/> (accessed).
- Gallardo, P.A.L., 2011. Static and Fatigue Analysis of Wind Turbine Blades Subject to Cold Weather Conditions Using Finite Element Analysis. University of Victoria [Online]. Available: <http://citeseerx.ist.psu.edu/viewdoc/download?doi=10.1.1.1.81.6.5835&rep=rep1&type=pdf>.
- Gholizadeh, S., 2016. A review of non-destructive testing methods of composite materials. *Procedia Structural Integrity* pp. 050-057. [Online]. Available: In: XV Portuguese Conference on Fracture, PCF 2016, vol. I. Paço de Arcos, Portugal [Online]. Available: www.sciencedirect.com.
- Gómez Muñoz, C.Q., García Márquez, F.P., Sánchez Tomás, J.M., 2016. Ice detection using thermal infrared radiometry on wind turbine blades. *Measurement* 93, 157-163. <https://doi.org/10.1016/j.measurement.2016.06.064>.
- Grahn, H., Geladi, P., 2007. Techniques and Applications of Hyperspectral Image Analysis. John Wiley & Sons.
- Gregoris, D., Yu, S., Teti, F., 2004. Multispectral imaging of ice. In: CCECE 2004-CCGEI 2004, Niagara Falls, 2004. IEEE.
- Hernandez Crespo, B., 2016. Damage sensing in blades. In: *Mare-Wint*, pp. 25-52 ch. (Chapter 3).
- Homola, M.C., Nicklasson, P.J., Sundsbø, P.A., 2006. Ice sensors for wind turbines. *Cold Reg. Sci. Technol.* 46 (2), 125-131. <https://doi.org/10.1016/j.coldregions.2006.06.005>.
- Hudecz, A., Hansen, M.O.L., Battisti, L., Villumsen, A., 2014. Icing Problems of Wind Turbine Blades in Cold Climates. DTU [Online]. Available: http://orbit.dtu.dk/files/103715241/Adri_na_Hudecz_Afhandling.pdf.
- Hwang, S., Choi, J., Yang, J., Sohn, H., 2015. Multi-spot laser scanning thermography for delamination inspection GFRP structure in CFRP/GFRP structure. In: 6th International Conference on Advances in Experimental Structural Engineering 11th International Workshop on Advanced Smart Materials and Smart Structures Technology. University of Illinois, Urbana-Champaign, United States.
- Ilinca, A., 2011. Analysis and mitigation of icing effects on wind turbines. In: *Wind turbines D. I. AlBahady Ed. Québec. UQAR, Canada* ch. 8.
- Jensen, F.M., 2009. "Ultimate strength of a large wind turbine blade," *Risø-PhD*, vol. 34, EN [Online]. Available: <http://orbit.dtu.dk/files/5434131/ris-phd-34.pdf>.
- Juengert, A., 2008. Damage detection in wind turbine blades using two different acoustic techniques. In: 7th fib PhD Symposium Stuttgart, Germany. The e-Journal of Nondestructive Testing.
- Juengert, A., Grosse, C., 2009. Inspection techniques for wind turbine blades using ultrasound and sound waves. In: *NDTCE'09, Non-destructive Testing in Civil Engineering*. Nantes, France.
- Kaushal, I.V., Kiran, H.S., 2014. A Review of Non Destructive Testing Methods for Composite Materials. ISSN: 2320-3706, 1. Yuva Engineers Mechanical Engineering.
- Khoder, M., Kashana, S., Khoder, J., Younes, R., 2017. Multicriteria classification method for dimensionality reduction adapted to hyperspectral images, 11 (2), 025001.
- Lamroufi, F., Fortin, G., Benoit, R., Perron, J., Masson, C.J.C.R.S., Technology, 2014. Atmospheric icing impact on wind turbine production 100, 36-49.
- Li, D., Ho, S.-C.M., Song, G., Ren, L., Li, H., 2015. A review of damage detection methods for wind turbine blades. *Smart Mater. Struct.* 24 (3) <https://doi.org/10.1088/0964-1726/24/3/033001>.
- Makki, I., et al., 2018. RBF neural network for landmine detection in hyperspectral imaging. In: 2018 7th European Workshop on Visual Information Processing (EUVIP). IEEE, pp. 1-6.
- Makkonen, L., 1994. Ice and Construction, Report 13. Rilem Chapman & Hall, London, England [Online]. Available: <https://www.scribd.com/document/94408074/ice-and-Construction-Rilem-Report-13>.
- Maniaci, D., Wilcox, B., White, E., Langel, C.M., 2016. Experimental measurement and CFD model development of thick wind turbine airfoils with leading edge erosion. *J. Phys. Conf. Ser.* 753 (2), 022013 <https://doi.org/10.1088/1742-6596/753/2/022013>.
- Manalakis, D., Marden, D., Shaw, G.A., 2003. Hyperspectral Image Processing for Automatic Target Detection Applications.
- McGugan, M., Pereira, G., Sorensen, B.F., Toftegaard, H., Branner, K., 2015. "Damage tolerance and structural monitoring for wind turbine blades," (in eng). *Philosophical transactions. Series A, Mathematical, physical, and engineering sciences* 373 (2035). <https://doi.org/10.1098/rsta.2014.0077>, Feb 28.
- Mishnaevsky, L., Branner, K., Petersen, H.N., Beauson, J., McGugan, M., Sorensen, B.F., 2017. Materials for wind turbine blades: an overview. *Materials (Basel)* 10 (11). <https://doi.org/10.3390/ma1011285>.
- Nakauchi, S., Nishino, K., Yamashita, T., 2012. "Selection of optimal combinations of band-pass filters for ice detection by hyperspectral imaging," (in eng). *Optics express, Research Support, Non-U.S. Gov't* 20 (2), 986-1000. <https://doi.org/10.1364/OE.20.000986>, Jan 16.
- Parent, O., Ilinca, A., 2011. Anti-icing and de-icing techniques for wind turbines: critical review. *Cold Reg. Sci. Technol.* 65 (1), 88-96. <https://doi.org/10.1016/j.coldregions.2010.01.005>.
- A. Pinho, "Turbine blade inspection methods," presented at the Brazil Windpower 2016 Conference and Exhibition, Rio de Janeiro, Brazil. [Online]. Available: <https://8p2.de/index.php/pt/downloads-pt/known-how-pt/wind-energy/67-turbine-blade-inspections-method/file>.
- Politovich, M.K., 2003. Aircraft Icing. Elsevier Science [Online]. Available: http://curry.eas.gatech.edu/Courses/6140/ency/Chapter5/Ency_Atmos/Aircraft_Icing.pdf.
- Qiu, L., Yuan, S., Liu, M., 2012. A phase synthesis based time reversal focusing method for impact and damage imaging of complex composite structures [Online]. Available: In: 4th International Symposium on NDT in Aerospace 2012 - We.2.A.4 [Online]. Available: <https://www.ndt.net/article/aero2012/papers/we2a4.pdf> <http://www.ndt.net/article/aero2012/papers/we2a4.pdf>.
- Ragheb, M., Vertical axis wind turbine [Online]. Available: <http://mragheb.com/NPRE%20475%20Wind%20Power%20Systems/Vertical%20Axis%20Wind%20Turbines.pdf>.
- Raisiutis, R., Jasiūnienė, E., Šlīteris, R., Vladisaukas, A., 2008. The review of non-destructive testing techniques suitable for inspection of the wind turbine blades. *Ultrasonics* 63 (2) [Online]. Available: www.ndt.net/search/docs.php3?MainSource=27.
- Rizk, R., Rizk, D., Kumar, A., Bayoumi, M., 2019. Demystifying emerging nonvolatile memory technologies: understanding advantages, challenges, trends, and novel applications. In: 2019 IEEE International Symposium on Circuits and Systems (ISCAS), 26-29 May 2019, pp. 1-5. <https://doi.org/10.1109/ISCAS.2019.8702390>.
- Sareen, A., Sapre, C.A., Selig, M.S., 2014. Effects of leading edge erosion on wind turbine blade performance. *Wind Energy* 17, 1531-1542 [Online]. Available: <https://m-selig.illinois.edu/pubs/SareenSapreSelig-2014-WindEnergy-Erosion.pdf>.
- Shohag, M.A.S., Hammel, E.C., Olawale, D.O., Okoli, O.I., 2017. Damage mitigation techniques in wind turbine blades: a review. *Wind Eng.* 41 (3), 185-210. <https://doi.org/10.1177/0309524x17706862>.
- Sorensen, B.F., 2009. Materials and structures for wind turbine rotor blades - a overview [Online]. Available: In: *ICCM-17 - 17th International Conference on Composite Materials, Edinburgh, United Kingdom* [Online]. Available: <http://www.iccm-central.org/Proceedings/ICCM17proceedings/Themes/Plenaries/P1.3%20Sorensen%20full.pdf> <http://www.iccm-central.org/Proceedings/ICCM17proceedings/Themes/Plenaries/P1.3%20Sorensen%20full.pdf>.
- Sorensen, B., et al., 2004. "Improved Design of Large Wind Turbineblade of Fibre Composites Based on Studies of Scale Effects (Phase 1) - Summary Report," *Risø, No. 1390*.
- Tchakoua, P., Wamkeue, R., Ouhrouche, M., Slaoui-Hassnoui, F., Tameghe, T., Ekemb, G., 2014. Wind turbine condition monitoring: state-of-the-art review, new trends, and future challenges. *Energies* 7 (4), 2595-2630. <https://doi.org/10.3390/en7042595>.
- Technical Application Papers No13, Wind Power Plants." *ABB*. [Online]. Available: <https://library.e.abb.com/public/92fa0c1913f5651c125793700288e8/1SDC007112G0201.pdf>.
- Tesaro, A., Pavese, C., Branner, K., 2014. "Rotor Blade Online Monitoring and Fault Diagnosis Technology Research," DTU Wind Energy E. No. 0042.
- Wang, L., Zhang, Z., 2017. Automatic detection of wind turbine blade surface cracks based on UAV-taken images. *IEEE Trans. Ind. Electron.* 64 (9), 7293-7303. <https://doi.org/10.1109/tie.2017.2682037>.
- World Wind Energy Association (Wwea), 2018. Wind Power Capacity Worldwide Reaches 597 GW, 50.1 GW Added In. <https://wwindea.org/blog/2019/02/25/wind-power-capacity-worldwide-reaches-600-gw-539-gw-added-in-2018/> (accessed).
- Yang, R., He, Y., Zhang, H., 2016. Progress and trends in nondestructive testing and evaluation for wind turbine composite blade. *Renew. Sustain. Energy Rev.* 60, 1225-1250. <https://doi.org/10.1016/j.rser.2016.02.026>.
- Yang, W., Peng, Z., Wei, K., Tian, W., 2017. Structural health monitoring of composite wind turbine blades: challenges, issues and potential solutions. *IET Renew. Power Gener.* 11 (4), 411-416. <https://doi.org/10.1049/iet-rpg.2016.0087>.
- Yang, J., et al., 2013. Structural investigation of composite wind turbine blade considering structural collapse in full-scale static tests. *March 2013 Compos. Struct.* 97, 15-29. <https://doi.org/10.1016/j.compstruct.2012.10.055> [Online]. Available: <https://doi.org/10.1016/j.compstruct.2012.10.055> [Online]. Available: <https://doi.org/10.1016/j.compstruct.2012.10.055>.
- Young, A., 2017. Atmospheric Correction and Anomaly Detection of Remotely Sensed Hyperspectral Imagery. University of Strathclyde, Glasgow. Centre for Excellence in Signal and Image Processing.
- Yu, Y., Cao, H., Liu, S., Yang, S., Bai, R., 2017. Image-based damage recognition of wind turbine blades. In: 2017 2nd International Conference on Advanced Robotics and Mechatronics (ICARM). IEEE.
- Zhang, H., 2016. Reducing Uncertainty in Wind Turbine Blade Health Inspection with Image Processing Techniques. Iowa State University, Ames, Iowa.
- Zhang, H., Jackman, J., 2013. A feasibility study of wind turbine blade surface crack detection using an optical inspection method. In: *International Conference on Renewable Energy Research and Applications*, Madrid, Spain, 2013.
- Zhang, L., Du, B., Zhong, Y., 2010. Hybrid detectors based on selective endmembers, 48 (6), 2633-2646.
- Zhang, S., Kill, S., Dam-Johansen, K., Bernad Jr., P.L., 2014a. Accelerated Rain Erosion of Wind Turbine Blade Coatings. *Danmarks Tekniske Universitet (DTU), Kgs. Lyngby* [Online]. Available: <https://pdfs.semanticscholar.org/7695/a976113048ffcc1e9e219f3d0eb24baa7075.pdf>.
- Zhang, D., Han, X., Newaz, G., 2014b. Sonic IR Crack Detection of Aircraft Turbine Engine Blades with Multi-Frequency Ultrasound Excitation.

APPENDIX III
WIND TURBINE BLADE DEFECT DETECTION USING
HYPERSPECTRAL IMAGING

Publié dans Remote Sensing Applications: Society and Environment - ELSEVIER

Volume 22, April 2021

Citation:

P. Rizk, R. Younes, A. Ilinca, and J. Khoder, "Wind turbine blade defect detection using hyperspectral imaging," Remote Sensing Applications: Society and Environment, vol. 22, p. 100522, 2021/04/01/ 2021, doi: <https://doi.org/10.1016/j.rsase.2021.100522>.

Résumé:

Cet article présente les concepts, les avancées et les applications de la technologie d'imagerie spectroscopique dans la détection non destructive des défauts des pales d'éoliennes. Il décrit la mise en œuvre de l'imagerie hyperspectrale dans l'acquisition, le traitement et la reconnaissance des défauts ainsi que la détection des fissures et de l'érosion. Il aborde également le dispositif expérimental, les éléments essentiels, ainsi que les méthodes de traitement et d'analyse associées. Cette technique présente des avantages par rapport aux autres méthodes discutées. L'article démontre le rôle potentiel de l'imagerie hyperspectrale dans le contrôle de la sécurité des éoliennes et la réduction des coûts de l'énergie éolienne. Les résultats de cette technique sur le terrain montrent que l'exactitude et la précision de la détection des défauts des pales sont considérablement améliorées [269].



Contents lists available at ScienceDirect

Remote Sensing Applications: Society and Environment

journal homepage: www.elsevier.com/locate/rsase

Wind turbine blade defect detection using hyperspectral imaging

Patrick Rizk^{a,b,c,*}, Rafic Younes^c, Adrian Ilinca^a, Jihan Khoder^d

^a Wind Energy Research Laboratory (WERL), Université du Québec à Rimouski, 300 allée des Ursulines, Rimouski, QC, G5L3A1, Canada

^b Doctoral School of Science and Technology (EDST), Lebanese University, Beirut, Lebanon

^c Faculty of Engineering, Third Branch, Lebanese University, Rafic Hariri Campus, Hadath, Beirut, Lebanon

^d LISV Laboratory, University of Versailles Saint-Quentin-en-Yvelines, 10-12 Avenue de l'Europe, 78140, Vélizy, France

ARTICLE INFO

Keywords:
Blade defect
Hyperspectral imaging
Damage detection
Crack
Erosion

ABSTRACT

Regardless of the evolution in the wind turbine industry, the operation of wind farms faces critical challenges when it comes to maintaining the lowest possible cost of energy. It is essential to early detect or predict wind turbine breakdowns due to different factors such as material degradation, electrical or mechanical failures, faults, or environmental damage. Wind turbine blades are the most expensive and most exposed parts of a wind turbine and suffer from many shortcomings, mainly cracks and erosion, which reduces their performance. Hence, there is an essential requirement for using non-destructive diagnostic of wind turbine blades. This paper lists some of the current non-destructive techniques for wind turbine blades analysis, their applicability, advantages, and drawbacks. Nevertheless, these methods face drawbacks that can be overcome by remote sensing. Hyperspectral imaging is a spectral imaging technique that integrates imaging and spectroscopy. It also enables the analysis and identification of distinctive spectral signatures and assigns them to the examined sample elements. Thus, this paper describes hyperspectral imaging implementation in image acquisition, handling, and flaw recognition as well as the detection of cracks and erosion. This technique's field output results show that blade defect detection's accuracy and precision are significantly enhanced.

1. Introduction

Driven by technological advancement and limited fossil fuel sources, industry and population's increased energy needs requires an accelerated development of renewable energy sources (Ellabban et al., 2014). Wind energy has experienced an exponential growth for the last 20 years. The total installed capacity is over 600 GW. Today, it is a mature technology, with a serial production of megawatt size wind turbines (Drewry and Georgiou, 2007). The share of wind energy is estimated to reach 20% of the total energy supply in the next years (Li et al., 2015).

Wind turbines are compound structures mainly composed of rotor blades, and a nacelle, both installed on the top of a tower (The Inside of a Wind Turb). The blades are an essential and expensive component of the wind turbine. They must be durable and rigid, yet the need to be as light as possible. The largest wind turbines use blades as long as 107 m for offshore sites (Onshore turbine capacity, 2021) and rotor diameter as long as 170 m for onshore sites (How Long Are Wind Turbin, 2021), the stresses should be kept as small as possible not only in the blades but also on the nacelle, tower and foundation. Blade materials are typically fiber-reinforced composites that provide low weight, high strength and

stiffness and optimal fatigue performance. Most of them are made of fiberglass/epoxy, fiberglass/polyester, or carbon-fiber/epoxy composites (Jureczko et al., 2005). Blades are expected to have a lifetime of up to 20 years, during which time they will be exposed to different atmospheric conditions and dynamic loads. The design should withstand different types of damage and faults such as cracks and erosion, which will negatively affect their performance (Li et al., 2015).

The available data for wind farm operation show that the downtime likelihood for each failure of wind turbine blades is: 9 h/year per turbine in WMEP database, 62 h/year per turbine in LWK database, 18 h/year per turbine in VTT database, 36 h/year per turbine in WindStats Germany database, 8 h/year per turbine in WindStats Denmark database, and 31 h/year per turbine in CREW database. This corresponds to time percentages of 0.10%, 0.71%, 0.21%, 0.41%, 0.09%, and 0.35% respectively (Branner Ghadirian, 2014).

Thus, there is an exigency towards overcoming the lengthy and costly maintenance of wind turbine blades to prevent breakdowns (Li et al., 2015). Various methods are available to evaluate the blade status and detect potential defaults, the non-destructive techniques being of interest for wind farm operators. These techniques can be extended to

* Corresponding author. Wind Energy Research Laboratory (WERL), Université du Québec à Rimouski, 300 allée des Ursulines, Rimouski, QC, G5L3A1, Canada. E-mail addresses: patrickrk17@gmail.com, patrick.rizk@uqar.ca (P. Rizk).

<https://doi.org/10.1016/j.rsase.2021.100522>

Received 18 February 2021; Received in revised form 14 April 2021; Accepted 17 April 2021

Available online 6 May 2021

2352-9385/© 2021 Elsevier B.V. All rights reserved.

other applications (Gholizadeh, 2016) such as aerospace (LiewVeidt et al., 2011), manufacturing and industry of pipes, tubes and storage tanks (Venkataraman, 2001; Hufenbach et al., 2011; Schneider, 1984; CastaingsHosten, 2008), nuclear industry (VavilovPlesovskikh et al., 2015), military and defense (BennettLewis and Hungler, 2013), compound flaws identification and classification (FotsingRoss and Ruiz, 2014).

Non-destructive testing entails recognizing and delineating destructions on the surface and inside materials without splitting or modifying the material (Lockard, 2015). Therefore, there is a necessity to use a non-destructive evaluation of wind turbine blades to identify faults and defects without harming the tested blade (Newswire, 2013).

The main methods referred in the composite non-destructive evaluation field are Acoustic Emission Testing (SarasiniSantulli et al., 2014), Infrared Testing (VavilovBudadin and Kulkov, 2015), Fiber Grating Testing (Li et al., 2014), Ultrasonic Testing (PengZhang et al., 2012), Guided Wave Testing (CastaingsHosten, 2008), Thermal Imaging (Kroeger, 2014), Terahertz Imaging (Rizk et al., 2020), Visual Inspection (BossiGiurgiutiu et al., 2015), Tap Test (Rizk et al., 2020), Electromagnetic Testing (YangKim et al., 2013) and Vibration Analysis (Rizk et al., 2020). Nevertheless, the inspection of wind turbine blades depends on the controller's precision and capacity, the detection method's reliability, and the equipment's efficiency (Yang et al., 2016).

Regular imaging and spectroscopy cannot obtain spectral information over large tested areas (Adaoet al., 2017). With the fast evolution of information science and image processing technology, remote sensing technologies have become useful in the non-destructive detection of blade faults (Xiaona Li et al., 2017). Hyperspectral imaging, belongs to the family of spectral imaging technologies, and it is a promising candidate among the available wind turbine blade defect-recognition solutions (Young et al., 2016). By merging spectroscopy methods and conventional imaging, hyperspectral imaging can create a spatial map over a broad range of spectral information, leading to various uses in the blade defect-recognition (Xiaona Li et al., 2017).

In this work Section 1 introduced wind turbine technology and the challenges facing its widespread adaptation. Section 2 presents a brief survey of the non-destructive wind turbine blade inspection and surface flaws detection techniques. Section 4 presents the basic concepts of hyperspectral imaging and its application for detecting blade material defaults. We continue with an experiment's setup completed on a GFRP blade sample showing different severity of cracks and erosion on its surface, whereas section 6 explains the methodology. Finally, section 7 lists and analyses the results of this experiment. We conclude with a summary of the work and highlight the potential of the hyperspectral imaging technique and its benefits in identifying blade defaults.

2. Non-destructive blade defects detection methods

2.1. Acoustic emission testing

The acoustic emission method passes a signal from a source through a propagation medium and is captured by a transducer (SarasiniSantulli et al., 2014; Yu et al., 2017). This latter sends an electrical signal, that indicates the tested sample's state (Xie, 2009; Tchakoua et al., 2014). In the presence of mechanical breakdowns or material defects such as cracks and erosion, a non-stationary time-varying acoustic emission signal is generated by the wind turbine's blades (Gholizadeh, 2016; Li et al., 2014; Tchakoua et al., 2014). This method can be used, even during operation, and can cover large areas and many micro-damage types (Yang et al., 2016; Yu et al., 2017). However, the static condition is not covered, and errors in processing algorithms can lead to misleading results (Zhongkui Zhu and Wang, 2005; RaisutisJasiunien et al., 2008).

2.2. Infrared testing

Every material whose temperature is over 0 K emits infrared radiation due to the vibration of its molecules. This radiation can be measured using an infrared thermal imager-receiver (Dahao Yue et al., 2011). This latter transfers the energy disseminated onto a photosensitive element (Li et al., 2014). The heat variation of the tested sample appears on the monitor via infrared thermography. In the presence of blade defects, the cooling during the heat conduction process is disturbed (Drewry and Georgiou, 2007). The size and shape of the flaws are visualized (Chady, 2016). This method is highly sensitive, efficient and relatively easy to implement (ChengTian, 2012). Nevertheless, it is costly and can hardly detect a point temperature (BoopathySurendar et al., 2017).

2.3. Fiber grating testing

This method draws the incident light into the fiber core using the light-sensitivity of optical fiber materials. Therefore, its sensor measures the variations of the refractive index inside the fiber core (Rao, 1997). A fiber grating sensor can be positioned anywhere on the wind turbine blade to test and detect any damage signal. Then, the blade damage can be identified by analyzing the data (Ying Shi, 2010). This method helps predict blade lifetime and blade stress level. Furthermore, it works for either static or dynamic signal defect detection (Li et al., 2014). Yet, this method has many drawbacks for long-term monitoring, such as its sensitivity to power source alterations (Ciang et al., 2008).

2.4. Ultrasonic testing

This method uses the change of materials' ultrasonic diffusion wave reflection and energy during the conveyance to detect internal faults (Tchakoua et al., 2014). The distance between the surface and the flaw is determined using the transit time. Furthermore, the flaw size is determined by referring to the echo signal's size and the transmitting transducer location (Yu et al., 2017). In the presence of defects, the received signal has reduced wave amplitude and velocity, in addition to variation in frequency and others (Tchakoua et al., 2014; RaisutisJasiunien et al., 2008). This method is rapid and inexpensive. It is also efficient, sensitive, and safe. Nonetheless, it is a tough inspection technique, especially for non-smooth surface evaluation, and pretentious to subjective and objective factors (Gholizadeh, 2016; Yu et al., 2017).

2.5. Guided wave testing

This method uses an actuator that generates high-frequency guided waves (Croxford ADrinkwater et al., 2007). They act as stress waves and propagate following the studied sample's boundaries (Lowe MJS, 1998). If the guided waves diffuse in all directions and its regular pattern is changed, structural damage such as cracks and erosion is present (Yang et al., 2016). This method can inspect large areas for external and internal flaws that are not far from the sensing equipment (Yuan SShi et al., 2008). However, the guided wave detection method's equipment is expensive and occupies large spaces (Hernandez Crespo, 2016). For instance, Zhao et al. introduced wireless and wired approaches in guided wave testing on an aircraft wing and shows the advantages and disadvantages of each one (Zhaoet al., 2007; Zhaoet al.). Moreover, Kwan et al. compared these approaches and showed that the wirelessly acquired signal matches well with the acquired signal with its wired predecessor (Kwan et al., 2018).

2.6. Thermal imaging

This method uses the thermoelastic effect (Avdelidis N Plbarra-Castanedo et al., 2006). In other words, variations in stresses lead to variations in temperature, detected by sensors or cameras (Ciang et al., 2008). Higher temperature indicates the presence of defects in the

tested region (Hahn FPaynter et al., 2002). This method helps in structural health monitoring by locating hot spots on the blade and reducing the damage (Hahn FPaynter et al., 2002). Yet, it is a very costly technique. Moreover, the spotting of temperature variations is affected by conduction and convection processes. These facts make the inspection more difficult on a localized scale (Tesauro et al., 2014).

2.7. Terahertz imaging

This method uses a non-ionizing, non-invasive and non-contact inspection of dielectric structures by propagating electromagnetic radiations with frequency ranging from 0.1 to 10 THz (Yang et al., 2016). In the presence of flaws, the refractive index shows variations (Chady, 2016). Flaws are located by pulse terahertz time-domain spectroscopy, and thickness is computed by taking into consideration the difference in hindrances of the propagated pulses and their echo (Mittelman D. MNeelamani et al., 1999). Although this method is recommended for detailed inspection of the defect area (Rizk et al., 2020), its main drawback is the lengthy duration as the analysis is done point by point (Chady, 2016).

2.8. Visual inspection

This method is based on the technician's experience and his/her vision capacity (Kim DYJung et al., 2013). Its present applications are expanded to be remotely performed (Marsh, 2011) via drones that scan and send the image to a processing algorithm for further investigation (Cripps, 2011). This method is cheap as no equipment is required. However, it is time-consuming and affected by human subjectivity and light conditions (Hanson, 1920). Whereas, Drone inspection technique is also affected by the poor battery endurance and the weather conditions (WIND TURBINE, 2021).

2.9. Tap test

This method consists of hitting lightly the inspected structure and checking for any variations in emitted sound due to alterations in material, variations in thickness or the presence of material degradation or faults (Yang et al., 2016). It can also be automated, using a Computer-Aided Tap Tester System (Drewry and Georgiou, 2007). This method helps discover irregularities in the tested sample, and its results can be automated (Juengert and Grosse, 2009). However, it leads to ineffective results for thick structures (Rizk et al., 2020).

2.10. Electromagnetic testing

This method uses electric or magnetic fields and studies the electromagnetic response of the structure (Gholizadeh, 2016). An example is the Eddy Current Testing that produces eddy currents at the magnetic field application on a sample (KoyamaHoshikawa and Kojima, 2013). The coil impedance and the intensity of these currents change in the presence of faults (Kaushalkiran, 2014). This technique is cheap, simple, and can detect surface and subsurface flaws (ChengTian, 2012). However, it is a time-consuming testing (Yang et al., 2016).

2.11. Vibration analysis

This method is based on exciting the examined structure by external forces and analyzing its dynamic response illustrated by modal specifications and vibration characteristics (DolinskiKrawczuk, 2009). The change in these responses can detect the flaws, and the location can be determined using vibration transducers (RaisutisJasiunien_e et al., 2006; Juengert and Grosse, 2009). This method can be applied during both the static and fatigue laboratory tests of wind turbine blades (Rizk et al., 2020). Nonetheless, it is unreliable for structural health monitoring as the various transducers on the blade can provide misleading

results (Yu et al., 2017).

2.12. Internal inspection

Internal wind turbine blade inspections usually necessitate an inspector crawling into a blade to collect visual data. They not carried out often enough for some reasons. Firstly, they take a long time to complete. Secondly, they necessitate some specialized knowledge in terms of confined space entry from the inspectors, and while they are a good source of information, they are also restricted by the visual examination of the inside or outside of the blade. Furthermore, there are limits in determining the degree of harm caused by lightning strikes (The Uptime Wind Energy P, 2021).

2.13. Ground-based inspection

At a Duke Energy wind farm, EPRI and Digital Wind Systems, Inc. successfully demonstrated a new wind turbine blade inspection technology, known as SABRE method (Beyond Speculation and S, 2014). It has many improvements over traditional inspection techniques. When the blades are in use, the machine inspects them from the ground. It incorporates a sophisticated long-wave infrared (IR) camera for spotting minor IR emissions from structural defects in rotating blades that reveal as hot or cold spots. Broadband high sensitivity microphones are used in acoustic spectral analysis technologies to detect and locate lightning strike gaps, cracks, and irregular surfaces. Phase imaging photography is also encompassed in the device, which can detect surface irregularities (Ground-Based Wind Turbine, 2015). However, this industry somehow relies on visual inspection by staff who climb the turbines, which is time-consuming and expensive due to turbine shutdowns (Beyond Speculation and S, 2014).

3. Hyperspectral imaging technique

The hyperspectral imaging technique combines modern imaging and spectroscopy to obtain both spectral and spatial information from an object simultaneously (Zhang BLi et al., 2014). The Goetz et al. were the first researchers to introduce hyperspectral or spectroscopy imaging in remote sensing applications, especially the direct translation of surface materials into images (Goetz AFSolomon and Rock, 1985). Spectroscopy imaging has currently arisen as a scientific tool for detecting surface and subsurface defects of structures with the growth of optical sensing and imaging techniques (Khoder et al., 2017). Hyperspectral imaging aims to acquire the spectrum for each pixel in a scene image to locate objects, recognize materials or detect mechanisms (Cl, 2003; Makkiet al., 2018). Using conventional RGB images, rare events that are not visible to the human eyes may go undetected or unseen. Compared to traditional RGB images, whose gamut is limited to three bands, the hyperspectral images provide a broad monochromatic image up to hundreds of bands (Zhang et al., 2014). The required number of bands depends on the application. For instance, Kwan et al. showed the potential of using convolutional neural network (CNN) for land cover classification using 4 bands (RGB + NIR) to achieve somehow the same results of the best performing methods using all the hyperspectral bands (Kwanet al., 2020). Indeed, the target object's spatial position in the image is conserved by the contiguous band images at different wavelengths (Elmasry GSun and Allen, 2012). Thus, at each waveband image, the rare event can be detected using a specific detection algorithm such as the Adaptive cosine/coherent estimator that proved its robustness in target detection in real-time applications (Khodoret al., 2021), the cluster kernel RX that proved its high performance in anomaly detection with good computational requirements (Zhou et al., 2016).

4. Experimental setup

Hyperspectral imaging was applied for surface fault detection, like

crack and erosion, for a wind turbine blade section. Scratch is used as notation in this paper to better illustrate the early stage of cracks occurrence. A crack eventually forms in the zone of a notch, scratch, or change in section and spreads slowly at first, then quickly, until the blade fails. As a result, abrupt changes in section or scratches are extremely dangerous in high-cycle fatigue, frequently shortening the fatigue life. For the detection of these flaws, three hyperspectral sensors are used. These sensors cover a bandwidth from 340 nm to 1700 nm with a spectral resolution of 3 nm. These three sensors cover the range from 340 to 840 nm, from 640 to 1050 nm, and from 950 to 1700 nm. The GFRP blade sample illustrated in Fig. 1, has 53.0 cm in length, 34.5 cm in width, and a thickness of 4.0 cm. Also, we induced some predefined scratches and erosion on the blade. These faults were of different sizes ranging from unseen defects to moderate ones.

5. Methodology

Before starting the experiment, two reference signals must be retrieved: the white reference and the dark reference signal. These two signals will be used in the image calibration phase using the equation:

$$R = \frac{RS - D}{W - D} \tag{1}$$

In equation (1), *R* is the calibrated/normalized image, *RS* is the retrieved/scanned image, *D* is the dark reference signal, and *W* is the white reference signal.

The original hyperspectral image, built on black and white reference images, can be arranged into the reflectance mode. While the dark reference picture suppresses the area detectors' obscure current effect, the white reference picture stands for the uppermost intensity values.

After the calibration phase, a normalized data cube is built. Five hundred forty-two (542) bands compose this hyperspectral image. Also, a preprocessing step removes the effect of dust and moisture on the blade. The spectra's physical effects are removed to boost the resulting diversified regression, classification model, or exploratory research. This hypercube is fed into the detection algorithm "hyperACE" to check the detection capacity and ensure a 100% detection for crack and erosion signals. Spectral data of modern spectroscopy technologies have many wavelengths that make the computation complex, the detection ineffective, and the inspection slow. A band reduction reduces the computational time and the amount of data computed during the detection process. The optimal variables are selected and the calibrated wavelengths using Multicriteria Classification and Net Analyte Signal Algorithm. The Multicriteria Classification focuses on preserving the rare event inside the scanned scene while maintaining an optimum band reduction. Also, the Net Analyte Signal algorithm has a vital role in computing the figures of interest in a calibrated model's characterization.



Fig. 1. Blade section.

Fig. 2 illustrates the flowchart for the hyperspectral imaging experiment.

6. Results

Fig. 3 illustrates a 3D hyperspectral cube image of the wind turbine blade specimen consisting of one wavelength and two spatial dimensions. It comprises 542 bands, 44 pixels in blade length and 29 pixels in blade width. This result is obtained by scanning the wind turbine blade specimen by moving the detector along two spatial dimensions.

Fig. 3 also shows that the reflectance intensity is varying with the wavelength in an unarranged manner. Furthermore, it varies slightly along the wind turbine blade specimen concerning the faults' regions' effects. For instance, at the uppermost band index, the reflectance is around 0.8 at regions of faults and negligible elsewhere.

The explored defaults of the wind turbine blade specimen are of two types: crack and erosion, as shown in Figs. 4–7. Fig. 4 illustrates a hairline crack, a minor scratch, on the wind turbine blade specimen's surface, one type of external flaw that splits the surface without crashing apart. Fig. 5 presents a light erosion, which is another type of shell fault that gradually destructs the surface and diminishes the structure. The moderate ones, moderate scratch, and moderate erosion are shown respectively in Figs. 6 and 7.

Reflectance mode allows us to inspect these surface flaws on the wind turbine blade and avoid specular reflection. The illuminated sample absorbs a small portion of the incident light, whereas the largest percentage of the transmitted light conveys the more appreciated information. The detector stands opposite to the light source to capture this data, the spectral signatures, as described in the following paragraphs.

The illustration of the scratch surface signature with its different width value, in red, and that of the undefective blade signature, in blue, are shown in the following figures. The scratch widths in Figs. 8–11 are respectively 0.1, 0.3, 1.0, and 2.0 mm. These figures prove that the scratch reflectance values for the different tested thicknesses are lower than those of the normal blade signature for the wavelengths ranged between 300 and 600 nm and between 1000 and 1700 nm. Whereas, between these two ranges, the normal blade signature achieves higher reflectance values than the scratch signature. The difference in reflectance values for these two signatures is not very important in Fig. 8,

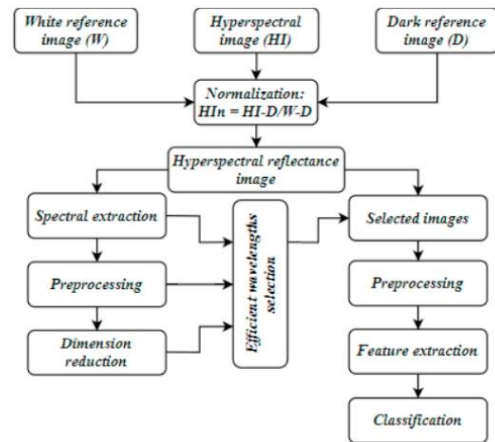


Fig. 2. The flowchart (methodology) of the hyperspectral imaging experiment.

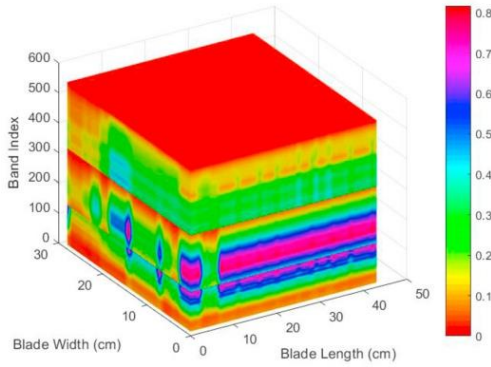


Fig. 3. 3D hyperspectral cube of the wind turbine blade specimen.



Fig. 4. Minor scratch on the blade specimen.

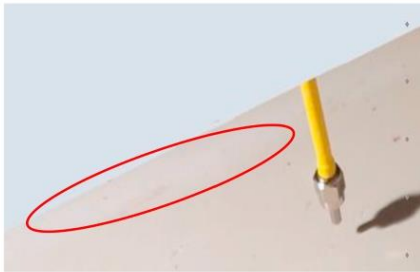


Fig. 5. Light erosion on the blade specimen.

where the tested scratch width is 0.1 mm. For instance, these two signatures overlap for the wavelengths less than 1000 nm. This difference increases and is easily noticeable in Figs. 9–11 with scratch width growth. It is noted that the normal blade signature and the scratch signature have the same shape and achieve their peaks at the same wavelengths, such as 600, 800, 1100, 1300, and 1500 nm. At 1700 nm, the reflectance of the scratch signature in these figures becomes zero.

Figs. 12 and 13 present the erosion flaw blade surface's spectral signature ranging from light to moderate, in red, versus normal blade surface signature in blue. For the light erosion signature illustrated in Fig. 12, its reflectance is lower than that of the normal blade for the wavelength ranged between 300 and 400 nm. Then, for wavelengths

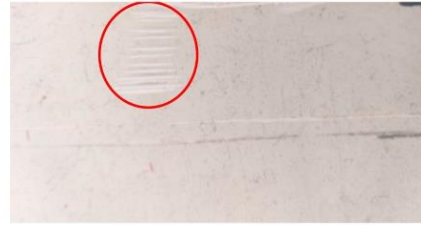


Fig. 6. Moderate scratch on the blade specimen.



Fig. 7. Moderate erosion on the blade specimen.

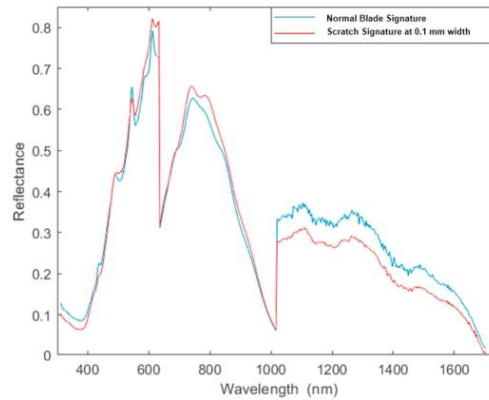


Fig. 8. The spectrum of 0.1 mm width scratch versus normal blade signature.

between 400 and 500 nm, these two signals overlap. After 500 nm, the spectral signature of light erosion is higher than the normal blade signature. This difference switches starting for wavelengths higher than 1000 nm. Slope variations are similar for both signatures, and peak locations appear at the same wavelengths, 600, 800, 1100, 1300, and 1500 nm. Furthermore, a zero-reflectance value appears for a wavelength of 1700 nm. For the moderate erosion illustrated in Fig. 13, the reflectance signature is lower than the normal blade for the wavelengths ranging between 300 and 1700 nm. The difference is as large as 50%. Same signature shapes are noticeable for the normal and moderate erosion signature with peaks at wavelengths equal to 600, 750, 1100, 1300, and 1500 nm. The moderate erosion signature's reflectance becomes zero at a wavelength equal to 1700 nm, as for the light erosion.

At this step, the hyperACE algorithm is applied based on an adaptive

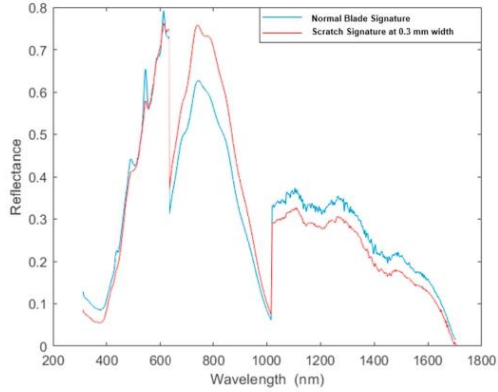


Fig. 9. The spectrum of 0.3 mm width scratch versus normal blade signature.

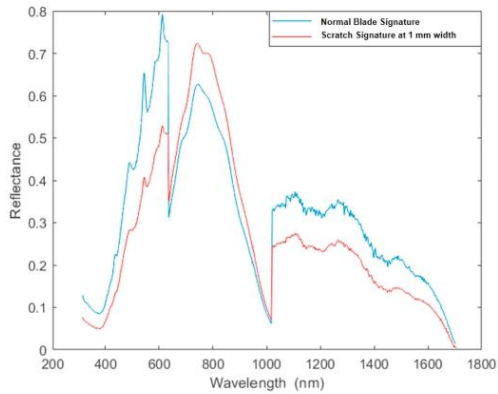


Fig. 10. The spectrum of 1.0 mm width scratch versus normal blade signature.

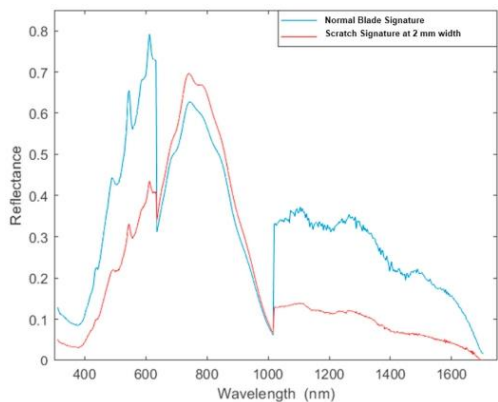


Fig. 11. The spectrum of 2.0 mm width scratch versus normal blade signature.

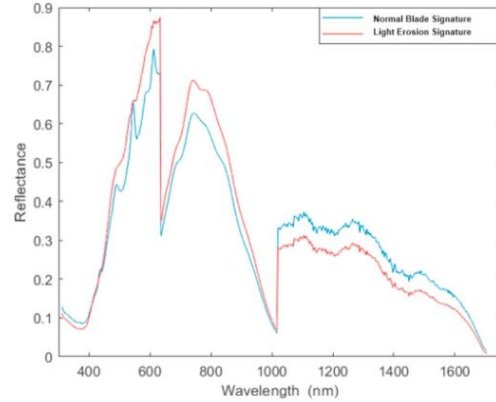


Fig. 12. The spectrum of light erosion signature versus normal blade signature.

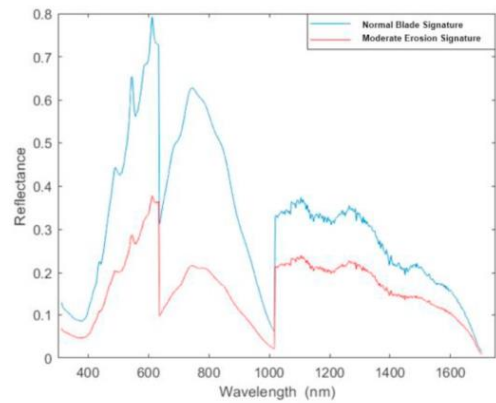


Fig. 13. The spectrum of moderate erosion signature versus normal blade signature.

cosine/coherent estimator algorithm to detect crack and erosion regions. It sees the points of defects by scanning the sample and locating the faults on its signature. The detection probability of both types of surface flaws (crack and erosion) is 100%, and the likelihood of its false alarm rate is 0%, as shown in Table 1. In conclusion this detection algorithm using hyperspectral imaging technique leads to a full and reliable detection of surface flaws.

The scratch abundance factor on a 2D illustration of the wind turbine blade surface appears in Fig. 14. In this figure, the regions free of scratches are dark blue, light scratch locations are light blue, and the moderate ones are yellow. Fig. 15 presents a 3D illustration of the scratch detection on the wind turbine blade sample's surface. In this

Table 1
The detection probability (Pd) and false alarm rates (FAR) for defect types using a hyperspectral image.

	Pd (%)	FAR (%)
Crack	100	0.00
Erosion	100	0.00

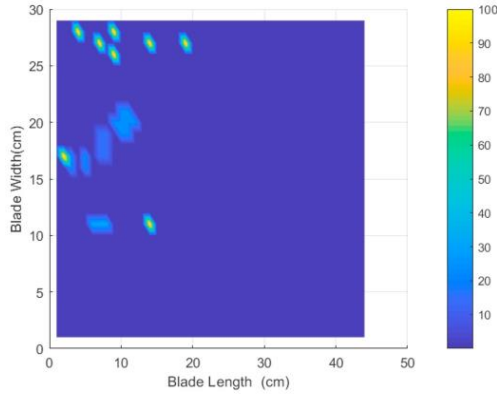


Fig. 14. 2D illustration of the scratch detection.

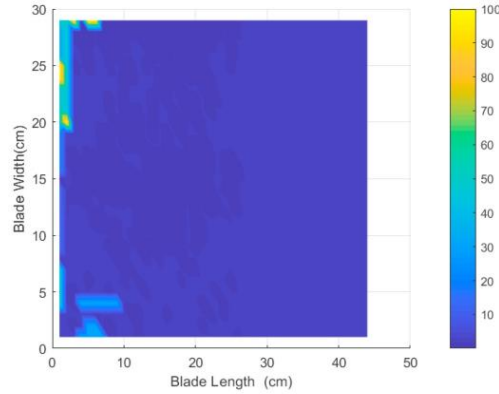


Fig. 16. 2D illustration of the erosion detection.

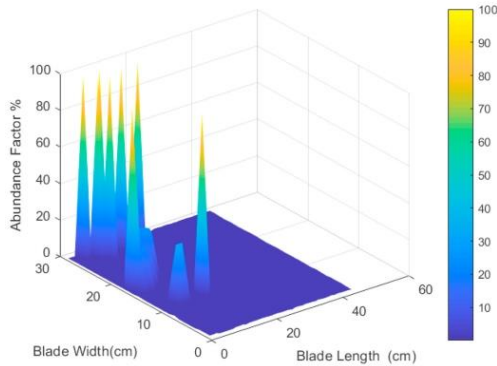


Fig. 15. 3D illustration of the scratch detection.

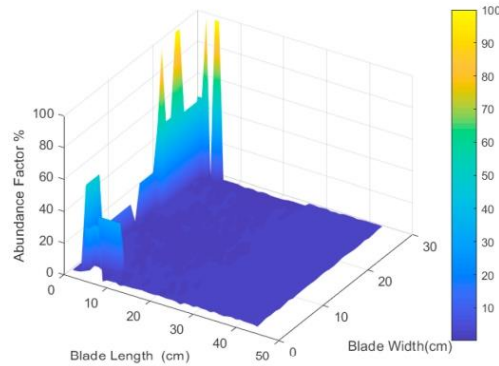


Fig. 17. 3D illustration of the erosion detection.

figure, the scratches on the surface of the wind turbine blade specimen appear as spikes. Their severity is indicated by the scaled color, as for the 2D illustration, and the spike height. The scratches of width less than 1 mm appear as a light scratch and the others as moderate ones.

Fig. 16 displays the erosion abundance factor in a 2D illustration of the wind turbine blade sample. In this figure, dark blue indicates the areas uneroded, light blue designates the light erosion regions, and yellow, the moderate ones. Also, a 3D representation of the erosion inspection of the blade sample appears in Fig. 17. The spikes represent the eroded regions. The light erosion spikes have the top in light blue, the moderate ones in yellow, and the uneroded areas appear dark blue. As shown in Figs. 16 and 17, light and moderate erosion are at two corners of the wind turbine blade sample's surface.

Finally, the detection performance is explored using a reduced spectrum to accelerate image processing. Table 2 presents the detection performance parameters (*Pd* and *FAR*) with a band reduction of the image's full spectrum. The original hyperspectral image consists of 542 bands. After performing a 90% reduction, only 55 bands are sufficient to maintain 100% detection of crack and erosion. The bandwidth ranges from 706 to 822 nm.

Table 2
Summary of band reduction results.

Percentage of Reduction	Number of Bands	Crack		Erosion	
		Pd	FAR	Pd	FAR
95%	28	62.07%	37.93%	79.59%	20.41%
90%	55	100.00%	0.00%	100.00%	0.00%
80%	109	100.00%	0.00%	100.00%	0.00%
70%	163	100.00%	0.00%	100.00%	0.00%
60%	217	100.00%	0.00%	100.00%	0.00%
50%	271	100.00%	0.00%	100.00%	0.00%
40%	326	100.00%	0.00%	100.00%	0.00%
30%	380	100.00%	0.00%	100.00%	0.00%
20%	434	100.00%	0.00%	100.00%	0.00%
10%	488	100.00%	0.00%	100.00%	0.00%

7. Conclusion

In conclusion, non-destructive techniques are essential to improve wind turbines' efficiency and availability and reduce wind energy costs. A thorough and systematic review of non-destructive blade inspection techniques is presented. First, the wind turbine blade material and the usual fault and defect in the blade's production and operation are

explored. Next, the various non-destructive techniques (acoustic emission, infrared, fiber grating, ultrasonic, guided wave, thermal imaging, terahertz imaging, visual, tap, electromagnetic, and vibration non-destructive techniques for composite blade inspection) were summarized and discussed. The research concentrated on the use of hyperspectral imaging for the detection of wind turbine blade flaws. The technique has increasingly evolved over the past decades and is broadly used in the non-destructive analysis of materials. Finally, this paper sets out the concepts, advances, and applications of spectroscopy imagery technology in the non-destructive detection of wind turbine blade defects. It also discusses the experimental setup, essential elements, and the related processing and analytical methods. This technique shows advantages compared with the other discussed methods. The paper demonstrates hyperspectral imaging's potential role in monitoring wind turbines' safety and saving wind energy costs. We assume the different energy fields will benefit from this research.

Ethical statement

- 1) this material has not been published in whole or in part elsewhere.
- 2) the manuscript is not currently being considered for publication in another journal.
- 3) all authors have been personally and actively involved in substantive work leading to the manuscript and will hold themselves jointly and individually responsible for its content.

CRedit authorship contribution statement

Patrick Rizk: Conceptualization, Investigation, Methodology, Software, Validation, Formal analysis, Investigation, Data curation, Writing – original draft, Writing – review & editing, Visualization. **Rafic Younes:** Conceptualization, Methodology, Validation, Resources, Writing – review & editing, Supervision, Project administration, Funding acquisition. **Adrian Ilincă:** Conceptualization, Methodology, Validation, Writing – review & editing, Supervision, Project administration, Funding acquisition. **Jihan Khoder:** Resources, Writing – review & editing, Supervision, Project administration.

Declaration of competing interest

The authors declare that they have no known competing financial interests or personal relationships that could have appeared to influence the work reported in this paper.

Acknowledgement

The authors acknowledge financial support from NSERC (Natural Sciences and Engineering Research Council) Canada and Azm&Saade association in the completion of this study.

References

WIND TURBINE AND BLADE INSPECTIONS." <http://rovdron.eu/drone-en/industrial-inspections/inspekcie-farm-wiatrowych> (accessed 11 April, 2021).

Beyond speculation and sci-fi: researchers help drive plans and technologies to secure the grid. Winter 2014, no. R&D Quick Hits *Epr J: Electric Power Research Institute*, 2014 17 [Online]. Available: http://eprijournal.com/wp-content/uploads/2015/07/EPRJ-Journal-Winter2014-complete_3002004850_Small2.pdf.

Ground-based wind turbine blade inspection system successfully demonstrated at Duke energy wind farm. Success Story vol. 2015-206 *Wind Generation Epr J: Electric Power Research Institute*, 2015 [Online]. Available: <https://www.epri.com/research/products/3002005126>.

How Long Are Wind Turbine Blades?" <https://www.clean-energy-ideas.com/wind-turbines/how-long-are-wind-turbine-blades/> (accessed 11 April, 2021).

Onshore turbine capacities smash 6 MW, pressuring logistics." Ed Pearcey. <https://www.reuters.com/renewables/wind-energy-update/onshore-turbine-capacities-smash-6-mw-pressuring-logistics/> (accessed 11 April, 2021).

The Inside of a Wind Turbine." Office of ENERGY EFFICIENCY & RENEWABLE ENERGY, vol. Wind Energy Technologies Office. [Online]. Available: <https://www.energy.gov/eere/wind/inside-wind-turbine>.

"The Uptime Wind Energy Podcast - Episode Details." Weather Guard Lightning Tech. <https://weatherguardwind.com/wind-turbine-force-majeure-lightning/> (accessed 11 April, 2021).

Adão, T., et al., 2017. Hyperspectral imaging: a review on UAV-based sensors, data processing and applications for agriculture and forestry. *Rem. Sens.* 9 (11) <https://doi.org/10.3390/rs9111110>.

Avdelidis N P, A.D.P., Ibarra-Castanedo, C., Bendada, A., Kenny, S., Maldague, X., 2006. Structural integrity assessment of materials by thermography. In: Presented at the Damage in Composite Materials CDCM 2006, Stuttgart, Germany.

Bennett, L.G.I., Lewis, W.J., Hungler, P.C., 2013. The development of neutron radiography and tomography on a SLOWPOKE-2 reactor. *Physics Procedia* 43, 21–33. <https://doi.org/10.1016/j.phpro.2013.03.003>.

Boopathy, G., Surendar, G., Nema, A., Anand, T.P.P., 2017. Review on non-destructive testing of composite materials in aircraft applications. *Mech. Eng. Technol.* 8 (8), 1334–1342. <https://iaeme.com/Home/issue/LJMET?Volume=8&Issue=8>.

Bossi, R.H., Giurgiutiu, V., 2015. 15 - nondestructive testing of damage in aerospace composites. In: Irving, P.E., Soutis, C. (Eds.), *Polymer Composites in the Aerospace Industry*. Woodhead Publishing, pp. 413–448.

Branner, K., Ghadirian, A., 2014. Database about blade faults, 0067 DTU Wind Energy [Online]. Available: https://backend.orbit.dtu.dk/ws/portalfiles/portal/118222161/Database_about_blade_faults.pdf.

Cripps, David, 2011. The future of blade repair. *Reinforc Plast* 55, 28–32.

Castains, M., Hosten, B., 2008. Ultrasonic guided waves for health monitoring of high-pressure composite tanks. *NDT E Int.* 8 (41), 648–655. <https://doi.org/10.1016/j.ndteint.2008.03.010>.

Chady, T., 2016. Wind turbine blades inspection techniques. *Przeład Elektrotechniczny* 1 (5), 3–6. <https://doi.org/10.15199/48.2016.05.01>.

Cheng, L., Tian, G.Y., 2012. Comparison of nondestructive testing methods on detection of delaminations in composites. *Sensors* 1–7. <https://doi.org/10.1155/2012/408437>.

Cl, C., 2003. *Hyperspectral Imaging: Techniques for Spectral Detection and Classification*. Plenum Publishing Co.

Ciang, C.C., Lee, J.-R., Bang, H.-J., 2008. Structural health monitoring for a wind turbine system: a review of damage detection methods. *Meas. Sci. Technol.* 19 (12) <https://doi.org/10.1088/0957-0233/19/12/122001>.

Croxford A, W.P., Drinkwater, B., et al., 2007. Strategies for guided-wave structural health monitoring. *Proc. Roy. Soc. Lond.: Mathematical, Physical and Engineering Sciences* 463, 2961–2981.

Dahao Yue, X.L., Zhang, Haojun, Li, Yeshu, 2011. IR thermography inspection of wind turbine blades [J]. *Infrared Technology* 10 (33), 614–617 etc.

Dolinski, L., Krawczuk, M., 2009. Damage detection in turbine wind blades by vibration based methods. *Phys 181*. <https://doi.org/10.1088/1742-6596/181/1/012086> [Online]. Available.

Drewry, M.A., Georgiou, G.A., 2007. A review of NDT techniques for wind turbines. *Insight* 49 (3) [Online]. Available: www.ndt.net/search/docs.php3?id=4550.

Ellabban, O., Abu-Rub, H., Blaabjerg, F.J.R., Reviews, S.E., 2014. Renewable Energy Resources: Current Status, Future Prospects and Their Enabling Technology, vol. 39, pp. 748–764.

Elmsary G, K.M., Sun, D., Allen, P., 2012. Principles and applications of hyperspectral imaging in quality evaluation of agro-food products: a review. *Crit. Rev. Food Sci. Nutr.* 52, 999.

Fotsing, E.R., Ross, A., Ruiz, E., 2014. Characterization of surface defects on composite sandwich materials based on deflectometry. *NDT E Int.* 62, 29–39. <https://doi.org/10.1016/j.ndteint.2013.11.004>.

Gholizadeh, S., 2016. A review of non-destructive testing methods of composite materials. In: XV Portuguese Conference on Fracture, PCF 2016, vol. I. Paço de Arcos, Portugal. *Procedia Structural Integrity* pp. 050–057. [Online]. Available: www.sciencedirect.com [Online]. Available: www.sciencedirect.com.

Goetz AF, V.G., Solomon, J.E., Rock, B.N., 1985. Imaging spectrometry for Earth remote sensing. *Science* 228, 1147–1153.

Hanson, R.J.E., 1920. Visual fatigue and eye strain in the use of telescope. *Trans. Opt. Soc.* 22–26.

Hahn F, K.C.W., Paynter, R.J.H., Dutton, A.G., Kildegaard, C., Kosgaard, J., 2002. Design, fatigue test and NDE of a sectional wind turbine rotor blade. *Thermoplastic Composite Material* 15, 267–277.

Hernandez Crespo, B., 2016. Damage sensing in blades. In: *Mare-Wint*, pp. 25–52.

Hufenbach, W.B., Thieme, R., Tyczynski, M., T, 2011. Damage monitoring in pressure vessels and pipelines based on wireless sensor networks. *Procedia Engineering* 10, 340–345. <https://doi.org/10.1016/j.proeng.2011.04.058>.

Juengert, A., Grosse, C., 2009. Inspection techniques for wind turbine blades using ultrasound and sound waves. In: *NDTCE'09, Non-destructive Testing in Civil Engineering*. Nantes, France.

Jureczko, M., Pawlak, M., Mezgy, A., 2005. Optimisation of wind turbine blades. *J. Mater. Process. Technol.* 167 (2), 463–471.

Kaushal, I.V., Kiran, H.S., 2014. A Review of Non Destructive Testing Methods for Composite Materials. *Yuva Engineers Mechanical Engineering*.

Khoder, M., Kashana, S., Khoder, J., Younes, R., 2017. Multicriteria Classification Method for Dimensionality Reduction Adapted to Hyperspectral Images, vol. 11, 025001 no. 2.

Khodor, M., et al., 01/14 2021. Landmine detection in hyperspectral images based on pixel intensity. *Remote Sensing Applications: Society and Environment* 21, 100468. <https://doi.org/10.1016/j.rsase.2021.100468>.

Kim DY, K.H.-B., Jung, W.S., Lim, S., Hwang, J.-H., Park, C-w, 2013. Visual testing system for the damaged area detection of wind power plant blade. In: *Proceedings of the 2013 44th International Symposium on Robotics (ISR)*. IEEE, Seoul, pp. 1–5.

- Koyama, K., Hoshikawa, H., Kojima, G., 2013. Eddy current nondestructive testing for carbon fiber-reinforced composites. *J. Pressure Vessel Technol.* 4, 135. <https://doi.org/10.1115/1.4023253>.
- Kroeger, T., 2014. Thermographic inspection of composites. *Reinforc. Plast.* 4 (58), 42–43.
- Kwan, C., Huang, H., Islam, M.M., Ayhan, B., 2018. Unpowered Wireless Ultrasound Generation and Sensing for Structural Health Monitoring of Composites.
- Kwan, C., et al., 2020. Deep learning for land cover classification using only a few bands. *Rem. Sens.* 12 (12), 2000 [Online]. Available: <https://www.mdpi.com/2072-4292/12/12/2000>.
- Li, R., Du, W.L., Shen, X.J., Li, F.X., 2014. Overview of fault detection and state diagnosis technology in wind turbine blades. *Appl. Mech. Mater.* 513–517, 2983–2988. <https://doi.org/10.4028/www.scientific.net/AMM.513-517.2983>.
- Li, D., Ho, S.-C.M., Song, G., Ren, L., Li, H., 2015. A review of damage detection methods for wind turbine blades. *Smart Mater. Struct.* 24 (3) <https://doi.org/10.1088/0964-1726/24/3/033001>.
- Liew, C.K., Veidt, M., Rajic, N., Tsui, K., Rowlands, D., Morton, H., 2011. Inspections of helicopter composite airframe structures using conventional and emerging nondestructive testing methods. *J. Test. Eval.* 39 (6).
- Lockard, C.D., 2015. Anomaly Detection in Radiographic Images of Composite Materials via Crosshatch Regression. (1586713 M.A.), Mills College, Ann Arbor. ProQuest Dissertations & Theses Global database.
- Lowe MJS, A.D.a.C.P., 1998. Defect detection in pipes using guided waves. *Ultrasonics* 36, 147–154.
- Marsh, George, 2011. Meeting the challenge of wind turbine blade repair. *Reinforc. Plast.* 55 (6), 32.
- Makki, I., et al., 2018. RBF neural network for landmine detection in hyperspectral imaging. In: 2018 7th European Workshop on Visual Information Processing (EUVIP). IEEE, pp. 1–6.
- Mittelman, D.M., Neelamani, R., Baraniuk, R.G., Rudd, J.V., Koch, M., 1999. Recent advances in terahertz imaging. *Appl. Phys.* 68, 1085–1094. *Lasers and Optics*.
- Newswire, P., 2013. Global Non-destructive Testing (NDT) Equipment Market - by Technology (Ultrasonic, Eddy Current, Electromagnetic, Radiography, Thermography), Verticals (Manufacturing, Petrochemical, Aerospace, Automotive, Power Generation) & Geography (2013 - 2018). PR Newswire.
- Peng, W., Zhang, Y., Qiu, B., Xue, H., 2012. A brief review of the application and problems in ultrasonic fatigue testing. *AASRI Procedia* (2), 127–133. <https://doi.org/10.1016/j.aasri.2012.09.024> no. 0.
- Raisutis, R., Jasiunienis, E., Sliteris, R., Vladisaukas, A., 2008. The review of nondestructive testing techniques suitable for inspection of the wind turbine blades. *Ultrasonics* no 2, 63. www.ndt.net/search/docs.php3?MainSource.
- Rao, Y.J., 1997. In-fiber bragg grating sensors. *Mens. Sci. Technol.* 4 (8), 355–375.
- Rizk, P., Al Saleh, N., Younes, R., Ilincea, A., Khoder, J., 2020. Hyperspectral imaging applied for the detection of wind turbine blade damage and icing. *Remote Sensing Applications: Society and Environment* 18, 100291. <https://doi.org/10.1016/j.rsase.2020.100291>, 2020/04/01/.
- Sarasini, F., Santulli, C., 2014. 10 - non-destructive testing (NDT) of natural fibre composites: acoustic emission technique. In: Hofzic, A., Shanks, R. (Eds.), *Natural Fibre Composites*. Woodhead Publishing, pp. 273–302.
- Schneider, H., 1984. The nondestructive testing of tubes and pipes for nuclear application. *Nucl. Eng. Des.* 1 (81), 69–76.
- Tchakoua, P., Wankoue, R., Ouhrouche, M., Slaoui-Hannoui, F., Tameghe, T., Ekemb, G., 2014. Wind turbine condition monitoring: state-of-the-art review, new trends, and future challenges. *Energies* 7 (4), 2595–2630. <https://doi.org/10.3390/en7042595>.
- Tesauro, A., Pavese, C., Branner, K., 2014. Rotor Blade Online Monitoring and Fault Diagnosis Technology Research. Report vol. DTU Wind Energy E, No. 0042. DTU Wind Energy [Online]. Available: www.orbit.dtu.dk.
- Vavilov, V.P., Budadin, O.N., Kulkov, A.A., 2015. Infrared thermographic evaluation of large composite grid parts subjected to axial loading. *Polym. Test.* 41, 55–62 no. 0.
- Vavilov, V.P., Plesovskikh, A.V., Chulkov, A.O., Nesteruk, D.A., 2015. A complex approach to the development of the method and equipment for thermal nondestructive testing of CFRP cylindrical parts. *Compos. B Eng.* 68, 375–384.
- Venkataraman, B., 2001. NDT as a Support for Materials Processing and Manufacturing." *Encyclopedia of Materials: Science and Technology*, second ed. Elsevier, Oxford, pp. 5959–5963.
- Xiaona Li, R.L., Wang, Mengyu, Liu, Yaru, Zhang*, Baohua, Zhou, Jun, 2017. Hyperspectral imaging and their applications in the nondestructive quality assessment of fruits and vegetables. *Hyperspectral Imaging in Agriculture, Food and Environment*. <https://doi.org/10.5772/intechopen.72250>. December 20th 2017.
- Xie, C., 2009. Research of AE signal processing methods [J]. *China science and technology information* 5, 131–132.
- Yang, R., He, Y., Zhang, H., 2016. Progress and trends in nondestructive testing and evaluation for wind turbine composite blade. *Renew. Sustain. Energy Rev.* 60, 1225–1250. <https://doi.org/10.1016/j.rser.2016.02.026>.
- Yang, S.-H., Kim, K.-B., Oh, H.G., Kang, J.-S., 2013. Non-contact detection of impact damage in CFRP composites using millimeter-wave reflection and considering carbon fiber direction. *NDT E Int.* 57, 45–51 no. 0.
- Ying Shi, C.C., 2010. Study on A new method for condition monitoring of the large-scale wind turbine blades. In: 12th National Conference Proceedings of Fault Diagnosis.
- Young, A., Kay, A., Marshall, S., Torr, R., Gray, A., 2016. Hyperspectral imaging for erosion detection in wind turbine blades. In: HSI 2016, England.
- Yu, Y., Cao, H., Liu, S., Yang, S., Bai, R., 2017. Image-based damage recognition of wind turbine blades. In: 2017 2nd International Conference on Advanced Robotics and Mechatronics (ICARM), 27–31 Aug. 2017, pp. 161–166. <https://doi.org/10.1109/ICARM.2017.8273153>.
- Yuan S, L.D., Shi, L., et al., 2008. Recent progress on distributed structural health monitoring research at NUAU. *J. Intell. Mater. Syst. Struct.* 19, 373–386.
- Zhang B, H.W., Li, J., Zhao, C., Fan, S., Wu, J., Liu, C., 2014. Principles, developments and applications of computer vision for external quality inspection of fruits and vegetables: a review. *Food Res. Int.* 62, 326–343.
- Zhang, B., et al., 2014. Principles, developments and applications of computer vision for external quality inspection of fruits and vegetables: a review. *Food Res. Int.* 62, 326–343.
- Zhao, G., et al., 06/29 2007. Active health monitoring of an aircraft wing with embedded piezoelectric sensor/actuator network: I. Defect detection, localization and growth monitoring. *Smart Mater. Struct.* 16, 1208. <https://doi.org/10.1088/0964-1726/16/4/032>.
- Zhao, G., et al., 08/01 2007. Active health monitoring of an aircraft wing with an embedded piezoelectric sensor/actuator network: II. Wireless approaches. *Smart Mater. Struct.* 16, 1218–1225. <https://doi.org/10.1088/0964-1726/16/4/033>.
- Zhongkui Zhu, Z.C., Wang, Chunyang, 2005. Bearing transient feature detection and extraction based on reassigned scalogram [J]. *J. Data Acquis. Process.* 3 (20), 356–360.
- Zhou, J., Kwan, C., Ayhan, B., Eismann, M.T., 2016. A novel cluster kernel RX algorithm for anomaly and change detection using hyperspectral images. *IEEE Trans. Geosci. Rem. Sens.* 54 (11), 6497–6504. <https://doi.org/10.1109/TGRS.2016.2585495>.

APPENDIX IV
WIND TURBINE ICE DETECTION USING HYPERSPECTRAL
IMAGING

Publié dans Remote Sensing Applications: Society and Environment – ELSEVIER

Volume 26, April 2022

Citation:

P. Rizk, R. Younes, A. Ilinca, and J. Khoder, "Wind turbine ice detection using hyperspectral imaging," Remote Sensing Applications: Society and Environment, vol. 26, p. 100711, 2022/04/01/ 2022, doi: <https://doi.org/10.1016/j.rsase.2022.100711>.

Résumé:

Cet article offre un aperçu des technologies de détection du givrage et explore les applications de l'imagerie par spectroscopie pour la détection de l'accrétion de givre dans les parcs éoliens. Cette étude décrit l'application de la technique d'imagerie hyperspectrale (HSI) dans la télédétection du givrage incident sur une pale d'éolienne. Cet article décrit l'approche expérimentale menée sur un échantillon de pale avec une partie couverte de glace. Le modèle de givrage, sur lequel cette méthode de détection est basée, est conçu, simulé et confirmé pour acquérir une meilleure connaissance du givrage de la pale. Cette technologie a démontré un grand potentiel pour repérer le givrage aux premiers stades de son accumulation, quels que soient son épaisseur et son type. Les résultats expérimentaux de cette technique révèlent que l'exactitude et la précision de la détection du givrage des pales sont considérablement améliorées. Cette étude indique que l'imagerie spectroscopique et l'évaluation à distance sur le terrain peuvent détecter les événements de givrage avec une résolution, une précision et une discrimination élevées. Il s'agit d'un outil non invasif et fiable pour identifier les variations entre les surfaces givrées et les surfaces propres, ce qui confère une puissante

capacité de surveillance, notamment pour la détection précoce des événements de givrage. La surveillance à distance par HSI des pales d'éoliennes pour la détection du givrage peut être un outil utile [271].



Contents lists available at ScienceDirect

Remote Sensing Applications: Society and Environment

journal homepage: www.elsevier.com/locate/rsase

Wind turbine ice detection using hyperspectral imaging

Patrick Rizk^{a,b,c,*}, Rafic Younes^c, Adrian Ilinca^a, Jihan Khoder^d^a Wind Energy Research Laboratory (WERL), Université du Québec à Rimouski, 300 allée des Ursulines, Rimouski, QC, G5L3A1, Canada^b Doctoral School of Science and Technology (EDST), Lebanese University, Beirut, Lebanon^c Faculty of Engineering, Third Branch, Lebanese University, Rafic Hariri Campus, Hadath, Beirut, Lebanon^d LISV Laboratory, University of Versailles Saint-Quentin-en-Yvelines, 10-12 Avenue de l'Europe, 78140, Velizy, France

ARTICLE INFO

Index Terms:

Wind turbine blade
Hyperspectral imaging
Ice detection
Icing

ABSTRACT

Wind energy has been playing a pivot role in replacing the traditional energy sources. This emerging paradigm has proved itself as a good candidate among all renewable energy sources. Although the exponential growth of the wind industry, wind turbines still suffer from blade icing especially in cold regions. Blade icing disturbs aerodynamic performance and results in power losses, safety risks, mechanical and electrical breakdowns, measurement, and control faults. Anti-icing and de-icing techniques mitigate these adverse effects. It is mandatory to rigorously evaluate the meteorological operating conditions during the assessment phase to determine the need and advantages of installing an anti-icing or a de-icing system. Moreover, this diagnostic is also essential during the operation to detect icing, prevent failure, and enhance production. Different ice detection methods, such as double anemometry, vane, relative humidity, and dew point, are used. These techniques have few drawbacks that can be overcome using hyperspectral imaging. This paper offers an overview of icing detection technologies and explores spectroscopy imaging applications for detecting ice accretion in wind farms. This study describes the application of this non-destructive and fast monitoring technique in remote sensing of icing incident on a wind turbine blade. This paper outlines the experimental approach conducted on a blade sample with an ice-covered portion. The icing model, on which this detection method is based, is designed, simulated, and confirmed to acquire enhanced blade icing knowledge. The hyperspectral imaging validation results for icing occurrence detection in their initial development phases are satisfactory. The experimental findings of this technique reveal that the accuracy and precision of blade icing detection are considerably enhanced.

1. Introduction

Wind energy is one of the fastest-growing renewable energy (Jaeger, 2021; Gómez Muñoz et al., 2016). Wind farms are often located in high-altitude sites (Carlsson, 2010; Fortin and Ilinca, 2005) where each 100 m elevation corresponds to an average wind speed increase of 0.1 m/s (Parent and Ilinca, 2011; Kim et al., 2017). Recent studies show that 20% of wind farms are located in areas with a high icing likelihood (Gómez Muñoz et al., 2016; Barati-Boldaji and Komareji, 2017; Tammelin et al., 2000). However, during winter in cold high-altitude regions, icing events are negatively affecting the performance of the wind turbines (Parent and Ilinca, 2011) resulting in mechanical and electrical breakdowns (Ilinca, 2011), and power production losses (Tammelin et al., 2000; Shajiee et al., 2013; Pliego Marugán and Pinar Pérez, 2016). For instance, for a total installed power of 682 MW produced by 517 wind

* Corresponding author. Wind Energy Research Laboratory (WERL), Université du Québec à Rimouski, 300 allée des Ursulines, Rimouski, QC, G5L3A1, Canada.
E-mail address: patrickr17@gmail.com (P. Rizk).

<https://doi.org/10.1016/j.rsase.2022.100711>

Received 29 October 2021; Received in revised form 3 January 2022; Accepted 13 February 2022

Available online 16 February 2022

2352-9385/© 2022 Elsevier B.V. All rights reserved.

turbines, icing accretion on wind turbine blades leads to a power loss of 18,966 MWh in 29 months (Márquez et al., 2018).

Furthermore, these energy losses increase the operating and maintenance costs (Gómez Muñoz et al., 2016). Anti-icing and de-icing systems reduce these consequences (Ilinca, 2011). There are many methods described in the literature for icing detection on wind turbines: the double anemometry with relative humidity observations during the assessment phase, ice sensors and the power curve method during the operation phase (Kabardinet al., 2021). However, none of the methods is reliable and accurate. Each one gives a different result of icing detection, which is affected mainly by the freezing precipitation and in-cloud icing (Marjanemiet al., 2000; Liu et al., 2019). However, these deficiencies can be overcome by using hyperspectral imaging technology. This technology is one of the remote sensing techniques that combines ordinary imagery and spectral imaging to obtain spatial and spectral information about an inspected feature. This specification generates a spectral signature or a fingerprint, which is later employed in the detection procedure (Ahmed et al., 2019). Nevertheless, hyperspectral imaging has demonstrated strong promise in different target detection disciplines, including fault identification on wind turbine blades (Rizk et al., 2020a), sea ice detection (Han et al., 2017), and many other forensic investigations that require a high precision and accuracy (Zulfiqar et al., 2021; Melit Devassy and George, 2021). In this paper, we present a comparison of the existing ice detection techniques and propose a hyperspectral imaging application in remote sensing of icing events on wind turbine blades. Section 2 shows the effects of ice accumulation on wind turbines, whereas section 3 defines the different types of atmospheric icing. A review of ice detection methods is detailed in section 4. Section 5 describes the experiment performed on a Glass Fiber Reinforced Plastic (GFRP) blade sample to detect the ice layer of different thicknesses. Section 6 discusses the experimental results. Finally, section 7 concludes with a synopsis of the discussed work and illustrates our vision on the promise of the hyperspectral imaging technique and its advantages in detecting ice accretion.

2. Impacts of ice accretion on wind turbines

In cold regions, wind turbine blades are susceptible to icing events disturbing their aerodynamic performance. Icing events occur during both the wind assessment and the operating phases (Parent and Ilinca, 2011). These adverse effects include power losses (Chen et al., 2019; Qiang et al., 2016), safety risks (Abdel-Moati et al., 2018), mechanical and electrical breakdowns (Madi et al., 2019), and measurement and control faults (Niemann et al., 2018; Szwedo and Hellstein, 2014; Yang et al., 2016).

2.1. Power losses

Small quantities of ice accretion on a wind turbine blade's surface can diminish its aerodynamic properties by varying the blade's shape and roughness (Marjanemi and Peltola, 1998). Consequently, the incurred power loss varies mainly with the applied detection technique, the intensity, and the duration of the icing, with a range from 0.005 to 50% of the annual production (Botta et al., 1998; Gillenwater, 2008; Tammelin et al., 2005).

2.2. Safety risk

For a site with moderate icing events, having an average of 5 days of icing per year, the probability of being thrown by a mass of ice varying between 0.18 and 0.36 kg is 0.1. This value is determined by the Monte-Carlo simulation executed by Battisti et al. (Battisti et al., 2005) and valid for a person on the site during 10 h of the turbine's operation subjected to the de-icing system. The estimated daily ice accretion is 75 kg per rotor. The radial distance around any turbine that can be susceptible to this safety hazard is one and a half of the combined rotor diameter and the turbine's height (Tammelin et al., 2000).

2.3. Mechanical and electrical breakdowns

Ice accretion affects the mechanical and electrical elements of the wind turbine. With the accreted ice on the blades, the mechanical load increases and causes a mass imbalance that may lead to dangerous vibrations. Furthermore, variations in oil viscosity and condensation in the wind turbine's electronics occur during operation in low temperatures (Botta et al., 1998; Seifert, 2003).

2.4. Measurement and control faults

During icing events, the anemometers can face faults and errors in measuring wind speed that can be as high as 30% (Laaksoet al., 2003) and can reach 40% for an ice-free anemometer and 60% for a standard anemometer (Fortin and Ilinca, 2005). Furthermore, the wind vanes subjected to icing can lead to a misleading wind direction. In addition, temperature sensors can also be affected and lead to wrong measurements (Parent and Ilinca, 2011).

Table 1
Types of ice.

Type	Description
Precipitation	Precipitation icing occurs as freezing rain when rainfall drops on a surface having a temperature below 0°C and as wet snow when slightly liquid snow falls on a surface with an air temperature between 0°C and -3°C (Boluk, 1996).
In cloud icing	In-cloud icing occurs when water droplets at very low temperatures, sometimes as low as -30°C, touch a surface below 0°C and freeze (Fikloet al., 2006). The form of ice accretion varies from rime at lowest temperatures to glaze at highest (IGO-12494, 2001).
Frost	Frost occurs when water vapor deposits on a cool surface and hardens upon impact (Boluk, 1996; Richert, 1996).

3. Types of ice

The most frequent types of atmospheric icing on a wind turbine are precipitation, in-cloud, and frost (Parent and Ilinca, 2011). Table 1 presents a definition of icing types.

4. Icing detection survey

Ice accretion on solid surfaces is measured using three approaches. The first method reveals the variations in physical properties such as mass, inductance, thermal conductivity, etc. Indirect measurements identify meteorological conditions resulting in icing, such as a combination of wind speed, humidity, and temperature. A decrease in power production or other icing effects is also an indirect method (Parent and Ilinca, 2011). In comparison, a numerical approach uses an empirical model that determines the duration and severity of icing situations (Homola et al., 2006).

4.1. Icing detection during the site assessment stage

The study of icing events during wind assessment aims to evaluate the need and financial feasibility of installing a de-icing or anti-icing solution on wind turbines. To do that, the severity and duration of icing events and the potential wind energy loss should be determined (Laakso et al., 2003). The turbine's geometry and operation are integrated with the observed weather conditions related to icing events (wind speed, humidity, liquid water content, temperature, pressure, etc.) to predict production losses (Parent and Ilinca, 2011). The measurements of these meteorological parameters are costly or unreliable. Furthermore, icing duration is empirically calculated (Kimura et al., 2000), and its severity is barely ever accessible (Battisti et al., 2005). We should also note that the icing events should be evaluated reliably at the same elevation of the top blade tip (Homola et al., 2006) in the intended implementation site (Fikke et al., 2006) with a radial distance from the turbine of 1 km (Laakso et al., 2003).

The following subsections describe the icing evaluation methods during the site assessment phase.

4.1.1. Double anemometry and vane

Icing events can be detected using heated and unheated anemometers when the measured wind velocities' difference exceeds 5% (Laakso et al., 2003) and sometimes can achieve 20% for values above 2 m/s (Tallhaug, 2003). This method is cheap, can depict the ice climate and its persistency (Laakso et al., 2003), and reliable at temperatures around 0°C (Craig, 1996). Craig proposes using a permanently heated anemometer, an unheated anemometer, and a second heated anemometer (Craig, 1996). This latter serves when a 15% difference in wind speeds is measured using the first two anemometers. With the relative humidity measurements, these methods can determine the icing event duration that will affect the blade's performance (Laakso et al., 2005) by correlating it to the duration of ice disturbance of the unheated anemometer (Laakso et al., 2003), which is longer than the real icing period. The main drawback of the double anemometry is the difference in elevation between the anemometers and the blade's tip, where icing is most severe (Tammelin et al., 2005). Another issue is the false indication of icing provided by the unheated anemometer and caused by low temperatures (Laakso et al., 2003), as this equipment displays both higher and lower wind velocities. Furthermore, at zero speed wind, no indication can be provided (Seifert, 2003). During snowfalls, at low wind speeds, the inertial characteristics can affect the measurements and provide misleading results.

Tallhaug suggests calculating the standard deviation of an unheated wind vane, at temperatures below zero, from 6 succeeding 10-min averages to state the occurrence of an icing event (Parent and Ilinca, 2011).

4.1.2. Ice sensors

The ice sensors use different physical characteristics to detect ice accretion: vibrating probes, longitudinal wire waves, ice mass measurement method (ISO-12494, 2001) and others (Tammelin et al., 2005; Fikke et al., 2005). However, they are either costly or inaccurate, unreliable, and asynchronous with the real icing event (Tammelin et al., 2005). Sometimes, ice sensors undervalue the icing conditions due to the heating cycle. For that, a heated detector should serve to determine the severity of an icing event and an unheated one to define its duration (Parent and Ilinca, 2011; Tammelin et al., 2005).

4.1.3. Visibility and cloud base

In-cloud icing occurs on an object immersed in a cloud at a wind speed of 2 m/s approximately and a temperature less than 0°C. The horizontal visibility or the cloud base height via airport observation, video monitoring, a pyranometer or automatic sensors serve to identify the cloud presence.

When the cloudiness index measured by the airport observation is higher than 6/8, and the wind turbine is higher than the cloud base altitude, ice accretion occurs, and its intensity can be measured using this index (Tallhaug, 2003). Furthermore, cloud density can be numerically determined by video monitoring using tinted poles far from the met mast of 50 m–300 m (Dobesch et al., 2003). Simultaneously, a pyranometer can detect icing when its solar radiation intensity measurement is less than 300 W/m² (Kimura et al., 2000). Lastly, radar and microwave radiometers can fastly estimate the liquid water content and automatically detect icing events (Battisti et al., 2005).

However, this method is very costly and underestimates the real ice accretion (Tammelin et al., 2005).

4.1.4. Relative humidity and dew point

Ice events occur at a humidity above 95% and a temperature below 0°C. Furthermore, they can also be predicted using a dew point detector (Laakso et al., 2005). The use of a humidity sensor is more common, but icing conditions are not detected simultaneously with the ice detectors, and thus, the expectedness of icing events is low (Parent and Ilinca, 2011; Tammelin et al., 2005).

4.1.5. Models

Icing events can be detected using physical mesoscale and statistical models that consider further information such as temperature, wind speed and direction, cloud cover, and height. The frequency and rate of icing can be determined using this method (Parent and Ilinca, 2011; Laakso et al., 2003).

4.1.6. Other methods

Icing events can be detected visually by video filming of guy wires, and ice thickness is correlated with wire vibration. This method's results can be improved using the airport observations of the cloud base (Harstveit et al., 2005). Furthermore, icing conditions are identified by examining damages as the failure of power lines or climatic poles due to resonance or buckling (Parent and Ilinca, 2011; Seifert, 2003).

4.1.7. Recommendations on methods

Freezing precipitation and in-cloud icing are the events detected by the various ice detection methods. However, none of these methods are always reliable and accurate (Marjanemi et al., 2000). It is recommended to evaluate icing events during the assessment phase for a minimum of one year. Two or more methods should be used simultaneously to improve the icing event detection accuracy. None of the individual techniques show preeminence on others, and each one of them is appropriate for specific weather and determination (Tammelin et al., 2005). For instance, an ice detector could be used with the onsite weather indications. The ice severity affects the production losses, whereas the duration of icing events affects the required heating energy. These indications should be measured via different devices (Parent and Ilinca, 2011).

One heated and one unheated anemometer should be installed on the measuring mast to estimate icing events inexpensively. Chronological cloud base height results should be compared to the nearest airport observations. In addition, a dew point detector intended for the subzero temperatures could help detect the occurrence of in-cloud icing events (Laakso et al., 2005).

4.2. Icing detection during the operation stage

An optimized blade heating system is significantly related to an excellent controlling ice detector (Makkonen et al., 2001) that spots ice at its accretion start (Tammelin and Säänti, 1994), thereby preventing power production losses that can sometimes attain 15% (Peltola et al., 1996). Although blade de-icing techniques operated successfully, the ice sensors cannot consistently spot the beginning of icing events (Homola et al., 2006). Moreover, ice detection on the blade tip requires locating a high sensitivity sensor carefully. It should be able to spot icing at different points on the blade (Parent and Ilinca, 2011). Some of the methods that respect these requirements are presented in the following sub-sections.

4.2.1. Multiple anemometry

This method is similar to the one presented in detail in the assessment section. Its main drawback is the difference in elevation among the highest possible point by the anemometer, the nacelle roof, and the blade tip, the most exposed surface to icing. This makes the detection of all in-cloud icing events more difficult. Furthermore, the turbine wake effect should be considered to prevent misleading results (Marjanemi et al., 2000).

4.2.2. Ice detectors

It is the same method described in the assessment section and most used in anti-icing and de-icing system controlling. The heated detector measures the severity of icing, whereas the unheated one measures the icing's duration (Tammelin et al., 2005). However, slight ice masses cannot be instantly detected (Laakso et al., 2003).

4.2.3. Video monitoring

A webcam placed in the hub, filming the rotor blade's pressure side, can detect icing by correlation with other ice detection techniques. This method's main drawback is that it is costly, requires non-stop monitoring, and depends on the controller's visibility (Seifert, 2003). Thus, it can be appropriate for a short duration of detection (Homola et al., 2006).

4.2.4. Power curve

Continuous monitoring and comparison between calculated and actual production power curve with temperature and air pressure measurements can detect icing events for stall regulated wind turbines, with a power decrease of 50% as a reference (Tammelin et al., 2005). A difference between the calculated production power curve, indicated by the anemometer, and the actual production power curve (Laakso et al., 2003), can occur for reasons other than icing (Homola et al., 2006). A correlation with meteorological data and other detection methods should eliminate these possibilities.

4.2.5. Vibration and noise

Vibration sensors can be linked to the de-icing control system to detect the unusual high vibrations (Laakso et al., 2005). After that, the blade starts heating at the onset of turning off the turbine (Tammelin et al., 2005). Small masses of ice can result in aerodynamic noise increase at higher frequency ranges (Seifert, 2003). Furthermore, more studies are needed to determine how these results are affected by other factors as wind velocities and background noises (Parent and Ilinca, 2011). Along with the stall operation, these two methods cannot detect icing accurately (Tammelin et al., 2005).

4.2.6. Recommendations on methods

To summarize the study results by Homola et al. (2006), none of the 29 tested icing detection methods always show reliable results

(Homola et al., 2006). The main issue that limits the methods' application is that the equipment used, such as the double anemometry and ice collecting cylinders, is mounted on the turbine's nacelle, not on the blade tip. The most suitable methods for icing detection on a wind turbine are installing ice sensors near the blade tip: an internal ultrasound, a capacitance, impedance or inductance-based sensor, infrared spectroscopy via fiber optic wires or a flexible resonating diaphragm (Parent and Ilina, 2011).

5. Materials and methods

5.1. Sensor selection

After this review of available ice detection techniques, the hyperspectral imaging technology (HSI) offers some advantages that may reduce some of the other systems' limitations. This work aims to introduce the hyperspectral imaging technique into the world of blade inspection methods. The fundamental concept of HSI is that radiance reaching every pixel is fractured into very many narrow adjacent wavelengths (Makki et al., 2018; Rizk et al., 2020b). These spectral bands constitute the spectral signature of the scanned object. HSI provides both spatial and spectral information, which create a three-dimensional data cube, identified as "hypercube data" or as an "image cube" (Vasefi et al., 2016; Rizk et al., 2021). As stated, each material or object has its signature, which is used in detection and classification processes. Ice detection using HSI depends on the difference in spectral signatures between the accreted ice and the normal blade surface. For this application, the ice and the blade surface will mutually radiate and reflect energy at distinct ratios, giving a difference in each type of material's reflectance. Thus, the spectral range needed must cover the bandwidth from 300 to

Table 2
Hyperspectral sensors used.

Hyperspectral sensor	Spectral range	Spectral resolution
 Micro series	340–840 nm	3 nm
 MS series	640–1050 nm	3 nm
 TF series	950–1700 nm	3 nm

1700 nm. For this purpose, a combination of three hyperspectral sensors is used to cover the necessary bandwidth. In addition, all these sensors are optical spectrometers with a spectral resolution of 3 nm, but each has its spectral region. The three sensors cover 340–840 nm, 640–1050 nm, and 950–1700 nm respectively, and they are presented in Table 2 below.

5.2. Experimental setup

The glass fiber reinforced plastic (GFRP) wind turbine blade sample, shown in Fig. 1, is 53.0 cm long, 34.5 cm wide and 4.0 cm thick.

Cold water is sprayed on the surface of the sample to accrete ice, as shown in Fig. 2. The sample is placed in a freezer at a temperature of -25°C . The operation is performed in different steps to obtain the required thickness (0.5 mm, 0.7 mm, 4 mm, and 7 mm). The ice-covered surface constitutes 15 cm in length from the right corner of the blade specimen of Fig. 2.

Each of the samples, the normal blade, and the surface where different ice thicknesses have accreted (0.5 mm, 0.7 mm, 4 mm, and 7 mm) is scanned pixel per pixel using the hyperspectral sensors, one after another. Each data cube of information created in the process is analyzed to determine the ability to detect ice accretion features.

5.3. Methodology

This experiment aims to characterize ice accretion on a blade sample using the hyperspectral sensors. Thus, before scanning the sample, two main signals must be taken: the dark and white reference signals. These signals serve for calibration and to build a normalized image. Then, the sample blade is scanned with the same sensors for the acquisition of the hyperspectral image. This hyperspectral image is normalized for ice detection. It is done using the hyperspectral image (HI), the dark reference image (D) and the white reference image (W), following this relation:

$$HI_n = \frac{HI - D}{W - D} \quad \text{Equation 1}$$

where, HI_n is the calibrated normalized hyperspectral image.

After the normalization, the data cube is fed into the hyperACE algorithm, based on the adaptive cosine/coherent estimator algorithm is used in the detection process (Broadwater and Chellappa, 2007; Zhang et al., 2010). Then, we investigate the smallest bandwidth range that acquires the highest probability of icing detection. As end-to-end spectral bands are strongly related in the hyperspectral images, we reduce the volume of the processed data by removing the redundant information while preserving the rare event (Khoder et al., 2017; Rizk et al., 2019). We use the multicriteria classification and net analyte signal (NAS) techniques to perform this task. Multicriteria classification serves to remove highly similar images while preserving on the rare event within the scanned scene whilst maintaining an optimum band reduction (Khoder et al., 2017). The remaining ones are subjected to the NAS which holds a critical role in processing the figures of interest in a calibrated model's characterization. Also, it a section of the analyte gamut that is special to that analyte (Grahn and Geladi, 2007). Thus, NAS is an effective algorithm for determining a signal's figures of merit. Later on, these figures of merit are utilized to evaluate different models to find the optimum bandwidth (Bro and Andersen, 2003).

6. Results

After scanning the blade specimen using hyperspectral sensors in a whiskbroom mode, a snapshot of the specimen is obtained at each step. Using this approach, we were able to generate a hyperspectral cube of the tested blade. The section goes through the HSI scanning results in depth.

6.1. Ice fault signature retrieval

As mentioned in the previous section, the ice covers an area with a length of 15 cm on one side of the blade along its width, as shown in Fig. 3. The studied thickness of the ice, as cited before, is represented in Fig. 4. In order to retrieve the spectral signature of these different thicknesses, each case was retrieved on its own and added to the spectral signature library to be used later in the detection process.

The spectral signature of the desired thickness is derived solely based on scanning at one spot. The following figures present the normal blade spectral signature in blue versus the ice spectrum in red color, for different thicknesses. The ice thickness in Figs. 5–8 is 0.5 mm, 0.7 mm, 4.0 mm and 7.0 mm. In Figs. 5 and 6, the two signals almost overlapped for the wavelengths ranged between 400 and



Fig. 1. Blade sample.



Fig. 2. Ice accretion on blade sample.



Fig. 3. Ice on specimen.



Fig. 4. Zoom in on the ice blade sample in the studied cases.

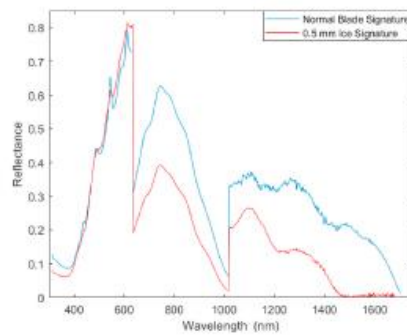


Fig. 5. The spectrum of 0.5 mm ice thickness versus clean blade signature.

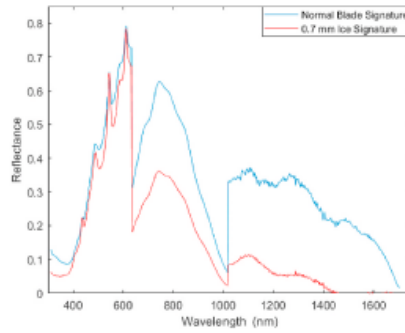


Fig. 6. The spectrum of 0.7 mm ice thickness versus clean blade signature.

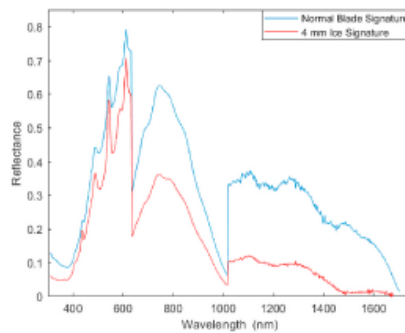


Fig. 7. The spectrum of 4.0 mm ice thickness versus clean blade signature.

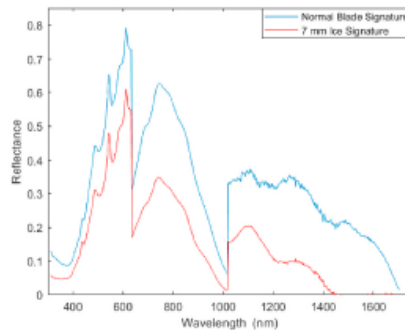


Fig. 8. The spectrum of 7.0 mm ice thickness versus clean blade signature.

600 nm. Starting from around 600 nm, the ice reflectance is lower than the clean blade signature reflectance and becomes zero at approximately 1450 nm. At about 600 nm, the ice reflectance is 0.2, and the clean one is almost 0.3.

Furthermore, we can notice that the peaks in signatures have the same wavelength. In other words, the shape of the graphs is similar for the clean and the iced blade. We observe similar behavior for the results in Fig. 7. Still, the ice reflectance becomes zero at approximately 1500 nm and then increases slightly to a reflectance of about 0.01 and decreases again to zero at 1700 nm. We should note that at zero reflectance, we have a total ice absorption of emitted light.

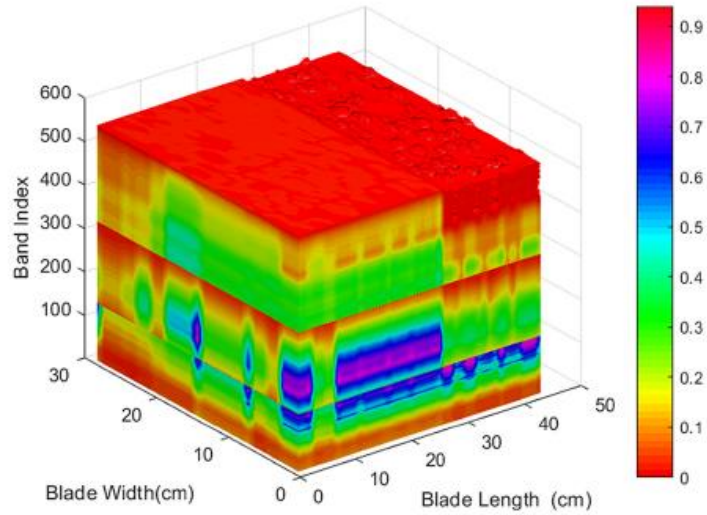


Fig. 9. 3D blade image.

6.2. 3D Image acquisition

After performing the scanning and calibration stages described in the previous section (Section 5.3. Methodology), the result shown in Fig. 9 is a scanned blade image having 29 by 44 pixels over 542 bands. This data cube presents the blade specimen over 542 layers of different frequencies. The reflectance increases according to the color scale in the figure. We notice, confirming the previous section’s conclusion, that ice reflectance at each band index is lower than the normal reflectance of the clean blade, where icing is accreted over a length of 15 cm at one side of the blade along its width.

6.3. Full-spectrum ice detection

The hyperimage consisting of 542 bands, shown in Fig. 9, is fed into the detection algorithm. The hyperACE algorithm shows an ice probability detection of 100% and a false alarm rate of 0%. These results are visualized in 2D in Fig. 10 and in 3D in Fig. 11.

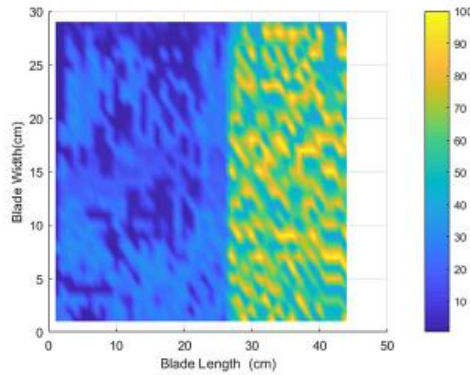


Fig. 10. 2D illustration of ice detection.

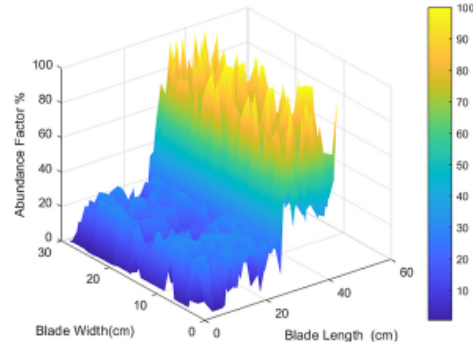


Fig. 11. 3D Illustration of ice detection.

Figs. 10 and 11 show the probability of detection for the region where ice is accreted, for the different thicknesses mentioned. These two figures depict a color scale representation, with yellow representing a full detection and blue representing no detection. In a 2D and 3D representation of the wind turbine blade sample, the icing abundance factor, where the ice is identified, is displayed. The uniced areas are shown in blue, while the ice-covered portions are shown in yellow. By means, as the thickness increases as the color approaches to yellow according to the scale.

6.4. Spectrum reduction

Transforming the "hyper image" through multicriteria classification, we reduce the number of bands from 542 to 134. In other words, 134 bands are enough to detect the ice accumulation while maintaining the rare event in the resulted scene. These bands are from 354 to 636 nm, 740 nm, 776 nm, 824 nm, 992 nm, 1020 nm, from 1400 to 1450 nm, 1474, 1500 nm, from 1670 to 1675 nm. However, bypassing the "data cube" through Net Analyte Signal, with a 90% reduction, the number of bands is reduced to 55 while sustaining a 100% of ice detection. These bands are from 706 to 822 nm.

After combining the multicriteria classification and the Net Analyte Signal, 160 bands remained after a 70% reduction for 100% of ice detection. These bands are from 360 to 636 nm, from 726 to 784 nm, 824 nm, 991 nm, 1020 nm, 1400–1500 nm, 1670 nm, and 1676 nm.

We can notice that the Net Analyte Signal makes the most considerable reduction, but this reduction is made at different stages, as shown in Table 3.

Nevertheless, the multicriteria classification reduces the number of bands at once. Furthermore, the combined result provides a higher number of reduced bands, which can help prevent the loss of the rare elements that are not representative of the ice detection points.

Table 3
Summary of net analyte signal results.

Percentage of Reduction	Number of Bands	Ice	
		Pd	FAR
95%	28	88.47%	11.53%
90%	55	100.00%	0.00%
80%	109	100.00%	0.00%
70%	163	100.00%	0.00%
60%	217	100.00%	0.00%
50%	271	100.00%	0.00%
40%	326	100.00%	0.00%
30%	380	100.00%	0.00%
20%	434	100.00%	0.00%
10%	488	100.00%	0.00%

7. Conclusion

After describing some conventional methods used for ice accretion detection on wind turbine blades, this paper proposes the hyperspectral imaging (HSI) technique, which has been rapidly evolving and broadly applied in many non-destructive diagnostics. This technology demonstrated a great potential for spotting icing at its early stages of accumulation regardless of its thickness and type. This study indicates that spectroscopy imaging and remote on-field assessment can detect icing events with high resolution, precision, and discrimination. It is a non-invasive and reliable tool for identifying variations between iced and clean surfaces, thus granting powerful monitoring capacity, especially in the early detection of icing events. The HSI remote monitoring of wind turbine blades for icing detection can be a useful tool. It could robustly and accurately measure and identify the ice at a thickness of 0.1 mm at its early formation stage. Thus, HSI is the upcoming ice detection module of wind turbine blades, which can offer a lower inspection shutdown time and lower maintenance costs by supplying simple routine inspection of the wind turbine blade. As for future applications, HSI can also serve for the non-destructive monitoring of wind turbine blades.

Author statement

Patrick Rizk: Conceptualization, Investigation, Methodology, Software, Validation, Formal Analysis, Investigation, Data Curation, Writing – Original Draft, Writing – Review & Editing, Visualization, Rafic Younes: Conceptualization, Methodology, Validation, Resources, Writing – Review & Editing, Supervision, Project administration, Funding acquisition, Adrian Ilinca: Conceptualization, Methodology, Validation, Writing – Review & Editing, Supervision, Project administration, Funding acquisition, Jihan Khoder: Resources, Writing – Review & Editing, Supervision, Project administration.

Ethical statement for Remote Sensing Applications: Society and Environment

I testify on behalf of all co-authors that our article submitted to Remote Sensing Applications: Society and Environment:

- 1) this material has not been published in whole or in part elsewhere.
- 2) the manuscript is not currently being considered for publication in another journal.
- 3) all authors have been personally and actively involved in substantive work leading to the manuscript and will hold themselves jointly and individually responsible for its content.

Declaration of competing interest

The authors declare that they have no known competing financial interests or personal relationships that could have appeared to influence the work reported in this paper.

Acknowledgement

The authors acknowledge the financial support from NSERC (Canada) and Azm & Saade Association through a research grant.

References

- Abdel-Mostaf, H., Morris, J., Zeng, Y., Corie, M.W., Yanni, V.G., 2018. Near field ice detection using infrared based optical imaging technology. *Opt Laser. Technol.* **99**, 402–410. <https://doi.org/10.1016/j.optlastec.2017.09.029>.
- Ahmed, A.M., Ibrahim, S.K., Yacout, S., 2019. Hyperspectral image classification based on logical analysis of data. In: 2019 IEEE Aerospace Conference, 2–9 March 2019, pp. 1–9. <https://doi.org/10.1109/AERO.2019.8742023>.
- Barati-Boldaji, R., Komareji, M., 2017. Techniques of identifying icing and de-icing of wind turbines. *Signal Process. Renew. Energy* **8**, 21–28, 12/01.
- Battisti, L., Brighenti, A., Dal Savio, S., Dell'Anna, S., 2005. Evaluation of Anti-icing Energy and Power Requirement for Wind Turbine Rotors in Cold Climates," BOREAS VII. FMI, Saariselkä, Finland, p. 13.
- Battisti, L., Pedrini, R., Dell'Anna, S., Rialdi, M., 2005. Ice Risk Assessment for Wind Turbine Rotors Equipped with De-icing Systems," BOREAS VII. FMI, Saariselkä, Finland, p. 11.
- Boluk, Y., 1996. Adhesion of Freezing Precipitates to Aircraft Surfaces. Transport Canada, p. 44.
- Botta, G., Cavaliere, M., Holtinen, H., 1998. Ice Accretion at Acqua Spruzza and its Effects on Wind Turbine Operation and Loss of Energy Production," BOREAS IV. FMI, Hetta, Finland, pp. 77–86.
- Bro, R., Andersen, C.M., 2003. Theory of Net Analyte Signal Vectors in Inverse Regression, **17**, pp. 646–652, 12.
- Broadwater, J., Chellappa, R., 2007. Hybrid Detectors for Subpixel Targets, **11**, pp. 1891–1903, 29.
- Carlsson, V., 2010. Measuring Routines of Ice Accretion for Wind Turbine Applications: the Correlation of Production Losses and Detection of Ice.
- Chen, X., Lei, D., Xu, G., 2019. Prediction of icing fault of wind turbine blades based on deep learning. In: 2019 IEEE 2nd International Conference on Automation, Electronics and Electrical Engineering (AUTEEE), 22–24 Nov. 2019, pp. 295–299. <https://doi.org/10.1109/AUTEEE46671.2019.9033143>.
- Craig, D., 1996. An Investigation of Icing Events on Haeskel Hill," BOREAS III. FMI, Saariselkä, Finland, pp. 169–193.
- Dobesch, H., Zach, S., Tran, H.V., 2003. A New Map of Icing Potentials in Europe — Problems and Results," BOREAS VI. FMI, Pyhäntunturi, Finland, p. 9.
- Fikse, S., et al., 2006. COST-727, atmospheric icing on structures: 2006, measurements and data collection on icing: state of the art. *MeteoGwiss* **75** (110).
- Fikse, S.M., Säänti, K., Laakso, T., 2005. Detectors for Atmospheric Icing," BOREAS VII. FMI, Saariselkä, Finland, p. 8.
- Fortin, J.P.G., Ilinca, A., 2005. A study of icing events at Murdochville: conclusions for the wind power industry. In: International Symposium "Wind Energy in Remote Regions", Magdalen's Island.
- Gillenswater, D., 2006. Pertes de Puissance Associées aux Phénomènes Givrants sur une Éolienne Installée en Climat Nordique," Master Thesis. ÉTS, Montréal, Canada, p. 162.
- Gómez Muñoz, C.Q., García Márquez, F.P., Sánchez Tomás, J.M., 2016. Ice detection using thermal infrared radiometry on wind turbine blades. *Measurement* **93**, 157–163. <https://doi.org/10.1016/j.measurement.2016.06.064>.
- Graham, H., Geladi, P., 2007. Techniques and Applications of Hyperspectral Image Analysis. John Wiley & Sons.
- Han, Y., Li, J., Zhang, Y., Hong, Z., Wang, J., 2017. sea ice detection based on an improved similarity measurement method using hyperspectral data. In: eng (Ed.), *Sensors* **17** (5), 1124. <https://doi.org/10.3390/s17051124>.

- Harstveit, K., Tallhaug, L., Fjidge, A., 2005. Ice Accumulation Observed by Use of Web Camera and Modelled from Meteorological Parameters, BOREAS VII. FMI, Saariselkä, Finland, p. 10.
- Homola, M.C., Nicklasson, P.J., Sundbom, P.A., 2006. Ice sensors for wind turbines. *Cold Reg. Sci. Technol.* 46 (2), 125–131. <https://doi.org/10.1016/j.coldregions.2006.06.005>.
- Ilinca, A., 2011. Analysis and Mitigation of Icing Effects on Wind Turbines. ISO-12494, 2001. Atmospheric Icing of Structures, 56. ISO Copyright Office, Geneva, Switzerland.
- Jaeger, J., 2021. Explaining the Exponential Growth of Renewable Energy. WORLD RESOURCES INSTITUTE. <https://www.wri.org/insights/growth-renewable-energy-sector-explained>.
- Kabardin, I., et al., 2021. Optical methods for measuring icing of wind turbine blades. *Energies* 14 (20), 6485 [Online]. Available: <https://www.mdpi.com/1996-1073/14/20/6485>.
- Khoder, M., Kashana, S., Khoder, J., Younes, R., 2017. 2. Multicriteria Classification Method for Dimensionality Reduction Adapted to Hyperspectral Images, 11, 025001.
- Kim, H.-G., Kang, Y.-H., Kim, J.-Y., 2017. Evaluation of wind resource potential in mountainous region considering morphometric terrain characteristics. *Wind Eng.* 41 (2), 114–123. April.
- Kimura, S., Tammelin, B., Sääntti, K., 2000. Estimation of Reduction of Power Due to Icing from the Existing Meteorological Data, BOREAS V. FMI, Levi, Finland, p. 12.
- Laakso, G.R.T., Tallhaug, L., Horbaly, R., Baring-Gould, I., Lacroix, A., Peltola, E., 2005. Wind Energy Projects in Cold Climates, 36. International Energy Agency [Online]. Available: <http://arcticwind.vtt.fi>.
- Laakso, T., et al., 2003. State-of-the-art of Wind Energy in Cold Climates. IEA Wind Annex XIX, p. 53.
- Laakso, T., Peltola, E., Antikainen, P., Peuranen, S., 2003. Comparison of Ice Sensors for Wind Turbines, BOREAS VI. FMI, Pyhänturi, Finland, p. 11.
- Liu, Y., Cheng, H., Kong, X., Wang, Q., Cui, H., 2019. Intelligent wind turbine blade icing detection using supervisory control and data acquisition data and ensemble deep learning. *Energy Sci. Eng.* 7 (6), 2633–2645. <https://doi.org/10.1002/ese3.449>.
- Madi, E., Pope, K., Huang, W., Iqbal, T., 2019. A review of integrating ice detection and mitigation for wind turbine blades. *Renew. Sustain. Energy Rev.* 103, 269–281. <https://doi.org/10.1016/j.rser.2018.12.019>, 2019/04/01/.
- Malkki, I., et al., 2018. RBF neural network for landmine detection in hyperspectral imaging. In: 2018 7th European Workshop on Visual Information Processing (EUVIP). IEEE, pp. 1–6.
- Makkonen, L., Laakso, T., Marjanemi, M., Finstad, K.J., 2001. Modelling and prevention of ice accretion on wind turbines. *Wind Eng.* 25 (1), 3–21.
- Marjanemi, M., et al., 2000. Wind Turbines in Light Icing Conditions — Experience of the Pori 8 MW Wind Farm, BOREAS V. FMI, Levi, Finland, p. 13.
- Marjanemi, M., Peltola, E., 1998. Blade Heating Element Design and Practical Experiences, BOREAS IV. FMI, Hetta, Finland, pp. 197–209.
- Márquez, F.P.G., Karyotakis, A., Papaefanis, M. (Eds.), 2018. Renewable Energies: Business Outlook 2050. Springer.
- Melit Devasoy, B., George, S., 2021. Forensic analysis of beverage stains using hyperspectral imaging. in *eng*, *Sci Rep* 11 (1). <https://doi.org/10.1038/s41598-021-85737-x>, 6512-6512.
- Niemann, H., Kjelstad Poulsen, N., Mirzaei, M., Henriksen, L.C., 2018. Fault diagnosis and condition monitoring of wind turbines. *Int. J. Adapt. Control Signal Process.* 32 (4), 586–613. <https://doi.org/10.1002/aca.2782>, 2018/04/01.
- Parent, O., Ilinca, A., 2011. Anti-icing and de-icing techniques for wind turbines: critical review. *Cold Reg. Sci. Technol.* 65 (1), 88–96. <https://doi.org/10.1016/j.coldregions.2010.01.005>.
- Peltola, E., Marjanemi, M., Kasz, J., Aarnio, E., 1996. Pyhänturi Operational Experiences, BOREAS III. FMI, Saariselkä, Finland, pp. 131–144.
- Piiego Marugán, F.P.G.M.A., Pinar Pérez, J.M., 2016. Optimal maintenance management of offshore wind farms. *Energies* 9 (46).
- Qiang, S., Lin, H., Yu, Z., 2016. Online faults diagnosis of wind turbine blades based on support vector machines. In: 2016 3rd International Conference on Systems and Informatics (ICSAI), 19–21 Nov. 2016, pp. 247–250. <https://doi.org/10.1109/ICSAI.2016.7610962>.
- Richert, F., 1996. Is Rotorcraft Icing Knowledge Transferable to Wind Turbines?, BOREAS III. FMI, Saariselkä, Finland, pp. 336–380.
- Rizk, R., Rizk, D., Kumar, A., Bayoumi, M., 2019. Demystifying emerging nonvolatile memory technologies: understanding advantages, challenges, trends, and novel applications. In: 2019 IEEE International Symposium on Circuits and Systems (ISCAS), 26–29 May 2019, pp. 1–5. <https://doi.org/10.1109/ISCAS.2019.8702390>.
- Rizk, P., Saleh, N., Younes, R., Ilinca, A., Khoder, J., 2020a. Hyperspectral imaging applied for the detection of wind turbine blade damage and icing. *Remote Sens. Appl.: Soc. Environ.* 18, 100291. <https://doi.org/10.1016/j.rse.2020.100291>, 02/01.
- Rizk, P., Al Saleh, N., Younes, R., Ilinca, A., Khoder, J., 2020b. Hyperspectral Imaging Applied for the Detection of Wind Turbine Blade Damage and icing Remote Sensing Applications: Society and Environment, 18, p. 100291. <https://doi.org/10.1016/j.rse.2020.100291>, 2020/04/01/.
- Rizk, P., Younes, R., Ilinca, A., Khoder, J., 2021. Defect Detection Using Hyperspectral Imaging Technology on Wind Turbine Blade, Remote Sensing Applications: Society and Environment, 22, p. 100522. <https://doi.org/10.1016/j.rse.2021.100522>, 05/01.
- Seifert, H., 2003. Technical Requirements for Rotor Blades Operating in Cold Climate, BOREAS VI. FMI, Pyhänturi, Finland, p. 13.
- Shajee, L.Y.P.S., Wagner, P.N., Moore, E.D., McLeod, R.R., 2013. Direct ice sensing and localized closed-loop heating for active de-icing of wind turbine blades. In: IEEE American Control Conference (ACC), pp. 634–639.
- Svevold, M., Hellstein, P., 2014. Qualitative Diagnostics of Wind-Turbine Blades Inspection Using Active Thermography.
- Tallhaug, L., 2003. Calculation of Potential Ice Risk in Norway, BOREAS VI. FMI, Pyhänturi, Finland, p. 8.
- Tammelin, H.H.B., Morgan, C., Richert, F., Seifert, H., Sääntti, K., Vølund, P., 2000. Wind Energy Production in Cold Climate.
- Tammelin, B., et al., 2000. Wind Energy Production in Cold Climate (WECO). FMI, Helsinki, Finland, p. 41.
- Tammelin, B., et al., 2005. Wind Turbines in Icing Environment: Improvement of Tools for Siting, Certification and Operation — NEW ICETOOLS. FMI, p. 127.
- Tammelin, B., Sääntti, K., 1994. Effect of Rime Accretion on Wind Energy Production in the Top Areas of Fella, BOREAS II. FMI, Pyhänturi, Finland, pp. 265–275.
- Vasefi, F., MacKinnon, N., Farkas, D.L., 2016. Chapter 16 - hyperspectral and multispectral imaging in dermatology. In: Hamblin, M.R., Avci, P., Gupta, G.K. (Eds.), *Imaging in Dermatology*. Academic Press, Boston, pp. 187–201.
- Yang, R., he, Y., Zhang, H., 2016. Progress and trends in nondestructive testing and evaluation for wind turbine composite blade. *Renew. Sustain. Energy Rev.* 60, 1225–1250. <https://doi.org/10.1016/j.rser.2016.02.026>, 07/01.
- Zhang, L., Du, B., Zheng, Y., 2010. Hybrid Detectors Based on Selective Endmembers, 6, pp. 2633–2646, 48.
- Zulficar, M., Ahmad, M., Sohaib, A., Maszara, M., Distefano, S., 2021. Hyperspectral imaging for bloodstain identification. *Sensors* 21 (9), 3045 [Online]. Available: <https://www.mdpi.com/1424-6220/21/9/3045>.

BIBLIOGRAPHIC REFERENCES

- [1] L. Shinn. "Renewable Energy: The Clean Facts." <https://www.nrdc.org/stories/renewable-energy-clean-facts> (accessed 15 June, 2020).
- [2] H. Longley. "DIGGING FOR OIL IN THE BOREAL FOREST." Hagley. <https://www.hagley.org/librarynews/digging-oil-boreal-forest> (accessed 18 March, 2020).
- [3] "Myth: The oil sands are destroying Canada's boreal forests." https://context.capp.ca/energy-matters/2019/mythbuster_oil-sands-extraction-and-canadas-boreal-forest#:~:text=The%20oil%20sands%20are%20found,is%20destroying%20Canada's%20boreal%20forest (accessed 2019).
- [4] L. Kimbrough. "More trouble with tar sands: oil extraction leading to big forest loss in Alberta." MONGABAY. <https://news.mongabay.com/2014/08/more-trouble-with-tar-sands-oil-extraction-leading-to-big-forest-loss-in-alberta/> (accessed 29 August, 2021).
- [5] "Renewables are Ready to Deliver a Renewable World: Time for Action for 100% Renewable Energy Globally." WWEA. <https://wwindea.org/renewables-are-ready-to-deliver-a-renewable-world-time-for-action-for-100-renewable-energy-globally/> (accessed 10 March, 2021).
- [6] "History of wind power." <https://www.eia.gov/energyexplained/wind/history-of-wind-power.php> (accessed 6 June, 2021).
- [7] J. Layton. "History of Wind Energy." <https://science.howstuffworks.com/environmental/green-science/wind-power.htm#pt3> (accessed 6 June, 2021).
- [8] "Where are wind turbines used." <https://icefi.org/obt/where-are-wind-turbines-used> (accessed 6 June, 2021).
- [9] E. R. PIERCE and D. WOOD. "WHAT IS A WIND TURBINE? ." <https://www.energy.gov/articles/how-wind-turbine-works> (accessed 6 June, 2021).
- [10] J. G. M. J.F. Manwell, A.L. Rogers, "History of Wind Energy " in *Wind Energy Explained – Theory, Design and Application*: John Wiley & Sons Ltd, 2002, ch. 1, pp. 11-19.
- [11] P. C. Putnam, *Power From the Wind*. New York: Van Nostrand Reinhold, 1948, p. 224.
- [12] F. R. Eldridge, *Wind Machines*, 2, illustrated ed. New York: Van Nostrand Reinhold Company, 1980, p. 214. the University of Michigan.

- [13] S. Gsänger, "Worldwide Wind Capacity Reaches 744 Gigawatts – An Unprecedented 93 Gigawatts added in 2020," *Press Releases, Statistics*. [Online]. Available: <http://wwindea.org/worldwide-wind-capacity-reaches-744-gigawatts/>
- [14] "Technical Application Papers No.13, Wind power plants," *ABB*. [Online]. Available: https://library.e.abb.com/public/92faf0c1913f5651c1257937002f88e8/1SDC007112_G0201.pdf.
- [15] M. Ragheb, "Vertical axis wind turbine." [Online]. Available: <http://mragheb.com/NPRE%20475%20Wind%20Power%20Systems/Vertical%20Axis%20Wind%20Turbines.pdf>
- [16] L. Qiu, S. Yuan, and M. Liu, "A phase synthesis based time reversal focusing method for impact and damage imaging of complex composite structures," presented at the 4th International Symposium on NDT in Aerospace 2012 - We.2.A.4, 2012. [Online]. Available: <https://www.ndt.net/article/aero2012/papers/we2a4.pdf>.
- [17] C. C. Ciang, J.-R. Lee, and H.-J. Bang, "Structural health monitoring for a wind turbine system: a review of damage detection methods," *Measurement Science and Technology*, vol. 19, no. 12, 2008, doi: 10.1088/0957-0233/19/12/122001.
- [18] M. A. S. Shohag, E. C. Hammel, D. O. Olawale, and O. I. Okoli, "Damage mitigation techniques in wind turbine blades: A review," *Wind Engineering*, vol. 41, no. 3, pp. 185-210, 2017, doi: 10.1177/0309524x17706862.
- [19] L. Z. J. Stutzmann, M. Muskulus, "Fatigue crack detection for lifetime extension of monopile-based offshore wind turbines," *Energy Procedia* vol. 137, pp. 143-151, 2017.
- [20] J. W. K. H.-B. Kim DY, Lim S, Hwang J-H, Park C-w, "Visual testing system for the damaged area detection of wind power plant blade," in *44th International symposium on robotics (ISR)*, Seoul, 2013: IEEE, pp. 1-5.
- [21] A. Young, A. Kay, S. Marshall, R. Torr, and A. Gray, "Hyperspectral imaging for erosion detection in wind turbine blades," in *HSI 2016*, England, 2016.
- [22] E. Adam, O. Mutanga, and D. Rugege, "Multispectral and hyperspectral remote sensing for identification and mapping of wetland vegetation: a review," *Wetlands Ecology and Management*, vol. 18, no. 3, pp. 281-296, 2010/06/01 2010, doi: 10.1007/s11273-009-9169-z.
- [23] M. Govender, K. Chetty, and H. Bulcock, "A review of hyperspectral remote sensing and its application in vegetation and water resource studies," *Water Sa*, vol. 33, no. 2, pp. 145-151, 2007.
- [24] G. J. Edelman, E. Gaston, T. G. van Leeuwen, P. J. Cullen, and M. C. Aalders, "Hyperspectral imaging for non-contact analysis of forensic traces," (in eng), *Forensic Sci Int*, vol. 223, no. 1-3, pp. 28-39, Nov 30 2012, doi: 10.1016/j.forsciint.2012.09.012.
- [25] D. Malkoff and W. Oliver, *Hyperspectral imaging applied to forensic medicine* (BiOS 2000 The International Symposium on Biomedical Optics). SPIE, 2000.
- [26] C. Fischer and I. Kakoulli, "Multispectral and hyperspectral imaging technologies in conservation: current research and potential applications," *Studies in Conservation*, vol. 51, no. sup1, pp. 3-16, 2006.

- [27] H. Liang, "Advances in multispectral and hyperspectral imaging for archaeology and art conservation," *Applied Physics A*, vol. 106, no. 2, pp. 309-323, 2012/02/01 2012, doi: 10.1007/s00339-011-6689-1.
- [28] J. Kuula *et al.*, *Using VIS/NIR and IR spectral cameras for detecting and separating crime scene details* (SPIE Defense, Security, and Sensing). SPIE, 2012.
- [29] P. J. Schubel and R. J. Crossley, "Wind Turbine Blade Design," *Energies*, vol. 5, no. 9, pp. 3425-3449, 2012, doi: 10.3390/en5093425.
- [30] R. L. Xiaona Li, Mengyu Wang, Yaru Liu, Baohua Zhang*, Jun Zhou, "Hyperspectral Imaging and Their Applications in the Nondestructive Quality Assessment of Fruits and Vegetables," *Hyperspectral Imaging in Agriculture, Food and Environment*, December 20th 2017, doi: 10.5772/intechopen.72250.
- [31] W. Tong, "CHAPTER 1: Fundamentals of wind energy," in *WIT Transactions on State of the Art in Science and Engineering* vol. 44, ed. Kollmorgen Corporation, Virginia, USA.: 2010 WIT Press, 2010, pp. 6-8.
- [32] "How Do Wind Turbines Work?" Wind Energy Technologies Office. <https://www.energy.gov/eere/wind/how-do-wind-turbines-work> (accessed 4 July, 2021).
- [33] J. G. M. a. A. L. R. J.F. Manwell, "Introduction: Modern Wind Energy and its Origins " in *Wind Energy Explained – Theory, Design and Application* John Wiley & Sons Ltd 2002, ch. 1, pp. 2-3.
- [34] T. J. Gasch R., *Wind turbines - design and components* (Wind Power Plants.). Berlin, Heidelberg: Springer, 2012.
- [35] L. S. David Rivkin, *Principal Rotor Components* (Wind Turbine Operations, Maintenance, Diagnosis, and Repair). Burlington, MA 01803: Jones & Bartlett Learning, LLC, 2013.
- [36] M. W. Wasilczuk, Filip & Gawarkiewicz, Rafał., "Drivetrain of a Wind Turbine," *Machine Dynamics Research*, no. 39, pp. 83-95, 2016.
- [37] A. M. Nektarios Karakasis, Thomas Nalmpantis, Christos Mademlis, "Active yaw control in a horizontal axis wind system without requiring wind direction measurement," doi: <https://doi.org/10.1049/iet-rpg.2016.0005>.
- [38] "Wind Turbine Towers." [Online]. Available: <http://www.windpower.org/en/tour/wtrb/tower.htm>
- [39] "How a Wind Turbine Works - Text Version." Office of Energy Efficiency & Renewable Energy. <https://www.energy.gov/eere/wind/how-wind-turbine-works-text-version> (accessed November, 2021).
- [40] J. P.-C. Brian Loza, Diego Cárdenas, Luis I. Minchala and Oliver Probst, "Comparative Fatigue Life Assessment of Wind Turbine Blades Operating with Different Regulation Schemes," *Applied Sciences*, vol. 9, no. 4632, 2019, doi: 10.3390/app9214632.
- [41] A. L. David A. Rivkin 'Laurel Silk, "The Rotor System," in *Wind Turbine Systems*, M. Johnson Ed. Burlington: Jones & Bartlett Learning, 2013, ch. 3.
- [42] J. G. M. J.F. Manwell, A.L. Rogers, *Wind Energy Explained: Theory, Design and Application*. University of Massachusetts, Amherst, USA: John Wiley & Sons, Ltd, 2002.

- [43] A. Ahlström, "Simulating Dynamical Behaviour of Wind Power Structures," Royal Institute of Technology, Stockholm, 2002, vol. 11.
- [44] D. A. Griffin, "WindPACT Turbine Design Scaling Studies Technical Area 1- Composite Blades for 80- to 120-Meter Rotor," in "Global Energy Concepts," National Renewable Energy Laboratory, Kirkland, Washington, NREL/SR-500-29492, 2001.
- [45] E. Hau, *Wind Turbines Fundamentals, Technologies, Applications, Economics* Springer, 2006.
- [46] "Wind Turbine Power Calculations " in "RWE npower renewables," The Royal Academy of Engineering.
- [47] A. P. K. Dykes, Y. Guo, A. Ning, R. King, T. Parsons, D. Petch, B. Resor, and P. Veers, "Effect of Tip-Speed Constraints on the Optimized Design of a Wind Turbine," National Renewable Energy Laboratory, 15013 Denver West Parkway Golden, CO 80401, NREL/TP-5000-61726, October 2014.
- [48] D. C. M. Brian R. Resor, Jonathan C. Berg, Phillip Richards, "Effects of Increasing Tip Velocity on Wind Turbine Rotor Design," Sandia National Laboratories, Albuquerque, New Mexico 87185 and Livermore, California 94550, SAND2014-3136, 2014.
- [49] D. E. A. H. Almkhtar, "Effect of drag on the performance for an efficient wind turbine blade design " *Energy Procedia*, vol. 18, pp. 404-415 2012.
- [50] M. Selig. UIUC Airfoil Coordinates Data Base [Online] Available: <http://amber.aae.uiucc.edu/~m-selig/ads.html>
- [51] G. S. Stavrakakis, "Wind Energy," *Comprehensive Renewable Energy*, vol. 2, no. 2.10 - Electrical Parts of Wind Turbines, pp. 269-328, 2012, doi: <https://doi.org/10.1016/B978-0-08-087872-0.00211-0>.
- [52] G. S. T. Maeda, "Wind turbine performance assessment and knowledge management for aerodynamic behaviour modelling and design: IEA experience," *Wind Energy Systems*, pp. 350-365, 2011, doi: <https://doi.org/10.1533/9780857090638.3.350>. Woodhead Publishing Limited.
- [53] J. M. Gordon, "Wind energy review," in *Solar Energy: The State of the Art*, D. Milborrow Ed. 2 Park Square, Milton Park, Abingdon, Oxon, OX14 4RN, USA and Canada: Earthscan, 2013, ch. 12, pp. 657-659. James & James (Science Publishers) Ltd.
- [54] "Orientation Of The Rotor Axis." Free Energy Planet. <https://www.freeenergyplanet.biz/wind-energy/orientation-of-the-rotor-axis.html> (accessed 11 May, 2021).
- [55] M. Selig, Tangler, J. L. , "Development of a Multipoint Inverse Design Method for Horizontal Axis Wind Turbines," *Wind Engineering*, vol. 19, 2, pp. 91-105, 1995.
- [56] J. Leon Mishnaevsky, Kim Branner, Helga Nørgaard Petersen, Justine Beauson, Malcolm McGugan, and Bent F. Sørensen, "Materials for Wind Turbine Blades: An Overview," *Materials (Basel)*, vol. 10, no. 1285, 11, 2017, Art no. PMC5706232.
- [57] "Wind Energy Technologies Office." <https://www.energy.gov/eere/wind/wind-energy-technologies-office> (accessed August, 2021).

- [58] H. Park, "Structural Design and Analysis of Wind Turbine Blade with Skin-Spar-Sandwich Composite Structure," *DEStech Transactions on Engineering and Technology Research*, 2017, doi: 10.12783/dtetr/apetc2017/11425.
- [59] D. J. Peery, Weingart, O. , "Low Cost Composite Blades for Large Wind Turbines," in *AIAA/SERI Conference*, Boulder CO. , 1980.
- [60] G. E. M. B. a. K. Y. Maalawi, "Structural Optimization of Wind Turbine Blades for Improved Dynamic Performance," *IntechOpen*, 2020, doi: 10.5772/intechopen.91643.
- [61] A. C. M. Little, "Fibre glass wind turbine blade manufacturing guide ", 2008.
- [62] N. R. Council, "Manufacturing Processes for Rotor Blades," in *Assessment of Research Needs for Wind Turbine Rotor Materials Technology*, C. o. A. o. R. N. f. W. T. R. M. Technology Ed. Washington, D.C.: National Academy Press, 1991, ch. 5.
- [63] E. Hau, *Windkraftanlagen (Windpower Plants)*. Berlin: Springer, 1996.
- [64] G. Gardiner. "Automated filament winding aids segmented blade production." (accessed February, 2021).
- [65] N. D. M. a. S. A. N. Tenguria, "Review on Horizontal Axis Wind Turbine Rotor Design and Optimization," *Trends in Applied Sciences Research*, vol. 6, pp. 309-344doi: 10.3923/tasr.2011.309.344.
- [66] "Pitch Control Critical for Wind Power." *Machine Design*. (accessed 2021).
- [67] G. S. Mathijs Peeters, Joris Degroote and Wim Van Paepegem, "The Concept of Segmented Wind Turbine Blades: A Review," *Energies*, vol. 10, no. 1112, 8, 2017, doi: <https://doi.org/10.3390/en10081112>.
- [68] E. S. F. Arias, "Strength and fatigue testing of large size wind turbines rotors," in "Full size natural vibration and static strength test, a reference case," Instituto de Energías Renovables, 1996, vol. 2.
- [69] P. M. W. Stephen Daynes, "A Morphing Wind Turbine Blade Control Surface," presented at the ASME 2011 Conference on Smart Materials, Adaptive Structures and Intelligent Systems, 2011.
- [70] T. J. L. Taeseong Kim, Anders Yde, "Investigation of potential extreme load reduction for a two-bladed upwind turbine with partial pitch," vol. 18, no. 8, pp. 1403-1419doi: <https://doi.org/10.1002/we.1766>.
- [71] P. D. S.L. Dixon B. Eng., C.A. Hall Ph.D., "Chapter 10 - Wind Turbines," in *Fluid Mechanics and Thermodynamics of Turbomachinery*, Seventh Edition ed.: Elsevier Inc, 2014, pp. 419-485.
- [72] R. NolanClark, "Wind Turbine Components and Descriptions: Essential Components to Have a Productive, Reliable, and Safe Wind Machine," in *Small Wind*: Elsevier Inc. , 2014, ch. 3, pp. 39-67.
- [73] "Type of hub." TU Delft. http://mstudioblackboard.tudelft.nl/duwind/Wind%20energy%20online%20reader/Static_pages/hub_type.htm (accessed 6 June, 2021).
- [74] L. Krashnappa, "Fatigue Analysis of a 7.5 MW wind turbine rotor hub," *ENGINEERING-AEROSPACE TECHNOLOGY*, GRIN Verlag, 2015. [Online]. Available: <https://www.grin.com/document/321444>

- [75] R. Gasch, *Windkraftanlagen (Windpower Plants)*. Stuttgart: B. G. Teubner, 1996.
- [76] P. H. Park Y, Ma Z, You J and Shi W, "Multibody Dynamic Analysis of a Wind Turbine Drivetrain in Consideration of the Shaft Bending Effect and a Variable Gear Mesh Including Eccentricity and Nacelle Movement," *Front. Energy Res.*, vol. 8, 604414, 2021, doi: 10.3389/fenrg.2020.604414.
- [77] B. C. Edward Hart, Gary Nicholas, Abbas Kazemi Amiri, James Stirling, James Carroll, Rob Dwyer-Joyce, Alasdair McDonald, and Hui Long, "A review of wind turbine main-bearings: design, operation, modelling, damage mechanisms and fault detection," *Wind Energy Science Discussions*, vol. 25, 2019, doi: <https://doi.org/10.5194/wes-2019-25>.
- [78] P. R.N.Childs, "Shafts " in *Mechanical Design Engineering Handbook*: Elsevier Ltd., 2014, ch. 7, pp. 255-315.
- [79] R. Harrison Hau, E., Snel, H., *Large Wind Turbines: Design and Economics*. . Chichester: John Wiley, 2000.
- [80] P. Dvorak, "What is the job of a coupling in a wind-turbine drivetrain?," *Renewable Energy Handbook*.
- [81] K. Zipp. "Couplings 101." Windpower Engineering & Development. <https://www.windpowerengineering.com/couplings-101/> (accessed 2021).
- [82] K. Zipp. "Gears & Gearboxes 101." Windpower Engineering & Development. <https://www.windpowerengineering.com/Gears-&-Gearboxes-101/> (accessed 2021).
- [83] P. Breeze, "Drive Trains, Gearboxes, and Generators," in *Wind Power Generation*: Elsevier Ltd., 2016, ch. 5, pp. 41-48.
- [84] A. G. M. Association, *Recommended Practices for Design and Specification of Gearboxes for Wind Turbine Generator Systems*. . 1500 King St, Suite 201, Alexandria, VA 22314. : American Gear Manufacturers Association 1997.
- [85] Y. G. a. R. G. Parker, "Dynamic modeling and analysis of a spur planetary gear involving tooth wedging and bearing clearance nonlinearity," *European Journal of Mechanics A/Solids*, vol. 29, pp. 1022-1033, 2010.
- [86] "Planetary Gears." Harmonic Drive SE. <https://harmonicdrive.de/en/glossary/planetary-gears> (accessed 2021).
- [87] A. f. A. Automation. "Basics of Gearbox Selection." Association for Advancing Automation. (accessed 2021).
- [88] J. M. Robert Errichello, *Application Requirements for Wind Turbines Gearboxes*. Albany, California: GEARTECH, 1994.
- [89] J. Ukonsaari, "WIND TURBINE GEARBOXES," 2016:279, 2016.
- [90] P. J. S. a. R. J. Crossley, "Wind Turbine Blade Design " *Energies* vol. 5, pp. 3425-3449, 2012, doi: doi:10.3390/en5093425.
- [91] R. Hicks, "Optimized gearbox design," in *Wind Power Generation and Wind Turbine Design*, vol. 44: WIT Press, 2010, ch. 15. WIT Transactions on State of the Art in Science and Engineering.
- [92] "DAMAGE TO GEARS." Kohara Gear Industry Co.,Ltd. https://khkgears.net/new/gear_knowledge/gear_technical_reference/damage_to_gears.html (accessed 2021).
- [93] G. Hennigan, "Maintenance and Lubrication of Wind Turbines," *Solar & Wind*

- [94] C.I.Park, "Noise characteristics of the simplified gear box by wind turbine load," presented at the International Gear Conference, 26th-28th August 2014, 2014.
- [95] Y. X. a. Z. T. Wenping Cao, "Wind Turbine Generator Technologies," in *Advances in Wind Power* R. Carriveau Ed.: IntechOpen, 2012.
- [96] "Mechanical Braking System." Danish Wind Industry Association. <http://xn--drmstrre-64ad.dk/wp-content/wind/miller/windpower%20web/en/tour/wtrb/safety.htm> (accessed 2021).
- [97] A. Bonk, "Clutch Disc and Brake Pad Friction." [Online]. Available: <https://www.motortrend.com/how-to/1604-clutch-disc-and-brake-pad-friction/>
- [98] S. Childs, Hughes, P., Saeed, A. , "Development of a Dynamic Brake Model. Proc. , " in *American Wind Energy Association Annual Conference*, Washington DC. , 1993: American Wind Energy Association.
- [99] *Regulation of the Certification of Wind Energy Conversion Systems*, Rules and Regulations IV, 1993.
- [100] M.A.Hyams, "Wind energy in the built environment," in *Metropolitan Sustainability: Understanding and Improving the Urban Environment*: Woodhead Publishing Limited, 2012, ch. 20, pp. 457-499.
- [101] M.-G. K. a. P. H. Dalhof, "Yaw Systems for wind turbines – Overview of concepts, current challenges and design methods," *Journal of Physics: Conference Series*, vol. 524 012086, 2014, doi: 10.1088/1742-6596/524/1/012086.
- [102] F. Perkins, Jones, R.W. , "The Effect of Delta 3 on a Yawing HAWT Blade and on Yaw Dynamics," presented at the Wind Turbine Dynamics, NASA Conference Publication 2185. , 1981.
- [103] S. Stubkier, Pedersen, H., Andersen, T., Markussen, K., "State of the art-hydraulic yaw systems for wind turbines," in *Proc. 12th Scandinavian International Conference on Fluid Power*, Tampere, Finland, 2011.
- [104] L. E. Van Bibber, Kelly, J. L. , "Westinghouse 600 kW Wind Turbine Design. ," in *Proc. of Windpower 1985*, Washington, DC. , 1985: American Wind Energy Association.
- [105] N. Sharpley, "Nacelles | How are they manufactured?."
- [106] G. J. Stefan Kock, D. Bosse, "Determination of Wind Turbine Main Bearing Load Distribution," *Journal of Physics Conference Series* vol. 1222, no. 012030, 1, 2019, doi: 10.1088/1742-6596/1222/1/012030.
- [107] N. Stavridou, E. Koltsakis, and C. C. Baniotopoulos, "Lattice and Tubular Steel Wind Turbine Towers.," *Energies*, vol. 13, 6325, 2020, doi: 10.3390/en13236325.
- [108] Seth J. Price and R. B. Figueira, "Corrosion Protection Systems and Fatigue Corrosion in Offshore Wind Structures: Current Status and Future Perspectives," *Coatings*, vol. 7, 25, 2017, doi: 10.3390/coatings7020025.
- [109] Xiong Liua, Cheng Lua, Gangqiang Lic, Ajit Godbolea, and Y. Chenb, "Tower load analysis of offshore wind turbines and the effects of aerodynamic damping " presented at the 8th International Conference on Applied Energy, 2016.
- [110] C Lavanya and N. D. Kumar, "Foundation Types for Land and Offshore Sustainable Wind Energy Turbine Towers," presented at the ICMED 2020, 2020.

- [111] J. Layne. "Types of Wind Turbines: Explained & Compared." <https://www.ablison.com/types-of-wind-turbines/> (accessed July, 2021).
- [112] C. A. Badurek. "Types." <https://www.britannica.com/technology/wind-turbine> (accessed July, 2021).
- [113] B. H. Jordan Hanania, Jason Donev. "Horizontal axis wind turbines." https://energyeducation.ca/encyclopedia/Types_of_wind_turbines#cite_note-WindTurbines-3 (accessed July, 2021).
- [114] Ramzy. "Types of Wind Turbines: The Quick and Easy Intro." <https://www.linquip.com/blog/types-of-wind-turbines/> (accessed 20 July, 2021).
- [115] "Types of Wind Turbines " *Centurion Energy*. [Online]. Available: <http://centurionenergy.net/types-of-wind-turbines>
- [116] B. H. Jordan Hanania, Jason Donev. "Types of wind turbines." https://energyeducation.ca/encyclopedia/Types_of_wind_turbines (accessed 20 July, 2021).
- [117] "Types of Wind Turbine." <https://www.renewableenergyhub.co.uk/main/wind-turbines/types-of-wind-turbines/> (accessed 2021).
- [118] "Types of Wind Turbines: The Quick and Easy Intro." <https://www.linquip.com/blog/types-of-wind-turbines/> (accessed 20 July, 2021).
- [119] "Savonius Wind Turbines." <http://www.reuk.co.uk/wordpress/wind/savonius-wind-turbines/> (accessed 21 July, 2021).
- [120] G. Z. Xin Jin, KeJun Gao, Wenbin Ju, "Darrieus vertical axis wind turbine: Basic research methods," *Renewable and Sustainable Energy Reviews*, vol. 42, pp. 212-225, February 2015 2014, doi: <https://doi.org/10.1016/j.rser.2014.10.021>.
- [121] T. M. Willy Tjiu, Mat Sohif, M.H. Ruslan, Kamaruzzaman Bin Sopian, "Darrieus vertical axis wind turbine for power generation I: Assessment of Darrieus VAWT configurations," *Renewable Energy*, vol. 75, pp. 50-67, 2015, doi: 10.1016/j.renene.2014.09.038.
- [122] R. O. Mcconell, "Giromill Overview," in *Wind Energy Inovative Systems Conference*, Colorado, May 23-25, 1979.
- [123] " Giromill Darrieus Wind Turbines." <http://www.reuk.co.uk/wordpress/wind/giromill-darrieus-wind-turbines/> (accessed 21 July, 2021).
- [124] Krzysztof Pytel *et al.*, "Testing the performance characteristics of specific profiles for applications in wind turbines," *E3S Web of Conferences*, vol. 108, no. Energy and Fuels, 01015, 2019.
- [125] P. McKenna, "Bladeless Wind Turbines May Offer More Form Than Function," *Massachusetts Institute of Technology's MIT Technology Review*, 2015. [Online]. Available: www.technologyreview.com.
- [126] C. Z. a. Y. Li, "Reliability Analysis of Wind Turbines," in *Stability Control and Reliable Performance of Wind Turbines*, 2018.
- [127] B. K. Cuong Dao, Christopher Crabtree, "Wind turbine reliability data review and impacts on levelisedcost of energy," *Wind Energy*, vol. 22, pp. 1848-1871, 2019, doi: <https://doi.org/10.1002/we.2404>.

- [128] S. Mein. "Top 3 Types of Wind Turbine Failure." Fire Trace International. (accessed 11 May, 2021).
- [129] K. Branner, & Ghadirian, A. Database about blade faults
- [130] *DESIGN AND MANUFACTURE OF WIND TURBINE BLADES, OFFSHORE AND ONSHORE WIND TURBINES*. DET NORSKE VERITAS, 2010.
- [131] B. Fitchett, "A WHITE PAPER ON BLADE DEFECT AND DAMAGE CATEGORIZATION," *EPRI Journal: Electric Power Research Institute*, 2020.
- [132] C. Red, "Wind turbine blades: Big and getting bigger," *Composites technology*, vol. 6, no. 1, 2008.
- [133] B. Yang and D. Sun, "Testing, inspecting and monitoring technologies for wind turbine blades: A survey," *Renewable and Sustainable Energy Reviews*, vol. 22, pp. 515-526, 2013/06/01/ 2013, doi: <https://doi.org/10.1016/j.rser.2012.12.056>.
- [134] P. A. L. Gallardo, "Static and fatigue analysis of wind turbine blades subject to cold weather conditions using finite element analysis," University of Victoria, 2011. [Online]. Available: <http://citeseerx.ist.psu.edu/viewdoc/download?doi=10.1.1.816.5835&rep=rep1&type=pdf>
- [135] E. I. Konstantinidis and P. Botsaris, "Wind turbines: current status, obstacles, trends and technologies," *IOP Conference Series Materials Science and Engineering*, vol. 161, no. 1, pp. 1-8, 2016, doi: 10.1088/1757-899X/161/1/012079.
- [136] C. Dao, B. Kazemtabrizi, and C. Crabtree, "Wind turbine reliability data review and impacts on levelised cost of energy," *Wind Energy*, vol. 22, no. 12, pp. 1848-1871, 2019, doi: 10.1002/we.2404. Wiley.
- [137] M. de Prada Gil, O. Gomis-Bellmunt, and A. Sumper, "Technical and economic assessment of offshore wind power plants based on variable frequency operation of clusters with a single power converter," *Applied Energy*, vol. 125, pp. 218-229, 15 July 2014, doi: <https://doi.org/10.1016/j.apenergy.2014.03.031>.
- [138] F. P. García Márquez, A. M. Tobias, J. M. Pinar Pérez, and M. Papaalias, "Condition monitoring of wind turbines: Techniques and methods," *Renewable Energy*, vol. 46, pp. 169-178, 10/01 2012, doi: <https://doi.org/10.1016/j.renene.2012.03.003>.
- [139] C. Marshman. "Comparison Chart: Relative Cost and Characteristics of 5 Common NDT Methods." Magnum. <https://www.magnumndt.com/comparison-chart-relative-cost-and-characteristics-of-ndt-methods-blog> (accessed 2020).
- [140] T. Oh, s.-h. Kee, J. S. Popovics, and R. W. Arndt, "Comparison of NDT Methods for Assessment of a Concrete Bridge Deck," *Journal of Engineering Mechanics*, vol. 139, no. 3, 2013, doi: 10.1061/(ASCE)EM.1943-7889.0000441.
- [141] S. Gholizadeh, "A review of non-destructive testing methods of composite materials," in *XV Portuguese Conference on Fracture, PCF 2016*, Paço de Arcos, Portugal, 2016, vol. I: Procedia Structural Integrity pp. 050-057. [Online]. Available: www.sciencedirect.com. [Online]. Available: www.sciencedirect.com
- [142] "Comparison of Non-Destructive Testing Methods." The Modal Shop. <https://www.modalshop.com/ndt/Comparison-of-Non-Destructive-Methods?ID=256> (accessed 2020).

- [143] S. Krohn, P.-E. Morthorst, and S. Awerbuch, "The Economics of Wind Energy," *European Wind Energy Association*, 2009. [Online]. Available: https://www.ewea.org/fileadmin/files/library/publications/reports/Economics_of_Wind_Energy.pdf.
- [144] R. Grigore and M. Ion, "Some considerations about operation and maintenance of wind turbine," *CIEI 2014*, vol. 1, 2014, doi: 10.13140/2.1.4734.2403.
- [145] E. J. Renaldas Raišutis, Reimondas Šliteris, Alfonsas Vladišauskas, "The review of non-destructive testing techniques suitable for inspection of the wind turbine blades," *Ultragarsas*, vol. 63, no. 2, pp. 26-30, 2008.
- [146] "World energy outlook," *IEA*, 2012. [Online]. Available: <https://www.iea.org/topics/world-energy-outlook>.
- [147] A. Sareen, C. A. Sapre, and M. S. Selig, "Effects of leading edge erosion on wind turbine blade performance," *Wind Energy*, vol. 17, pp. 1531-1542, 2014. [Online]. Available: <https://m-selig.ae.illinois.edu/pubs/SareenSapreSelig-2014-WindEnergy-Erosion.pdf>.
- [148] A. Hudecz, M. O. L. Hansen, L. Battisti, and A. Villumsen, "Icing problems of wind turbine blades in cold climates," *DTU*, 2014. [Online]. Available: http://orbit.dtu.dk/files/103715241/Adri_na_Hudecz_Afhandling.pdf.
- [149] L. J. and D. A., "Willingness to pay for reduced visual disamenities from offshore wind farms in Denmark," *Energy Policy (Elsevier)*, vol. 35, pp. 4059-4071, 2007.
- [150] A. N., "Wind turbine end of life: characterization of waste material," *Master Thesis, (Sweden: University of Gavle)*, pp. 14-15, 2015.
- [151] "Summary of Wind Turbine Accident data to 30 June 2020," *Caithness Windfarm Information Forum*. [Online]. Available: <http://www.caithnesswindfarms.co.uk/AccidentStatistics.htm>.
- [152] R. Yang, Y. He, and H. Zhang, "Progress and trends in nondestructive testing and evaluation for wind turbine composite blade," *Renewable and Sustainable Energy Reviews*, vol. 60, pp. 1225-1250, 2016, doi: 10.1016/j.rser.2016.02.026.
- [153] A. Pinho, "Turbine Blade Inspection Methods," *Brazil Windpower 2016 Conference and Exhibition, Rio de Janeiro, Brazil*, Conference 2016. [Online]. Available: <https://8p2.de/index.php/pt/downloads-pt/know-how-pt/wind-energy/67-turbine-blade-inspections-method/file>.
- [154] F. Sarasini, & Santulli, C. , "10 - Non-destructive testing (NDT) of natural fibre composites: acoustic emission technique," *A. Hodzic & R. Shanks (Eds.), Natural Fibre Composites* pp. 273-302, 2014. Woodhead Publishing.
- [155] Y. Yu, H. Cao, S. Liu, S. Yang, and R. Bai, "Image-based damage recognition of wind turbine blades," in *2nd International Conference on Advanced Robotics and Mechatronics (ICARM)*, 27-31 Aug 2017, pp. 161-166, doi: 10.1109/ICARM.2017.8273153.
- [156] C. Xie, "Research of AE Signal Processing Methods [J]," *China science and technology information*, no. 5, pp. 131-132, 2009.
- [157] P. Tchakoua, R. Wamkeue, M. Ouhrouche, F. Slaoui-Hasnaoui, T. Tameghe, and G. Ekemb, "Wind turbine condition monitoring: State-of-the-art review, new trends, and

- future challenges," *Energies*, vol. 7, no. 4, pp. 2595-2630, 2014, doi: 10.3390/en7042595.
- [158] R. Li, W. L. Du, X. J. Shen, and F. X. Li, "Overview of Fault Detection and State Diagnosis Technology in Wind Turbine Blades," *Applied Mechanics and Materials*, vol. 513-517, pp. 2983-2988, 2014, doi: 10.4028/www.scientific.net/AMM.513-517.2983.
- [159] Z. C. Zhongkui Zhu, Chuanyang Wang, "Bearing Transient Feature Detection And Extraction Based On Reassigned Scalogram [J]," *Journal of data acquisition and processing*, no. 3, 20, pp. 356-360, 2005.
- [160] R. Raisutis, Jasiunien_e, E., Sliteris, R., Vladisaukas, A., "The review of nondestructive testing techniques suitable for inspection of the wind turbine blades," *Ultragarsas* no. 2, 63, 2008, doi: www.ndt.net/search/docs.php3?MainSource.
- [161] "An Overview on Acoustic Emission Testing."
- [162] X. L. Dahao Yue, Haojun Zhang, Yesu Li, etc. , "IR Thermography Inspection of Wind Turbine Blades [J]," *Infrared Technology*, no. 10, 33, pp. 614-617, 2011.
- [163] M. A. Drewry and G. A. Georgiou, "A review of NDT techniques for wind turbines," *Insight*, vol. 49, no. 3, 2007. [Online]. Available: www.ndt.net/search/docs.php3?id=4550.
- [164] T. Chady, "Wind turbine blades inspection techniques," *Przegląd Elektrotechniczny*, vol. 1, no. 5, pp. 3-6, 2016, doi: 10.15199/48.2016.05.01.
- [165] L. Cheng, Tian, G.Y., "Comparison of nondestructive testing methods on detection of delaminations in composites," *Sensors* pp. 1-7, 2012, doi: <https://doi.org/10.1155/2012/408437>.
- [166] G. Boopathy, G. Surendar, A. Nema, and T. P. P. Anand, "Review on non-destructive testing of composite materials in aircraft applications," *Mech. Eng. Technol*, no. 8, pp. 1334-1342 2017. [Online]. Available: <http://www.iaeme.com/IJMET/issues.asp?JType=IJMET&VType=8&IType=8>.
- [167] P. J. a. Z. Z. Qu, "Development and Application of Infrared Thermography Non-Destructive Testing Techniques," *Sensors*, vol. 20, no. 14, 3851, 2020, doi: <https://doi.org/10.3390/s20143851>.
- [168] Y. J. Rao., "In-Fiber Bragg Grating Sensors " *Measurement science and technology*, no. 4, 8, pp. 355-375, 1997.
- [169] C. C. Ying Shi, "Study On A New Method For Condition Monitoring of The Large-Scale Wind Turbine Blades," *12th National Conference Proceedings of Fault Diagnosis*, 2010.
- [170] "Fibre Bragg grating sensor technology." [Online]. Available: <https://scaime.com/fibre-bragg-grating-technology>
- [171] K. A. Tiwari, R. Raisutis, and V. Samaitis, "Hybrid signal processing technique to improve the defect estimation in ultrasonic non-destructive testing of composite structures," (in eng), *Sensors (Basel)*, vol. 17, no. 12, Dec 9 2017, doi: 10.3390/s17122858.
- [172] W. P. Croxford A, Drinkwater B, et al. , "Strategies for guided-wave structural health monitoring," *Proceedings of the Royal Society of London A: Mathematical, Physical and Engineering Sciences* no. 463, pp. 2961-2981, 2007.

- [173] A. D. a. C. P. Lowe MJS, "Defect detection in pipes using guided waves," *Ultrasonics* vol. 36, pp. 147-154, 1998.
- [174] L. D. Yuan S, Shi L, et al. , "Recent progress on distributed structural health monitoring research at NUAA," *Journal of Intelligent Material Systems and Structures* vol. 19, pp. 373-386, 2008.
- [175] B. Hernandez Crespo, "Damage sensing in blades. In: Mare-Wint," pp. 25-52, 2016.
- [176] Kumar Anubhav Tiwari, Renaldas Raisutis, Olgirdas Tumsys, Armantas Ostreika, Kestutis Jankauskas, and J. Jakutavicius, "Defect Estimation in Non-Destructive Testing of Composites by Ultrasonic Guided Waves and Image Processing," *Electronics*, vol. 8, no. 315, 3, 2019, doi: <https://doi.org/10.3390/electronics8030315>.
- [177] A. D. P. Avdelidis N P, Ibarra-Castanedo C, Bendada A, Kenny S and Maldague X, "Structural integrity assessment of materials by thermography," presented at the Damage in Composite Materials CDCM 2006, Stuttgart, Germany, 2006.
- [178] K. C. W. Hahn F, Paynter R J H, Dutton A G, Kildegaard C and Kosgaard J "Design, Fatigue Test and NDE of a Sectional Wind Turbine Rotor Blade," *Thermoplastic Composite Material*, vol. 15, pp. 267-277, 2002.
- [179] A. Tesauo, C. Pavese, and K. Branner, "Rotor blade online monitoring and fault diagnosis technology research," *DTU Wind Energy*, Report vol. DTU Wind Energy E, No. 0042, 2014. [Online]. Available: www.orbit.dtu.dk.
- [180] G. M. Mittelman D. M., Neelamani R., Baraniuk R. G., Rudd J. V., Koch M., "Recent advances in terahertz imaging," *Applied Physics*, no. 68, Lasers and Optics, pp. 1085 – 1094, 1999.
- [181] P. Rizk, N. Al Saleh, R. Younes, A. Ilinca, and J. Khoder, "Hyperspectral imaging applied for the detection of wind turbine blade damage and icing," *Remote Sensing Applications: Society and Environment*, vol. 18, p. 100291, 04/01/2020, doi: <https://doi.org/10.1016/j.rsase.2020.100291>.
- [182] D. W. J. Frisch, L. Sripragash, Ch. Gleichweit, M. Mei, M. Goldammer, "NDT of Layered Structures Using Pulse-Thermography and THz-TDS Imaging," presented at the 14th Quantitative InfraRed Thermography Conference, 2018. [Online]. Available: <https://www.qirt2018.de/portals/qirt18/doc/We.4.A.2.pdf>.
- [183] K. H.-B. Kim DY, Jung WS, Lim S, Hwang J-H, Park C-w, "Visual testing system for the damaged area detection of wind power plant blade," *Proceedings of the 2013 44th International symposium on robotics (ISR)*, Seoul: IEEE, pp. 1-5, 2013.
- [184] M. G., "Meeting the challenge of wind turbine blade repair," *Reinf Plast* vol. 55, no. 6, 32, 2011.
- [185] C. D., "The future of blade repair," *Reinf Plast* no. 55, pp. 28-32, 2011.
- [186] H. R., "Visual fatigue and eye strain in the use of telescope," *Trans Opt Soc* pp. 22-26, 1920.
- [187] J. Baaran, "Study on visual inspection of composite structures," *European Aviation Safety Agency*, vol. 3, 2009. [Online]. Available: https://www.easa.europa.eu/sites/default/files/dfu/EASA_REP_RESEA_2007_3.pdf

- [188] M. LaMonica. "Not Afraid of Heights, Robot Inspects Wind Turbine." MIT Technology Review. <https://www.technologyreview.com/2012/06/14/185649/not-afraid-of-heights-robot-inspects-wind-turbine/> (accessed 2020).
- [189] A. Juengert and C. Grosse, "Inspection techniques for wind turbine blades using ultrasound and sound waves," in *NDTCE'09, Non-Destructive Testing in Civil Engineering*, Nantes, France, 2009.
- [190] D. P. Roach, "A Quantitative Assessment of Conventional and Advanced Nondestructive Inspection Techniques for Detecting Flaws in Composite Honeycomb Aircraft Structures," *Federal Aviation Administration*, vol. U.S. Department of Transportation, 2016. [Online]. Available: <http://www.tc.faa.gov/its/worldpac/techrpt/tc15-63.pdf>.
- [191] K. Koyama, Hoshikawa, H., & Kojima, G. , "Eddy Current Nondestructive Testing for Carbon Fiber- Reinforced Composites. Journal of Pressure Vessel Technology," no. 4, 135, 2013, doi: 10.1115/1.4023253.
- [192] I. V. Kaushal, Kiran, H.S., "A Review of Non Destructive Testing Methods for Composite Materials," 2014. Yuva Engineers Mechanical Engineering.
- [193] "Eddy Current Testing." http://www.ndttechnologies.com/products/eddy_current_testing.html (accessed 2020).
- [194] L. Dolinski, Krawczuk, M., "Damage detection in turbine wind blades by vibration based methods," *Phys.* , vol. 181, 2009. [Online]. Available: <https://doi.org/10.1088/1742-6596/181/1/012086>.
- [195] Y. H. Ryo KAWASAKIA, "Noise and Vibration Analysis of Elevator Traction Machine," *Semantic Scholar*, 2010. [Online]. Available: <https://www.semanticscholar.org/paper/Noise-and-Vibration-Analysis-of-Elevator-Traction-KAWASAKIA-HIRONAKAB/6d9da73f7ef542b3275842128d10810a15e840df/figure/2>.
- [196] Hui Hu, Linyue Gao, and Y. Liu, "Wind Turbine Icing Physics and Anti-/De-Icing," Iowa State University, 1st Edition - June 1, 2022.
- [197] L. Gao, "Experimental investigations on wind turbine icing physics and anti-/de-icing technology," Graduate Theses and Dissertations, Aerospace Engineering, Iowa State University, 17184, 2019.
- [198] T. T. Linyue Gao, Yongqian Liu, Hui Hu, "A field study of ice accretion and its effects on the power production of utility-scale wind turbines," *Renewable Energy*, vol. 167, pp. 917-928, 2021.
- [199] O. Parent and A. Ilinca, "Anti-icing and de-icing techniques for wind turbines: Critical review," *Cold Reg. Sci. Technol.* , vol. 65, pp. 88-96, 2011, doi: doi:10.1016/j.coldregions.2010.01.005.
- [200] F. Worth, "An Analysis of Freezing Rain , Freezing Drizzle , and Ice Pellets across the United States and Canada," 1976 – 90, pp. 377-390, 2004.
- [201] A.M.K.R., ROBERT M. RAUBER, and L. S. OLTHOFF, "The Relative Importance of Warm Rain and Melting Processes in Freezing Precipitation Events," *J. Appl. Meteorol.*, 2000.

- [202] Y. L. L. Gao, H. Hu, "Quantification of Dynamic Glaze Icing Process over an Airfoil Surface by using a Digital Image Projection (DIP) Technique," presented at the 2018 Atmos. Sp. Environ. Conf. , 2018.
- [203] A. Ilinca, "Analysis and Mitigation of Icing Effects on Wind Turbines," 2011.
- [204] L. Battisti, "Wind Turbines in Cold Climates," 2015, doi: 10.1007/978-3-319-05191-8.
- [205] M. R. E. Sagol, A. Ilinca, "Issues concerning roughness on wind turbine blades," *Renew. Sustain. Energy Rev.* 23 pp. 514-525, 2013, doi: 10.1016/j.rser.2013.02.034.28.
- [206] Z. F. O. Fakorede, H. Ibrahim, A. Ilinca, J. Perron, C. Masson, "Ice protection systems for wind turbines in a cold climate: characteristics, comparisons, and analysis," *Renew. Sustain. Energy Rev.* 65 pp. 662-675, 2016, doi: 10.1016/j.rser.2016.06.080.
- [207] D. J. K. Z.J. Wang, K. Lawrence DeVries, J.M. Park, "Frost formation and anti-icing performance of a hydrophobic coating on aluminum," *Exp. Therm. Fluid Sci.* 60 pp. 132-137, 2015, doi: 10.1016/j.expthermflusci.2014.09.003.
- [208] M. S. V. M.C. Homola, T. Wallenius, P.J. Nicklasson, P.A. Sundsbø, "Effect of atmospheric temperature and droplet size variation on ice accretion of wind turbine blades," *J. Wind Eng. Ind. Aerodyn.* 98 724-728 2010, doi: 10.1016/j.jweia.2010.06.007. .
- [209] G. F. F. Lamraoui, J. Perron, R. Benoit, "Canadian icing envelopes near the surface and its impact on wind energy assessment," *Cold Reg. Sci. Technol.* 120 pp. 76-88, 2015, doi: 10.1016/j.coldregions.2015.09.007.
- [210] Y. L. L. Gao, H. Hu, "An Experimental Investigation on the Dynamic Ice Accretion Process over the Surface of a Wind Turbine Blade Model," presented at the 9th AIAA Atmos. Sp. Environ. Conf. , 2017.
- [211] Y. L. L. Gao, H. Hu, "An Experimental Study on Icing Physics for Wind Turbine Icing Mitigation," pp. 1-16, 2017, doi: 10.2514/6.2017-0918.
- [212] Y. L. L. Gao, C. Kolbakir, H. Hu, "An Experimental Investigation on an ElectricThermal Strategy for Wind Turbines Icing Mitigation," presented at the 2018 Atmos. Sp. Environ. Conf. , 2018.
- [213] O. Parent and A. Ilinca, "Anti-icing and de-icing techniques for wind turbines: Critical review," *Cold Regions Science and Technology*, vol. 65, no. 1, pp. 88-96, 2011, doi: 10.1016/j.coldregions.2010.01.005.
- [214] M. C. Homola, P. J. Nicklasson, and P. A. Sundsbø, "Ice sensors for wind turbines," *Cold Regions Science and Technology*, vol. 46, no. 2, pp. 125-131, 2006, doi: 10.1016/j.coldregions.2006.06.005.
- [215] T. Laakso, et al., "State-of-the-art of wind energy in cold climates," *IEA Wind Annex XIX*, p. 53, 2003.
- [216] S. Kimura, Tammelin, B., Säntti, K., "Estimation ofReduction ofPower due to Icing from the Exixting Meteorological Data," *BOREAS V. FMI, Levi, Finland*, p. 12, 2000.
- [217] L. Battisti, Brighenti, A., Dal Savio, S., Dell'Anna, S., "Evaluation of Anti-Icing Energy and Power Requirement for Wind Turbine Rotors in Cold Climates," *BOREAS VII. FMI, Saariselkä, Findland*, p. 13, 2005.

- [218] S. Fikke, et al., "COST-727, atmospheric icing on structures: 2006, measurements and data collection on icing: state of the art," *MeteoSwiss*, vol. 75, 110, 2006.
- [219] T. Laakso, Peltola, E., Antikainen, P., Peuranen, S., "Comparison of Ice Sensors for Wind Turbines," *BOREAS VI. FMI, Pyhätunturi, Finland*, p. 11, 2003.
- [220] L. Tallhaug, "Calculation of Potential Ice Risk in Norway," *BOREAS VI. FMI, Pyhätunturi, Finland*, p. 8, 2003.
- [221] D. Craig, Craig, D., "An Investigation of Icing Events on Haeckel Hill," *BOREAS III. FMI, Saariselkä, Finland*, pp. 169-193, 1996.
- [222] G. R. T. Laakso, L. Tallhaug, R. Horbaty, I. Baring-Gould, A. Lacroix, E. Peltola "Wind Energy Projects in Cold Climates," *International Energy Agency* vol. 36, 2005. [Online]. Available: <http://arcticwind.vtt.fi>
- [223] B. Tammelin, et al., "Wind Turbines in Icing Environment: Improvement of Tools for Siting, Certification and Operation — NEW ICETOOLS," *FMI*, p. 127, 2005.
- [224] H. Seifert, "Technical Requirements for Rotor Blades Operating in Cold Climate," *BOREAS VI. FMI, Pyhätunturi, Finland*, p. 13, 2003.
- [225] M. Bellis. "History of the Anemometer." Thought co. <https://www.thoughtco.com/history-of-the-anemometer-1991222> (accessed 2020).
- [226] ISO-12494, "Atmospheric Icing of Structures," *ISO Copyright Office, Geneva, Switzerland*, p. 56, 2001.
- [227] S. M. Fikke, Säntti, K., Laakso, T., "Detectors for Atmospheric Icing," *BOREAS VII. FMI, Saariselkä, Finland*, p. 8, 2005.
- [228] "Primary & Advisory Ice Detection Systems," *UTC Aerospace Systems*. [Online]. Available: <https://www.collinsaerospace.com/-/media/project/collinsaerospace/collinsaerospace-website/product-assets/marketing/i/ice-detection/primary-and-advisory-ice-detection-systems.pdf?rev=5ecbc2a84b4c40a4adc75d08b5c5937e>.
- [229] H. Dobesch, Zach, S., Tran, H.V., "A New Map of Icing Potentials in Europe — Problems and Results," *BOREAS VI. FMI, Pyhätunturi, Finland*, p. 9, 2003.
- [230] L. Battisti, Fedrizzi, R., Dell'Anna, S., Rialti, M., "Ice Risk Assessment for Wind Turbine Rotors Equipped with De-Icing Systems," *BOREAS VII. FMI, Saariselkä, Finland*, p. 11, 2005.
- [231] "Automated Cloud Base and Visibility Measurement." SKYbrary. https://www.skybrary.aero/index.php/Automated_Cloud_Base_and_Visibility_Measurement (accessed 2020).
- [232] "Hygrometer for temperature, relative humidity and dew point measurement." BB Sensors. <https://shop.bb-sensors.com/en/Sale/Hygrometer-for-temperature-relative-humidity-and-dew-point-measurement.html> (accessed 2020).
- [233] S. Dimartino. "Mesoscale Models And Winter Forecasting." Weather Concierge. <https://www.weatherconciierge.com/mesoscale-models-and-winter-forecasting/> (accessed 2020).
- [234] K. Harstveit, Tallhaug, L., Fidje, A., "Ice Accumulation Observed by Use of Web Camera and Modelled from Meteorological Parameters," *BOREAS VII. FMI, Saariselkä, Finland*, p. 10, 2005.

- [235] M. Marjaniemi, et al., "Wind Turbines in Light Icing Conditions — Experience of the Pori 8 MW Wind Farm," *BOREAS V. FMI, Levi, Finland*, p. 13, 2000.
- [236] L. Makkonen, Laakso, T., Marjaniemi, M., Finstad, K.J., "Modelling and prevention of ice accretion on wind turbines," *Wind Engineering*, vol. 25, 1, pp. 3-21, 2001.
- [237] B. Tammelin, Säntti, K., "Effect of Rime Accretion on Wind Energy Production in the Top Areas of Fells," *BOREAS II. FMI, Pyhätunturi, Finland*, pp. 265-275, 1994.
- [238] E. Peltola, Marjaniemi, M., Kaas, J., Aarnio, E., "Pyhätunturi Operational Experiences," *BOREAS III. FMI, Saariselkä, Finland*, pp. 131-144, 1996.
- [239] "ViewEye 8 IR LED 1000TVL 3.5" Color LCD Monitor Underwater Ice Video Fishing Camera System Visual Video Fish Finder Fishcam." imall. <https://imall.com/product/ViewEye-8-IR-LED-1000TVL-3.5%27%27-Color-LCD-Monitor-Underwater-Ice-Video-Fishing-Camera-System-Visual-Fish-Finder-Fishcam/Security-Protection-Surveillance-Cameras/aliexpress.com/32836481382/567-3222316/en> (accessed 2020).
- [240] "Stall." BladeCleaning. http://www.bladecleaning.com/problematika_EN.htm (accessed 2020).
- [241] "Sensors." Bruel & Kjaer Vibro. <https://www.bkvbros.com/en/products/vibration-sensors.html> (accessed 2020).
- [242] A. M. Ahmed, S. K. Ibrahim, and S. Yacout, "Hyperspectral Image Classification Based on Logical Analysis of Data," in *2019 IEEE Aerospace Conference*, 2-9 March 2019, pp. 1-9, doi: 10.1109/AERO.2019.8742023.
- [243] P. Singh *et al.*, "8 - Hyperspectral remote sensing in precision agriculture: present status, challenges, and future trends," in *Hyperspectral Remote Sensing*, P. C. Pandey, P. K. Srivastava, H. Balzter, B. Bhattacharya, and G. P. Petropoulos Eds.: Elsevier, 2020, pp. 121-146.
- [244] D. R. Green, J. J. Hagon, C. Gómez, and B. J. Gregory, "Chapter 21 - Using Low-Cost UAVs for Environmental Monitoring, Mapping, and Modelling: Examples From the Coastal Zone," in *Coastal Management*, R. R. Krishnamurthy, M. P. Jonathan, S. Srinivasalu, and B. Glaeser Eds.: Academic Press, 2019, pp. 465-501.
- [245] "WHAT IS HYPERSPECTRAL IMAGING?" analytik. <https://analytik.co.uk/what-is-hyperspectral-imaging/> (accessed 2021).
- [246] N.-B. Chang; and K. Bai, *Multisensor Data Fusion and Machine Learning for Environmental Remote Sensing*, 1st ed. CRC Press, 2017, p. 528.
- [247] S. Lundeen. "AVIRIS - Airborne Visible/Infrared Imaging Spectrometer." Jet Propulsion Laboratory - NASA. <https://aviris.jpl.nasa.gov/> (accessed 2021).
- [248] J. Khoder and F. B. Ouezdou, "Nouvel algorithme pour la réduction de la dimensionnalité en imagerie hyperspectrale," Université de Versailles-Saint-Quentin-en-Yvelines, 2013.
- [249] M. Borengasser, W. S. Hungate, and R. Watkins, *Hyperspectral Remote Sensing: Principles and Applications*. CRC Press, 2007.
- [250] "What is hyperspectral imaging?" middleton SPECTRAL VISION. <https://www.middletonspectral.com/resources/what-is-hyperspectral-imaging/> (accessed 2021).

- [251] G. J. Edelman, E. Gaston, T. G. van Leeuwen, P. J. Cullen, and M. C. G. Aalders, "Hyperspectral imaging for non-contact analysis of forensic traces," *Forensic Science International*, vol. 223, no. 1, pp. 28-39, 30 November 2012, doi: <https://doi.org/10.1016/j.forsciint.2012.09.012>.
- [252] M. Khoder, S. Kashana, J. Khoder, and R. Younes, "Multicriteria classification method for dimensionality reduction adapted to hyperspectral images," vol. 11, no. 2, p. 025001, 2017.
- [253] E. Christophe, D. Leger, and C. Mailhes, "Quality criteria benchmark for hyperspectral imagery," *IEEE Transactions on Geoscience and Remote Sensing*, vol. 43, no. 9, pp. 2103-2114, 2005, doi: 10.1109/TGRS.2005.853931.
- [254] G. Hinton and S. Roweis, "Stochastic Neighbor Embedding," *Advances in neural information processing systems*, 2002.
- [255] S.-E. Qian, *Dimensionality Reduction of Hyperspectral Imagery* (Optical Satellite Signal Processing and Enhancement). SPIE (in English), 2013.
- [256] D. Ruiz Hidalgo, B. Bacca Cortés, and E. Caicedo Bravo, "Dimensionality reduction of hyperspectral images of vegetation and crops based on self-organized maps," *Information Processing in Agriculture*, vol. 8, no. 2, pp. 310-327, 01/06 2021, doi: <https://doi.org/10.1016/j.inpa.2020.07.002>.
- [257] D. N. Barnett, "Hyperspectral Imaging - a Technology Update." [Online]. Available: https://www.pro-lite.co.uk/File/blog_spectral_imaging_update.php
- [258] A. Smith *et al.*, *Hyperspectral mine detection phenomenology program* (AeroSense '99). SPIE, 1999.
- [259] P. S. Thenkabail and J. G. Lyon, *Hyperspectral remote sensing of vegetation*. CRC press, 2016.
- [260] M. Zulfiqar, M. Ahmad, A. Sohaib, M. Mazzara, and S. Distefano, "Hyperspectral Imaging for Bloodstain Identification," *Sensors*, vol. 21, no. 9, p. 3045, 2021. [Online]. Available: <https://www.mdpi.com/1424-8220/21/9/3045>.
- [261] P. Rizk, N. Saleh, R. Younes, A. Ilinca, and J. Khoder, "Hyperspectral imaging applied for the detection of wind turbine blade damage and icing," *Remote Sensing Applications: Society and Environment*, vol. 18, p. 100291, 02/01 2020, doi: 10.1016/j.rsase.2020.100291.
- [262] I. Makki *et al.*, "RBF Neural Network for Landmine Detection in Hyperspectral Imaging," in *2018 7th European Workshop on Visual Information Processing (EUVIP)*, 2018: IEEE, pp. 1-6.
- [263] F. Vasefi, N. MacKinnon, and D. L. Farkas, "Chapter 16 - Hyperspectral and Multispectral Imaging in Dermatology," in *Imaging in Dermatology*, M. R. Hamblin, P. Avci, and G. K. Gupta Eds. Boston: Academic Press, 2016, pp. 187-201.
- [264] J. Broadwater, Chellappa, R., "Hybrid detectors for subpixel targets," no. 11, 29, pp. 1891-1903, 2007.
- [265] L. Zhang, B. Du, and Y. Zhong, "Hybrid detectors based on selective endmembers," *IEEE Transactions on Geoscience and Remote Sensing* vol. 48, no. 6, pp. 2633-2646, 2010, doi: <https://doi.org/10.1109/TGRS.2010.2040284>.
- [266] R. Rizk, D. Rizk, A. Kumar, and M. Bayoumi, "Demystifying Emerging Nonvolatile Memory Technologies: Understanding Advantages, Challenges, Trends, and Novel

- Applications," in *2019 IEEE International Symposium on Circuits and Systems (ISCAS)*, 26-29 May 2019 2019, pp. 1-5, doi: 10.1109/ISCAS.2019.8702390.
- [267] H. Grahn, Geladi, P., "Techniques and Applications of Hyperspectral Image Analysis," *John Wiley & Sons*, 2007.
- [268] R. Bro and C. M. Andersen, "Theory of net analyte signal vectors in inverse regression," vol. 17, no. 12, pp. 646-652, 2003.
- [269] P. Rizk, R. Younes, A. Ilinca, and J. Khoder, "Wind turbine blade defect detection using hyperspectral imaging," *Remote Sensing Applications: Society and Environment*, vol. 22, p. 100522, 01/04 2021, doi: <https://doi.org/10.1016/j.rsase.2021.100522>.
- [270] D. Malacara, *Color Vision and Colorimetry: Theory and Applications*, 2nd ed. Bellingham, WA: SPIE Press, 2011, p. 188.
- [271] P. Rizk, R. Younes, A. Ilinca, and J. Khoder, "Wind turbine ice detection using hyperspectral imaging," *Remote Sensing Applications: Society and Environment*, vol. 26, p. 100711, 01/04 2022, doi: <https://doi.org/10.1016/j.rsase.2022.100711>.

